

UNIVERSITY OF NAPLES FEDERICO II

DEPARTMENT OF STRUCTURES FOR ENGINEERING AND
ARCHITECTURE

&

DEPARTMENT OF CIVIL, ARCHITECTURAL, AND
ENVIRONMENTAL ENGINEERING



PH.D. PROGRAMME IN
STRUCTURAL AND GEOTECHNICAL ENGINEERING AND
SEISMIC RISK

XXXV CYCLE

Coordinator: Prof. Iunio Iervolino

Francesco Gargiulo

MULTI-LEVEL ANALYSIS OF SEISMIC GROUND INSTABILITY IN THE VOLCANIC ISLAND OF ISCHIA (ITALY)

Tutor: Prof. Francesco Silvestri

Co-tutors: Prof. Anna d'Onofrio & Prof. Antonio Santo

2023

Vi siete mai chiesti cos'è il caffè? Il caffè è una scusa.
Una scusa per dire a un amico che gli vuoi bene.

Luciano De Crescenzo

In questo mondo del progresso, in questo mondo pieno di missili e di bombe atomiche, io penso che Napoli sia ancora l'ultima speranza che ha l'umanità per sopravvivere.

1984 - Così parlò Bellavista

Luciano De Crescenzo

Acknowledgments

The acknowledgements section is available only in the printed version.

Table of contents

1.	Introduction	27
1.1	Framework and objectives of the study	27
1.2	Outline of the thesis	29
2.	Study area	30
2.1	Structural and geological setting.....	30
2.2	Hydrogeological setting	36
2.3	Seismological setting.....	38
2.3.1	2017 Ischia Earthquake.....	45
3.	Earthquake-induced instabilities	50
3.1	Liquefaction	50
3.2	Slope stability.....	55
4.	Methodology	59
4.1	Seismic action definition.....	59
4.1.1	Synthetic parameters.....	60
4.1.2	Time histories	62
4.2	Analysis methods	69
4.2.1	Liquefaction.....	70
4.2.2	Slope stability.....	87
5.	Database of investigations	92
5.1	Casamicciola Terme study area.....	97

5.1.1 Boreholes, SPT, CPT.....	100
5.1.2 Down-hole tests.....	107
5.1.3 Electrical Resistivity Tomography.....	110
5.1.4 Microtremor Horizontal to Vertical Spectral Ratio analysis.....	113
5.1.5 Physical properties.....	117
5.1.6 Permeability tests.....	120
5.1.7 Oedometric test.....	121
5.1.8 Cyclic and monotonic resistance.....	123
5.1.9 Cyclic torsional shear test.....	139
5.2 Lacco Ameno study area.....	140
5.2.1 Boreholes, SPT.....	150
5.2.2 Down-hole tests.....	152
5.2.3 Inclinomeric measurements.....	154
5.2.4 Electrical Resistivity Tomography.....	156
5.2.5 Microtremor Horizontal to Vertical Spectral Ratio analysis.....	160
5.2.6 Physical properties.....	162
5.2.7 Direct shear tests.....	163
6. Geotechnical model.....	165
6.1 Casamicciola Terme test site.....	165
6.2 Lacco Ameno test site.....	170
7. Results.....	177
7.1 Seismic input.....	177

7.1.1 Synthetic parameters and shakemaps.....	177
7.1.2 Code-compatible accelerograms.....	181
7.1.3 Simulated accelerograms with EXSIM code	183
7.2 Liquefaction susceptibility assessment	193
7.2.1 Screening criteria	193
7.2.2 Semi-empirical methods	195
7.2.3 Simplified dynamic analyses	203
7.2.4 Advanced dynamic analyses with SCOSSA-PWP code	206
7.3 Slope stability assessment.....	219
7.3.1 Seismic performance at territorial scale.....	219
7.3.2 Advanced dynamic analyses with FLAC code.....	226
8. Conclusions	234
9. References	241
Appendix A.1	255
Appendix A.2	263

List of figures

Figure 2-1: Volcanic region of Campania Plain.....	30
Figure 2-2: Structural setting of the island of Ischia (Chiesa & Vezzoli, 1983) 1) Mt. Epomeo Horst, 2) Marginal depressed areas of the Mt. Epomeo Horst, 3) Stable block of Mt. Torone-Vezzi-Cotto, 4) Ischia Graben.	31
Figure 2-3: Conceptual scheme of horst and graben in extensional processes.	32
Figure 2-4: Geo-lithological map of the three municipalities (Casamicciola Terme, Lacco Ameno and Forio) of the N-W sector of the Island of Ischia.....	34
Figure 2-5: Hydrogeological map of the island of Ischia (Celico, 1999): 1) Ischia Graben sector, 2) Mt. Epomeo Horst sector, 3) Marginal areas sector, 4) Volcanic complexes sector...36	
Figure 2-6: Potential potentiometric surface of the basal aquifer under static conditions (Piscopo et al. 2019).....	38
Figure 2-7: Location of epicentres of main historical events that occurred on Ischia and associated area of maximum damage.....	39
Figure 2-8: History of seismic intensity in Ischia island.	40
Figure 2-9: Macroseismic field map of the 1828 (a), 1881 (b) and 1883 (c) events (modified from Alessio et al. 1996).....	43
Figure 2-10: Historical earthquake-induced instabilities in the N-W sector of Ischia Island (Guadagno & Mele, 1995; Del Prete & Mele, 2006; Martino et al. 2021).	44
Figure 2-11: View of the two landslides (EQ1883) above ‘Fango’ bolded in Figure 2-10 (from Johnston-Lavis, 1885).....	44
Figure 2-12: Location of the epicentre of the 2017 earthquake (INGV) and the ‘IOCA’ accelerometer station.	46
Figure 2-13: Waveforms from the 21 August 2017 event recorded at the ‘IOCA’ accelerometer station.	46
Figure 2-14: Pseudo-acceleration, pseudo-velocity and displacement spectra of all three ground motion components recorded at the IOCA station.	48
Figure 2-15: Horizontal to Vertical spectral ratio (H/V) for both components recorded at IOCA station.....	49
Figure 3-1: Particle configuration in a soil before, during and after liquefaction.....	51
Figure 3-2: Records of cyclic torsional shear tests on loose (a) and dense sand (b) (Ishihara, 1985).....	52
Figure 3-3: Stress-path and stress-strain curve for loose sand (shear stress τ is normalised with respect to the effective stress σ') (Ishihara, 1985).	52
Figure 3-4: Stress path and stress-strain curve for dense sand (shear stress τ is normalised with respect to the effective stress σ') (Ishihara, 1985).	53
Figure 3-5: Slope stability conditions: seismic and post-seismic displacements.....	55
Figure 3-6: Mechanisms of slope instability under static (a) and seismic (b) conditions.....	56

Figure 3-7: Mechanisms of earthquake-induced landslides according to Keefer's classification (1984).....	58
Figure 4-1: Steps of Deterministic Seismic Hazard Analysis (a) and Probabilistic Seismic Hazard Analysis (b).	59
Figure 4-2: Seismic hazard map of the national territory in terms of reference acceleration with probability of exceedance of 10% in 50 years (a) and Seismogenetic Zoning ZS9 of Italy (Meletti & Valensise, 2004) (b).	61
Figure 4-3: Flowchart for point-source stochastic ground motion simulation (from Boore, 2003).	64
Figure 4-4: Finite fault geometry.....	68
Figure 4-5: Empirical screening criteria for liquefaction phenomena (Galli, 2000).	71
Figure 4-6: Grain size distribution-based criteria for liquefaction susceptibility for the Italian Building Code (from NTC18).	72
Figure 4-7: CPT-based soil behaviour type classification chart by Robertson (1990).	73
Figure 4-8: Seismic action in pseudo-static analysis.	76
Figure 4-9: MSF relationship for clay and sand (Boulanger & Idriss, 2007).	77
Figure 4-10: Overburden correction factor relationships (Boulanger & Idriss, 2014) (a) and static shear stress correction factor (Harder & Boulanger, 1997) (b).	77
Figure 4-11: Schematic of the approach used to develop relationships between the in-situ CRR and the results of in-situ tests (Idriss & Boulanger, 2008).	78
Figure 4-12: Liquefaction abacuses for CPT (above) and SPT (below) (modified from Boulanger & Idriss, 2014).	79
Figure 4-13: Liquefaction abacus at varying normalised shear wave velocity V_{S1} as a function of fine content (Andrus & Stokoe, 2000).	81
Figure 4-14: Outline of procedure for simplified dynamic liquefaction analysis.	82
Figure 4-15: Relationship between post-liquefaction volumetric strain.....	85
Figure 4-16: Stress-void ratio path in the one-dimensional consolidation plane (NCL = Normal Consolidation Line).	85
Figure 4-17: Upper bound magnitude-distance curves for the three landslide categories (Cat I:	88
Figure 4-18: Flowchart of the procedure for the prediction of earthquake-induced displacements (Gargiulo et al. 2022).	90
Figure 5-1: Available surveys in the study area prior to the MASLIDE project: PRG (in green), SMIII (in blue) and others collected from various studies (in yellow).	92
Figure 5-2: Location of boreholes from which undisturbed samples were taken for static and/or cyclic laboratory tests: PRG (in green), SMIII (in blue) and others collected from various studies (in yellow).	93
Figure 5-3: Distribution of the available tests: boreholes (BH), down-holes (DH), surface wave tests (MASW), HVSR spectral ratios and ARRAY 2D.	94
Figure 5-4: Distribution of the available laboratory tests.	95

Figure 5-5: Potentially liquefiable areas (in light blue) and potentially unstable areas for landslide phenomena (in light red) in the N-W sector of the island of Ischia. The blue and red boxes indicate the representative areas for the two phenomena, respectively.	96
Figure 5-6: Study area for liquefaction susceptibility analysis.	97
Figure 5-7: Homogeneous micro-zones in seismic perspective (MOPS) classification (SM studies) in Casamicciola Terme study area.....	98
Figure 5-8: Stratigraphic column with lithostratigraphic description (MOPS 2003).	99
Figure 5-9: Boreholes location and depth reached in brackets UniNa (2022), Campania Region (2022), Master Plan (1990) in the Casamicciola Terme study area.....	101
Figure 5-10: Stratigraphic columns with geological description.	103
Figure 5-11: Stratigraphic columns with geo-lithological description (codes are from SM studies).....	104
Figure 5-12: SPT test results in Casamicciola Terme study area.	105
Figure 5-13: Location of CPT tests performed within the UniNA-MASLIDE project.	106
Figure 5-14: CPT test results for CPT1 (a) and CPT2 (b).	106
Figure 5-15: Dromochrone (a) and S-wave velocity profile (b) measured in BH1.	107
Figure 5-16: Dromochrone (a) and P-wave velocity profile (b) measured in BH1.	108
Figure 5-17: Dromochrone (a) and S-wave velocity profile (b) measured in BH2.	108
Figure 5-18: Dromochrone (a) and P-wave velocity profile (b) measured in BH2.	109
Figure 5-19: Comparison of shear wave velocity profiles in BH1 (black), BH2 (dark grey) and velocity ranges defined by the MS studies for MOPS 2003.	109
Figure 5-20: Location of ERT performed within the UniNA-MASLIDE project.....	110
Figure 5-21: ERT5 results in both Wenner-Schlumberger (above) and Dipole-Dipole (below) configuration.....	111
Figure 5-22: ERT6 results in both Wenner-Schlumberger (above) and Dipole-Dipole (below) configuration.....	111
Figure 5-23: ERT7 results in both Wenner-Schlumberger (above) and Dipole-Dipole (below) configurations.	112
Figure 5-24: Location of HVSR performed within the UniNA-MASLIDE project.....	113
Figure 5-25: Vertical (Z), north-south (N) and east-west (E) components of an example of signal	114
Figure 5-26: Location of the HVSR measurement points: the points in black and grey show a fundamental frequency around 0.5 Hz and 2 Hz respectively. The dashed black line roughly indicates the transition between the two zones: point C09 in red shows an intermediate amplification function between the two zones.	115
Figure 5-27: Fundamental frequencies and amplification functions measured in the western and eastern zone of the test area. The amplification function relevant to site C09, which falls in a transition zone, is plotted in red.....	116
Figure 5-28: Details of the laboratory tests carried out on the samples taken in the UniNA_BH1 (a) and UniNA_BH2 (b) survey.....	117

Figure 5-29: Grain-size distributions of the materials shown in Figure 5-28. The black dashed and non-dashed lines indicate the grain size ranges of the potentially liquefiable soils for $U_c < 3.5$ and $U_c > 3.5$, respectively.....	117
Figure 5-30: Casagrande plasticity chart of boreholes samples.....	119
Figure 5-31: Activity chart of boreholes samples.....	119
Figure 5-32: Results of permeability tests.....	120
Figure 5-33: Result of oedometric test on SMpi specimen in σ'_v -e plane.....	121
Figure 5-34: Result of oedometric test on SMpi specimen: oedometric modulus value in loading-unloading cycles.....	121
Figure 5-35: Experimental vs analytical oedometric compressibility curve.....	122
Figure 5-36: Basic system components of Cyclic Simple Shear (CSS) apparatus with confining pressure (Mele, 2020).	124
Figure 5-37: Results of monotonic test on SMpi (BH2-U.S.1) in the planes τ - γ (a), τ - σ'_v (b), Δu - γ (c) and τ/σ'_v - γ (d).	125
Figure 5-38: Results of monotonic test on SMca (BH2-U.S.3) in the planes τ - γ (a), τ - σ'_v (b), Δu - γ (c) and τ/σ'_v - γ (d).	126
Figure 5-39: Results of cyclic simple shear test on SMpi (BH2-U.S.1) with CSR=0.11 in τ - γ (a), CSR- N_{cyc} (b), τ - σ'_v (c) and γ - r_u - N_{cyc} (d) planes.	127
Figure 5-40: Results of cyclic simple shear test on SMpi (BH2-U.S.1) with CSR=0.13 in τ - γ (a), CSR- N_{cyc} (b), τ - σ'_v (c) and γ - r_u - N_{cyc} (d) planes.	128
Figure 5-41: Results of cyclic simple shear test on SMpi (BH2-U.S.1) with CSR=0.13 in τ - γ (a), CSR- N_{cyc} (b), τ - σ'_v (c) and γ - r_u - N_{cyc} (d) planes.	129
Figure 5-42: Results of cyclic simple shear test on SMpi (BH2-U.S.1) with CSR=0.16 in τ - γ (a), CSR- N_{cyc} (b), τ - σ'_v (c) and γ - r_u - N_{cyc} (d) planes.	130
Figure 5-43: Results of cyclic simple shear test on SMpi (BH2-U.S.1) with CSR=0.18 in τ - γ (a), CSR- N_{cyc} (b), τ - σ'_v (c) and γ - r_u - N_{cyc} (d) planes.	131
Figure 5-44: Results of cyclic simple shear test on SMpi (BH2-U.S.1) with CSR=0.19 in τ - γ (a), CSR- N_{cyc} (b), τ - σ'_v (c) and γ - r_u - N_{cyc} (d) planes.	132
Figure 5-45: Results of cyclic simple shear test on SMca (BH2-U.S.3) with CSR=0.11 in τ - γ (a), CSR- N_{cyc} (b), τ - σ'_v (c) and γ - r_u - N_{cyc} (d) planes.	133
Figure 5-46: Results of cyclic simple shear test on SMca (BH2-U.S.3) with CSR=0.12 in τ - γ (a), CSR- N_{cyc} (b), τ - σ'_v (c) and γ - r_u - N_{cyc} (d) planes.	134
Figure 5-47: Results of cyclic simple shear test on SMca (BH2-U.S.3) with CSR=0.16 in τ - γ (a), CSR- N_{cyc} (b), τ - σ'_v (c) and γ - r_u - N_{cyc} (d) planes.	135
Figure 5-48: Results of cyclic simple shear test on SMca (BH2-U.S.3) with CSR=0.19 in τ - γ (a), CSR- N_{cyc} (b), τ - σ'_v (c) and γ - r_u - N_{cyc} (d) planes.	136
Figure 5-49: CSS test results in the plane N_{cyc} -CRR.....	138
Figure 5-50: CSS test results in the plane N/N_L - r_u	138
Figure 5-51: Variation of normalised stiffness and damping with shear strain for the formation indicated with SFCO.....	139

Figure 5-52: Study area for slope stability analysis. The two perimeters refer to 2 landslides mapped by the CARG project falling in the same area.	140
Figure 5-53: Homogeneous micro-zones in seismic perspective (MOPS) classification (MS studies) in 'Fango' study area.....	140
Figure 5-54: MOPS 2001: stratigraphic column with lithostratigraphic description.	141
Figure 5-55: MOPS 2002: stratigraphic column with lithostratigraphic description.	142
Figure 5-56: MOPS 2003: stratigraphic column with lithostratigraphic description.	143
Figure 5-57: Velocity maps [mm/year] derived by processing of descending (above) and ascending (below) ERS (1992-2000) SAR data.....	145
Figure 5-58: Velocity maps [mm/year] derived by processing of descending (above) and ascending (below) ENVISAT (2003-2010) SAR data.....	146
Figure 5-59: Velocity maps [cm/year] derived by processing of COSMO-SkyMed (2017-2019) SAR data.....	147
Figure 5-60: Interferogram in terms of displacement before and after the 2017 earthquake event. The same figure shows the ground coseismic effects (Azzaro et al. 2017; EMERGEIO Working Group, Nappi et al. 2018).	148
Figure 5-61: Example of coseismic ruptures on Crateca road (from Nappi et al. 2017). ...	149
Figure 5-62: Boreholes location and depth reached in brackets UniNa (2022) for the characterisation of the landslide named 'Fango West'	150
Figure 5-63: Stratigraphic columns with geological description.	151
Figure 5-64: Stratigraphic columns with geo-lithological description (codes are from SM studies).....	152
Figure 5-65: Dromochrone (a) and S-wave velocity profile (b) measured in BH6.	153
Figure 5-66: Dromochrone (a) and P-wave velocity profile (b) measured in BH6.....	153
Figure 5-67: Dromochrone (a) and S-wave velocity profile (b) measured in BH8.	154
Figure 5-68: Dromochrone (a) and P-wave velocity profile (b) measured in BH8.....	154
Figure 5-69: Inclinomometer measurements taken at BH6 (a) and BH8 (b) from mid-September to the end of November 2022.....	155
Figure 5-70: Location of ERT performed in 'Fango' area within the UniNA-MASLIDE project.	156
Figure 5-71: ERT1 results in both Wenner-Schlumberger (above) and Dipole-Dipole (below) configuration.....	157
Figure 5-72: ERT2 results in both Wenner-Schlumberger (above) and Dipole-Dipole (below) configuration.....	158
Figure 5-73: ERT3 results in both Wenner-Schlumberger (above) and Dipole-Dipole (below)	159
Figure 5-74: ERT4 results in both Wenner-Schlumberger (above) and Dipole-Dipole (below) configuration.....	160
Figure 5-75: Location of HVSR performed within the UniNA-MASLIDE project.....	160

Figure 5-76: Fundamental frequencies and amplification functions separated by zone. The amplification function relevant to the sites A04 and A10 with higher fundamental frequency values are plotted in orange.	161
Figure 5-77: Grain-size distributions of the materials shown in Figure 5-63.	162
Figure 5-78: Results direct shear test of in plane τ - δ (above) and w - δ (below).	163
Figure 5-79: Results of the direct shear test: envelope of peak (a) and residual (b) values in the Mohr plane.	164
Figure 6-1: Location of environmental noise measurements adjacent to boreholes BH1 and BH2. The same figure also shows the location of a 2D array carried out during the SM studies.	166
Figure 6-2: Example of parameter input panel for inversion.	166
Figure 6-3: Best-fit model derived from inversion of array data (C15) for BH1: S-wave velocity profile (a) and comparison of experimental and analytical H/V ratio (b).	167
Figure 6-4: Best-fit model derived from inversion of array data (C04) for BH2: S-wave velocity profile (a) and comparison of experimental and analytical H/V ratio (b).	168
Figure 6-5: Experimental dependency of normalised shear modulus and damping ratio on shear strain for SM (from MS studies), SFCO (from this study) and SFGRS (Vinale et al. 1988).	169
Figure 6-6: Location of environmental noise measurements adjacent to boreholes BH6 and BH8. The same figure also shows the location of a 2D array carried out during the Microzonation studies.	170
Figure 6-7: S-wave (a) and P-wave (b) velocity profile obtained from the 2D array made in the same study area in SM studies.	171
Figure 6-8: Best-fit model derived from inversion of array data (A09) for BH6: S-wave velocity profile (a) and comparison of experimental and analytical H/V ratio (b).	172
Figure 6-9: Best-fit model derived from inversion of array data (A01) for BH8: S-wave velocity profile (a) and comparison of experimental and analytical H/V ratio (b).	173
Figure 6-10: 2D lito-stratigraphic section assumed for slope stability analyses.	174
Figure 6-11: 2D geo-lithological section assumed for slope stability analyses (codes are from Commissione Tecnica per la Microzonazione Sismica).	175
Figure 6-12: Experimental dependency of normalised shear modulus and damping ratio on shear strain for GC/GM (from MS studies), SFCO (from this study) and SFGRS (Vinale et al. 1988)	176
Figure 7-1: Hazard curves for 16th, 50th and 84th percentiles for Casamicciola Terme municipality.	177
Figure 7-2: De-aggregation analysis for Casamicciola Terme site study.	178
Figure 7-3: Maps of acceleration at bedrock (a) and surface (b).	179
Figure 7-4: Soil type classification (a) and stratigraphic amplification factor (b) maps. ...	180
Figure 7-5: Slope curvature (a) and topographic factor (b) maps.	180
Figure 7-6: Natural accelerogram time histories and response spectra (in black), average spectrum (in red) and reference NTC 2018, 475 year spectrum (in orange).	182

Figure 7-7: Definition sketch of fault plane dimension and geometry.	183
Figure 7-8: Source mechanisms proposed in the literature for the 2017 Ischia earthquake: in blue (De Novellis et al. 2018), in green (Calderoni et al. 2019) and in red (Nazeri et al. 2021). The black triangle indicates the location of the IOCA accelerometer station.	184
Figure 7-9: Crustal transfer function for EXSIM simulations.	186
Figure 7-10: Frequency-dependent quality factor function for EXSIM simulations.	186
Figure 7-11: Geometrical spreading function for EXSIM simulations.	187
Figure 7-12: Path duration function for EXSIM simulations.	187
Figure 7-13: Simulated signals at UniNA_BH1 (a) and their Fourier Amplitude (b) and pseudo-acceleration response (c) spectra. The different colours indicate the different source models used: in blue (De Novellis et al. 2018), in green (Calderoni et al. 2019) and in red (Nazeri et al. 2021).	188
Figure 7-14: Simulated signals at UniNA_BH2 (a) and their Fourier Amplitude (b) and pseudo-acceleration response (c) spectra. The different colours indicate the different source models used: in blue (De Novellis et al. 2018), in green (Calderoni et al. 2019) and in red (Nazeri et al. 2021).	189
Figure 7-15: Simulated signals at UniNA_Fango (a) and their Fourier Amplitude (b) and pseudo-acceleration response (c) spectra. The different colours indicate the different source models used: in blue (De Novellis et al. 2018), in green (Calderoni et al. 2019) and in red (Nazeri et al. 2021).	190
Figure 7-16: Geolithological map of the N-W sector of the island of Ischia (modified from Toscano et al. 2019) and (b) aquifer depth map (in m) of the same area (modified from Piscopo et al. 2019).	193
Figure 7-17: Screening criteria applied on a territorial scale: in light blue the potentially liquefiable areas. The same map shows the location of the CPT tests carried out within the UniNA-MASLIDE project.	194
Figure 7-18: CPT1 results: 'Soil Behaviour Type Index' trend with depth (a) and Robertson's abacus (b).	194
Figure 7-19: CPT2 results: 'Soil Behaviour Type Index' trend with depth (a) and Robertson's abacus (b).	195
Figure 7-20: Simplified liquefaction analyses for borehole BH1 from CPT test results: tip resistance q_c and respective corrected and normalised value q_{c1Ncs} with depth (above) and comparison between CSR and CRR (bottom).	197
Figure 7-21: Simplified liquefaction analyses for borehole BH2 from CPT test results: tip resistance q_c and respective corrected and normalised value q_{c1Ncs} with depth (above) and comparison between CSR and CRR (bottom).	198
Figure 7-22: Simplified liquefaction analyses for borehole BH1 from SPT test results: blows count N_{60} and respective corrected and normalised value $(N_1)_{60cs}$ with depth (above) and comparison between CSR and CRR (below).	199

Figure 7-23: Simplified liquefaction analyses for borehole BH2 from SPT test results: blows count N_{60} and respective corrected and normalised value $(N_1)_{60cs}$ with depth (above) and comparison between CSR and CRR (below). 200

Figure 7-24: Results of simplified liquefaction analyses for borehole BH1: LPI (on the left) and LSN (on the right) as a function of synthetic input motion parameters. The different colours indicate the different source models used: in blue (De Novellis et al. 2018), in green (Calderoni et al. 2019) and in red (Nazeri et al. 2021). In black code-compatible accelerograms. 201

Figure 7-25: Results of simplified liquefaction analyses for borehole BH2: LPI (on the left) and LSN (on the right) as a function of synthetic input motion parameters. The different colours indicate the different source models used: in blue (De Novellis et al. 2018), in green (Calderoni et al. 2019) and in red (Nazeri et al. 2021). In black code-compatible accelerograms. 202

Figure 7-26: Results of the assessment based on the comparison with cyclic resistance curve for BH1 (above) and BH2 (below). DN, C, and N refer respectively to the De Novellis et al. (2018), Calderoni et al. (2019) and Nazeri et al. (2021) source models. 204

Figure 7-27: Non-linearity curves of SM (light yellow), SFCO (dark blue) and SFGRS (light blue). 208

Figure 7-28: Experimental and modelled liquefaction strength of BH2-U.S.1 expressed as cyclic stress ratio vs number of cycles (a) and excess pore pressure ratio relationship (b)... 209

Figure 7-29: Experimental and modelled liquefaction strength of BH2-U.S.3 expressed as cyclic stress ratio vs number of cycles (a) and excess pore pressure ratio relationship (b)... 210

Figure 7-30: Geotechnical model for BH1 (a) and BH2 (b). 211

Figure 7-31: Seismic response analyses in effective stresses with the SCOSSA-PWP code for borehole BH1 using code-compatible accelerograms: profiles of a_{max} , τ_{max} and r_u with depth in undrained (above) and drained (bottom) conditions. 213

Figure 7-32: Seismic response analyses in effective stresses with the SCOSSA-PWP code for borehole BH1 using simulated accelerograms (blue, green and red are respectively associated with the De Novellis, Calderoni and Nazeri source models): profiles of a_{max} , τ_{max} and r_u with depth in undrained (above) and drained (bottom) conditions. 214

Figure 7-33: Seismic response analyses in effective stresses with the SCOSSA-PWP code for borehole BH2 using code-compatible accelerograms: profiles of a_{max} , τ_{max} and r_u with depth in undrained (above) and drained (bottom) conditions. 215

Figure 7-34: Seismic response analyses in effective stresses with the SCOSSA-PWP code for borehole BH1 using simulated accelerograms (blue, green and red are respectively associated with the De Novellis, Calderoni and Nazeri source models): profiles of a_{max} , τ_{max} and r_u with depth in undrained (above) and drained (bottom) conditions. 216

Figure 7-35: Results of advanced liquefaction analyses for borehole BH1: LSN (on the left) and I_{AM} (on the right) as a function of synthetic input motion parameters. The symbols full and empty refer to undrained and drained analyses respectively. The different colours indicate the different source models used: in blue (De Novellis et al. 2018), in green (Calderoni et al. 2019) and in red (Nazeri et al. 2021). In black code-compatible accelerograms. 217

Figure 7-36: Results of advanced liquefaction analyses for borehole BH2: LSN (on the left) and I _{AM} (on the right) as a function of synthetic input motion parameters. The symbols full and empty refer to undrained and drained analyses respectively. The different colours indicate the different source models used: in blue (De Novellis et al. 2018), in green (Calderoni et al. 2019) and in red (Nazeri et al. 2021). In black code-compatible accelerograms.....	218
Figure 7-37: Flowchart of the procedure followed at territorial scale showing the relevant maps (1).....	220
Figure 7-38: Flowchart of the procedure followed at territorial scale showing the relevant maps (2).....	221
Figure 7-39: Grain-size distribution of the soil formations shown in the Table 7-14. The thicker line type refers to the average curve.....	222
Figure 7-40: Unit weight and strength parameters maps for different percentile values.	223
Figure 7-41: Maps of critical acceleration for 16 th (a), 50 th (b) and 84 th (c) percentile.	224
Figure 7-42: Maps of earthquake-induced displacements for 16 th (a), 50 th (b) and 84 th (c) percentile. The same maps show the landslides within the study area.	225
Figure 7-43: Section (above) and FLAC dynamic scheme for the boundary conditions and numerical mesh (below).....	227
Figure 7-44: Comparison between the experimental and analytical non-linearity curves of the formations identified in Figure 6-11.	229
Figure 7-45: Results of advanced dynamic analysis with FLAC using as input the signals simulated with the source model of De Novellis (a), Calderoni (b) and Nazeri (c): contours of the maximum shear strain increment.	231
Figure 7-46: Results of advanced dynamic analysis with FLAC using as input the signals simulated with the source model of De Novellis (a), Calderoni (b) and Nazeri (c): contours of the horizontal displacements.	232
Figure 7-47: Results of advanced dynamic analysis with FLAC using as input the acc5 code-compatible accelerogram: maximum shear strain increment (above) and horizontal displacements (below) contours.	233

List of tables

Table 2-1: List of the cover soil and bedrock lithotypes, units of the geo-lithological map of Figure 2-4: codes are from <i>Commissione Tecnica per la Microzonazione Sismica</i> (2020).....	35
Table 2-2: Main historical earthquakes at Ischia (modified from De Vita et al. 2006).....	40
Table 2-3: Peak Ground Acceleration (PGA), Peak Ground Velocity (PGV), Peak Ground Displacement (PGD), Arias Intensity (AI), Housner Intensity (HI) and Significant Duration (D_{5-95}) per recorded component of ground motion at IOCA station.	47
Table 4-1: Hierarchy of seismic slope stability and liquefaction analysis methods (modified from Silvestri and d'Onofrio, 2014).....	70
Table 4-2: Coefficients of the piecewise constant-power law (Tropeano et al. 2018).	74
Table 4-3: Slope curvature (α') ranges and associated S_T (Forte, 2014).	75
Table 4-4: Simplified assessment of soil liquefaction risk based on LPI (Iwasaki et al. 1978).	84
Table 4-5: Evidences of liquefaction and damage degrees associated to LSN (Tonkin & Taylor, 2013).	86
Table 4-6: Damage scale for rigid body settlements due to earthquake-induced ground deformation.....	87
Table 5-1: Distribution of available site tests.....	93
Table 5-2: Distribution of available laboratory tests.....	93
Table 5-3: Overview of surveys in Casamicciola Terme study area.....	102
Table 5-4: Average grain-size distribution values.	118
Table 5-5: Average material properties.....	118
Table 5-6: Atterberg limits.	118
Table 5-7: Results of permeability tests.	120
Table 5-8: Values of C_c and C_s	122
Table 5-9: State of specimens in monotonic tests.....	125
Table 5-10: Summary of CSS tests on sample BH2-U.S.1 (SMpi).....	137
Table 5-11: Summary of CSS tests on sample BH2-U.S.3 (SMca).	137
Table 5-12: Overview of surveys carried out for the characterisation of the landslide 'Fango West'.....	150
Table 5-13: Grain-size distributions values.	162
Table 5-14: Material properties.	162
Table 5-15: Direct shear test results: peak values.	164
Table 5-16: Direct shear test results: residual values.	164
Table 6-1: Parameters of the best-fit model derived from the inversion of array data (C15) for BH1.	167
Table 6-2: Parameters of the best-fit model derived from the inversion of array data (C04) for BH2.	168
Table 6-3: Numerical values of the profiles in Figure 6-7.	171

Table 6-4: Parameters of the best-fit model derived from the inversion of array data (A09) for BH6.	172
Table 6-5: Parameters of the best-fit model derived from the inversion of array data (A01) for BH8.	173
Table 6-6: Strength parameters assigned to each formation identified in the Figure 6-11.	176
Table 7-1: De-aggregation of reference acceleration in terms of M, R and ε (median values).	178
Table 7-2: Peak surface acceleration used for liquefaction assessment with semi-empirical approaches.	178
Table 7-3: Parameters for DN (De Novellis et al. 2018), C (Calderoni et al. 2019) and N (Nazeri et al. 2021) source models.	185
Table 7-4: Crustal S-wave velocity model.	185
Table 7-5: Synthetic motion parameters for UniNA_BH1 for the different source mechanisms.	191
Table 7-6: Synthetic motion parameters for UniNA_BH2 for the different source mechanisms.	191
Table 7-7: Synthetic motion parameters for UniNA_Fango for the different source mechanisms.	191
Table 7-8: Coefficients for N_{eq} correlation (Biondi et al. 2012).	204
Table 7-9: MKZ and Phillips & Hashash (2009) model parameters.	207
Table 7-10: BH2-U.S.1: Parameters of pore water pressure (PWP) model.	209
Table 7-11: BH2-U.S.3: Parameters of pore water pressure (PWP) model.	210
Table 7-12: Input parameters for dynamic analyses with SCOSSA-PWP for borehole BH1.	212
Table 7-13: Input parameters for dynamic analyses with SCOSSA-PWP for borehole BH2.	212
Table 7-14: Unit weight and strength parameters.	222
Table 7-15: Physical-mechanical parameters of the model for each formation identified in Figure 6-11.	228
Table 7-16: Parameters of the sigmoid function for each formation.	230

List of symbols and abbreviations

AI	Arias Intensity
A(f)	Amplification function
a	parameter of the pore water pressure relationship
a_c	critical acceleration
a_{eq}	equivalent acceleration
a_r	reference acceleration
a_s	surface acceleration
a_{max}	maximum acceleration
BH	borehole
b	parameter of the pore water pressure relationship
CEDIT	Italian Catalogue of Earthquake-Induced Ground Failures
CPT	Cone Penetration Test
CRR	Cyclic Resistance Ratio
CSR	Cyclic Stress Ratio
CSR_r	reference value of the cyclic resistance curve
CSR_t	threshold value of the shear stress ratio
CSS	Cyclic Simple Shear test
c	parameter of the pore water pressure relationship
c'	effective cohesion
DH	downhole test
DPSH	Dynamic Penetrometer Super Heavy test
DS	Drained Shear test
DSC	Dynamic Servo-Controller
DSHA	Deterministic Seismic Hazard Analysis
DTM	Digital Terrain Model

D₀	initial damping ratio
D_r	relative density
D_w	saturated soil thickness above the sliding surface
D_{exp}	hysteretic damping measured in laboratory test
D_{mas}	hysteretic damping calculated using Masing rules
D₅₋₉₅	Significant duration
d	parameter of the pore water pressure relationship
d₁₀	particles diameter in the grain-size distribution curve corresponds to 10% passing
d₅₀	particles diameter in the grain-size distribution curve corresponds to 50% passing
ENVISAT	Environmental Satellite
ERS	European Remote Sensing
ERT	Electrical Resistivity Tomography
E_{oed}	Oedometric modulus
e	void ratio
F	Normalized ratio expressing the sleeve resistance
F_{bb}(γ)	backbone curve
F_{ur}(γ)	unloading-reloading curve
F*(γ_m)	damping reduction factor
FC	Fine Content
FFT	Fast Fourier Transform
FS	Factor of Safety or Free Surface factor
f	frequency
f_M	probability density functions of magnitude
f_R	probability density functions of distance
f_c	corner frequency

f_0	fundamental frequency
f_s	sleeve friction
f_{\max}	cut-off frequency value
GMPE	Ground Motion Prediction Equation
GPS	Global Position System
G	shear modulus
G_0	initial shear modulus
$G(\gamma_m)$	secant modulus corresponding to the maximum shear strain level, γ_m
HAPC	Hydraulic Automatic Pressure Controller
HVSR	Microtremor Horizontal to Vertical Spectral Ratio
IFFI	Inventory of landslides of Italy
I_{AM}	Induced Damage parameter
I_c	Soil Behaviour Type Index
K	Bulk modulus
k, k_w	hydraulic conductivity
k_0	coefficient of earth pressure at rest
k_α	correction factor to account for the initial static shear on the horizontal plane
k_σ	correction factor to account for the effective overburden stress
LIQ	Liquefaction
LPI	Liquefaction Potential Index
LSN	Liquefaction Severity Number
MCS	Mercalli-Cancani-Sieberg macroseismic intensity
MHE	Maximum Historical Earthquake
MKZ	Modified Kondner-Zelasko model
MOPS	Homogeneous micro-zone in seismic perspective
MSF	Magnitude Scaling Factor

M_l	local magnitude
M₀	seismic moment
M_w	moment magnitude
m	saturated soil thickness above the sliding surface
N, N_{cyc}	Number of cycles
N_L	Number of cycles corresponding to the liquefaction condition
N_{SPT}	dynamic penetrometric resistance
(N₁)_{60cs}	equivalent clean sand standard penetration resistance
N_{eq}	number of equivalent cycles
N_r	reference number of cycles
PAI	Hydrogeological Management Plan
PGA	Peak Ground Acceleration
PGD	Peak Ground Displacement
PGV	Peak Ground Velocity
PI	Plasticity Index
PRG	Master Plan
PRTITN	S-wave energy partitioning factor
PSHA	Probabilistic Seismic Hazard Analysis
PWP	Pore Water Pressure model
PZ	Piezometer
P_r	Probability of exceedance
Q	Normalized ratio expressing the tip resistance
Q(f)	frequency dependent quality factor
p₁	first non-dimensional parameter of the damping reduction factor $F^*(\gamma_m)$
p₂	second non-dimensional parameter of the damping reduction factor $F^*(\gamma_m)$
p₃	third non-dimensional parameter of the damping reduction factor $F^*(\gamma_m)$

q_c	tip resistance
q_{c1ncs}	equivalent clean sand cone penetration resistance
ℳ^{θ_r}	radiation pattern
R	distance from fault rupture surface
RC	Campania Region
R.S.	Reconstituted Sample
R_{jb}	Joyner-Boore distance
r_d	deformability reductive coefficient
r_u	pore pressure ratio
SAR	Synthetic Aperture Radar
SCOSSA	Seismic COde for Stick-Slip Analysis
SLV	Life-Saving limit state (according to NTC2018)
SMIII	III level Seismic Microzonation studies
SPT	Standard Penetration Test
SS	Slope Stability
S_s	Stratigraphic amplification factor
S_T	Topographic amplification factor
S_a	Spectral pseudo-acceleration
S_d	Spectral displacement
S_v	Spectral pseudo-velocity
s'	dimensionless factor of the MKZ model
ssi	shear strain increment
T_d	fault slip duration
T_m	Mean period
T_p	Predominant period
T_R	Return period
UniNA	University of Naples Federico II

UC	Uniformity Coefficient
U.S.	Undisturbed Sample
u	pore pressure
V_p	P-wave velocity
V_s	S-wave velocity
V_{s,eq}	Equivalent S-wave velocity
w_L	Liquid limit
w_p	Plastic limit
z_w	water table depth
α	slope angle or ratio between P-wave and S-wave velocities
α'	slope curvature
β	dimensionless factor of the MKZ model
Δσ	static stress-drop
δ_G	modulus degradation index function
δ_τ	stress degradation index function
ε_v	post-liquefaction volumetric reconsolidation strain
ε_{xx}	horizontal strain component of the strain tensor
ε_{yy}	vertical strain component of the strain tensor
ε_{xy}	shear strain component of the strain tensor
γ	unit volume weight of the soil or shear strain
γ_{DA}	Double Amplitude shear deformation
γ_w	water unit weight
γ_r	reference shear strain of the MKZ model
φ'	friction angle
κ	damage parameter
λ	wavelength

λ_Y	mean annual frequency of exceedance of a generic ground motion parameter Y
ν_i	mean annual rate of occurrence of the event at the i-th source
ν	poisson coefficient
ρ	density
σ_{v0}	total vertical stress
σ'_{v0}	effective vertical stress
σ'	effective stress
σ_h	horizontal stress
τ	shear stress
τ_c	reversal shear stress
τ_{eq}	equivalent shear stress
τ_{lim}	limit shear stress

1. Introduction

1.1 Framework and objectives of the study

Even after the seismic event occurred on August 21, 2017, the island of Ischia has historically been affected by a series of earthquakes of MCS Intensity varying between VI and X, mainly affecting the N-W sector of the island. Historical records and more recent geomorphological studies, carried out after these events, have highlighted the occurrence of numerous slope instability phenomena. These events have motivated several studies aimed at assessing the susceptibility of Ischia territory in terms of seismically induced landslide phenomena, studies, however, limited to seismic hazard and/or susceptibility assessments of an empirical-qualitative nature (Rapolla et al. 2010), or in any case not adequately supported by a robust geotechnical characterisation (Caccavale et al. 2017). As a matter of fact, the volcanic granular deposits covering a great part of the N-W area of the island are characterised by a high degree of heterogeneity and are poorly investigated under the geotechnical viewpoint. These deposits have been also involved in ruinous rapid flows along the incisions of the Epomeo volcanic rock slopes, induced even in very recent times (e.g. Monte Vezzi in 2006, see e.g. Nocentini et al. 2015; Casamicciola in 2009, see e.g. Santo et al. 2012; the recent one occurred in November 26, 2022) by critical weather events.

Granular pyroclastic soils also outcrop along the coastal areas of the municipalities historically affected by earthquakes, where they lie under the ground water table. These conditions constitute predisposing factors to the occurring of liquefaction phenomena, also evidenced by some historical documentation (De Rossi M.S., 1884). It is also worth highlighting that the peculiar lithological features of pyroclastic soils such as the presence of fragile pumice sand particles and the non-plastic ash fine content make particularly complex the assessment of the liquefaction potential of these materials (Licata et al. 2018).

Notwithstanding the significant fragility of the Ischian territory and its evident susceptibility to seismic-induced instability phenomena, no comprehensive studies have been carried out adopting a multi-hazard approach.

The recent Seismic Microzonation (SM) studies carried out after the 2017 seismic event for the municipalities of Casamicciola Terme, Lecco Ameno, and Forio were limited to the evaluation of the transient effects of seismic motion, being the main objective for the planning and management of re-construction process. These studies represent however a valuable starting point for the evaluation of the seismic induced instability conditions of the subsoil of these three municipalities with respect to landslides and liquefaction. As matter of fact, SM studies provided an advanced knowledge in terms of stratigraphic, geomorphologic, geophysical and geotechnical characterisation of the deposits thanks to the investigations specifically carried out. However, they cannot be considered sufficient to quantify the seismic safety related to slope instability and liquefaction phenomena and achieve a more conscious management and planning of the urban territory.

All these motivations encouraged the development of this Ph.D. thesis in Structural Engineering, Geotechnics and Seismic Risk, endorsed by the *Committee for the emergency management after the 2017 Ischia earthquake* and self-financed by the University of Napoli Federico II (F.R.A. project - MASLIDE).

Liquefaction and slope stability analyses in seismic conditions will be conducted through a multi-level approach, i.e. at increasing levels of complexity. An important part of the work was devoted to the collection of available as well as new investigations in the study area. Great importance was also given to the definition of seismic action. In this perspective, it was significant to take into account the detailed seismological studies on the source mechanisms and wave propagation carried out by seismology researchers of the University of Naples Federico II, in collaboration with the National Institute of Geophysics and Volcanology - Vesuvian Observatory, which made available seismic source models for the 2017 earthquake.

1.2 Outline of the thesis

After this introduction and before the last conclusive section - where results are summarised, and an outlook is provided - the core of the thesis consists of six chapters.

Chapter 2 provides a geological, hydrogeological and seismological overview of the island of Ischia.

Chapter 3 describes earthquake-induced instability phenomena accounted in this work in terms of physics of the process and study approaches.

Chapter 4 explains the multi-level methodology for liquefaction susceptibility and slope stability assessment adopted in this study.

Chapter 5 first gives an overview of the existing investigations collected in the study area and then details all the site and laboratory tests carried out as part of the UniNA-MASLIDE project for the characterisation of the volcanic soils of interest.

Chapter 6 describes the geotechnical subsurface model used in the liquefaction and slope stability analyses.

Chapter 7 presents the results of the applied methods.

2. Study area

2.1 Structural and geological setting

The island of Ischia, in the gulf of Naples, belongs to the westernmost active volcanic field of the Campanian Plain (southern Italy), a volcanic district that includes the Phlegrean Fields, the Procida Island and the Mt. Somma-Vesuvius complex (Figure 2-1). The volcanic activity in this area, which started in the Upper Pleistocene accompanying extensional processes, is controlled by regional strain fields along NE-SW and subordinately NW-SE trending fractures (Figure 2-2). The island represents the emerged top of a large volcanic complex located along one of the NE-SW trends. It extends over an area of about 42 km², morphologically dominated by Mt. Epomeo.

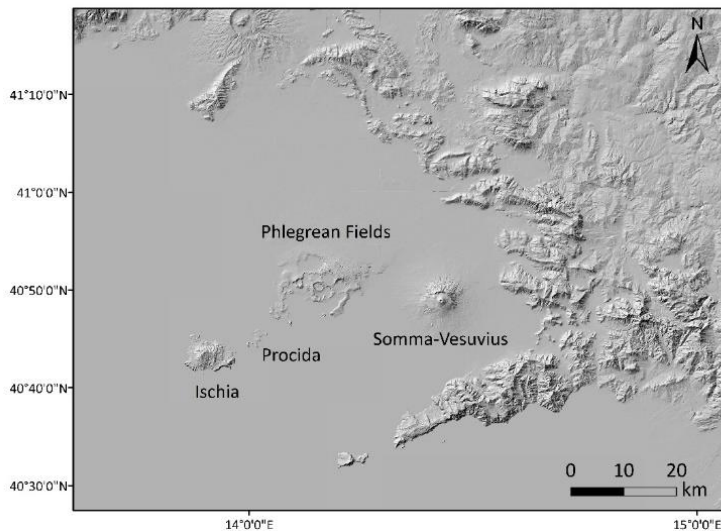


Figure 2-1: Volcanic region of Campania Plain.

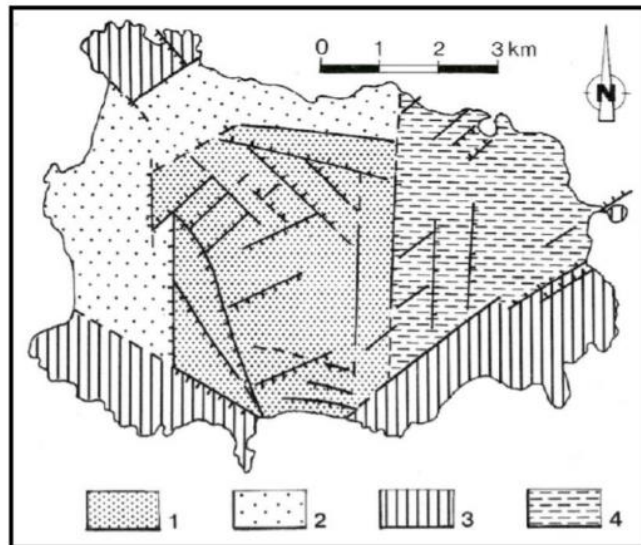


Figure 2-2: Structural setting of the island of Ischia (Chiesa & Vezzoli, 1983) 1) Mt. Epomeo Horst, 2) Marginal depressed areas of the Mt. Epomeo Horst, 3) Stable block of Mt. Torone-Vezzi-Cotto, 4) Ischia Graben.

Ischia is an active volcanic field that has profoundly changed its appearance several times throughout its history. The island is made up of volcanic rocks, landslide deposits and, subordinately, sedimentary rocks, which derive from the accumulation and cementation of fragments of pre-existing rocks, dismembered by erosive processes. The volcanic rocks present on the island are the product of both effusive eruptions, which formed lava flows and lava domes, and explosive eruptions, which generated extensive ash and pyroclastic flows. The beginning of volcanic activity is placed around 150000 years ago (Cassignol & Gillot, 1982), continuing, with various periods of quiescence, until 1302 A.D., when a lava flow emerged from the eruptive centre of the Arso. Five phases of volcanic activity are recognized, the first two of which constitute the ancient cycle (between 150000 and 75000 years ago) and the next three the recent cycle (between 55000 years ago and 1302). The separation between the two cycles is marked by the most intense eruption recorded on the island, which occurred in the southern sector about 55000 years ago, and produced the Green Tuff deposit. As can

be seen in Figure 2-2 structurally and morphologically, the area of Ischia can be divided into four areas:

- *Mt. Epomeo Horst*. This area consists essentially of the Green Tuff resulting from a highly explosive eruption some 55000 years ago. This eruption led to the formation of a caldera in the central area of the island. This event sanctioned the birth of pyroclastic flows that partially filled the caldera depression, which had previously been invaded by the sea, and partially covered the areas then emerged. Following the eruption of the Green Tuff of Mt. Epomeo, the emersion of the central part of the island occurred, due to the establishment of an uplift from the bottom of the caldera. This phenomenon is called resurgence;
- *Ischia Graben*. It is represented by the depressed area of the north-eastern sector of the island. Lithologically, it consists of both lava and pyroclastic products from recent volcanic centres;

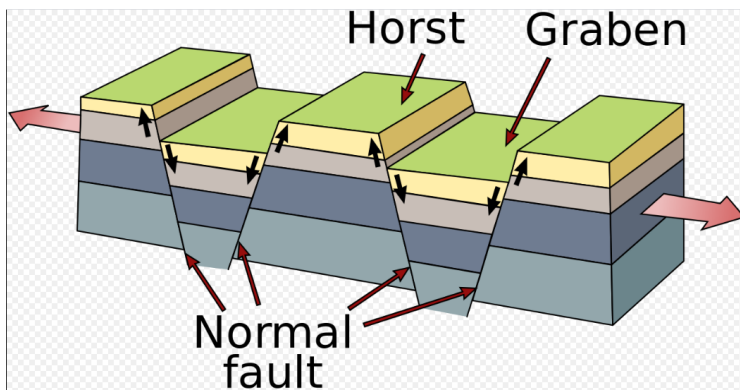
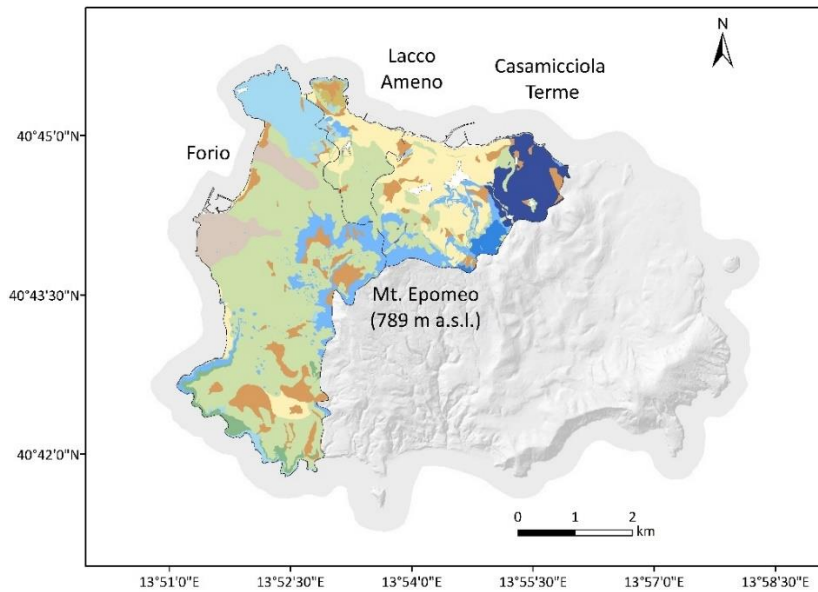


Figure 2-3: Conceptual scheme of horst and graben in extensional processes.

- *Stable block of Mt. Torone-Vezzi-Cotto*. This area is evidence of the ancient volcanic complex that ceased its activity 130000 years ago with the calderic collapse at the current central area of the island;

- *Marginal depressed areas of the Mt. Epomeo Horst.* Areas located in the north-west part of the island, consisting of a series of landslide accumulations of Green Tuff materials.

Ischia is composed mainly of volcanic rocks deriving from a number of eruptive centres which have been largely destroyed or covered by subsequent activity and can now be identified only in part (Carlino et al. 2006). Also marine sediments and landslide deposits crop out, so the presence of all these products defines a complex geological setting resulting from the interplay of tectonism, volcanism, erosion, sedimentation and slope instability (de Vita et al. 2006). This complex stratigraphic setting of the island has been reconstructed by Mancini et al. 2021 based on previous geological studies (e.g. Vezzoli, 1988; Sbrana & Toccaceli, 2011) integrated with new investigation and geological surveys. The results of this work, that includes only the western portion of the island, have been summarized in the geo-lithological map of Figure 2-4. Lithotypes were represented on the map according to the basic units encoding suggested by *Commissione Tecnica per la Microzonazione Sismica (2020)*. Details of the local lithotypes and related codes are reported in Table 2-1, distinguishing bedrock from cover soil units.



Geological bedrock

- Tuff and lavas alternated (SFALS)
- Clay and siltstone (SFCO)
- Tuffite sandstone and stratified tuffs (SFGRS)
- Fractured lavas (SFLP)

Soil covers

- Anthropic deposits (Rizz)
- Sandy-silty epiclastic deposits (SMep, pi, sp, fd, cd, tm; SWzz)
- Ashy and Pumiceous pyroclastic deposits (SMig, pc)
- Lahar deposits (SMlh, SWlh)
- Silt and sandy colluvial deposits (MLec, SMec)
- Gravel-sized epiclastic deposits (GCep; GMep, tm)
- Gravel-sized pyroclastic deposits (GWsc, pc)

Figure 2-4: Geo-lithological map of the three municipalities (Casamicciola Terme, Lacco Ameno and Forio) of the N-W sector of the Island of Ischia.

Table 2-1: List of the cover soil and bedrock lithotypes, units of the geo-lithological map of Figure 2-4: codes are from *Commissione Tecnica per la Microzonazione Sismica* (2020).

<i>Geological bedrock</i>	
SFALS: Multilayered and alternating, fractured/altered rocks (interbedded lavas and pyroclastites)	
SFCO: Cohesive, overconsolidated, fractured/altered bedrock (marine siltstone and claystone)	
SFGRS: Granular, bedded, cemented or welded, fractured/altered bedrock (ignimbrites, welded tuffs, epiclastic sandstone)	
SFLP: Fractured and altered bedrock (lavas)	
<i>Soil covers</i>	
RIzz: Anthropogenic deposits	SM-SWlh: Silty and gravelly sand from lahar flows
SMep: Talus, epiclastic sand	SMec: Eluvial-colluvial silty sand
SMpi: Alluvial and coastal plain silty sand	MLec: Eluvial/colluvial, inorganic silt with low plasticity
SMsp: Shoreface and beachface silty sand	GCep: Epiclastic clayey-sandy gravel from talus
SMfd-cd: Talus, silty sand	GMep: Epiclastic sandy-silty gravel from scree cones, talus and minor alluvial fans
SMtm: Coastal terrace silty sand	GMtm: Coastal terrace sandy-silty gravel
SWzz: Gravelly sand of undefined environment	GWsc: welded scorias
SMig-pc: Ashes with small lapilli and pumices	GWpc: Lapilli-sized pyroclastites, pumices with ashy matrix

From the ridge of Mt. Epomeo, in the centre of the island, towards the coast, morphologically and lithologically homogeneous areas are identified:

- the resurgent block of Epomeo, consisting of an outcrop of the lithoid tuffaceous substratum ("Green Tuff" Auct.), which was heavily affected by landslides;

- an intermediate band of the slope, where the lithoid tuff is covered by thick and extensive layers of loose pyroclastic and epiclastic depo-sites with a prevalent gravelly-sandy texture;
- a coastal strip, where cover deposits are interspersed with sands and silts of the marginal marine environment;
- the north and south-western promontories of the island, characterised by a lithoid substratum consisting of ancient lavas and local intercalations of more recent lavas, tuffs and silty-clayey sediments.

2.2 Hydrogeological setting

The complex stratigraphic setting and the volcano-tectonic events that affected the island have an impact on the hydrogeological setting and groundwater flow paths. In order to understand this aspect, various hydrogeological and hydrogeochemical investigations were carried out (Celico et al. 1999; Piscopo et al. 2019), which made it possible to identify two zones with different hydrogeological behaviour (Figure 2-5).

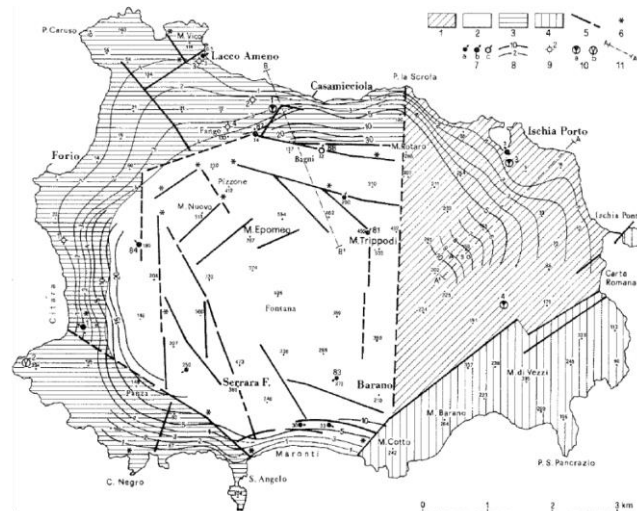


Figure 2-5: Hydrogeological map of the island of Ischia (Celico, 1999): 1) Ischia Graben sector, 2) Mt. Epomeo Horst sector, 3) Marginal areas sector, 4) Volcanic complexes sector.

In the Ischia graben sector, the shallower aquifer (the first 100-200 m of saturated thickness) consisting of pyroclastic deposits and lavas, is characterised by a relatively high transmissivity and hosts a single aquifer fed by both direct infiltration waters and marine ingression waters. The main outlet of the aquifer is the sea, in undisturbed conditions. In the Mt. Epomeo Horst sector, on the other hand, and in marginal areas, permeable levels (detritus and loose sands), semi-permeable levels and impermeable levels are present in the first 100-200m of the saturated aquifer. Consequently, the aquifer is less transmissive, more heterogeneous and anisotropic than in the Graben area. For this reason, several overlapping aquifers are present, with the sea as the main outlet. Another complication of the hydrogeological scheme is the presence of the numerous faults and fractures that affect the island, because these represent preferential paths for ground-water flow. Also in this area, the incidence of feeding with sea waters and also with fluids of deep origin has been observed. Piscopo et al. (2019) have improved the knowledge on the hydrogeology of Ischia, combining previously published and unpublished data with new data collection, analysis and numerical processing. The investigation involved a review of the conceptual hydrogeological model of the volcanic island and mainly included: hydrogeological characterisation of the volcanic units, inventory and new discharge measurements of springs, wells data acquisition and processing (around 350 across the whole island), new water level, temperature and electrical conductivity measurements of selected wells and meteorological data processing. The results can be seen in Figure 2-6. In the resurgent block of Mt. Epomeo, an independent and uplifted basal groundwater circulation can be inferred by a cross-check of the ignimbrite stratigraphic succession and hydrogeological and hydrogeochemical data of a few wells and springs located at its edge. The marginal faults of the resurgent block constitute the hydrogeological partial barriers to the basal groundwater flow of this part of the island's aquifer; furthermore, they represent the preferential paths of ascending deep fluids.

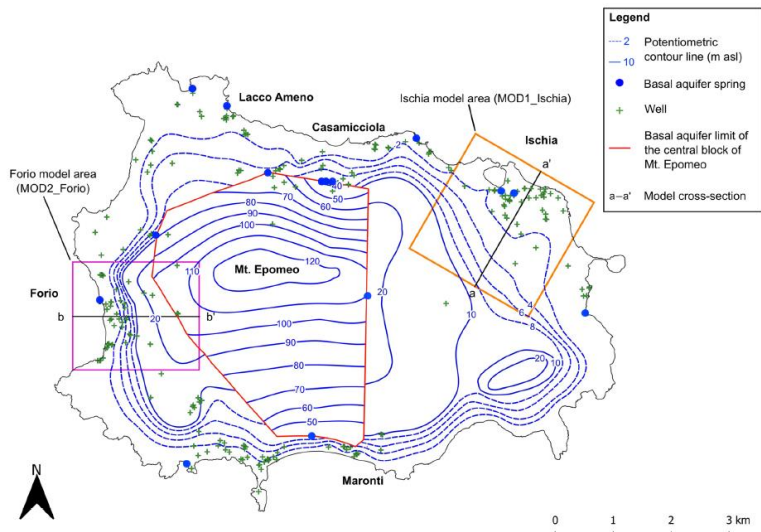


Figure 2-6: Potential potentiometric surface of the basal aquifer under static conditions (Piscopo et al. 2019).

In the peripheral areas of Mt. Epomeo, groundwater flow is mainly influenced by the nature of the aquifer formations. In the northern, western and southern areas, a continuous basal aquifer and local discontinuous perched aquifers can be distinguished consistently with a succession of tuffs, ignimbrites and epiclastic deposits. In the north-eastern area, characterised by the most recent volcanic deposits of the island, a single and continuous basal aquifer with the highest permeability on the island can be found. In these peripheral areas of Mt. Epomeo, the flow and the chemical characteristics of the waters of shallow aquifers depend not only on natural phenomena but also on the intensive groundwater abstraction supplying the numerous thermal establishments.

2.3 Seismological setting

The observations of seismicity in volcanic areas show that earthquakes have a significantly lower magnitude than those in tectonic areas. Most of the time these are

earthquakes with a maximum magnitude of four. This low seismic energy is due to the lack of sufficient stress accumulation that can be associated to various factors such as the anomalous thermal state of the crust, the intense fracturing of the medium, the reduction in potential seismogenic volume and the action of concentrated local stress (Cubellis et al. 2007; Carlino et al. 2010). At the same time, significant volcanic earthquakes of moderate magnitude may occur and produce serious damage. This is the case of the island of Ischia, historically hit by strong earthquakes that occurred in the north-western sector of the island, without the exception of the recent 2017 earthquake (Figure 2-7).

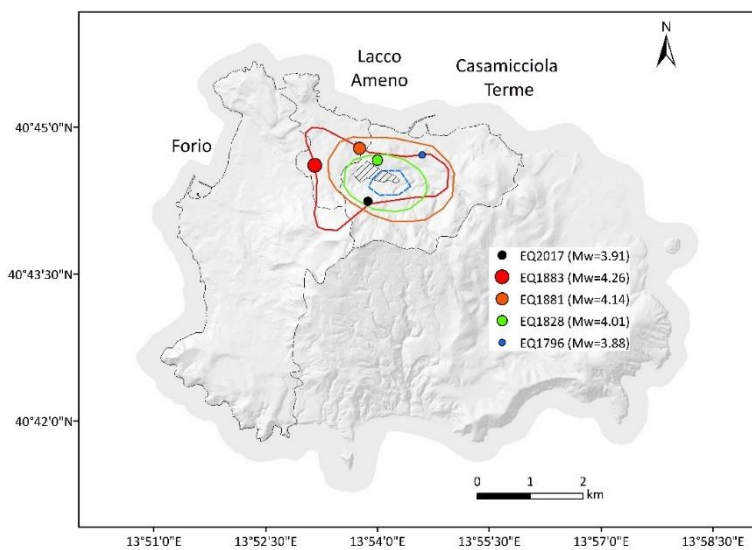


Figure 2-7: Location of epicentres of main historical events that occurred on Ischia and associated area of maximum damage.

The oldest information on the seismicity of the island of Ischia is reported in classical literature, up to the 3rd-4th centuries AD; after 300 AD, for almost a thousand years, there is no memory of either earthquakes or eruptions occurring on the island of Ischia. Table 2-2 reports the date, epicentral area and intensity of only the main and/or most recent earthquakes of the island.

The next reliable news dates back to 1228, when in July, a large landslide was reported along the northern slope of Mt. Epomeo. This phenomenon was associated with the collapse of numerous houses and 700 victims. In 1302, in conjunction with the eruption of the Arso, seismic events are reported with the collapse of many buildings.

Table 2-2: Main historical earthquakes at Ischia (modified from De Vita et al. 2006).

Year	Epicentral area	I _{max} (MCS)
1228	Casamicciola	IX-X
1302	Arso	VIII
1557	Campagnano	VII-VIII
1762	Casamicciola	VII
1767	Northern sector of the island	VII-VIII
1796	Casamicciola	VII
1828	Casamicciola	VIII-IX
1841	Casamicciola	VII
1863	Casamicciola	VII
1867	Casamicciola	VI
1881	Casamicciola	IX
1883	Casamicciola/Lacco Ameno	X
1980	Sea	V
2017	Casamicciola	VIII

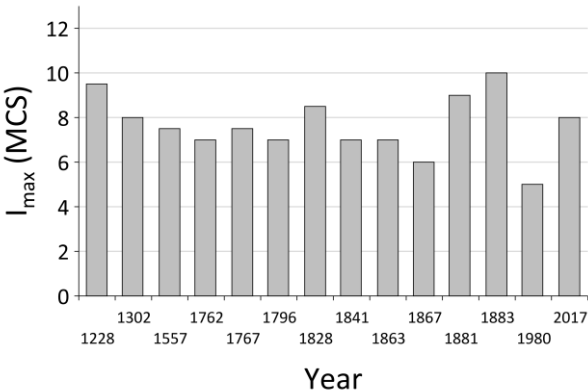


Figure 2-8: History of seismic intensity in Ischia island.

More complete information on seismicity is available from the end of the 18th century. Worthy of note is the report of an earthquake in 1557, which is said to have caused the collapse of the church in Campagnano. From 1700 until the end of the 19th century, there is intense seismic activity that produces substantial damage and deaths.

From the 1700s until the end of the 1800s, there is an intense seismic activity that produces substantial damage and deaths. On 4 March 1881, after 1 p.m., preceded by a slight tremor, a disastrous earthquake occurred with Casamicciola as its epicentre; the tremor was accompanied by a rumble and lasted 7 seconds, causing almost all the houses in the upper part of the town of Casamicciola to collapse. The municipalities of Lacco Ameno and Forio were also hit. On the basis of the damage distribution, it is possible to delimit the area of maximum intensity, assessed as VIII MCS grade (with IX peaks), which extends in an E-W direction to the north of Epomeo and affects the upper part of Casamicciola and Lacco Ameno.

The Casamicciola earthquake of 28 July 1883, also felt in Naples, represents the peak of seismic energy released in historical times on the island of Ischia. The number of victims according to various sources (Baratta, 1901; Mercalli, 1884; Palmieri & Oglialoro, 1884) exceeded 2000. The seismic event caused intense damage not only to the municipality of Casamicciola, but also to the upper part of the town of Lacco Ameno. Bibliographic sources and historical documentation of this earthquake are particularly rich and have made it possible to faithfully reconstruct the damage in Casamicciola and throughout the island, obtaining a detailed macroseismic field (De Rossi, 1884; Mercalli, 1884; Johnston-Lavis, 1885; Palmieri & Oglialoro, 1884; Luongo et al. 1987; Cubellis & Luongo, 1998; Molin et al. 2003; CPT04 Working Group, 2004; Luongo et al. 2006).

This shows the rapid decay of intensity values with distance from the area of maximum intensity (X-XI degree MCS), indicating a strong attenuation of seismic energy in wave propagation and the considerable shallowness of the source.

Figure 2-9 shows the MCS intensities of the 1828, 1881 and 1883 earthquakes; it is possible to observe the pattern of the macroseismic field of the 1883 earthquake that resembles those of the 1828 and 1881 earthquakes, with MCS intensities ranging from VI to X. The 1883 earthquake has been related to the resurgence activity and, more specifically, to the E–W striking faults that affect the northernmost area of Ischia (Cubellis, 1985; Alessio et al. 1996).

These historical earthquakes have caused instability phenomena as demonstrated by morphological surveys, historical reports and archeological evidences.

Figure 2-10 shows the earthquake-induced landslides that occurred in the N-W sector of the island. The same map shows the ground effects catalogued by CEDIT (Italian Catalogue of Earthquake-Induced Ground Failures) by Martino et al. 2021 and the landslide-prone area mapped by local authorities PAI (Hydrogeological Management Plan) and IFFI (Inventory of landslides of Italy), which represents about half of the study area.

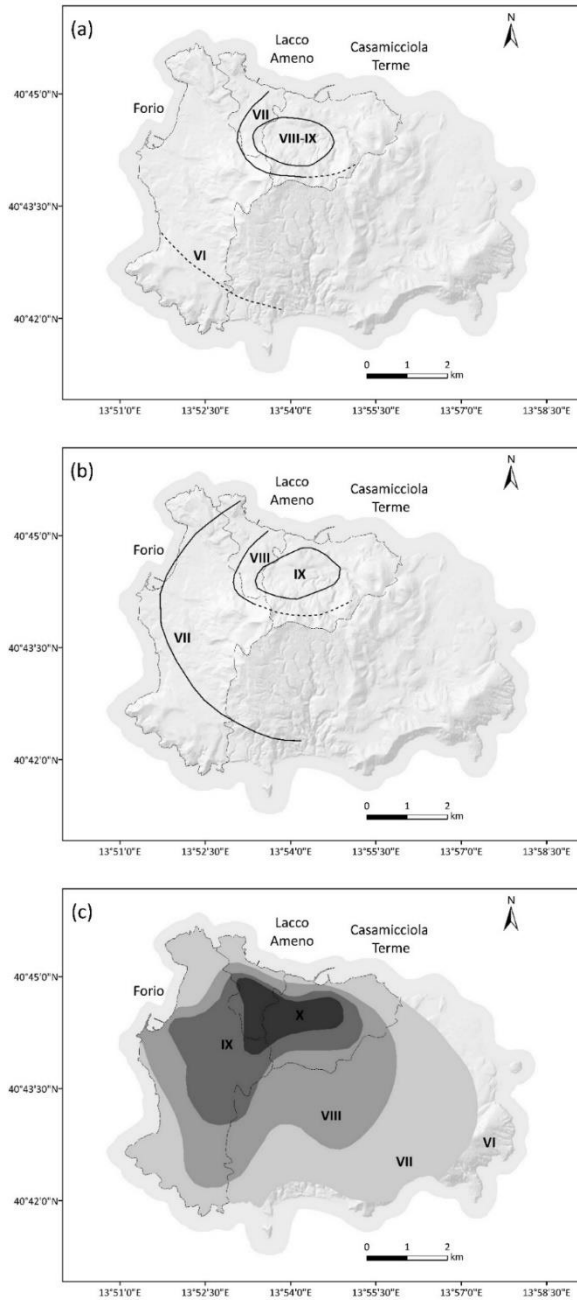


Figure 2-9: Macroseismic field map of the 1828 (a), 1881 (b) and 1883 (c) events (modified from Alessio et al. 1996).

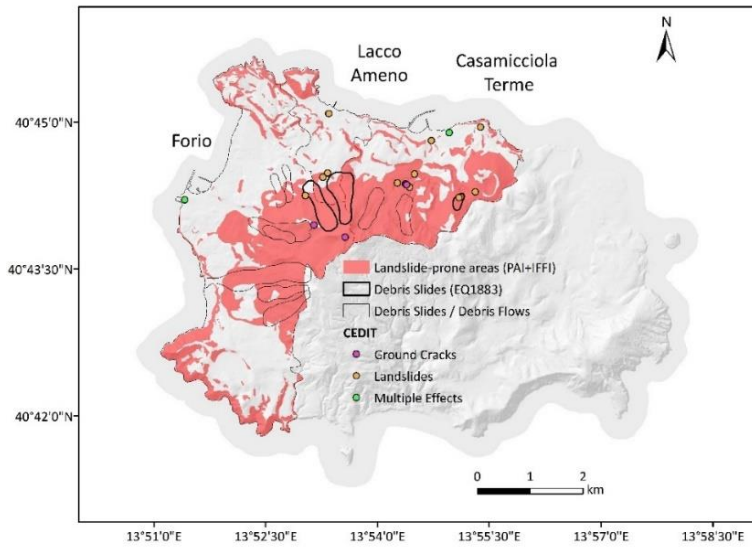


Figure 2-10: Historical earthquake-induced instabilities in the N-W sector of Ischia Island (Guadagno & Mele, 1995; Del Prete & Mele, 2006; Martino et al. 2021).



Figure 2-11: View of the two landslides (EQ1883) above 'Fango' bolded in Figure 2-10 (from Johnston-Lavis, 1885).

As far as liquefaction is concerned, the only historical evidence is reported by De Rossi M.S. in “Raccolta di fatti, relazioni, bibliografie sul terremoto di Casamicciola del 28 Luglio 1883 con brevi osservazioni”, in “*Bullettino del Vulcanismo Italiano*”:

<<In the days before the earthquake, the thermo-mineral waters had risen in temperature, in some cases becoming turbid. The few wells on the island decreased in capacity; the waters of some springs underwent chemical alterations; these phenomena ceased a few days after the quake. At various points on Mt. Epomeo, the earthquake caused landslides to fall and cracks to form in the ground. Some fumaroles increased their activity, while others interrupted it. At sea, opposite the northern coast, a large quantity of mud rose to the surface. In the same area, an uplift of the coastline was reported. Electrical phenomena (lightning, fire globes, flames) were observed by many people at the time of the quake.>>

2.3.1 2017 Ischia Earthquake

On 21 August 2017, at 20.57, a $M_w=3.91$ earthquake was felt in Ischia and the Phlegraean area of the municipality of Naples. The event, with a hypocentral depth of about 2 km, was recorded on the island by the 'IOCA' accelerometric station (Figure 2-12) located near the Geophysical Observatory located in Gran Sentinella, in the municipality of Casamicciola Terme. The station is situated at an elevation of 123 m from sea level and the soil classification according to national code NTC 2018 is reported as C (inferred from geological maps). The epicentral distance of the station is less than 1 km. Figure 2-13 reports the corrected acceleration, velocity and displacement time histories recorded in the East-West (HNE), North-South (HNN) and Vertical (HNZ) directions by the IOCA station. Table 2-3 summarizes the significant parameters of the seismic motion.

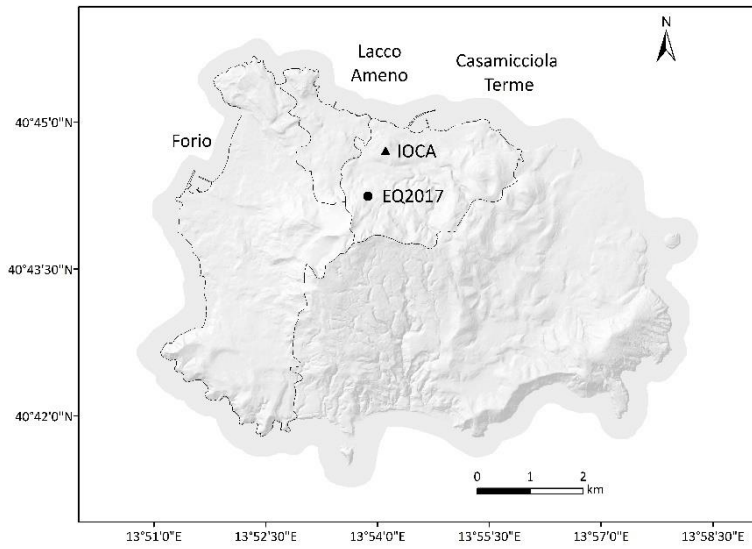


Figure 2-12: Location of the epicentre of the 2017 earthquake (INGV) and the 'IOCA' accelerometer station.

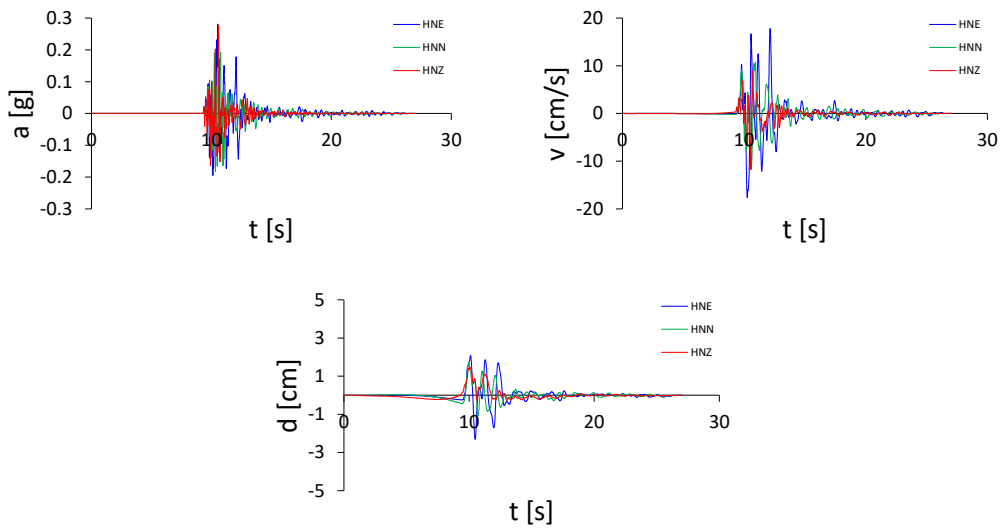


Figure 2-13: Waveforms from the 21 August 2017 event recorded at the 'IOCA' accelerometer station.

Table 2-3: Peak Ground Acceleration (PGA), Peak Ground Velocity (PGV), Peak Ground Displacement (PGD), Arias Intensity (AI), Housner Intensity (HI) and Significant Duration (D_{5-95}) per recorded component of ground motion at IOCA station.

	PGA	PGV	PGD	AI	HI	D_{5-95}
	[g]	[cm/s]	[cm]	[cm/s]	[cm]	[s]
HNE	0.281	17.80	2.31	39.4	66.31	2.85
HNN	0.192	11.46	1.72	22.2	43.47	3.58
HNZ	0.276	11.78	1.46	19.9	25.56	2.73

Figure 2-14 shows the 5% damped pseudo-acceleration (S_a), pseudo-velocity (S_v) and displacement (S_d) spectra of all three ground motion components, compared to the national code (NTC 2018) spectrum with a return period of 475 years. It can be observed that the East-West component exhibits a PGA of 0.281g, comparable to the Vertical component (0.276g). Maximum Arias Intensity among the components was calculated at 39.4 cm/s and Significant Duration D_{5-95} at 3.58s. Despite the low magnitude of this earthquake, the response spectra exceed the design spectrum in different vibration period intervals. Such exceedances can be explained by several factors such as the proximity of the source, the shallow hypocentral depth and local site conditions (Iervolino & Giorgio, 2018). The latter are evident if one focuses attention on the horizontal component spectra, in which the existence of local amplification peaks can be noted in a vibration period interval of 0.5-0.8s. Also from the ratios of Fourier spectra (Figure 2-15) it is observed a local effect, both stratigraphic and topographic, between frequencies of 1.2 Hz and 2.0 Hz. This amplification is also confirmed by the INGV report based on ad hoc environmental noise measurements (EMERSITO Working Group, 2017).

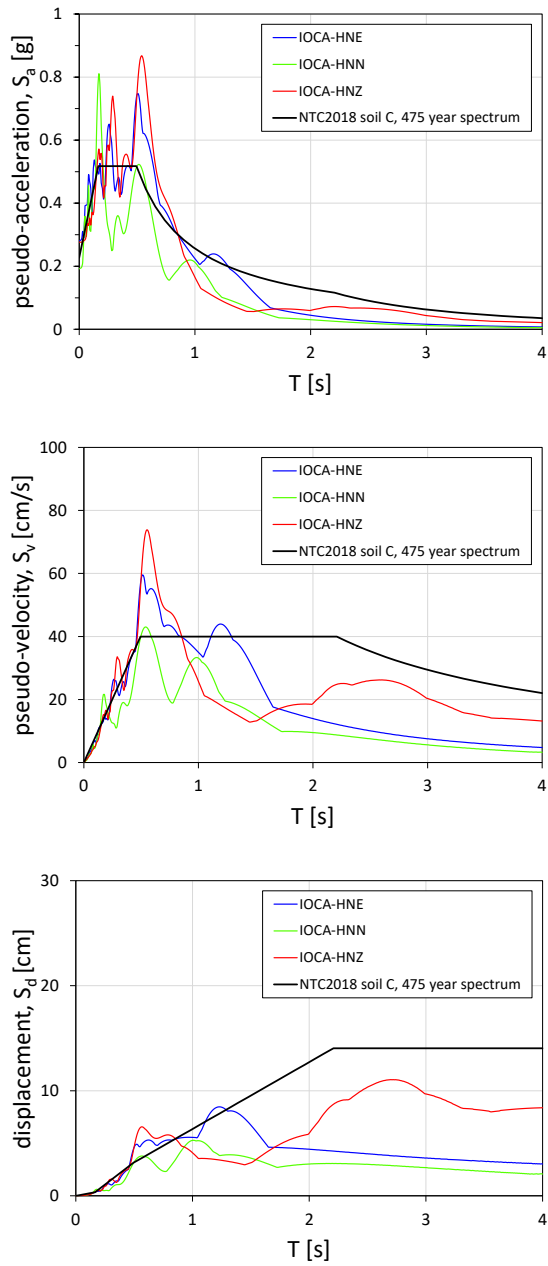


Figure 2-14: Pseudo-acceleration, pseudo-velocity and displacement spectra of all three ground motion components recorded at the IOCA station.

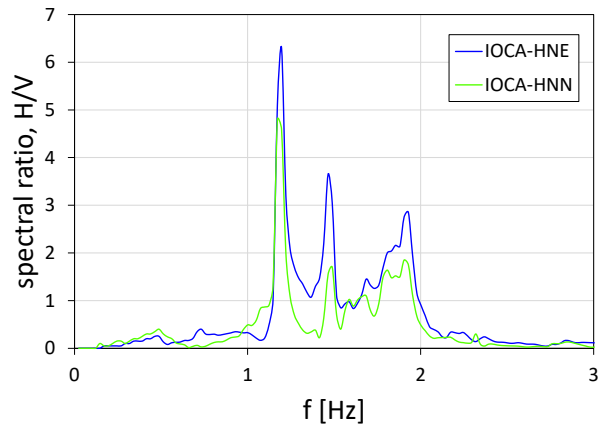


Figure 2-15: Horizontal to Vertical spectral ratio (H/V) for both components recorded at IOCA station.

3. Earthquake-induced instabilities

Earthquake-induced instability phenomena can occur in soils with horizontal morphology (in the case of liquefaction) as well as in natural (slopes) or artificial (e.g. embankments or earthen constructions) slopes (Silvestri & Santucci de Magistris, 2015). They generally develop as a result of the interaction between seismic waves and the subsoil, which induces a deterioration of pre-existing stability conditions through two sets of factors:

- temporary increase in instabilising actions, consisting of the inertia forces induced by the earthquake on the potentially unstable volume, varying in time and amplified due to stratigraphy and topographical irregularities;
- reduction in the shear resistance characteristics of the ground, due to both the cyclical degradation of the soil skeleton's response and the generation and accumulation of excess pore pressure.

The combination of the various causes tends to produce damaging effects of both immediate and deferred nature, as evidenced by numerous cases of liquefaction and/or post-seismic instability of slopes in saturated fine soils. The damage caused to the physical and built environment is typically associated with displacement of land masses, and is therefore the greater the higher the energy content of the earthquake and the greater the potentially unstable volume.

3.1 Liquefaction

Liquefaction is a phenomenon that affects loose and saturated coarse-grained soils, which tend to be subject to a low initial state of confinement (i.e. limited depth from ground level). When external loads are applied very quickly, as in the case of an earthquake, even for coarse-grained soils the conditions are undrained: thus there is an increase in pore pressure that reduces the contact stresses between solid particles and, therefore, the stiffness and strength of the soil. In the case of soils characterised

by low values of effective stress, high porosity and in conjunction with seismic events of strong intensity, the pore pressure can reach such high values that the solid particles lose mutual contact. At this state, no effective stress or intergranular stress is acting on the sand and the particles released from any confinement exist as floating in the water. Such state is called liquefaction. At ground level, liquefaction effects appear as surface cracks, sand volcanoes and ejecta. An outline of what is described is given in Figure 3-1.

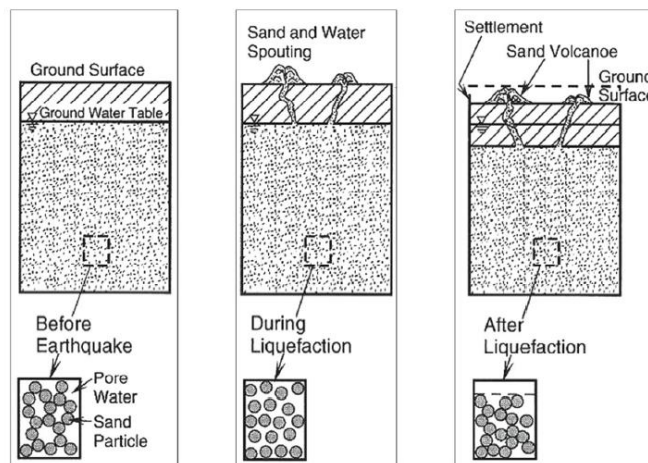


Figure 3-1: Particle configuration in a soil before, during and after liquefaction.

After the earthquake, a return to a condition of equilibrium under the action of static loads is expected, which may be a more stable condition than the previous one. In fact, the particles tend to settle in a denser configuration than the initial one. The consequence of this is a settlement of the ground surface.

The above consideration has been concerned with an overall interpretation of the liquefaction mechanism. A more in-depth understanding of the liquefaction phenomenon can be gained from observation of behaviour of Fuji River (Japan) sand samples undergoing cyclic stress application in the laboratory test apparatus (Ishihara, 1985). The results of tests (Figure 3-2) show that the pore water pressure builds up as the cyclic stress is applied, and eventually approaches a value equal to the initially applied confining pressure, producing large cyclic deformations.

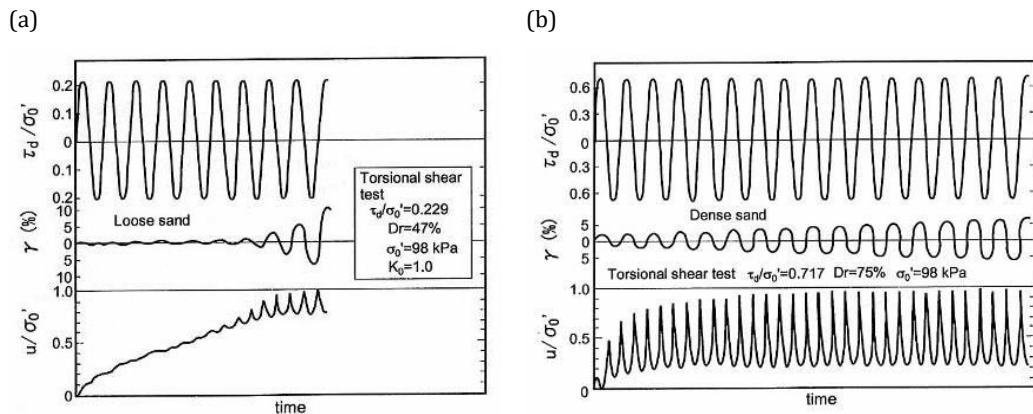


Figure 3-2: Records of cyclic torsional shear tests on loose (a) and dense sand (b) (Ishihara, 1985).

However, the development of the deformations is different for loose sand ($D_r=47\%$) and dense sand ($D_r=75\%$). In fact, in the first case, the pore water pressure increases suddenly and large shear deformations occur quickly; on the other hand, in the second case, the pore water pressure increases slowly and the shear strain never becomes larger than a certain limit. Whether in the case of loose sands we have the characteristic feature of *earthquake-induced liquefaction*, in the case of dense sands we have the so-called *cyclic mobility* (Castro, 1975).

The two different types of behaviour are better understood if the cyclic behaviour is expressed in terms of stress-strain curves and in terms of stress paths (Figure 3-3 and Figure 3-4).

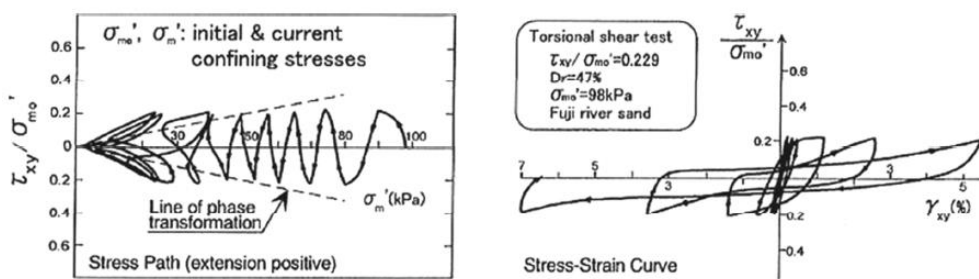


Figure 3-3: Stress-path and stress-strain curve for loose sand (shear stress τ is normalised with respect to the effective stress σ') (Ishihara, 1985).

The cycles degrade very conspicuously and, when the material begins to liquefy, assume a typical distorted pattern; this is related to strong degradation and energy dissipation. In each cycle, when the loading process is reversed, the material appears to increase in stiffness: this is due to the related pore pressures discharge, which produces an increase in the slope of the diagram along the cycle.

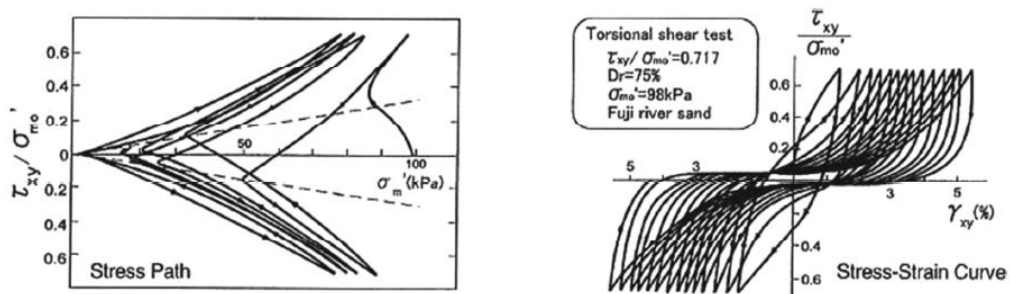


Figure 3-4: Stress path and stress-strain curve for dense sand (shear stress τ is normalised with respect to the effective stress σ') (Ishihara, 1985).

The test results for loose sands in Figure 3-3 show that the confining effective stress decreases steadily as the number of cycles increases and as the stress path touches the *phase transformation line* in the τ - σ' plane, it is turned right upwards during loading and directed left downwards in the unloading process. Also the stress-strain curves indicate that as the stress cycle proceeds, the sand deforms largely producing a shear strain greater than 5%. The cycles begin to take on a distorted appearance with a slope that decreases towards the horizontal, which means that the stiffness tends to gradually cancel out (unstable behaviour).

The test results for dense sands reported in Figure 3-4 show that the effective stress σ' tends to decrease as the pore pressure builds up; as the stress path approaches the line of phase transformation, it goes up to the right along the failure line in the course of increasing shear stress and comes down to the left during the unloading process, eventually reaching a state of near-zero effective confining pressure upon complete removal of shear stress. There, the effective stress is completely lost because the excess

u increases up to initial effective stress σ' , causing a sudden increase of induced shear strain amplitude γ , as indicated in Figure 3-4. The first arrival of the stress path at the origin O is called the state of initial liquefaction or liquefaction onset. In the stress-strain curve shown in Figure 3-4 the secant modulus tends to become evidently lower, and strain ranges with very low mobilized shear resistance is widening with increasing loading cycles. However, the modulus can never be so low for dense sand as to behave like a liquid because the shear resistance starts to pick up at some strains in every cycle due to the positive dilatancy of the soil skeleton. This type of behaviour is named “cyclic mobility” and should be considered differently from liquefaction of very loose contractive soils which may undergo truly liquid-like flow failures. This latter occurs when the shear stresses required to ensure equilibrium conditions for earthquake-induced inertia forces (τ_{eq}) are greater than the available shear strength of the ground (τ_{lim}). In this case, the deformations continue after the earthquake. This phenomenon generally involves large volumes of material and is characterised by high and very fast displacements.

However, the cyclic mobility phenomenon occurs when the strength of the ground is significantly reduced, but still exceeds the shear stresses necessary for static equilibrium. In this case the deformations develop incrementally during an earthquake. A possible effect related to cyclic mobilisation is lateral spreading of the soil, which can occur even on slopes that are not too steep.

Cases of liquefaction are mainly observed near rivers, natural or artificial bodies of water, and in coastal areas (Youd & Perkins, 1978). It follows that among the buildings most vulnerable to liquefaction phenomena are port and hydraulic infrastructures (embankments and dams), and transport infrastructures; the problems induced in buildings derive essentially from the instantaneous loss of load-bearing capacity of the foundation soils, as a result of which these buildings, while retaining an apparent structural integrity, tend to lose their functionality, becoming dangerously tilted or even completely sagging on the ground level.

3.2 Slope stability

Slope failures caused by strong earthquakes can be very large in terms of number, volume as well as travel distance and hence very hazardous. It is also known that the significance of earthquake-induced slope failures is closely correlated with rainfalls before or after the earthquake.

Mechanical impacts of earthquakes on slope failures may be classified into an inertial effect to drive the soil mass, and a cyclic loading effect to weaken the shear resistance of the slope materials by pore pressure build-up and disturbance of soil structures. After the initiation of sliding, the shear resistance of the soil mass may be further weakened during sliding (Figure 3-5).

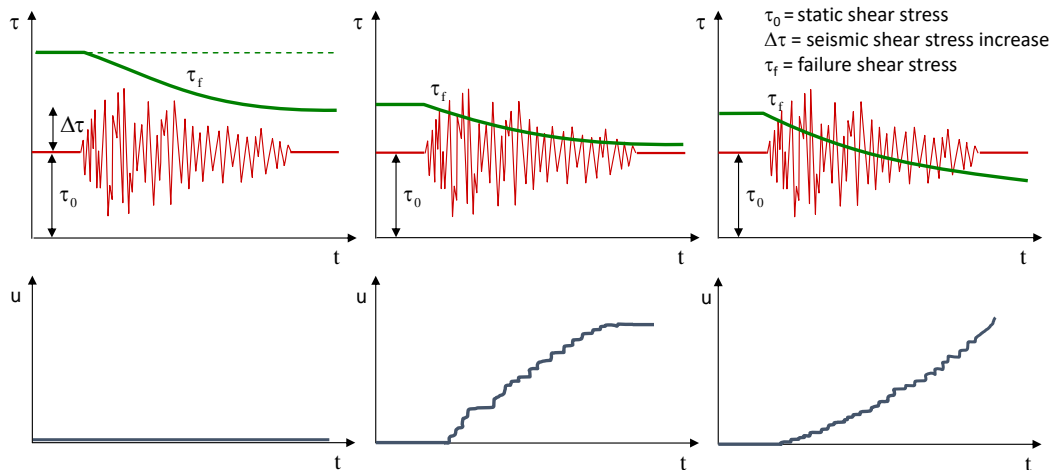


Figure 3-5: Slope stability conditions: seismic and post-seismic displacements.

The slope is considered stable if the increment of static and seismic shear stresses is such that the failure shear stress is not exceeded during an earthquake or if the shear stress is high enough. Nevertheless, if shear stress is exceeded in some intervals but at the end of the seismic action it remains equal or less of the failure value, the slope will have some permanent displacements but it will remain stable. The last case corresponds to having displacements for an exceedance of the resistance during the earthquake and to a post event higher static action compared to the available one. In

particular this may happen only if degradation phenomena occur. For this last scenario, the slope remains in unstable condition even after the end of the event.

Slope instability occurs as:

- *first detachment landslides*, characterised by shear failure at newly formed sliding surfaces, coinciding, in whole or in part, with stratigraphic discontinuities or levels of lower resistance in homogeneous formations;
- *reactivation of quiescent landslides*, with movement along pre-existing sliding surfaces;
- *acceleration of movement of active landslides*, still along pre-existing surfaces.

The volume of unstable subsoil (Figure 3-6) under seismic conditions is the pre-existing one, for active or quiescent landslides, while for first-triggering landslides it is generally shallower than under static conditions (Silvestri & Santucci de Magistris, 2015).

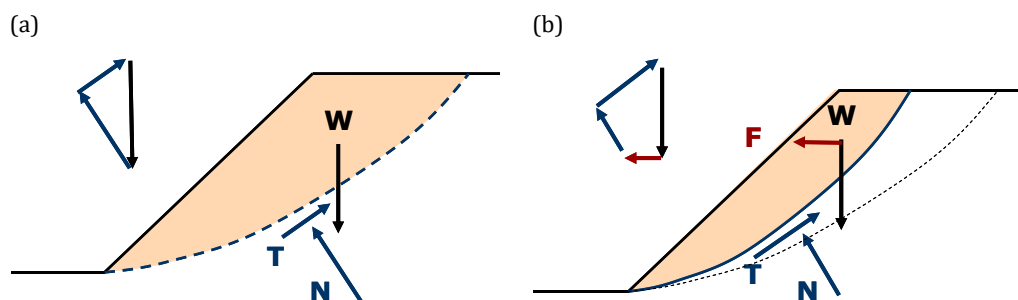


Figure 3-6: Mechanisms of slope instability under static (a) and seismic (b) conditions.

Previous phenomenologies are not dissimilar in kinematism to landslides triggered by non-seismic causes, and are therefore referable to the well-known classification criterion for slope movements proposed by Varnes (1978), in which landslides are distinguished according to the nature of the materials (rock or soil), the type of movement (collapse, overturning, sliding, flow, lateral expansion) and according to the speed of the movement (from extremely slow, $v \leq 1$ mm/a, to extremely fast, $v \geq 1$ m/s).

For first detachment landslides, the classification system proposed by Keefer (1984) is more widespread (Figure 3-7). It recognises three different categories of mechanisms:

- Category I: *Disrupted Slides and Falls*. It encompasses rock and soil falls, rock and disrupted soil slides, rock and soil avalanches. Landslides in this category typically originate on steep slopes, travel relatively fast, and are capable of transporting material far beyond the bases of the steep slopes on which they originate. Except for rock avalanches, landslides in this category are also typically thin, with initial failure depths of less than 3 m;
- Category II: *Coherent Slides*. It encompasses rock and soil slumps, rock and soil block slides, slow earthflows. These landslides exhibit a slight to moderate amount of internal disruption, typically consisting of a few moving blocks, each of which may be little deformed except for localized internal fissuring. These types of landslides occur most commonly on moderately steep slopes, typically move relatively slowly, and displace material less than 100 m. These landslides are also relatively thick, with typical initial failure depths greater than 3 m;
- Category III. *Lateral Spreads and Flows*. It includes those landslides for which fluid-like flow is the predominant movement mechanism. Landslides in this category initiate only in soil materials and involve either blocks of relatively intact material moving on a subsurface liquefied zone (soil lateral spreads) or more completely liquefied masses that move by fluid-like flow throughout (rapid soil flows). In many cases, these landslides are the results of soil liquefaction in saturated soils.

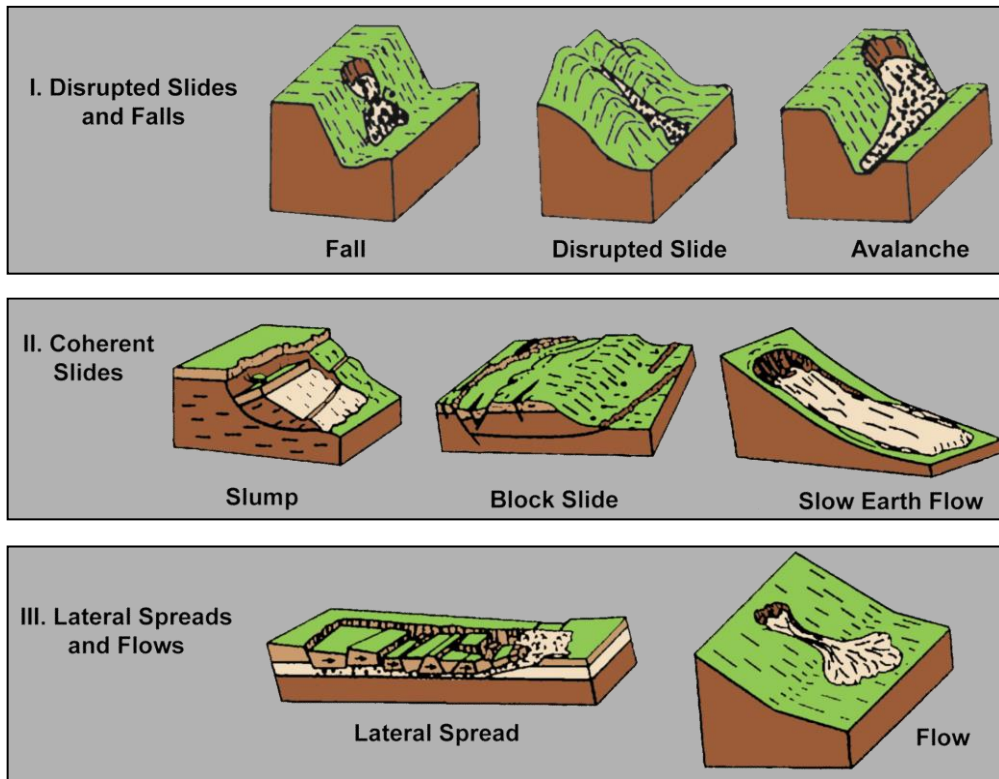


Figure 3-7: Mechanisms of earthquake-induced landslides according to Keefer's classification (1984).

Mechanisms included in Category I are the most recurrent since they occur in the fractured rock mass and are induced by short-duration motions characterised by high-frequency content, typical of features of weak motions. On the other hand, deep landslide phenomena (Category II) occurring in fine-grained soils and flow slides (Category III) can be triggered by ground motions characterised by increasing energy and duration, and for this reason, are less frequent since requiring higher magnitude motions.

4. Methodology

4.1 Seismic action definition

As is typical in Geotechnical Earthquake Engineering, depending on the methodology chosen and the type of analysis to be performed, the reference input motion can be expressed through either representative synthetic parameters (e.g. the peak ground acceleration) or a complete knowledge of the time history of the acceleration. Two approaches can be used for defining synthetic parameters or spectral values:

- DSHA, *Deterministic Seismic Hazard Analysis*;
- PSHA, *Probabilistic Seismic Hazard Analysis*.

Figure 4-1 shows schematically the steps for both approaches (Kramer, 1996).

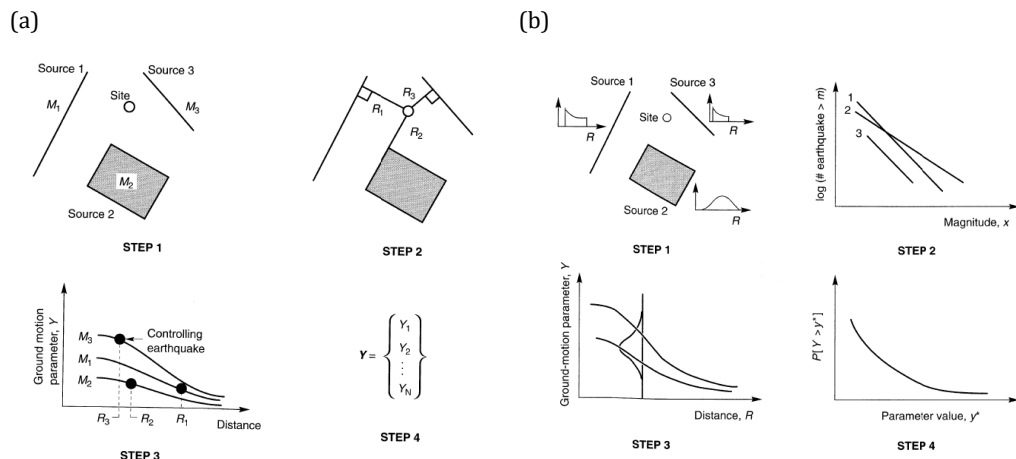


Figure 4-1: Steps of Deterministic Seismic Hazard Analysis (a) and Probabilistic Seismic Hazard Analysis (b).

In the following sub-sections, the seismic action is first introduced in terms of a synthetic motion parameter and then moves on to the time-histories that will be used for the dynamic analyses. In particular, both the code-compatible accelerograms and the procedure used to generate simulated signals ad hoc for the case study will be reported.

4.1.1 Synthetic parameters

In DSHA, an historical-empirical approach can be adopted. In particular, an expected ground motion parameter at a given site can be estimated on the basis of the maximum seismic potential of all seismogenic sources affecting the seismic hazard at a site. For each zone a source-to-site distance parameter and a controlling earthquake are selected. The latter is generally expressed in terms of some ground motion parameters, at the site. The selection is made by comparing the levels of shaking produced by earthquakes (Step 1 in Figure 4-1a) assumed to occur at a distance identified (Step 2 in Figure 4-1b).

In this approach the seismic action is typically estimated through *Ground Motion Predicted Equation* (GMPE), derived from statistical interpretations of recorded seismic data:

$$\log(Y) = f_1(F) + f_2(M) + f_3(R) + f_4(S) + \sigma \cdot \varepsilon \quad \text{Eq. 4-1}$$

where:

- Y is the mean value of the ground motion parameter;
- F represents one or more variables describing the source mechanism;
- M is the magnitude of the expected event;
- R is a measure of the source-site distance;
- S represents one or more variables describing the local subsurface conditions;
- ε is the random variable with zero mean and σ is the standard deviation.

The hazard at the site is in terms of ground motions produced at the site by the controlling earthquake. The GMPEs (i.e. attenuation laws) combined with the location of the source and the assessment of the magnitude, make it possible to generate deterministic scenarios on a territorial scale through so-called *shakemaps*.

As an alternative to deterministic scenarios, the site-specific hazard can be obtained from probabilistic analyses (PSHA), based on the geographical distribution, seismogenic potential and the activity of the different seismic sources affecting the site (Kramer, 1996). Through the use of appropriate attenuation laws, PSHA leads to the

definition of a *hazard curve* of a generic ground motion parameter Y , expressing the latter as a function of the mean annual frequency of exceedance λ , through the equation:

$$\lambda_Y = \sum_i v_i \int_M \int_R P[Y > y^* | m, r] f_M(m) f_R(r) dm dr \quad \text{Eq. 4-2}$$

where v_i is the mean annual rate of occurrence of the event at the i -th source, f_M and f_R are the probability density functions of magnitude and distance (Step 1 in Figure 4-1b). The probability of exceeding a given value y^* , requires the definition of the probability distribution of Y , the mean value and the standard deviation of which are generally obtained from the attenuation law used (Step 2-3 in Figure 4-1b). The outcome of the PSHA (Step 4 in Figure 4-1b) applied to the whole national territory consists of curves and maps of seismic hazard defined in terms of reference accelerations, a_r (Figure 4-2a), and of spectral ordinates, $S_a(T)$, deduced point by point over the national territory.

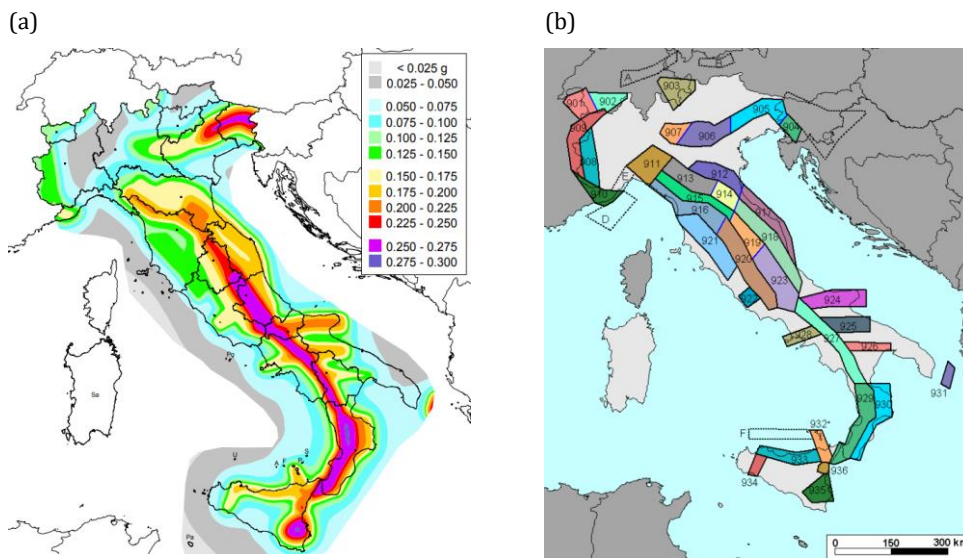


Figure 4-2: Seismic hazard map of the national territory in terms of reference acceleration with probability of exceedance of 10% in 50 years (a) and Seismogenetic Zoning ZS9 of Italy (Meletti & Valensise, 2004) (b).

4.1.2 Time histories

The seismic motion at a point on the free surface depends not only on so-called site effects but also on the characteristics of the seismic motion at the source as well as the distance of the site from the source. The seismic motion mainly depends on the energy released in the process of rupture (measured by the moment magnitude M_w) and the source mechanism.

The national code (NTC 2018) does not allow the use of artificial accelerograms for geotechnical applications, while it specifies the use of simulated (“synthetic”) and natural (“recorded”) reference input motions.

The selection of natural accelerograms is carried out from available databases by means of computer codes (e.g. *REXEL*, Iervolino et al. 2009 and *IN-SPECTOR*, Acunzo et al. 2014), mainly on the basis of magnitude-distance pairs deduced from seismotectonic and historical seismicity. Accelerograms should be selected so that they were recorded by stations close to the site of interest, or even because they were recorded in different areas, but produced by earthquakes with magnitude, focal mechanism, depth and distance comparable with those expected for the site. The time-histories should be scaled so that the PGA values coincide with those predicted by the national scale hazard studies (Figure 4-2a). The task is facilitated by the knowledge of the mean depth and fault mechanism expected with reference to the seismogenic zonation of the Italian territory (zonation ZS9, Figure 4-2b).

In the absence of representative records of seismic motion in the study area, it is more appropriate to generate simulated signals. The simplest seismologically-based strong motion simulation method is the stochastic method (Boore, 1983). This approach is used for high frequencies, generally higher than 1 Hz. Stochastic strong ground motion simulation methods can be referred either to point-source or finite-fault models, which are described in the following sub-sections.

4.1.2.1 Stochastic point-source modeling

To model the high-frequency components of S-wave in acceleration time series, a method was developed by Boore (1983) where S-waves is assumed as propagation finite duration, band-limited, white Gaussian noise. The finite duration is $0 \leq t-R/V_s \leq T_d$. In this interval, R is the source-to-receiver distance; β is the S-wave velocity and T_d is the faulting slip duration. The band is delimited within the frequency range of $f_c \leq f \leq f_{max}$ where f_c is the corner-frequency and f_{max} is the highest frequency. The objective is to generate a transient time series where the amplitude spectrum matches the reference spectrum. The flowchart is reported in Figure 4-3.

In this modeling approach, first random band-limited Gaussian white noise is generated with a unit variance for a specified finite duration of motion (Figure 4-3a). This noise is windowed by Saragoni-Hart to get a more realistic acceleration-time series (Figure 4-3b). By transforming the ground motions from the time domain to the frequency domain (Figure 4-3c), the amplitudes are normalized (Figure 4-3d) by eliminating the frequency content above the cut-off value f_{max} frequency (Brune, 1970). Thereafter, the modeled and shaped-noise spectrum (Figure 4-3e) is transferred by inverse Fourier transformation to stochastic acceleration-time series (Figure 4-3a). The essential ingredient for the stochastic method is the spectrum of the ground motion: this is where the physics of the earthquake process and wave propagation are contained, usually encapsulated and put into the form of simple equations.

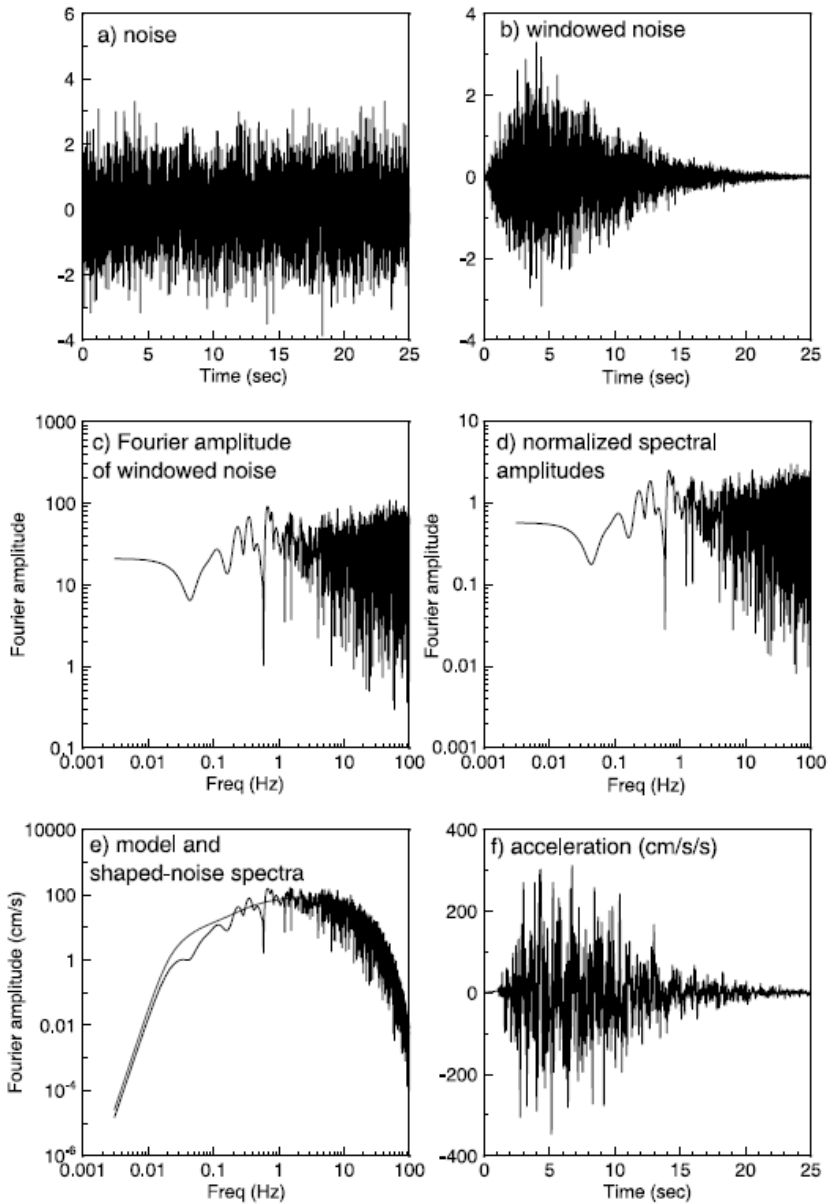


Figure 4-3: Flowchart for point-source stochastic ground motion simulation (from Boore, 2003).

It is convenient to express the total spectrum of the motion at a site $A(M_0, R, f)$ into contributions from earthquake source (E), path (P), site (G); consequently, the Fourier amplitude spectrum of a seismic signal in stochastic point-source modeling is given as:

$$A(M_0, R, f) = E(M_0, f) \cdot P(R, f) \cdot G(f) \quad \text{Eq. 4-3}$$

where f is the frequency, R is the source-to-receiver distance and M_0 is the seismic moment. The latter is related to the moment magnitude, as proposed by Hanks & Kanamori (1979):

$$M_w = \frac{2}{3} \log(M_0) - 10.7 \quad \text{Eq. 4-4}$$

Both the shape and the amplitude of the source spectrum must be specified as a function of earthquake energy. The most commonly used model of the earthquake source spectrum is the ω^2 model proposed by Aki (1967). The scaling of the spectra for different magnitudes is determined by specifying the dependence of the corner frequency f_c on seismic moment. Following Brune (1970, 1971), the corner frequency is given by:

$$f_c = 4.9 \times 10^6 \cdot V_s \cdot \left(\frac{\Delta\sigma}{M_0} \right)^{\frac{1}{3}} \quad \text{Eq. 4-5}$$

where the corner frequency f_c is in Hz, shear-wave velocity V_s in km/s, the stress-drop $\Delta\sigma$ in bars and the seismic moment M_0 in dyne·cm.

In general, the source function is expressed as the product of seismic moment, source displacement spectrum and a constant C :

$$E(M_0, f) = C \cdot M_0 \cdot S(f, f_c) \quad \text{Eq. 4-6}$$

C can be expressed as:

$$C = \frac{\mathfrak{R}^{\theta_r} \cdot FS \cdot PRTITN}{4\pi\rho V_s^3} \quad \text{Eq. 4-7}$$

where ρ is the density in the vicinity of the source and FS is the free surface amplification factor which is assumed as 2 in general. $PRTITN$ is a factor which is applied to reflect the effect of shear-wave energy partitioning into two horizontal components. Its value is taken as $1/\sqrt{2}$ in general. \mathfrak{R}^{θ_r} is the radiation pattern reflecting

the variation of the displacement field for different directions due to a shear dislocation (constant and taken to be 0.55 for shear waves).

The source displacement spectrum is defined as follows:

$$S(f, f_c) = \frac{1}{1 + \left(\frac{f}{f_c}\right)^2} \quad \text{Eq. 4-8}$$

Once the source has been specified, the next component of the process that affect the spectrum of motion at a particular site is the path effect. The factors involved are the functions defining geometric spreading, quality factor (anelastic attenuation factor) and duration functions. Geometrical spreading can be defined as a factor that reflects wave amplitude reduction because of the traveled distance of seismic waves. It is defined as a piecewise continuous function, as follows:

$$Z(R) = \left\{ \begin{array}{ll} \frac{R_0}{R} & R \leq R_1 \\ Z(R_1) \left(\frac{R_1}{R}\right)^{p_1} & R_1 \leq R \leq R_2 \\ \dots & \dots \\ Z(R_n) \left(\frac{R_n}{R}\right)^{p_n} & R \leq R_n \end{array} \right\} \quad \text{Eq. 4-9}$$

In applications, R is usually taken as the closest distance to the rupture surface, rather than the hypocentral distance.

The frequency-dependent quality factor, is given as follows:

$$Q(f) = Q_0 f^n \quad \text{Eq. 4-10}$$

Then, the path function used in stochastic modeling is given in Eq. 4-11:

$$P(R, f) = Z(R) \cdot e^{-\frac{\pi f R}{Q(f) V_s}} \quad \text{Eq. 4-11}$$

To obtain the time history of ground motion simulations is required a duration is required. This is the sum of the source duration, which is related to the inverse of a corner frequency and a path-dependent duration.

Finally, the $G(f)$ factor expressing site effects should be evaluated generally using a one-dimensional approach. The most important function parameters are soil type, layer thickness, and S-wave velocity. The transfer function can be evaluated using methods well known in the literature (see e.g. Kramer, 1996; Lanzo & Silvestri, 1999).

4.1.2.2 Stochastic Finite Fault Modeling

Stochastic point-source modeling can give accurate simulations for stations that are located at distances from the fault larger than fault dimensions (far-field stations). Instead, the near-field simulations should be accomplished by taking into account the fault dimensions. One of the most useful methods to simulate ground motion is based on the simulation of several small earthquakes as subevents that comprise a large fault-rupture event. A fault is divided into N sub-faults and each sub-fault is considered a small point source. The rupture spreads radially from the hypocenter. The ground motions of sub-faults, each of which is calculated by the stochastic point-source method previously described, are summed with a proper time delay in the time domain to obtain the ground motion acceleration, $a(t)$, from the entire fault:

$$a(t) = \sum_{i=1}^{nl} \sum_{j=1}^{nw} a_{ij} \cdot (t + \Delta t_{ij}) \quad \text{Eq. 4-12}$$

where nl and nw are the numbers of sub-faults along the length and width of the main fault (see Figure 4-4), respectively ($nl \times nw = N$), and Δt_{ij} is the relative delay time for the radiated wave from the ij^{th} sub-fault to reach the site.

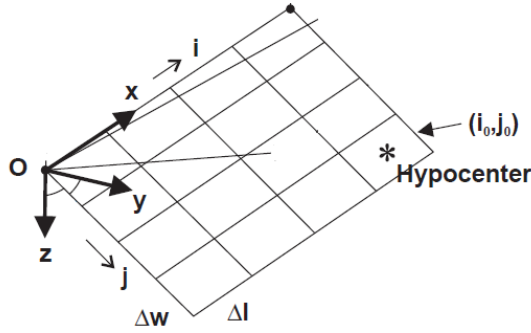


Figure 4-4: Finite fault geometry.

The acceleration spectrum for a sub-fault at a distance R_{ij} may be modeled as a point source with a displacement spectrum, defined by Eq. 4-8. The acceleration spectrum of shear wave of the ij^{th} sub-fault, $A_{ij}(f)$, is described by:

$$A_{ij} = C \cdot M_{0ij} \cdot \frac{(2\pi f)^2}{\left[1 + \left(\frac{f}{f_{cij}}\right)^2\right]} \cdot e^{-\frac{\pi f R_{ij}}{Q(f) V_s}} \quad \text{Eq. 4-13}$$

where M_{0ij} , f_{cij} , and R_{ij} are the ij^{th} sub-fault seismic moment, corner frequency, and distance from the observation point, respectively.

The dynamic corner frequency is given as:

$$f_{cij} = N_R(t)^{-\frac{1}{3}} \cdot 4.9 \cdot 10^6 \cdot V_s \cdot \left(\frac{\Delta\sigma}{M_{0ave}}\right)^{\frac{1}{3}} \quad \text{Eq. 4-14}$$

where $N_R(t)$ is the cumulative number of ruptured sub-faults at time t and $M_{0ave} = M_0/N$ is the average seismic moment of sub-faults.

The moment of each sub-fault is controlled by the ratio of its area to the area of the main fault ($M_{0ij} = M_0/N$, where M_0 is the seismic moment of the entire fault). If the sub-faults are not identical we can express the seismic moment of each sub-fault as follows:

$$M_{0_{ij}} = \frac{M_0 \cdot S_{ij}}{\sum_{k=1}^{nl} \sum_{l=1}^{nw} S_{kl}} \quad \text{Eq. 4-15}$$

where S_{ij} is the assigned relative slip weight of the ij^{th} sub-fault.

In this study, for simulating high-frequencies of the volcanic earthquakes on Ischia island, the stochastic finite-fault methodology with a dynamic corner frequency concept has been adopted by using the *EXSIM* software (Motazedian & Atkinson, 2005; Boore, 2009; Atkinson & Assatourians 2015).

4.2 Analysis methods

The following sub-sections summarise the methodologies and procedures that were adopted in this study to predict the occurrence of liquefaction and slope instability phenomena at territorial and local scale. These methods can be classified into levels corresponding to increasing degrees of detail, in terms of: definition of the seismic action, the accuracy of the geological surveys and geotechnical characterisation, complexity of the analysis, and engineering significance of the parameters representing the effects (ISSMGE, 1999; AGI, 2005; Silvestri & d'Onofrio, 2014; Silvestri et al. 2016). As the level of detail increases, the ratio of reference scales increases accordingly, from those typical for the territorial scale (e.g. for microzonation maps), to those representative of the single phenomenon at the local scale (for engineering design analyses).

Table 4-1: Hierarchy of seismic slope stability and liquefaction analysis methods (modified from Silvestri and d'Onofrio, 2014).

Analysis Method	Reference Seismic Motion	Constitutive Model	Investigations and Tests	Typical Output
Screening criteria (Level I)	magnitude and distance	-	-	phenomenon yes/no
Pseudo-static Semi-empirical (Level II)	a_{max} magnitude other synthetic motion parameters	rigid-plastic deformability coefficients	traditional in situ and lab tests Vs measurements	safety factor (LIQ,SS) displacements (SS)
Simplified dynamic (Level III)	accelerograms $a(t)$	single-phase medium linear-equivalent / non- linear (LIQ) rigid-plastic (SS)	as above, plus cyclic and dynamic laboratory tests	accelerations displacements total stresses strains safety factor
Advanced dynamic (Level IV)		multi-phase medium elasto-plastic		as above, plus excess pore water pressure effective stresses
SS=Slope Stability, LIQ=Liquefaction				

Table 4-1 summarises the basic characteristics of the procedures, which can be divided into four levels, which imply increasingly complex methods of analysis, requiring an increasing degree of knowledge and detail of the geological, geophysical and geotechnical characteristics of the area. In this study all the analysis procedures were developed under free-field conditions.

4.2.1 Liquefaction

In analyses at the regional scale, attributable to Level I according to the methodological hierarchy adopted, liquefaction susceptibility can be characterised with empirical indicators by adopting classification criteria for litho-stratigraphic units (HAZUS, 2003) and magnitude-distance of activation relationships (Galli, 2000). This latter study compiled the location of sites in Italy where liquefaction phenomena have been identified and defined an upper-bound curve relating the magnitude of the

event to the epicentral distance of the farthest site where a liquefaction phenomenon was observed for that event (Figure 4-5). The relatively limited number of events, identified predominantly through water or sand volcanos or other related phenomena (ground cracking), is attributable to the relatively limited energy content of Italian earthquakes and the low susceptibility of the formations present even in the epicentral areas relative to the main seismogenic sources.

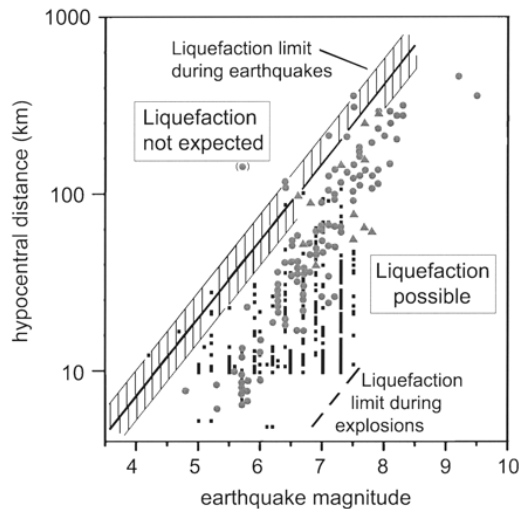


Figure 4-5: Empirical screening criteria for liquefaction phenomena (Galli, 2000).

Design standards provide empirical criteria to exclude liquefaction. For instance, according to the national code (NTC 2018), liquefaction analyses are not needed if one of the following conditions is met:

- 1) the maximum expected acceleration in free field condition is less than 0.1g;
- 2) the mean seasonal depth of the water table is greater than 15 m from the surface (for horizontal ground surface and shallow foundations);
- 3) the number of SPT for clean sand, corrected for 60% energy release and normalised confinement stress (N_{160cs}), is greater than 30; the cone tip resistance corrected for confinement stress (q_{c1Ncs}) is greater than 180;

4) the grain size distribution curve falls inside the range of soils susceptible to liquefaction (Figure 4-6).

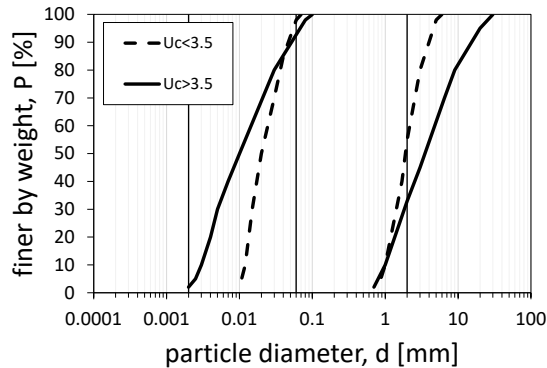


Figure 4-6: Grain size distribution-based criteria for liquefaction susceptibility for the Italian Building Code (from NTC18).

An example of the application of the above criteria at urban scale is given by Evangelista & Santucci de Magistris (2011) for the city of Naples. If anyone of the conditions listed above occurs the probability of liquefaction occurrence is very low. If none of the exclusion criteria is met, it is common practice to conduct liquefaction susceptibility analyses, typically using in-situ tests rather than laboratory tests, due to the well-known difficulty of taking undisturbed samples in cohesionless sandy soils when saturated.

In the international technical literature, there are further screening criteria for the identification of soils susceptible to liquefaction, often based on particle size distribution, Atterberg limits and on-site water content. The most famous among them in the literature is that by Robertson & Wride (1998).

This method, based on CPT test results, refers to the *Soil Behaviour Type Index*, I_c :

$$I_c = \left[(3.47 - \log(Q))^2 + (1.22 + \log(F))^2 \right]^{0.5} \quad \text{Eq. 4-16}$$

where Q and F are normalized ratios expressing the tip resistance, q_c , and the sleeve friction, f_s , as follows:

$$Q = \left(\frac{q_c - \sigma_{v0}}{p_a} \right) \left(\frac{p_a}{\sigma_{v0}} \right)^n \quad \text{Eq. 4-17}$$

$$F = \left(\frac{f_s}{q_c - \sigma_{v0}} \right) \cdot 100\% \quad \text{Eq. 4-18}$$

The exponent n varies from 0.5 in sands to 1 in clays, while σ_{v0} and σ'_{v0} are the total and effective vertical stress and p_a is the atmospheric pressure.

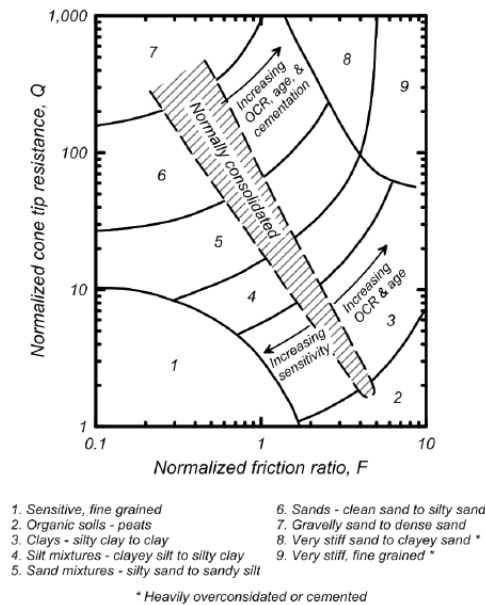


Figure 4-7: CPT-based soil behaviour type classification chart by Robertson (1990).

The calculation of the index I_c has fundamental importance for the identification of the soil layers on which to perform the simplified verification. Conventionally, the assessment must be performed for $I_c < 2.6$, while for higher values it is assumed that the soil is not liquefiable (Robertson, 2016).

For a Level II liquefaction analysis, it is necessary to introduce the seismic action, expressed in terms of synthetic motion parameters. The amplified peak acceleration, a_s can be deduced by multiplying the reference acceleration a_r (see § 4.1.1) for both

stratigraphic, S_s , and topographic, S_T , amplification factors. The latter can be evaluated using the national code (NTC 2018) criteria. Alternatively, can be computed considering the soil types based on the equivalent shear wave velocity, $V_{s,eq}$, and expressing the decrease of amplification with ground motion amplitude by a piecewise constant-power relationship:

$$S_s = \begin{cases} m & a_r \leq x_i \\ \frac{a(a_r - x_0)^b}{a_r} & a_r > x_i \end{cases} \quad \text{Eq. 4-19}$$

Eq. 4-19 was calibrated by Tropeano et al. (2018) based on weak- to strong-motion Italian seismic records and numerical simulations accounting for non-linear and dissipative soil behaviour. S_s is equal to 1 for soil class A, while the coefficients for the other soil classes are reported in Table 4-2.

Table 4-2: Coefficients of the piecewise constant-power law (Tropeano et al. 2018).

Soil type	m	a	b	x_0	x_i
B	1.70	0.924	0.798	0.004	0.02
C	1.90	0.635	0.521	0.024	0.05
D	2.25	0.402	0.351	0.026	0.04

Theoretical studies in the literature (e.g. Sanchez-Sesma, 1990) suggest to associate S_T to the slope curvature α' , accounting for the amplification of seismic waves due to focusing on ridges, as well as for their attenuation in canyons. The effectiveness of this approach was validated by dynamic numerical analyses on different slope models and adopted by several studies (Torgoev et al. 2013; Forte, 2014; Silvestri et al. 2016; Forte et al. 2017), which directly correlated the curvature to the topographic amplification. The range of S_T adopted in this case derives from the results of the above-mentioned studies, combined with the values traditionally suggested by the European and Italian seismic codes, as shown in Table 4-3.

Table 4-3: Slope curvature (α') ranges and associated S_r (Forte, 2014).

Slope curvature (α')	S_r
-10 ÷ -0.9	0.5
-0.9 ÷ -0.2	0.7
-0.2 ÷ +0.2	1
> +0.2	1.4

The maximum shear stress at reference depth z can be expressed by imposing pseudo-static equilibrium with reference to the horizontal translation of the soil column down to the depth z , up on which the inertia forces produced by the earthquake act (Figure 4-8):

$$\tau = \int_0^z \rho \cdot a(z) dz = \int_0^z \gamma \cdot \frac{a(z)}{g} dz \quad \text{Eq. 4-20}$$

In Eq. 4-20, ρ is the density, γ is the unit weight volume, $a(z)$ is the acceleration distribution and g is the gravity acceleration. If the soil column is assumed to move horizontally as a rigid body, and if the maximum horizontal acceleration on the ground surface is a_{\max} , the maximum shear stress, τ_{\max} , acting at the bottom of the soil column is:

$$\tau_{\max,r} = \frac{a_{\max}}{g} \sigma_v \quad \text{Eq. 4-21}$$

Taking into account the deformability through a reductive coefficient $r_d(z)$ and the variability in time of the cyclic stress through a coefficient β , usually set equal to 0.65, an equivalent tangential stress can be expressed as:

$$\tau_{eq} = \beta \cdot \tau_{\max,d} = \beta \cdot r_d \cdot \tau_{\max,r} = \beta \cdot r_d \cdot \frac{a_{\max}}{g} \sigma_v \quad \text{Eq. 4-22}$$

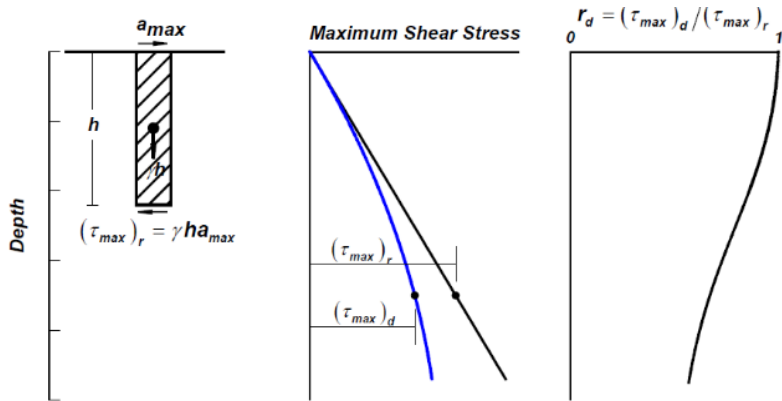


Figure 4-8: Seismic action in pseudo-static analysis.

Idriss (1999), in extending work of Golesorkhi (1989), performed several parametric site response analyses and concluded that the parameter r_d could be expressed as:

$$r_d = \exp[\alpha(z) + \beta(z) \cdot M] \quad \text{Eq. 4-23}$$

$$\alpha(z) = -1.012 - 1.126 \sin\left(\frac{z}{11.73} + 5.133\right) \quad \text{Eq. 4-24}$$

$$\beta(z) = 0.106 + 0.118 \sin\left(\frac{z}{11.28} + 5.142\right) \quad \text{Eq. 4-25}$$

where z is depth below the ground surface in meters, M is the moment magnitude of the expected seismic event and the arguments of the sinus functions are in radians.

Geotechnical properties are usually derived from in-situ investigations (penetrometric or geophysical tests) and laboratory tests related to the determination of index properties.

The physical-mechanical parameters required for the analyses are:

- the unit volume weight, γ ;
- the dynamic penetrometric resistance, N_{SPT} , or static resistance, q_c , or shear wave velocity, V_s ;
- the index properties, typically fine content, FC ($d < 0.075$ mm), and/or plasticity index, PI .

The occurrence or non-occurrence of liquefaction, assessed through simplified analysis procedures, can be expressed through the calculation of a factor of safety, FS_{liq} , defined as the ratio of Cyclic Resistance Ratio (CRR) and Cyclic Stress Ratio (CSR), as follows:

$$FS_{liq} = \frac{CRR}{CSR} = \left(\frac{CRR_{M=7.5; \sigma'_v=1}}{CSR} \right) \cdot MSF \cdot K_{\sigma} \cdot K_{\alpha} \tag{Eq. 4-26}$$

In Eq. 4-26 $CRR_{M=7.5; \sigma'_v=1}$ is the resistance referred to a magnitude $M=7.5$ and $\sigma'_v=100$ kPa, MSF is the magnitude scaling factor, introduced to account for the effect of duration of the seismic event (Figure 4-9), K_{σ} and K_{α} (Figure 4-10) are correction factors to account for the effective overburden stress and initial static shear on the horizontal plane.

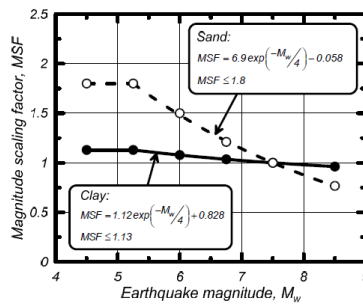


Figure 4-9: MSF relationship for clay and sand (Boulanger & Idriss, 2007).

(a)

(b)

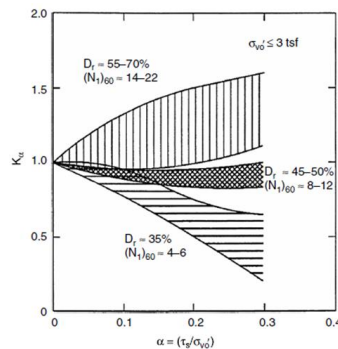
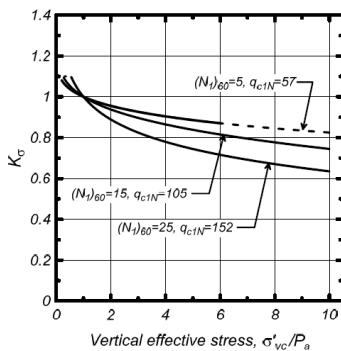


Figure 4-10: Overburden correction factor relationships (Boulanger & Idriss, 2014) (a) and static shear stress correction factor (Harder & Boulanger, 1997) (b).

From Eq. 4-22, CSR can be computed as follows:

$$CSR = \frac{\tau_{eq}}{\sigma_v} = 0.65 \frac{a_{max}}{g} \frac{\sigma_v}{\sigma_v'} r_d \quad \text{Eq. 4-27}$$

The moment magnitude value of 7.5 is in fact referred to by the empirical relation based on the interpretation of case studies in which evidence of liquefaction was or was not observed (Figure 4-11). Typically, the abacuses available in the literature refer to clean sands, i.e. with a fine content FC less than 5%.

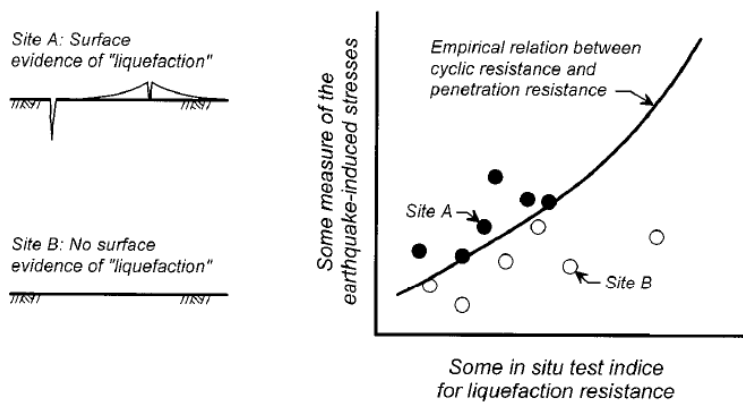


Figure 4-11: Schematic of the approach used to develop relationships between the in-situ CRR and the results of in-situ tests (Idriss & Boulanger, 2008).

The mechanical properties adopted in empirical abacuses can be deduced from Cone Penetration Test (CPT), Standard Penetration Test (SPT) or shear-wave velocity measurements.

It should be emphasised that penetrometric tests provide measurements of strength, and therefore their use is justified since liquefaction is a phenomenon in which the soil reaches failure; on the other hand, shear wave velocity, being a measure of stiffness at very low shear strains, refers to conditions far from failure and therefore far from the liquefaction phenomenon. However, in some cases, it may be appropriate to refer to the shear wave velocity in verifying liquefaction, when penetrometric strengths are such that the resistance is underestimated, such as in the case of volcanic soils, like those in this study.

Figure 4-12 shows the abacus proposed by Boulanger & Idriss (2014).

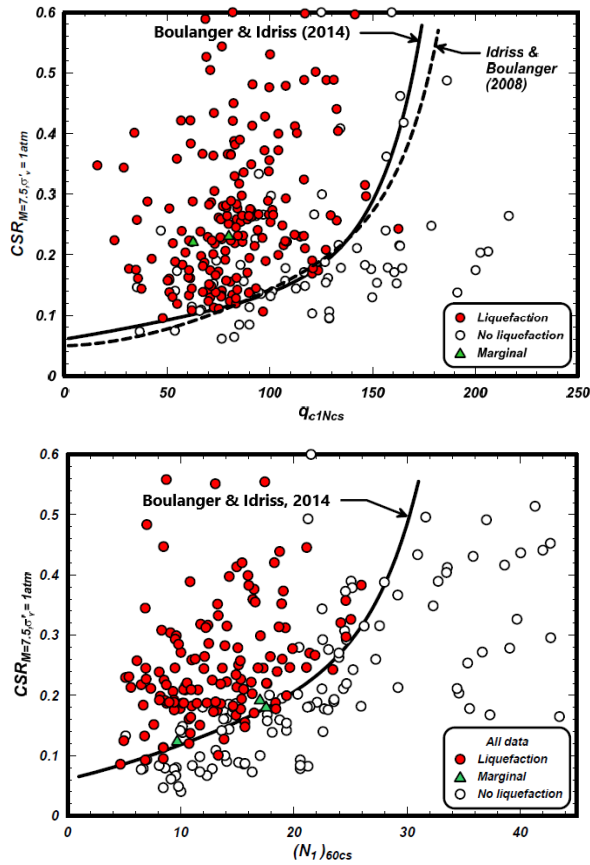


Figure 4-12: Liquefaction abacuses for CPT (above) and SPT (below) (modified from Boulanger & Idriss, 2014).

The limit curves shown in Figure 4-12 are defined by the following analytical expressions:

$$CRR_{M=7.5, \sigma'_v=1atm} = \exp\left(\frac{q_{c1Ncs}}{113} + \left(\frac{q_{c1Ncs}}{1000}\right)^2 - \left(\frac{q_{c1Ncs}}{140}\right)^3 + \left(\frac{q_{c1Ncs}}{137}\right)^4 - 2.8\right) \quad \text{Eq. 4-28}$$

$$CRR_{M=7.5, \sigma'_v=1} = \exp\left(\frac{(N_1)_{60cs}}{14.1} + \left(\frac{(N_1)_{60cs}}{126}\right)^2 - \left(\frac{(N_1)_{60cs}}{23.6}\right)^3 + \left(\frac{(N_1)_{60cs}}{25.4}\right)^4 - 2.8\right) \quad \text{Eq. 4-29}$$

where the equivalent clean sand penetration resistances, q_{c1Ncs} and $(N_1)_{60cs}$ are expressed respectively as:

$$q_{c1Ncs} = q_{c1N} + \Delta q_{c1N} \quad \text{Eq. 4-30}$$

$$(N_1)_{60cs} = (N_1)_{60} + \Delta(N_1)_{60} \quad \text{Eq. 4-31}$$

The first terms of the above two equations are respectively given by:

$$q_{c1N} = C_N \cdot q_{cN} \quad \text{Eq. 4-32}$$

$$(N_1)_{60} = C_N \cdot N_{60} \quad \text{Eq. 4-33}$$

The coefficient C_N is a function of the effective vertical stress, σ_v' , and atmospheric pressure p_a :

$$C_N = \left(\frac{p_a}{\sigma_v'} \right)^m \leq 1.7 \quad \text{Eq. 4-34}$$

where the exponent m is equal to:

$$m = 1.338 - 0.249 \cdot (q_{c1Ncs})^{0.264} \quad \text{Eq. 4-35}$$

$$m = 0.784 - 0.0768 \cdot \sqrt{(N_1)_{60cs}} \quad \text{Eq. 4-36}$$

The second terms of Eq. 4-30 and Eq. 4-31 are functions of fine content (FC), expressed as a percentage:

$$\Delta q_{c1N} = \left(11.9 + \frac{q_{c1N}}{14.6} \right) \exp \left(1.63 - \frac{9.7}{FC + 2} - \left(\frac{15.7}{FC + 2} \right)^2 \right) \quad \text{Eq. 4-37}$$

$$\Delta(N_1)_{60} = \exp \left(1.63 + \frac{9.7}{FC + 0.01} - \left(\frac{15.7}{FC + 0.01} \right)^2 \right) \quad \text{Eq. 4-38}$$

The latter correction terms represent the expected increase in soil strength in relation to the presence of fine material of plastic nature. In the case of non-plastic fine content, no correction must be made.

As mentioned earlier, for some types of soil it might be preferred to perform simplified verifications from shear wave velocity. Figure 4-13 shows the abacus proposed by Andrus & Stokoe (2000) as a function of normalised shear wave velocity. The latter is a function of the effective vertical stress, σ_v' , and atmospheric pressure, p_a , as follows:

$$V_{S1} = V_S \cdot C_V = V_S \cdot \left(\frac{p_a}{\sigma_v'} \right)^{0.25} \quad \text{Eq. 4-39}$$

with $C_V < 1.4$ and V_{S1c} is the vertical asymptote of the limit curve, expressed as a function of fines content, FC , as follows:

$$V_{S1c} = \begin{cases} 215 & FC \leq 5\% \\ 215 - 0.5(FC - 5) & 5\% < FC \leq 35\% \\ 200 & FC > 35\% \end{cases} \quad \text{Eq. 4-40}$$

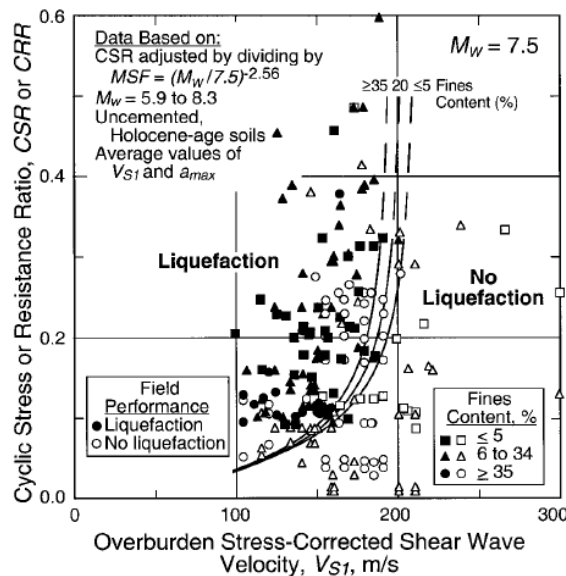


Figure 4-13: Liquefaction abacus at varying normalised shear wave velocity V_{S1} as a function of fine content (Andrus & Stokoe, 2000).

In the so-called decoupled Level III approaches, the liquefaction assessment is preceded by a seismic response analysis (Lanzo & Silvestri, 1999), aimed at defining

the dynamic action acting on the potentially liquefiable volume through an equivalent accelerogram $a_{eq}(t)$, representative of the overall inertial actions on that volume. Liquefaction analysis is therefore conducted by reducing the equivalent seismic action at the depth of interest to a cyclic stress ratio, CSR, and a number of equivalent cycles, N_{eq} (Figure 4-14); the latter can be estimated with predictive relationships as a function of a limited number of synthetic parameters of the seismic motion (cfr. e.g. Biondi et al. 2012). In this way, verification can be carried out by comparing the seismic action with a cyclic resistance curve $CRR-N_{cyc}$ measured by laboratory tests.

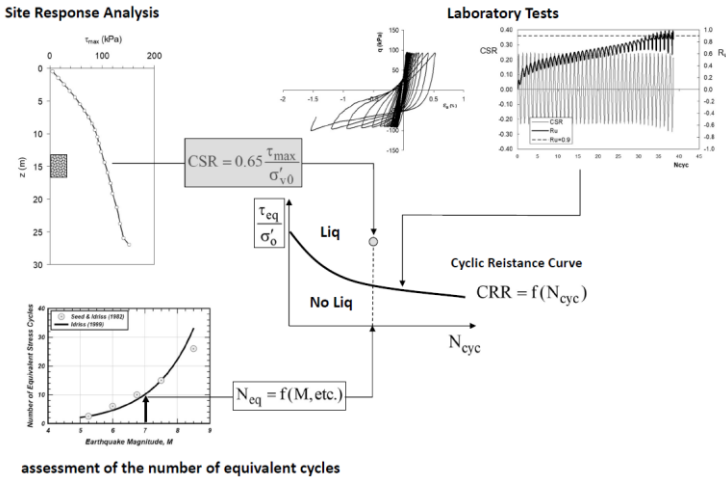


Figure 4-14: Outline of procedure for simplified dynamic liquefaction analysis.

For a more complete quantification of the effects produced by the phenomenon in terms of excess pore water pressures and displacements, it is necessary to resort to approaches that envisage the execution of coupled non-linear analyses (Level IV), adopting increasingly complex models in relation to the degree of knowledge of the constitutive parameters of the soil, which are sometimes, however, numerous and of complex experimental determination. An approach that represents a satisfactory balance between simplicity and reliability of numerical simulations is the so-called 'loosely coupled' approach, developed by Tropeano et al. (2019) using a calculation code for one-dimensional nonlinear analysis (SCOSSA-PWP); the code implements a

constitutive model based on a relatively small number of parameters of clear physical significance, which can be obtained through direct interpretation of cyclic and dynamic laboratory tests. The approach makes it possible to quantify pore pressures induced by the earthquake and to verify the effect of their accumulation and dissipation over time on stability conditions and kinematics, respectively, during and after the earthquake (for more details see Chiaradonna et al. 2018; Tropeano et al. 2019).

4.2.1.1 Integral index

The need to summarise into a single synthetic value the result of a liquefaction assessment along a soil profile was translated into the definition of appropriate integral parameters describing the liquefaction potential at a site. They make it easy to compare the overall liquefaction susceptibility between different sites and set the basis to draw up related maps. The indicators adopted in this study are three. For semi-empirical methods, reference will be made to the ‘Liquefaction Potential Index’ *LPI* (Iwasaki et al. 1978) and the ‘Liquefaction Severity Number’ *LSN* (Tonkin & Taylor, 2013), while for advanced analyses, the ‘Induced Damage Parameter’ *I_{AM}* (Chiaradonna et al. 2020) index will also be adopted.

The *LPI* is derived from a weighted average, in inverse proportion to the depth *z*, of the unit complement of the safety factor *FS*, when the latter is lower than unity:

$$LPI = \int_0^{20} [1 - FS(z)] w(z) dz \quad \text{Eq. 4-41}$$

The weighing function *w(z)* is assumed to be linear, and is such that it has a zero value at the limit depth of 20 m and a maximum value of 10 at the surface:

$$w(z) = 10 - 0.5z \quad \text{Eq. 4-42}$$

where *z* is expressed in meters. The *LPI* value obtained allows for an overall assessment of the potential failure induced along a whole soil profile (Table 4-4).

Table 4-4: Simplified assessment of soil liquefaction risk based on LPI (Iwasaki et al. 1978).

Index	Potential failure
LPI = 0	Very low
$0 < \text{LPI} \leq 5$	Low
$5 < \text{LPI} \leq 15$	High
LPI ≥ 15	Very high

The main limitation of this indicator is determined by the fact that layers that are not completely liquefied ($FS > 1$) are not taken into account in the calculation. The effects resulting from high values of the excess pore pressure ratio, even when not enough to induce complete liquefaction, are therefore neglected.

On the basis of studies developed after the seismic sequence occurred in 2010-11 in Christchurch (New Zealand), the LSN indicator was developed with the aim of providing indications of the intensity of the liquefaction effects and the potential damage induced to above ground structures. This indicator is defined as the integral of the post-liquefaction volumetric reconsolidation strains (ε_v):

$$LSN = 1000 \int \frac{\varepsilon_v}{z} dz \quad \text{Eq. 4-43}$$

LSN has the advantage of taking into account the contribution of non-liquefied ($FS \geq 1$) soil layers, thus removing the most critical shortcoming of LPI . The hyperbolic depth weighing function ($1/z$) gives higher relevance to the shallower liquefiable formations, correctly reducing the risk of overestimating the site vulnerability.

The value of ε_v in Eq. 4-43 can be computed with the procedure suggested by Zhang et al. (2002), who proposed a relationship between post-liquefaction volumetric strain and equivalent clean sand normalized CPT tip resistance, q_{c1Ncs} , for different factors of safety, these latter varying between 0.6 and 1.3 (Figure 4-15).

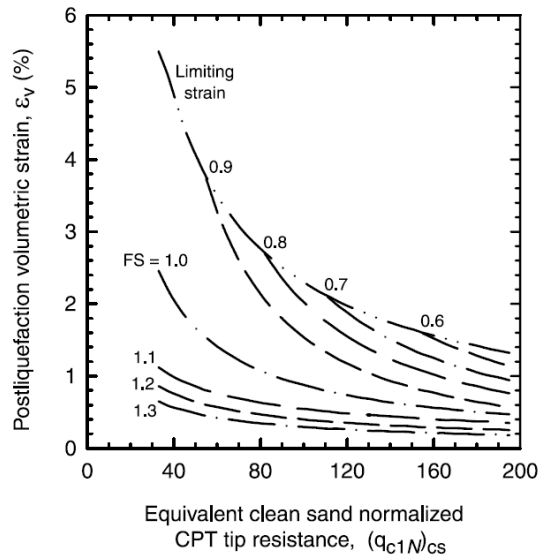


Figure 4-15: Relationship between post-liquefaction volumetric strain and equivalent clean sand normalized CPT tip resistance for different factors of safety (Zhang et al. 2002).

The results of the coupled analyses in terms of excess pore water pressure ratio (r_u) allow for a straightforward evaluation ε_v from the oedometric compression curve (Figure 4-16).

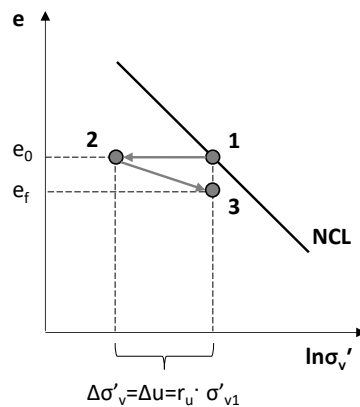


Figure 4-16: Stress-void ratio path in the one-dimensional consolidation plane (NCL = Normal Consolidation Line).

For a given initial void ratio e_0 , after the end of the undrained seismic shaking the effective stress is reduced by the generation of the excess pore pressure Δu (path 1-2 in Figure 4-16):

$$\Delta\sigma'_v = -\Delta u = -r'_u \cdot \sigma'_{v0} \quad \text{Eq. 4-44}$$

For each soil layer, by knowing the excess pore pressure, Δu , and the variation of the void ratio, e_0 - e_f , along the re-compression curve (path 2-3 in Figure 4-16), it is possible to evaluate the vertical strain, ε_z , that in one-dimensional conditions coincides with volumetric strain, ε_v , necessary to evaluate LSN through Eq. 4-43.

The amount of the expected damage as a function of the value assumed by LSN is shown in Table 4-5.

Table 4-5: Evidences of liquefaction and damage degrees associated to LSN (Tonkin & Taylor, 2013).

LSN	damage description
0 < LSN < 10	nil to minimum evidence of liquefaction
10 < LSN < 20	from minimum evidence of liquefaction to presence of sand boils
20 < LSN < 30	moderate to intense liquefaction evidence and probable subsidence
30 < LSN < 40	from intense liquefaction evidence to severe structural failure
LSN > 50	severe and widespread surface damage

From the values of r_u it is also possible to evaluate the 'Induced Damage Parameter', I_{AM} , (Chiaradonna et al. 2020), corresponding to the free-field post-seismic volumetric consolidation settlement:

$$I_{AM} = \frac{0.003}{(1 + z_{\min})^{0.3}} \cdot \int_{z_{\min}}^{z_{\max}} \frac{r_u(z)}{1 - r_u(z)} dz \quad \text{Eq. 4-45}$$

where z_{\min} and z_{\max} are, respectively, the minimum and maximum depths of the uppermost saturated liquefiable soil layer. In Eq. 4-45, depths are expressed in m.

Table 4-6 shows the damage scale suggested for rigid body settlements due to earthquake-induced excess pore pressures.

Table 4-6: Damage scale for rigid body settlements due to earthquake-induced ground deformation.

Damage state	Settlement	I _{AM}
Low	$\Delta \leq 0.1\text{m}$	$I_{AM} \leq 0.1$
Moderate	$0.1\text{m} < \Delta \leq 0.3\text{m}$	$0.1 < I_{AM} \leq 0.3$
Extensive	$0.3\text{m} < \Delta \leq 1.0\text{m}$	$0.3 < I_{AM} \leq 1.0$
Severe	$\Delta > 1.0\text{m}$	$I_{AM} > 1.0$

4.2.2 Slope stability

The Level I zoning procedure is based on empirical-statistical screening criteria, which do not require any geotechnical characterisation of the formations. Such methods consider the earthquake-induced landslide hazard expressed as a binary function, which depends on magnitude (M) and distance (R). In this way, it is possible to evaluate for different earthquakes the maximum distance at which a given landslide mechanism could occur. The pioneering studies of this topic are due to Keefer (1984), who collected a database of 40 worldwide earthquakes that triggered landslides between 1811 and 1980 in the same study proposing the seismic landslides classification depicted in Figure 3-7. Consequently, the upper bound magnitude-distance curves reported in Figure 4-17 were proposed for the assessment of the triggered landslides hazard.

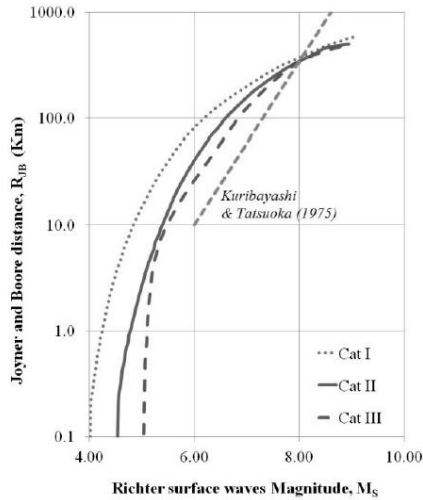


Figure 4-17: Upper bound magnitude-distance curves for the three landslide categories (Cat I: disrupted rock and soil slides; Cat II: coherent rock and soil slides; Cat III: lateral spreads and flow slides) proposed by Keefer (1984).

These simple empirical correlations point out that the susceptibility to co-seismic landslides is limited by a magnitude threshold (below which landslides are not expected to occur even in the epicentral area) equal to 4 and 4.5 for rockfalls and sliding mechanisms, respectively.

The two landslides depicted in the Figure 2-11 were triggered at an estimated magnitude of 4.26 and therefore represent an outlier. On the other hand, the 2017 Ischia earthquake ($M_w=3.91$) fits the predictive curves proposed by Keefer (1984), as for this low value of magnitude no landslide occurred.

For liquefaction-induced landslides, like lateral spreads, the threshold magnitude is 5 and it is in accordance with the upper bound liquefaction limit curves identified by Kuribayashi and Tatsuoka (1975). The procedure was applied at a territorial scale by Silvestri et al. (2006, 2016), for generating regional scale maps in terms of susceptibility indicators attributable to a territorial unit typically corresponding to a single municipality. These maps therefore constitute a preliminary screening tool of potentially susceptible areas.

In the Level II methods, the degree of the earthquake-induced instability at a territorial scale can be implemented in a Geographic Information System (GIS) by combining hydrogeological, geotechnical, topographic and seismological data, as shown in the flowchart of Figure 4-18. The mapping scale usually varies between 1:25.000 and 1:5.000, depending on the reference geological survey, with a cell grid size determined by the resolution of the Digital Terrain Model (DTM).

At such scale ratios, the seismic slope instability for category II mechanisms can be evaluated using the displacement-based approach. Following the well-known method by Newmark (1965), the potential landslide is modelled as a rigid friction block sliding on an inclined plane. The susceptibility to triggering of seismic-induced landslides can be expressed independently of the evaluation of seismic actions, by determining the critical acceleration, a_c , i.e. the value activating the slope movement:

$$a_c = (FS - 1) g \sin \alpha \quad \text{Eq. 4-46}$$

where g is the gravity acceleration, α is the slope angle and FS is the factor of safety. In the conservative hypothesis for infinite slope geometry, the latter can be calculated as:

$$FS = \frac{c'}{\gamma D \sin \alpha} + \frac{\tan \varphi'}{\tan \alpha} - \frac{m \gamma_w \tan \varphi'}{\gamma \tan \alpha} \quad \text{Eq. 4-47}$$

where:

- γ is the unit volume weight of the soil;
- γ_w is the water unit weight;
- c' and φ' are the effective cohesion and friction angle;
- D is the depth of the sliding surface;
- $m = D/D_w$, with $D_w = D - z_w$, i.e. the saturated soil thickness above the sliding surface, being z_w the depth of the water table.

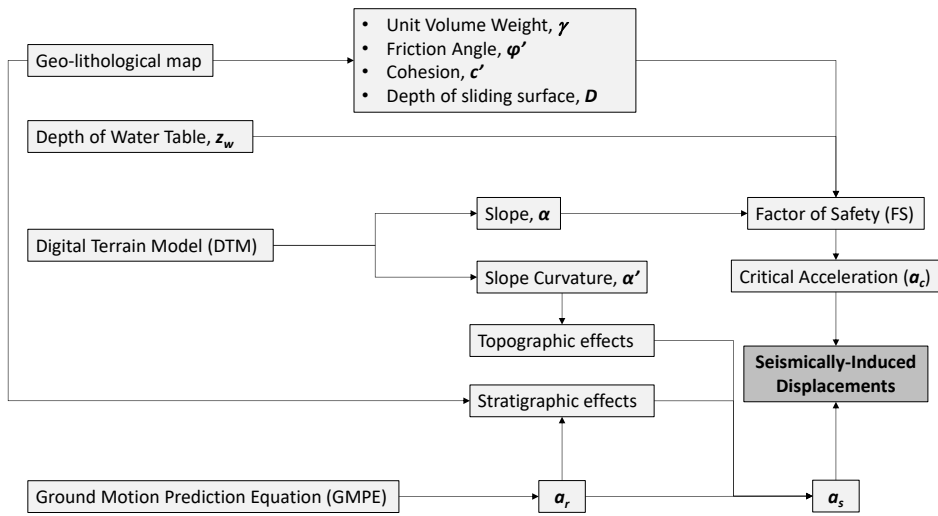


Figure 4-18: Flowchart of the procedure for the prediction of earthquake-induced displacements (Gargiulo et al. 2022).

The map of the critical acceleration, combined with the spatial distribution of the seismic action, constitutes the prerequisite for the prediction of the co-seismic displacements, which can be obtained by applying various correlations available in the literature, typically expressed as a function of the ratio $\eta = a_c / a_{\max}$ between critical and peak surface acceleration (see e.g. Simonelli & Fortunato, 1996; Rampello et al. 2006; Ausilio et al. 2008; Madiati, 2009; Biondi et al. 2011; Tropeano et al. 2012; Tropeano et al. 2017; Gaudio et al. 2020). These correlations are obtained by extensively applying Newmark's simplified dynamic analysis method to infinite slopes, using numerous accelerograms extracted from different reference databases, and applying statistical criteria to obtain mean (or median) and upper bound (or 90th percentile) displacement values.

The results obtained by applying the Level II approach will make it possible to outline the most susceptible areas, which will require specific insights through higher level dynamic analyses at the single slope scale. These approaches require a specific geomorphological and stratigraphic site characterisation, as well as geo-structural investigations. The physical-mechanical properties of the main formations must also

be characterised by *ad hoc* site investigations and specific laboratory tests on samples taken on site.

Simplified Level III dynamic analyses can be carried out by adopting so-called 'decoupled' or 'coupled' approaches. In the first case, the contribution of soil deformability is taken into account through the definition of an 'equivalent accelerogram' which is applied as an input motion to the rigid block model for predicting its displacements. This accelerogram can be evaluated starting from the time history of the shear stresses acting on the sliding surface, to be obtained from a simplified dynamic analysis of the seismic response of the slope, taking into account the variation of soil stiffness and damping ratio with the shear strain (Tropeano et al. 2017). In coupled approaches, on the other hand, the effects due to soil deformability and permanent displacements are evaluated simultaneously (Tropeano et al. 2015).

Finally, advanced Level IV dynamic analyses use nonlinear dynamic algorithms in the time domain (implemented in finite element or finite difference computational codes) and more advanced elasto-plastic constitutive laws (e.g. mixed isotropic-kinematic hardening models). The latter requires careful calibration of the various parameters, not only based on routine geotechnical investigations but also through non-conventional cyclic laboratory tests (triaxial, simple or torsional shear). The advanced analyses ultimately allow for predictions of the slope behaviour also in terms of effective stresses, as well as of both distortional and volumetric strains; therefore, they permit to describe both the co-seismic mechanisms and the possible post-seismic evolution of the instability phenomenon.

5. Database of investigations

Earthquake-induced instabilities analyses require the knowledge of the geological and geotechnical conditions, at the territorial scale or detailed scale, depending on the level of the analysis. This knowledge usually requires the acquisition of a certain amount of data in order to outline the complex natural situation and set a rational model for engineering, namely the subsoil model. The collection and organization of pre-existing knowledge through the constitution of a database of geological and geotechnical investigations represent the backbone of every large-scale project aimed at territorial analysis. Hence an essential part of this work was devoted to this task. The retrieved information was organized through GIS (*Geographical Information Systems*) technology adopting the *ESRI ArcGis 10.8* software.

Figure 5-1 and Figure 5-2 show the available surveys in the study area before the MASLIDE project from municipal master plan PRG (in green), III level Seismic Microzonation studies SMIII (in blue) and others collected from various studies and local companies (in yellow).

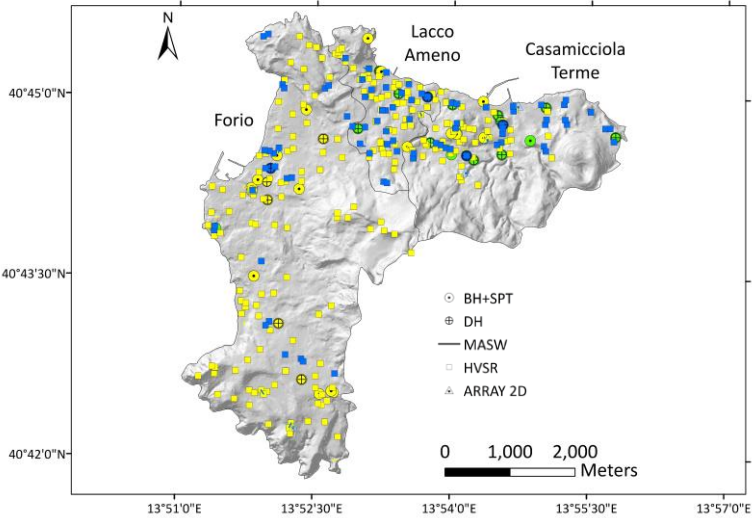


Figure 5-1: Available surveys in the study area prior to the MASLIDE project: PRG (in green), SMIII (in blue) and others collected from various studies (in yellow).

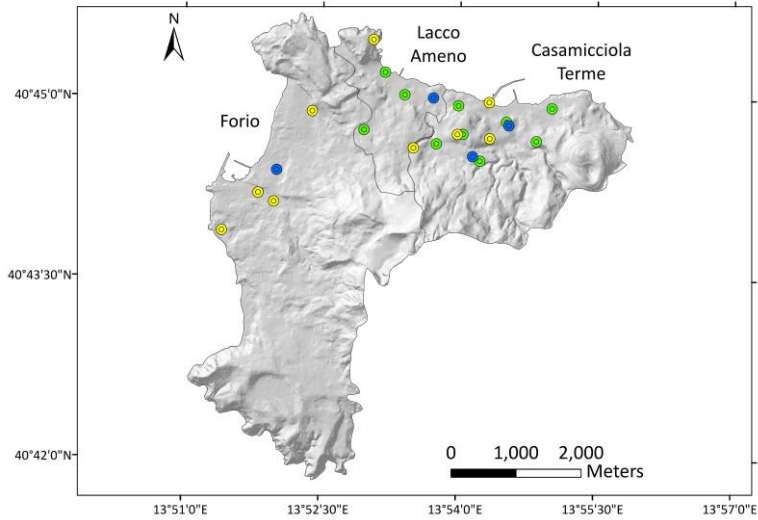


Figure 5-2: Location of boreholes from which undisturbed samples were taken for static and/or cyclic laboratory tests: PRG (in green), SMIII (in blue) and others collected from various studies (in yellow).

Table 5-1 and Table 5-2 show the distribution of available tests.

Table 5-1: Distribution of available site tests.

	PRG	SMIII	others
BH+SPT	15	4	21
DH	11	4	5
MASW	0	37	34
HVSR	0	84	212
ARRAY 2D	0	6	4

Table 5-2: Distribution of available laboratory tests.

	PRG	SMIII	others
grain-size distribution	18	16	12
n- γ -w	18	16	12
Atterberg limits	0	3	1
simple shear/triaxial tests	13	0	11
cyclic/dynamic tests	0	9	0

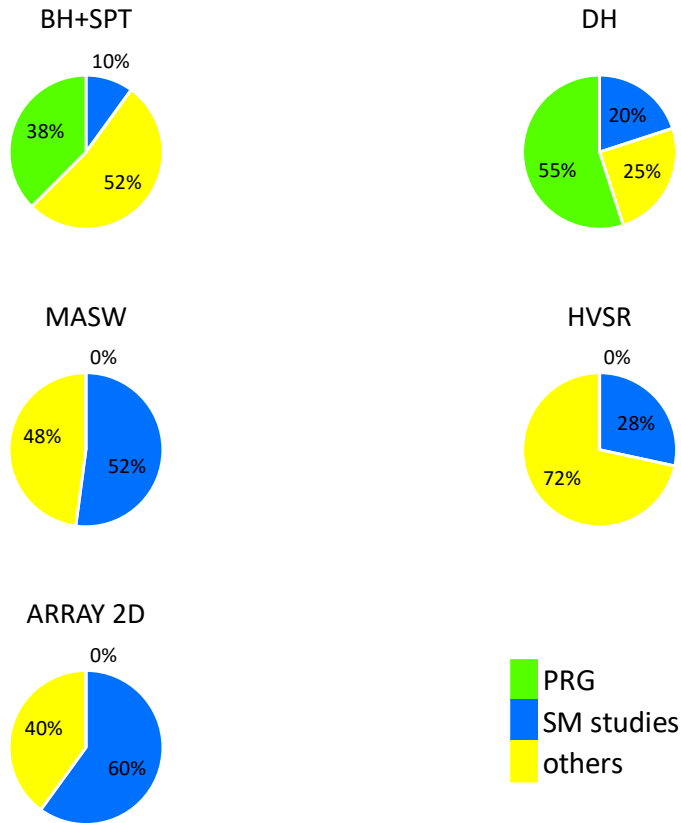


Figure 5-3: Distribution of the available tests: boreholes (BH), down-holes (DH), surface wave tests (MASW), HVSR spectral ratios and ARRAY 2D.

A great amount of data was due to the post-2017 Casamicciola Terme earthquake reconstruction activities (SMIII+others). A minor part of the data came from a city master plan (PRG). This database constitutes the main part of the geotechnical investigations shown in Figure 5-3 and Figure 5-4.

Available surveys show a lack of data both in potentially liquefiable areas and in areas unstable due to landslide phenomena.

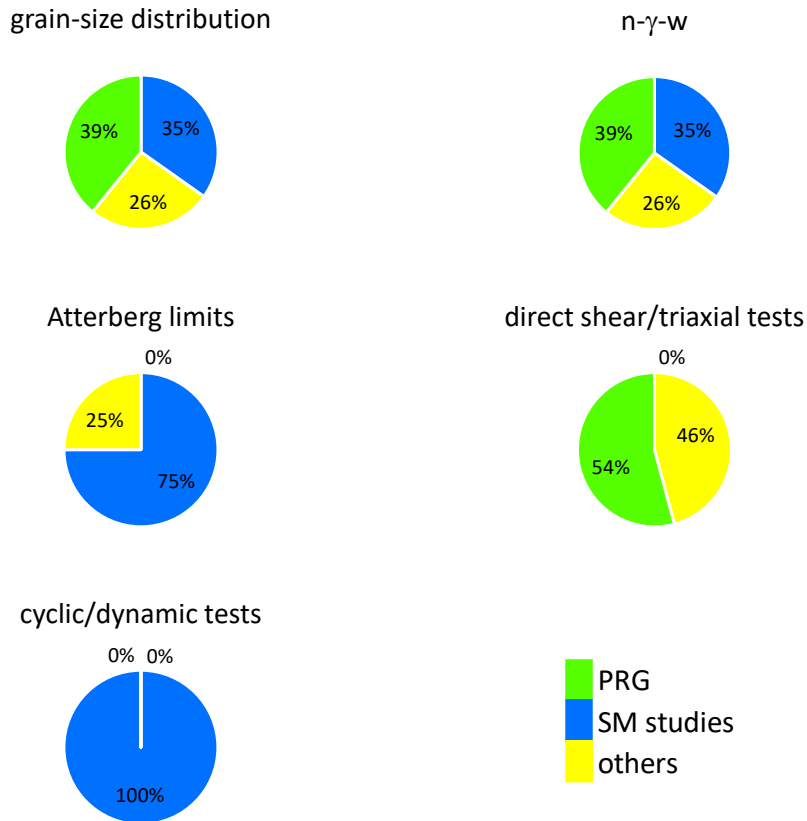


Figure 5-4: Distribution of the available laboratory tests.

The need for new investigations is essentially attributable to the following factors:

- lack of sufficiently deep soundings capable of intercepting the seismic bedrock;
- need for well-defined subsurface velocity profiles;
- the need to precisely define the non-linear behaviour of certain materials that have not yet been characterised, as well as the resistance under cyclic actions.

The new geotechnical investigation program (UniNA-MASLIDE) was specifically designed to fill these gaps. The field investigation program described in this study was

performed between 2021 and 2022 in the areas highlighted in Figure 5-5 with the blue and red boxes for liquefaction and slope stability respectively. The area chosen for liquefaction testing, in the coastal area of the municipality of Casamicciola Terme, was selected downstream of the Level I zoning shown in Figure 7-17 (§7.2.1): it falls within the ‘attention area’ identified by the SM studies. On the other hand, the area identified for slope stability analyses, which falls within the ‘Fango’ area in the Lacco Ameno municipality, contains two landslides mapped by the CARG project (Sbrana & Toccaceli, 2011).

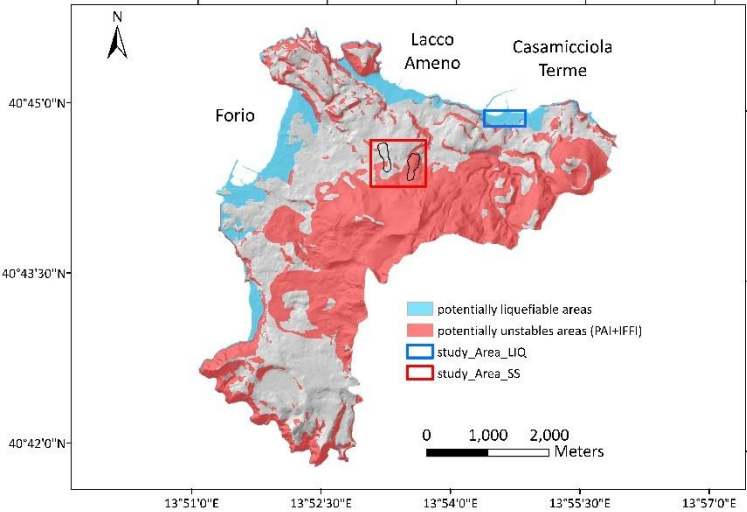


Figure 5-5: Potentially liquefiable areas (in light blue) and potentially unstable areas for landslide phenomena (in light red) in the N-W sector of the island of Ischia. The blue and red boxes indicate the representative areas for the two phenomena, respectively.

The details of the new investigations are given in the following sub-sections.

5.1 Casamicciola Terme study area

The area under study falls within the coastal area of the municipality of Casamicciola Terme (Figure 5-6).



Figure 5-6: Study area for liquefaction susceptibility analysis.

The area falls within the micro-zone 2003 identified by the MS studies (Figure 5-7). The latter, representative of the area of the Ancient Baths, consists of sandy deposits, 20 to 50 m thick (SMca), covered by medium fine sands (SMpi) with thicknesses of 5 to 15 m and fill with a thickness of 5 m, resting on geological substrates consisting of clayey deposits clayey-silty deposits up to 15-20m thick (SFCO), massive silty epiclastic deposits with 20 to 30m thick and finally on tuffaceous deposits (SFGRS). For lithostratigraphic and morphological characteristics (alluvial conoids and escarpment hemlines), local seismic amplification phenomena are possible.

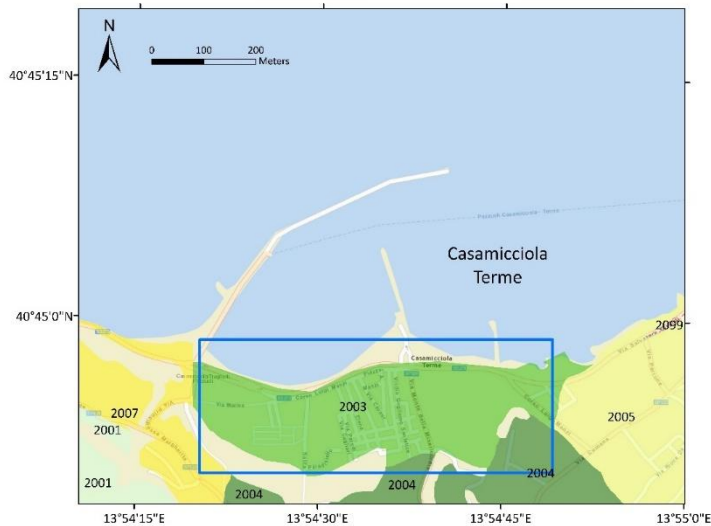


Figure 5-7: Homogeneous micro-zones in seismic perspective (MOPS) classification (SM studies) in Casamicciola Terme study area.

The following is a list of the surveys carried out in the municipality of Casamicciola Terme as part of the MASLIDE project:

- No. 2 Boreholes (BH) with continuous coring at a depth of 50 m equipped for the execution of 2 Down-Hole (DH) tests;
- No. 13 Standard Penetration (SPT) tests;
- No. 2 Cone Penetration (CPT) tests;
- No. 16 Microtremor Horizontal to Vertical Spectral Ratio (HVSr) recordings;
- No. 3 Electrical Resistivity Tomographies (ERT);

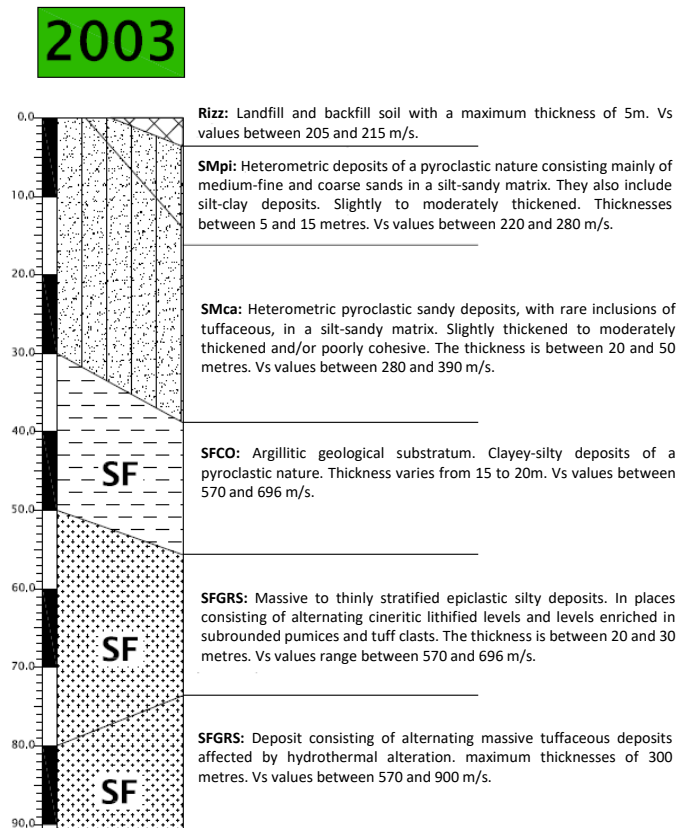


Figure 5-8: Stratigraphic column with lithostratigraphic description (MOPS 2003).

- No. 10 undisturbed and No. 3 reconstituted samples were taken on which were performed:
 - No. 6 grain size distribution analyses with n- γ -w evaluation;
 - No. 3 Atterberg's limits evaluation;
 - No. 12 Cyclic Simple Shear (CSS) tests;
 - No. 4 Dynamic laboratory tests (Resonant Column and Cyclic Torsional Shear tests);
 - No. 2 Simple Shear tests;
 - No. 1 Oedometric test;
 - No. 2 Permeability tests.

In addition, further surveys carried out for the “Reconstruction plan for the island of Ischia”, to be carried out for the areas of attention identified for liquefaction phenomena in the territories municipalities of Forio, Lacco Ameno and Casamicciola Terme, damaged by the earthquake of 21 August 2017 by Campania Region in the same area:

- No. 2 Boreholes (BH) with continuous coring at a depth of 20 m equipped with standpipe (PZ);
- No. 10 Standard Penetration (SPT) tests;
- No. 6 Dynamic Penetrometer Super Heavy (DPSH) tests;
- No. 4 undisturbed samples were taken on which they were performed:
 - No. 4 grain-size distribution analyses with n- γ -w evaluation.

An important part of this work has been completely dedicated to the characterisation of volcanic materials in the coastal area of the municipality of Casamicciola Terme. With the main aim to evaluate the cyclic behaviour and consequently, the cyclic resistance curves of the materials, undrained simple shear tests have been performed. For the definition of a geotechnical model, also grain size analyses and Atterberg's limit tests were carried out on soil samples retrieved from boreholes sampling. In addition permeability, oedometric and cyclic torsional shear tests have been performed.

5.1.1 Boreholes, SPT, CPT

Figure 5-9 shows the location of the boreholes carried out within the MASLIDE project. The first BH1, was carried out at Pio Monte della Misericordia and the second BH2 was carried out at Piazza delle Scuole. The same figure shows the surveys carried out in the same area by the Campania Region as part of the ‘reconstruction plan’ in

Piazza Marina (BH3) and Piazza Municipio (BH5) and a survey carried out as part of the master plan (BH6) in Salita Paradisiello.

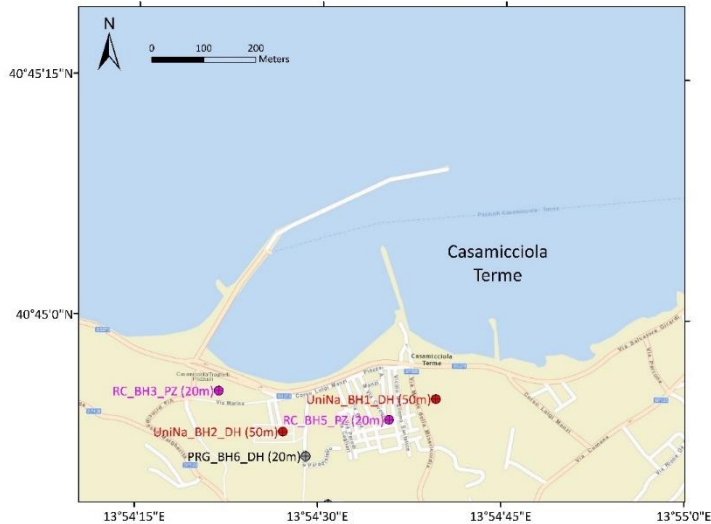
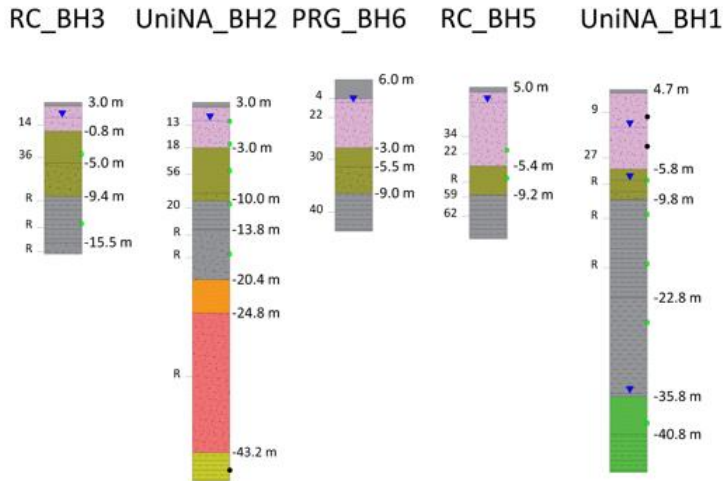


Figure 5-9: Boreholes location and depth reached in brackets UniNa (2022), Campania Region (2022), Master Plan (1990) in the Casamicciola Terme study area.

A summary of the investigations carried out is given below in both tabular (Table 5-3) and graphic form: the stratigraphic columns are described in terms of formations from both a geological (Figure 5-10) and geo-lithological (Figure 5-11) point of view (codes are from *Commissione Tecnica per la Microzonazione Sismica*, 2020).

Table 5-3: Overview of surveys in Casamicciola Terme study area.

ID	depth from ground level	SPT	samples collected
UniNA_BH1_DH	50m	SPT1 (3.00-3.45m): 2;5;4 SPT2 (9.00-9.45 m): 12;14;13 SPT3 (12.50-12.83 m): 33;27;R SPT4 (17.00-17.30 m): 15;28;R SPT5 (23.50-23.70 m): 43;R	R.S.1 (3.60-3.90m) R.S.2 (7.50-7.90 m) U.S.1 (12.00-12.50 m) U.S.2 (16.50-17.00 m) U.S.3 (23.00-23.50 m) U.S.4 (30.70-31.20 m) U.S.5 (44.00-44.50 m)
UniNA_BH2_DH	50m	SPT1 (3.00-3.45m): 2;6;7 SPT2 (6.00-6.45 m): 5;7;11 SPT3 (9.50-9.95 m): 18;22;34 SPT4 (13.9-14.35m): 11;10;10 SPT5 (17.50-17.95 m): 19; 33;R SPT6 (20.50-20.95 m): 17;31;R SPT7 (36.20-36.50 m): 33;R	U.S.1 (2.50-3.00 m) U.S.2 (5.50-6.00 m) U.S.3 (9.00-9.50 m) U.S.4 (13.40-13.90 m) U.S.5 (20.00-20.50m) R.S.1 (48.50-49.00 m)
RC_BH3_PZ	20m	SPT1 (3.00-3.45 m): 10; 6; 8 SPT2 (8.80-9.25 m): 18; 19; 17 SPT3 (13.00-13.30 m): 38; 39; R SPT4 (16.50-16.70 m): 39; R SPT5 (19.70-20.00 m): 29; R	U.S.1 (6.80-7.30 m) U.S.2 (16.00-16.50 m)
RC_BH5_PZ	20m	SPT1 (6.50-6.95 m): 15; 17;17 SPT2 (8.80-9.25 m): 8;11;11 SPT3 (12.50-12.80 m): 25; R SPT 4 (14.55-15.00 m): 26;28;31 SPT 5 (17.00-17.45 m): 27; 30; 32	U.S.1 (8.30-8.80 m) U.S.2 (12.00-12.50 m)
PRG_BH6_DH	20m	SPT1 (2.50-2.95 m): 4;3;1 SPT2 (5.50-5.95 m): 6;8;14 SPT3 (10.50-10.95 m): 8;14;16 SPT4 (17.50-17.95 m): 14;18;22	-



*elevations refer to sea level

▼ water table depth

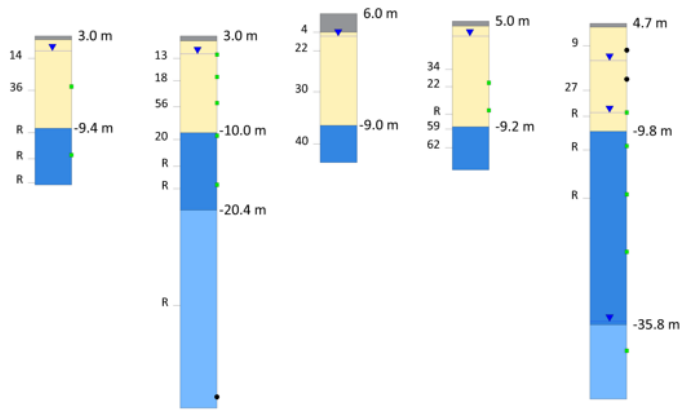
• U.S. (undisturbed sample)

• R.S. (remodulated sample)

- backfill material: pyroclastic deposit with gravels and pebbles (Rtzz)
- in situ volcanic deposits consisting of red-brown lava slag (cm), sands and cinerites (SMpi)
- yellowish gray and reddish sandy volcanic deposits with clay matrix (SMpi/SMca)
- chaotic sandy deposit with volcanic pebbles and clasts (tuffs and scoriae) and subrounded pumices (cm) in medium coarse sandy matrix varying in color from grayish green to reddish (SMpi/SMca)
- sandy clays of marine origin with eruptive episodes deposited in water (SFCO)
- as above with a prevalent clay fraction (SFCO)
- scoriae in abundant clay matrix (SFCO)
- volcanic sands reworked in water (SFGRS)
- sandy pyroclastic deposits in a clayey matrix with fossils (marine environment) (SFGRS)
- cineritic sandy level havana-reddish color (SFGRS)
- volcanic breccia with abundant black slags in sandy clay matrix (SFGRS)
- alternating yellowish-brown clays with low plasticity and sandy pyroclastic deposits (SFGRS)

Figure 5-10: Stratigraphic columns with geological description.

RC_BH3 UniNA_BH2 PRG_BH6 RC_BH5 UniNA_BH1



*elevations refer to sea level

- ▼ water table depth
- U.S. (undisturbed sample)
- R.S. (remoduled sample)
- Rizz (terreni contenenti resti di attività antropica): Anthropogenic deposits
- SMpi/SMca (sabbie limose di piana alluvionale e costiera/depositi sabbiosi eterometrici in matrice limo-sabbiosa): Alluvial and coastal plain silty sand/Heterometric sandy deposits in silt-sandy matrix
- SFCO (substrato coesivo sovraconsolidato, fratturato/alterato): Cohesive, overconsolidated fractured/weathered bedrock (marine siltstone and claystone)
- SFGRS (substrato granulare, cementato/saldato, stratificato fratturato/alterato): Granular, layered, cemented or welded, fractured/altered bedrock (ignimbrites, welded tuffs, epiclastic sandstone)

Figure 5-11: Stratigraphic columns with geo-lithological description (codes are from SM studies).

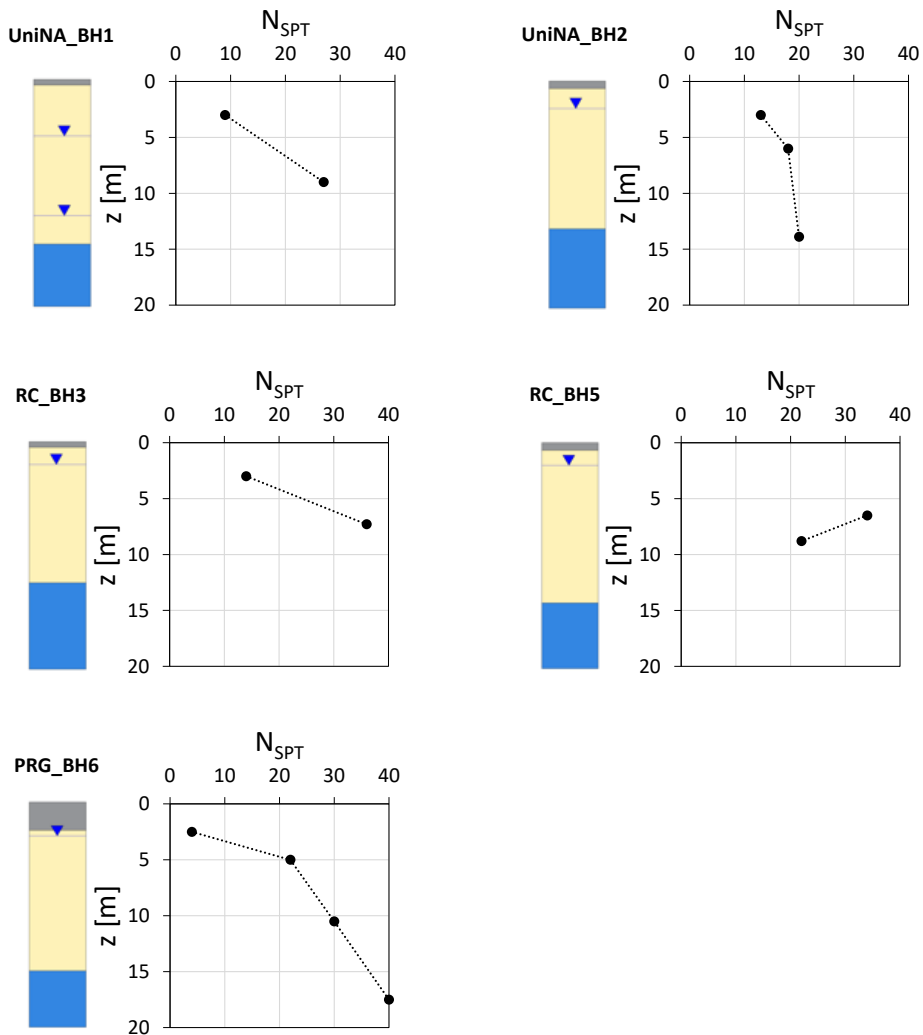


Figure 5-12: SPT test results in Casamicciola Terme study area.

The CPT tests were performed close to boreholes BH1 and BH2, and reached depths of about 10 m and 6 m respectively. The location of the two CPTs, denoted CPT1 and CPT2, within the municipality of Casamicciola and their results are reported in Figure 5-13.

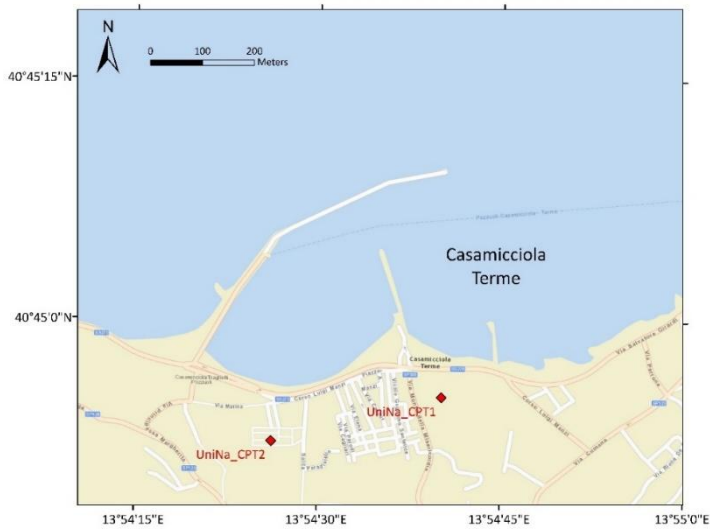


Figure 5-13: Location of CPT tests performed within the UniNA-MASLIDE project.

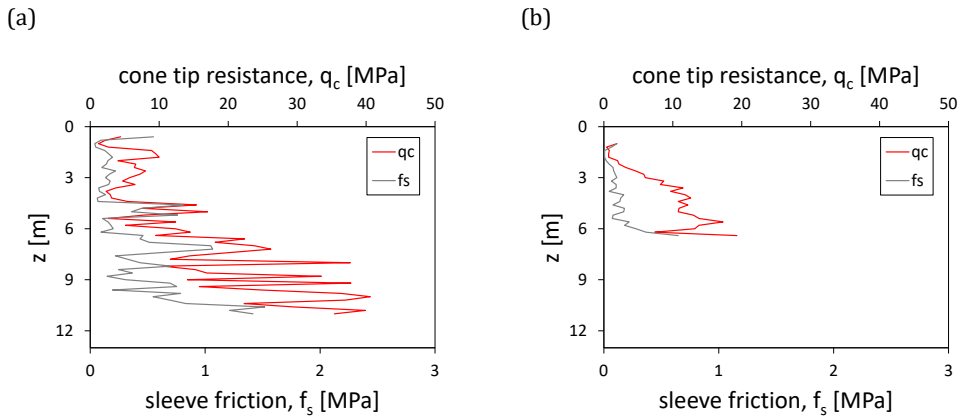


Figure 5-14: CPT test results for CPT1 (a) and CPT2 (b).

The static penetration tests (CPT) were carried out with a self-moving equipment characterised by a maximum thrust capability of 20 ton (0.2 MN) provided by hydraulic jack. The measurements of the 60°-10 cm² cone tip and 150 cm² sleeve resistances were recorded each 20 cm.

The conical tip at both points reached depths of no more than 10 and 6 meters. As a result, the values of q_c and f_s are based on a single material, specifically the material indicated with SMpi. In addition to the measured point values of q_c and f_s , this report also includes the average trends of these values per meter.

5.1.2 Down-hole tests

Boreholes BH1_DH and BH2-DH were equipped with PVC tubes and a zero-shrinkage mortar casting in the borehole-pipe cavity to perform down-hole tests necessary for the definition of the shear wave velocity profile up to a depth of 50 m. The figures below show the S-wave and P-wave velocity profiles for BH1 (Figure 5-15 and Figure 5-16) and BH2 (Figure 5-17 and Figure 5-18).

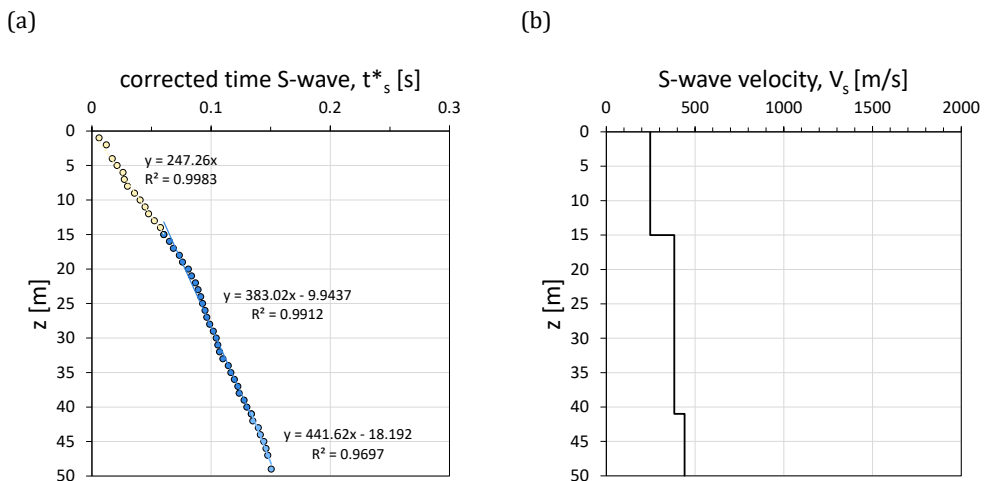
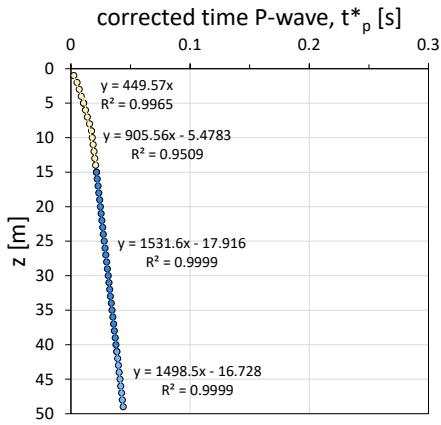


Figure 5-15: Dromochrone (a) and S-wave velocity profile (b) measured in BH1.

(a)



(b)

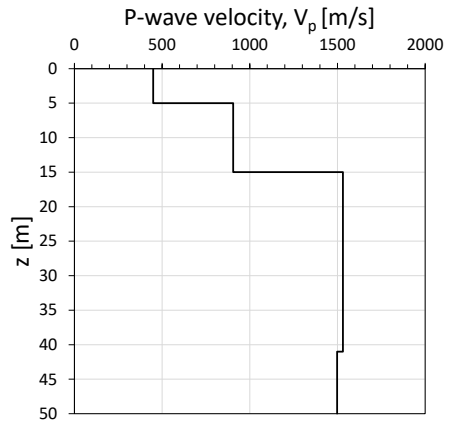
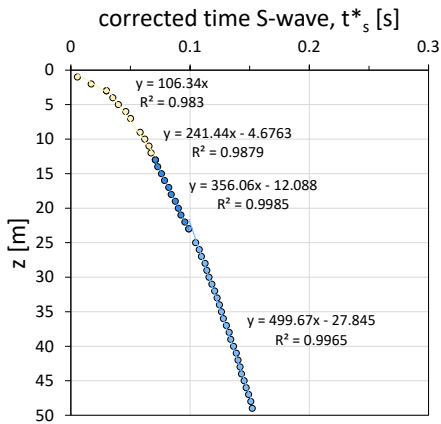


Figure 5-16: Dromochrone (a) and P-wave velocity profile (b) measured in BH1.

(a)



(b)

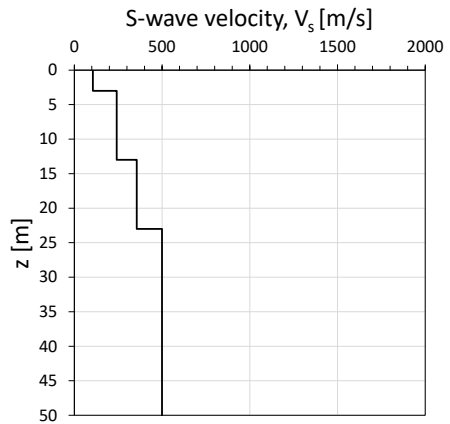


Figure 5-17: Dromochrone (a) and S-wave velocity profile (b) measured in BH2.

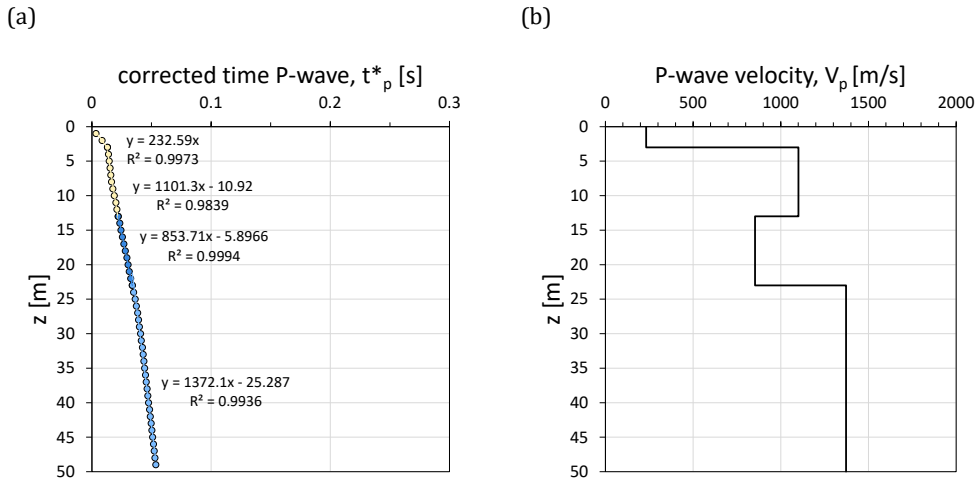


Figure 5-18: Dromochrone (a) and P-wave velocity profile (b) measured in BH2.

The first two layers SMpi and SMca exhibit S-wave velocity values less than 250 m/s; the SFCO layer shows values between 356 and 383 m/s, while the last layer, denoted SFGRS, shows velocity values of 442 and 500 m/s. The value of the equivalent shear wave velocity $V_{s,eq}$, as defined by national code (NTC 2018) is 301 m/s and 267 m/s for BH1 and BH2, respectively. Therefore the area under consideration can be classified as 'ground type C' according to NTC2018.

The values of shear wave velocities obtained from the down-hole are consistent with the velocity ranges defined in the MOPS columns (Figure 5-19).

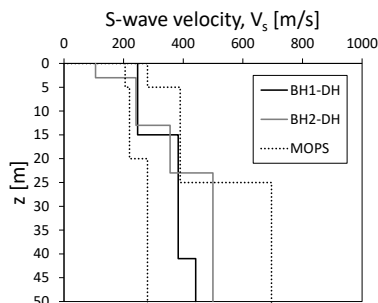


Figure 5-19: Comparison of shear wave velocity profiles in BH1 (black), BH2 (dark grey) and velocity ranges defined by the MS studies for MOPS 2003.

5.1.3 Electrical Resistivity Tomography

Results from Electrical Resistivity Tomography (ERT) are useful to identify general trends of the thicknesses and any heterogeneity of the soils under examination. The location of the ERTs carried out in Casamicciola Terme is shown in Figure 5-20.

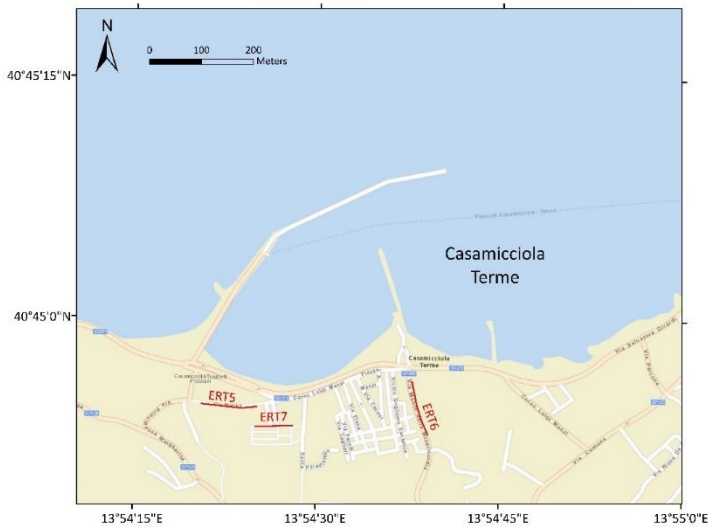


Figure 5-20: Location of ERT performed within the UniNA-MASLIDE project.

In order to provide more detailed subsurface resistivity models, it was decided to adopt both the Wenner-Schlumberger configuration (so as to be able to highlight any variations in resistivity horizontally and vertically) and the Dipole-Dipole configuration (thus obtaining a greater depth of investigation and greater horizontal resolution) for each individual standoff. The length of the arrays, for logistical issues, is limited.

ERT5 and ERT6, approximately 93.00 m long, were constructed respectively along Corso Luigi Manzi near Piazza Marina and along Via Monte della Misericordia, with an electrode spacing of 3.00 m. The resistivity models for both configurations are reported in Figure 5-21 and Figure 5-22.

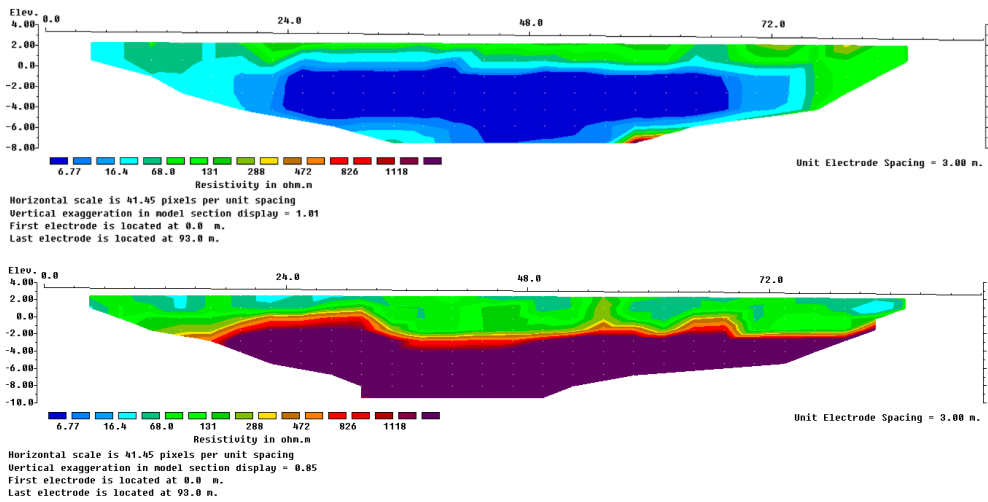


Figure 5-21: ERT5 results in both Wenner-Schlumberger (above) and Dipole-Dipole (below) configuration.

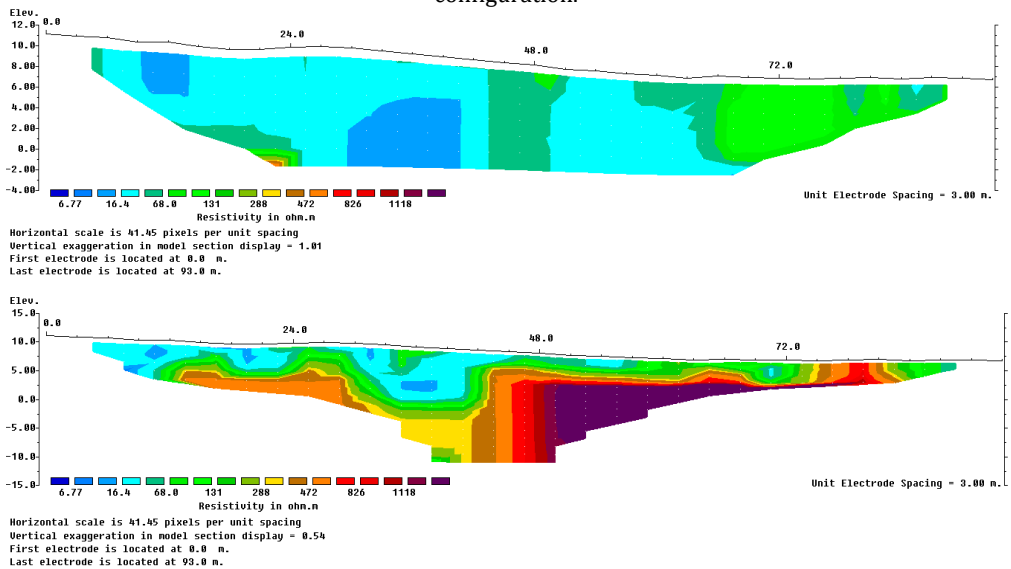


Figure 5-22: ERT6 results in both Wenner-Schlumberger (above) and Dipole-Dipole (below) configuration.

ERT7, approximately 62.00 m long, was constructed along Piazza delle Scuole, with an electrode spacing of 2.00 m. The resistivity model of both configurations is reported in Figure 5-23.

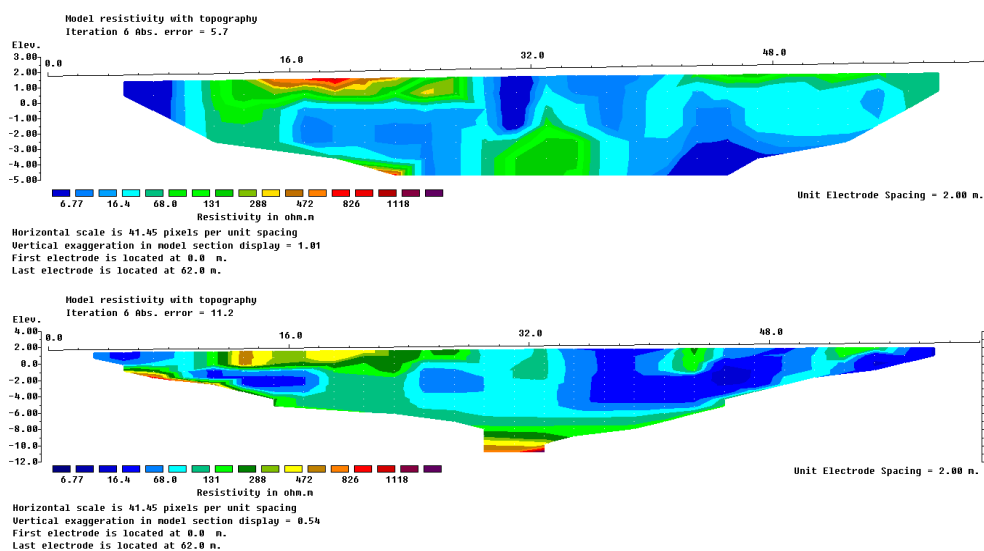


Figure 5-23: ERT7 results in both Wenner-Schlumberger (above) and Dipole-Dipole (below) configurations.

The resistivities found in the volumes investigated are in agreement with the lithologies present and identified in the surveys carried out in the area under investigation. The soils found present a good homogeneity, both laterally and vertically. The most superficial deposits present resistivity correlated with the presence of reworked and backfilled materials. In the central sector of the pseudo-sections of resistivity in the Wenner-Schlumberger configuration deposits can be detected, characterised by low values in the resistivities measured, probably due to the presence of deposits with a high degree of saturation. Finally, in the resistivity sections in the Dipole-Dipole configuration, a clear increase in resistivity values is observed starting from about a few meters from ground level, which can be correlated with the presence of coarse-grained deposits (pumice and scoriae).

5.1.4 Microtremor Horizontal to Vertical Spectral Ratio analysis

16 ambient noise measurements, called C01-C16, were carried out in the same area (Figure 5-24).

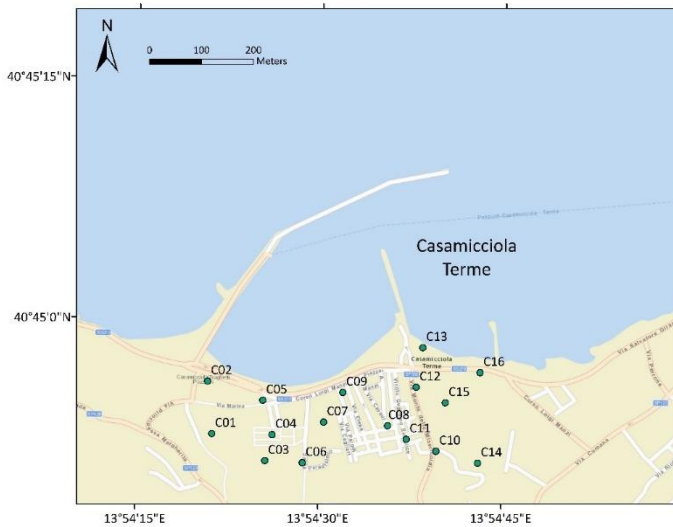


Figure 5-24: Location of HVSR performed within the UniNA-MASLIDE project.

The data processing was carried out as per the recommendations of the SESAME (Site Effects Assessment Using Ambient Excitations) consortium found in Acerra et al. (2004). Using the *GEOPSY* software, the ambient noise data were processed both in terms of resonance frequency and azimuth. An example of the results of the ambient noise data processing is shown in Figure 5-25.

To determine the local ground resonance frequency, the ratio between the mean Fourier spectrum of the 2 horizontal components and that of the vertical component was computed. Acquisition windows were automatically selected.

A window length of 50 seconds was chosen and for each window selected, the Fast Fourier transform (FFT) was applied and a Konno-Ohmachi smoothing algorithm was applied on the Fourier spectra. Then, the ratio between the mean of

the horizontal and vertical spectra (H/V ratio) was calculated. The final H/V ratio curve was computed as the average of all the windows H/V ratios. The ambient noise data were analyzed for frequencies between 0.1 and 20 Hz.

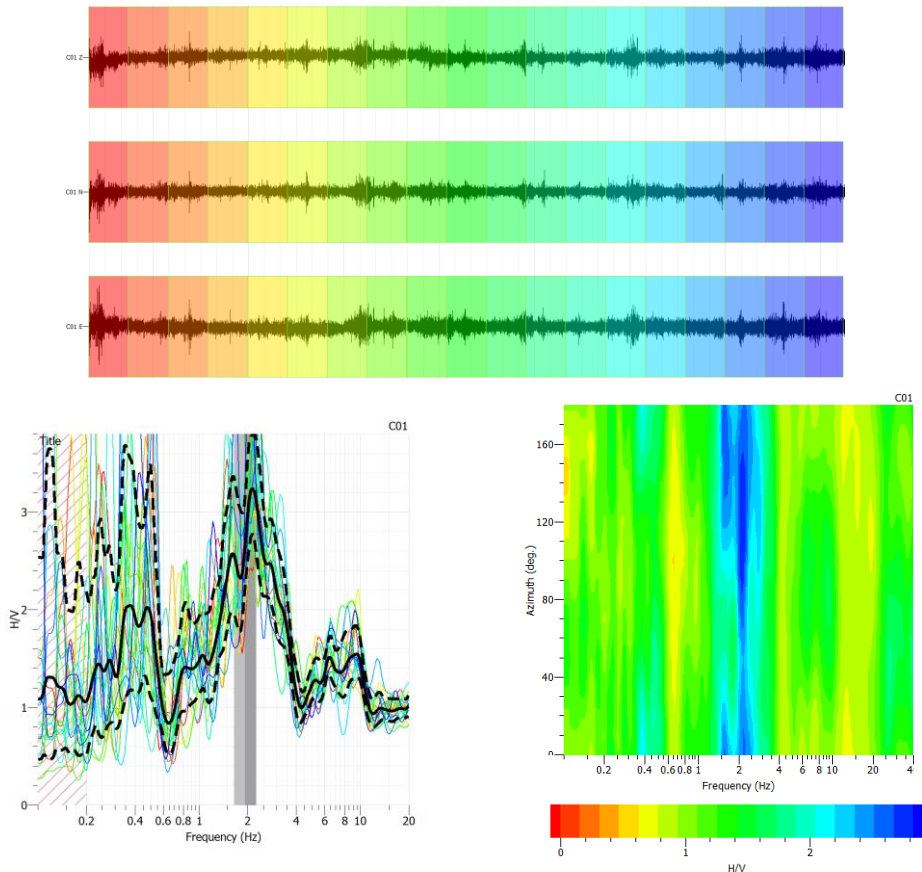


Figure 5-25: Vertical (Z), north-south (N) and east-west (E) components of an example of signal recorded (above). Each color corresponds to a selected window which is represented in the HVSR graph (bottom left) by an individual colored line curve. The final HVSR curve which is the average of all the colored curves is the solid black line. The dotted black lines indicate the amplitude standard deviation. The picture (bottom right) is the azimuth graph.

Details of each individual registration are given in Appendix A.1.

In Figure 5-26 the measurement points are plotted with the same colours according to their similarities in terms of amplification functions and fundamental frequency. Two zones with different dynamic response can be clearly distinguished, with the western zone being characterized by higher value of fundamental frequency that can be associated to the presence of a lower depth of the seismic bedrock. The values of the fundamental frequency and H/V functions are shown in Figure 5-27.

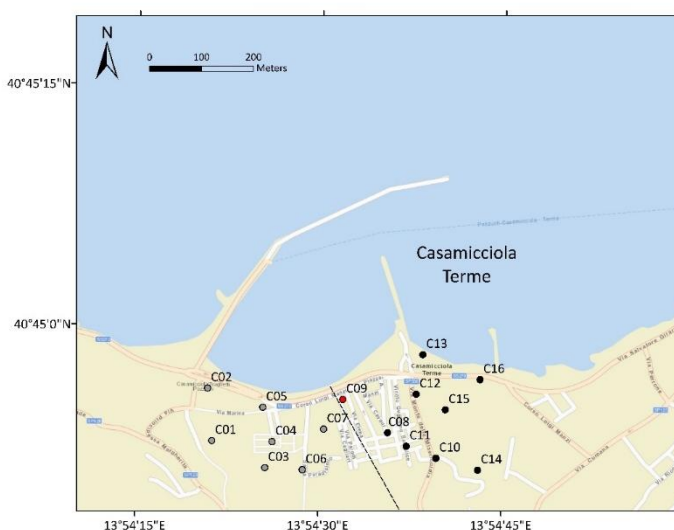


Figure 5-26: Location of the HVSR measurement points: the points in black and grey show a fundamental frequency around 0.5 Hz and 2 Hz respectively. The dashed black line roughly indicates the transition between the two zones: point C09 in red shows an intermediate amplification function between the two zones.

id	f_0 [Hz]
C01	1.93
C02	2.30
C03	2.29
C04	2.19
C05	2.11
C06	2.26
C07	2.01
C08	0.47
C09	0.46
C10	0.46
C11	0.48
C12	0.48
C13	0.35
C14	0.49
C15	0.48
C16	0.53

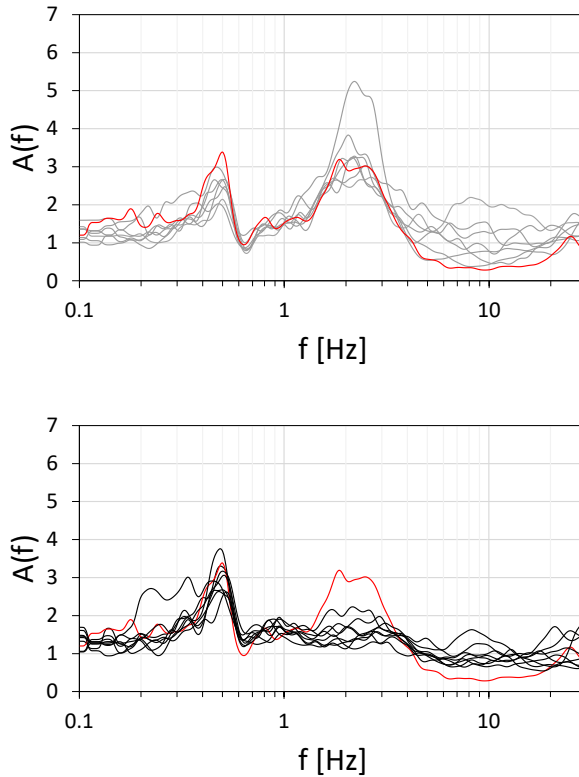


Figure 5-27: Fundamental frequencies and amplification functions measured in the western and eastern zone of the test area. The amplification function relevant to site C09, which falls in a transition zone, is plotted in red.

It can be seen that the measurements taken along the transition zone (C09) show intermediate characteristics, with a first peak around 0.5 Hz and a second at 2 Hz. The point in question was nevertheless assigned to the west zone following the SESAME criteria.

5.1.5 Physical properties

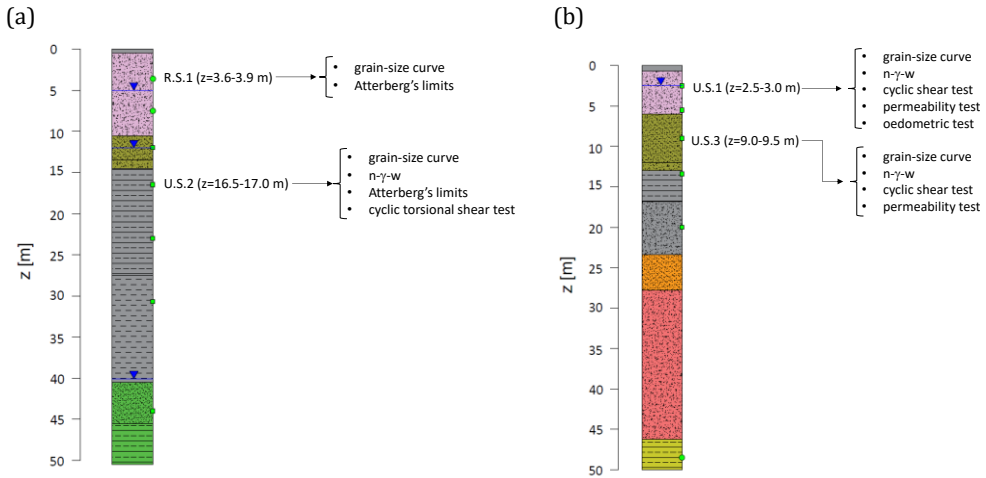


Figure 5-28: Details of the laboratory tests carried out on the samples taken in the UniNA_BH1 (a) and UniNA_BH2 (b) survey.

The grain size distribution curves and values from boreholes BH1 and BH2 are reported in Figure 5-29 and Table 5-4, while the main physical properties are shown in Table 5-5.

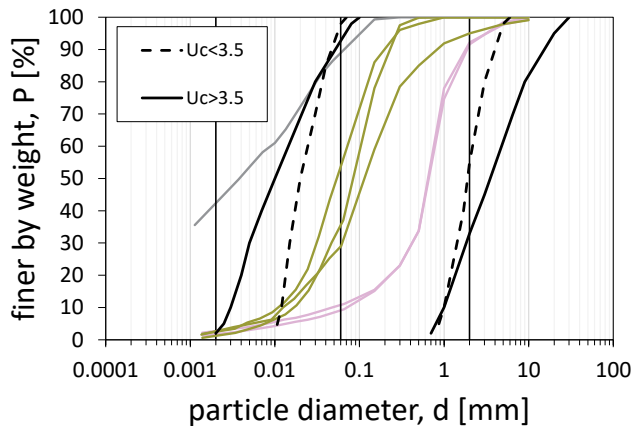


Figure 5-29: Grain-size distributions of the materials shown in Figure 5-28. The black dashed and non-dashed lines indicate the grain size ranges of the potentially liquefiable soils for $U_c < 3.5$ and $U_c > 3.5$, respectively.

Table 5-4: Average grain-size distribution values.

	material	gravel	sand	silt	clay
	[-]	[%]	[%]	[%]	[%]
	SMpi	8	82	8	2
	SMca	1	60	37	2
	SFCO	0	12	47	41

Table 5-5: Average material properties.

	material	G_s	d₅₀	UC	FC
	[-]	[g/cm ³]	[mm]	[-]	[%]
	SMpi	2.6	0.691	13.3	11
	SMca	2.4	0.090	8.7	45
	SFCO	2.7	0.002	-	90

Atterberg limit tests (where possible) were carried out on the same materials. Table 5-6 shows the Atterberg's limits. The Plasticity Index (PI) has been evaluated for two samples and it is plotted versus Liquid Limit (w_L) in Figure 5-30. It can be noted that the shallow soil (SMpi) is characterised by low plasticity, with a value of PI equal to 12.0 while the deep finer soil (SFCO) is highly plastic, with a value of PI equal to 32.6. It must be pointed out that despite a fine content of 45%, the limits on SMca material could not be assessable: this is due to the fact that it is non-plastic fine. In addition, Figure 5-31 shows the activity chart.

Table 5-6: Atterberg limits.

	material	w_L	w_P	PI
	[-]	[%]	[%]	[%]
	SMpi	37.6	25.6	12.0
	SFCO	51.7	19.1	32.6

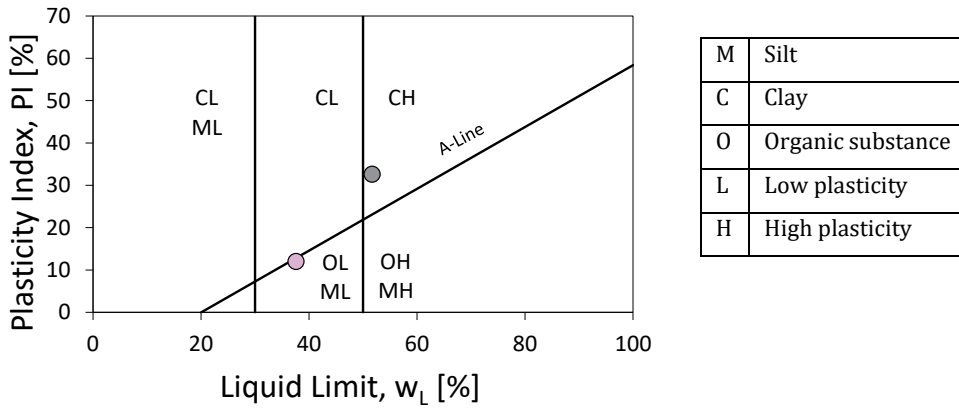


Figure 5-30: Casagrande plasticity chart of boreholes samples.

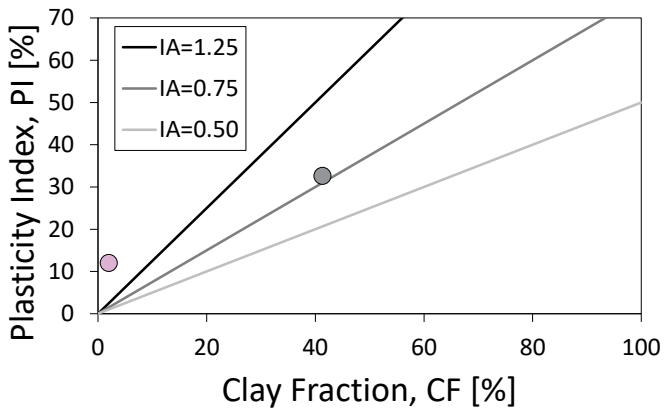


Figure 5-31: Activity chart of boreholes samples.

5.1.6 Permeability tests

Two permeability tests have been performed on SMpi and SMca sands, whose results are shown in Figure 5-32, where the values of permeability coefficient to water (k) versus time have been plotted. The k values of the performed tests have been summarized in Table 5-7.

Table 5-7: Results of permeability tests.

	sample	material	e	FC [%]	k [m/s]
	BH2-U.S.1 (2.50-3.00m)	SMpi	0.66	11	3.2E-06
	BH2-U.S.3 (9.00-9.50m)	SMca	0.89	45	1.5E-05

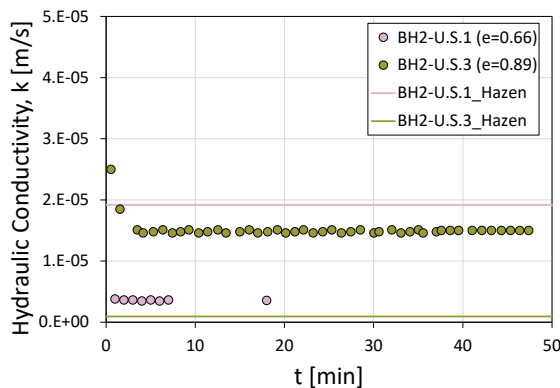


Figure 5-32: Results of permeability tests.

Despite the higher fine content that characterises the SMca sample, this latter shows a higher permeability value than SMpi material, which could be attributed to a higher void ratio that characterises the former sample SMca. The same figure shows the comparison with the permeability values calculated using Hazen's formula as a function of d_{10} . Clearly, by not taking into account the field conditions of the material, Hazen's formula yields a higher permeability for the layer with less fine content. In any case, the values obtained are comparable with those reported in the literature for sands in the Ischia area (see e.g. Piscopo et al. 2019).

5.1.7 Oedometric test

An oedometric compressibility test has been carried out on SMpi sand. The results are shown in Figure 5-33 and Figure 5-34.

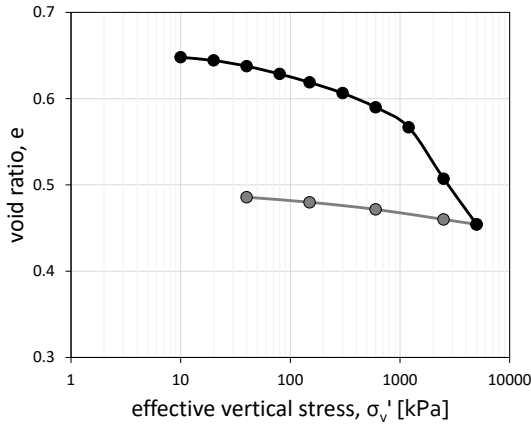


Figure 5-33: Result of oedometric test on SMpi specimen in σ'_v -e plane.

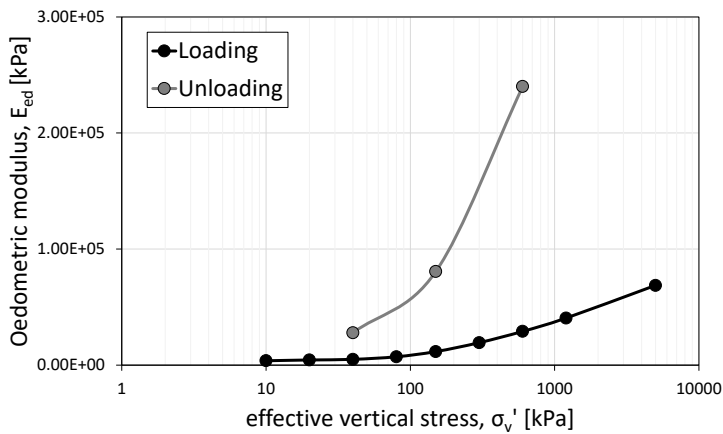


Figure 5-34: Result of oedometric test on SMpi specimen: oedometer modulus value in loading-unloading cycles.

From the interpolation of the loading and unloading-reloading lines, an analytical formulation could be derived (Eq. 5-1 and Eq. 5-2, respectively).

$$e = e_0 - C_c \log\left(\frac{\sigma'_v}{\sigma'_{v0}}\right) \tag{Eq. 5-1}$$

$$e = e_0 - C_s \log\left(\frac{\sigma'_v}{\sigma'_{v0}}\right) \tag{Eq. 5-2}$$

C_c and C_s represent the slope of the loading and unloading-reloading lines in $\log\sigma'_v$ - e plane. Values are given in Table 5-8.

Table 5-8: Values of C_c and C_s .

C_c	0.1816
C_s	0.0147

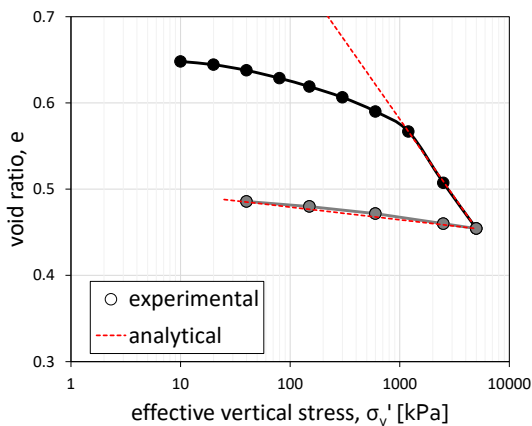


Figure 5-35: Experimental vs analytical oedometric compressibility curve.

5.1.8 Cyclic and monotonic resistance

The cyclic and monotonic resistance of the materials has been evaluated with a simple shear apparatus. As well known, a simple shear condition implies that the diameter of the specimen (or more in general, the transversal section) is maintained constant. Generally, it can be performed by means of concentric rings, while the apparatus of the University of Napoli Federico II is much more sophisticated because it is able to work according to two different configurations: the first one obtained acting on the confining pressure (flexible boundary), the second one is realized by means of confining rings (rigid boundary). In both cases, the simple shear state should be guaranteed. The apparatus consists of a dynamic servo-controller (DSC), able to control two electro-mechanical dynamic actuators for applying the vertical and horizontal loads to the specimen. The vertical and horizontal displacements are measured by Encoders which are part of the servo motors. Vertical and horizontal loads are measured by using two load cells with a maximum measure of 5kN. In the configuration with confining pressure a simple shear condition can be obtained by means of a sophisticated control system. In the consolidation phase (k_0 condition) the apparatus can adjust the vertical load to maintain a constant diameter, one measured the volume of water that is going out from the specimen and the vertical displacements. In this case, a latex membrane is used to confine the specimen, while the pressurized water allows to apply a given pressure by means of an air/water interface device, reported in Figure 5-36 together with the other basic components of that system. The Hydraulic Automatic Pressure Controller (HAPC) is connected to the base of the specimen and allows to impose a back-pressure and measure the volume of water that goes in or out from the specimen by means of a volume gauge. In other words, the cyclic simple shear apparatus can control the confining cell pressure, vertical load, horizontal load and back pressure independently.

To best reproduce the loading conditions in the field, imposed by a seismic event, undrained cyclic simple shear tests were performed with flexible boundary.



Figure 5-36: Basic system components of Cyclic Simple Shear (CSS) apparatus with confining pressure (Mele, 2020).

The specimens ($d=70$ mm and $h=26$ mm) were saturated by increasing both cell and back pressure to reach an effective stress of 10 kPa. The saturation of the specimens was checked by B-value through a B-test. For B higher than 0.95, the specimens were considered saturated. Thereafter, the specimens were consolidated. As mentioned above, in the configuration with a flexible boundary a k_0 consolidation can be applied, adjusting the vertical load to have a constant diameter, knowing the water volume goes out during consolidation and the vertical settlements. After the consolidation phase, different amplitude Cyclic Stress Ratios (CSR) were applied. Sinusoidal wave forms were used with a frequency of 0.05 Hz.

In cyclic simple shear tests the attainment of liquefaction was identified according to stress ($r_u=0.90$) and strain criteria ($\gamma_{DA} \geq 7.5\%$).

The main goal was the analysis of the undrained cyclic and monotonic behaviour of SMca and SMpi soils in order to define the cyclic resistance curve.

Table 5-9 shows the initial conditions of the specimens on which the monotonic tests were performed.

Table 5-9: State of specimens in monotonic tests.

	sample	material	e^*	σ'_v [kPa]	σ'_h [kPa]	k_0
	BH2-U.S.1 (2.50-3.00 m)	SMpi	0.536	51.7	19.7	0.381
	BH2-U.S.3 (9.00-9.50m)	SMca	0.951	109.3	42.1	0.385

*at the end of consolidation phase

In Figure 5-37 and Figure 5-38, the results of the undrained test are illustrated for SMpi and SMca.

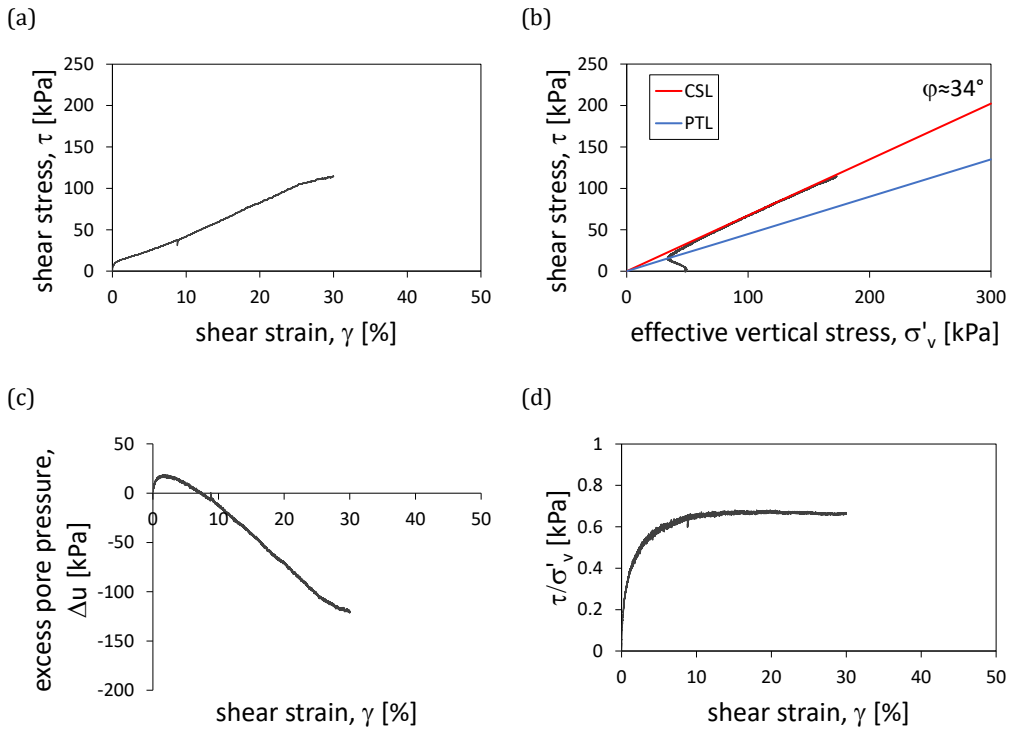


Figure 5-37: Results of monotonic test on SMpi (BH2-U.S.1) in the planes τ - γ (a), τ - σ'_v (b), Δu - γ (c) and τ/σ'_v - γ (d).

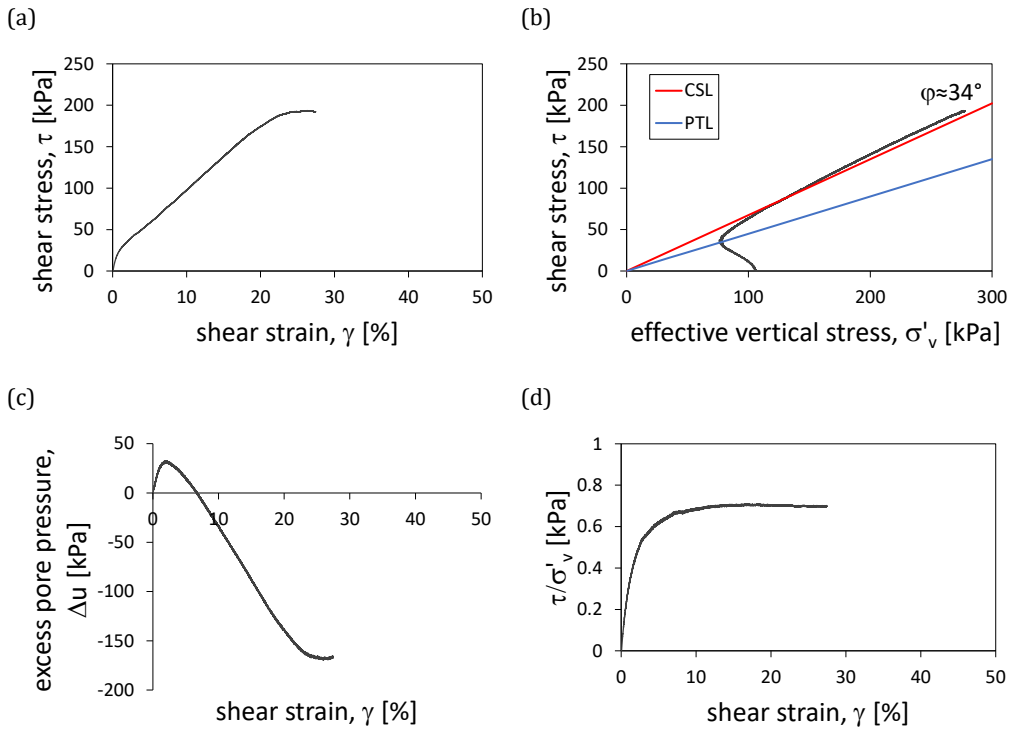
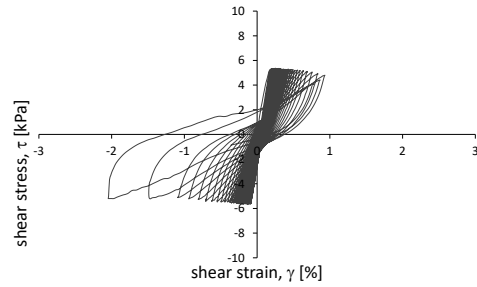
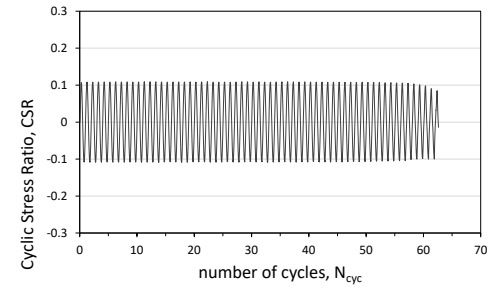


Figure 5-38: Results of monotonic test on SMca (BH2-U.S.3) in the planes τ - γ (a), τ - σ'_v (b), Δu - γ (c) and τ/σ'_v - γ (d).

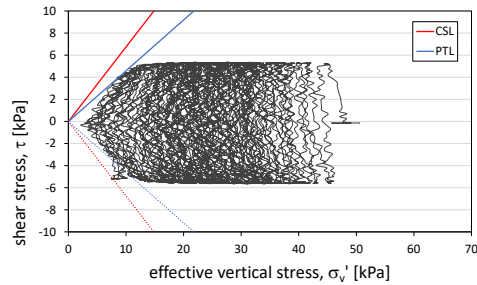
(a)



(b)



(c)



(d)

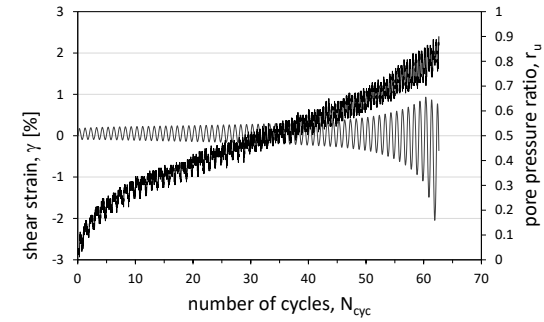
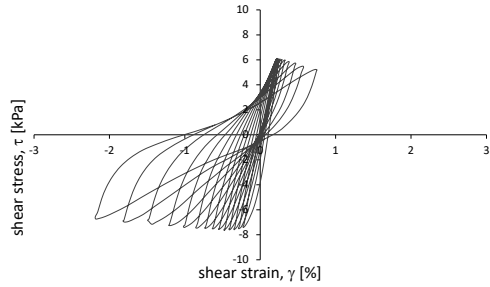
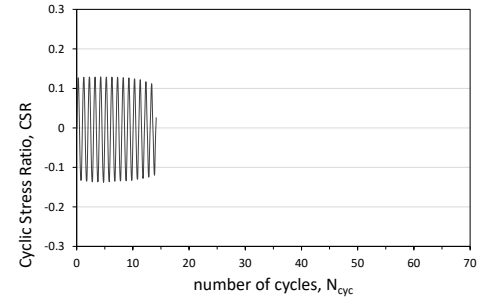


Figure 5-39: Results of cyclic simple shear test on SMpi (BH2-U.S.1) with CSR=0.11 in τ - γ (a), CSR- N_{cyc} (b), τ - σ'_v (c) and γ - r_u - N_{cyc} (d) planes.

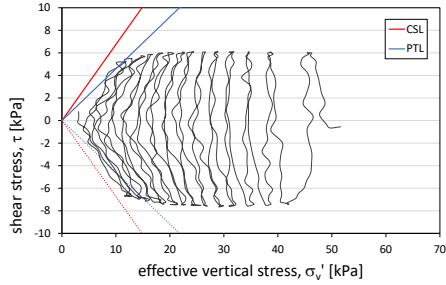
(a)



(b)



(c)



(d)

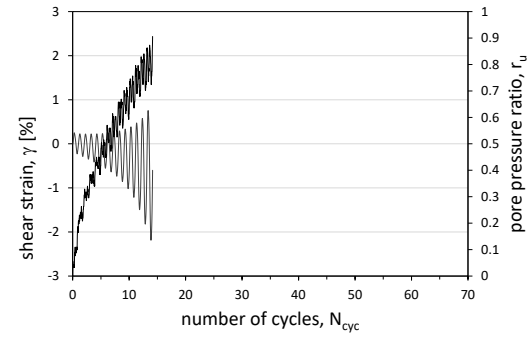
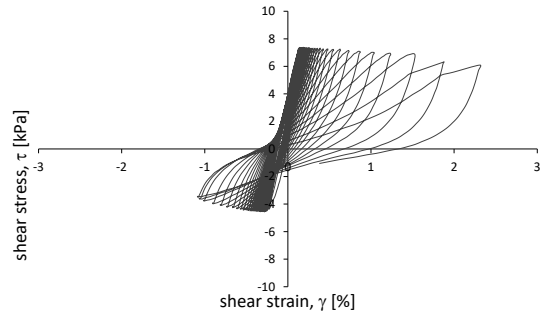
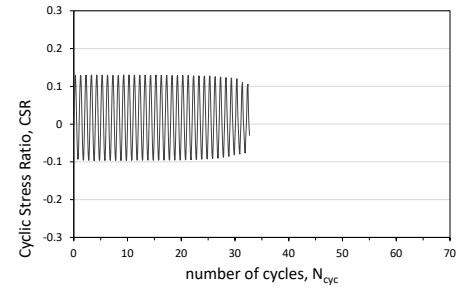


Figure 5-40: Results of cyclic simple shear test on SMpi (BH2-U.S.1) with CSR=0.13 in τ - γ (a), CSR- N_{cyc} (b), τ - σ_v' (c) and γ - r_u - N_{cyc} (d) planes.

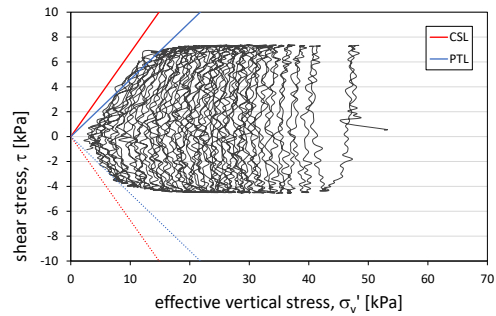
(a)



(b)



(c)



(d)

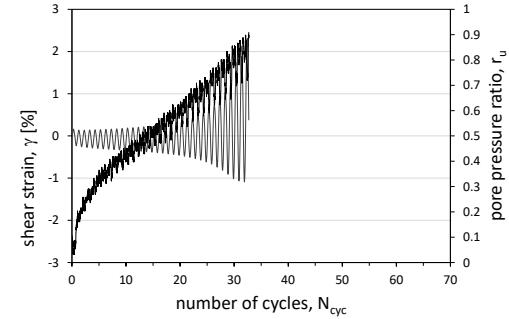
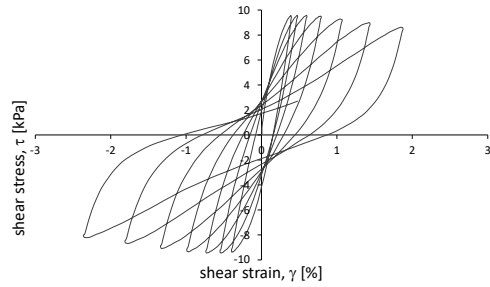
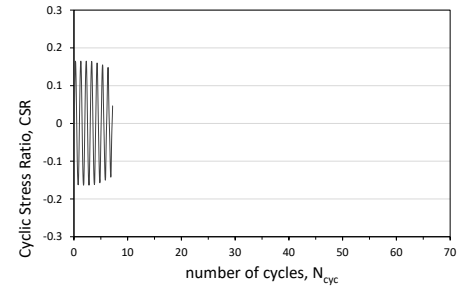


Figure 5-41: Results of cyclic simple shear test on SMpi (BH2-U.S.1) with CSR=0.13 in τ - γ (a), CSR- N_{cyc} (b), τ - σ'_v (c) and γ - r_u - N_{cyc} (d) planes.

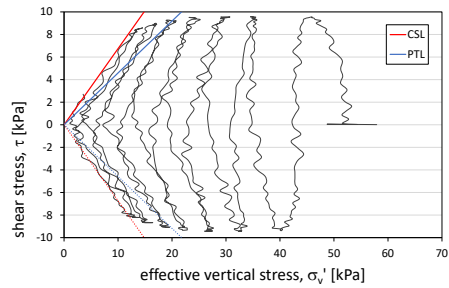
(a)



(b)



(c)



(d)

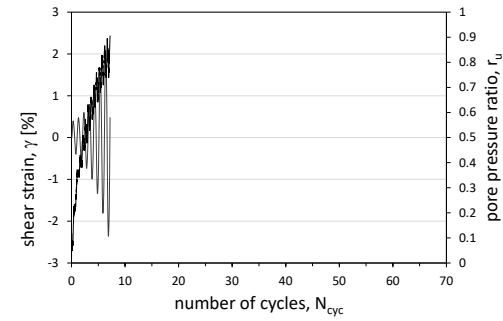
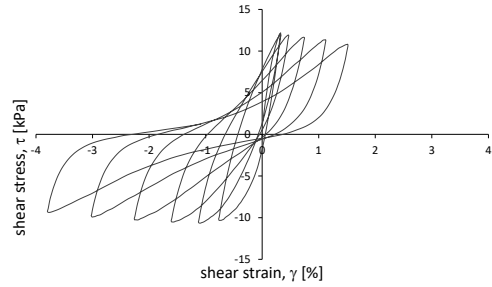
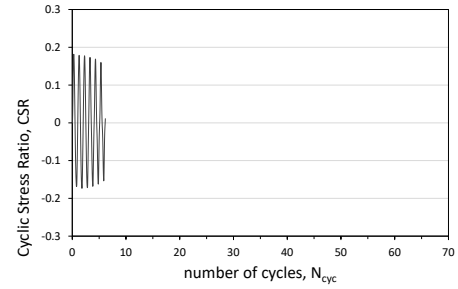


Figure 5-42: Results of cyclic simple shear test on SMpi (BH2-U.S.1) with CSR=0.16 in τ - γ (a), CSR- N_{cyc} (b), τ - σ'_v (c) and γ - r_u - N_{cyc} (d) planes.

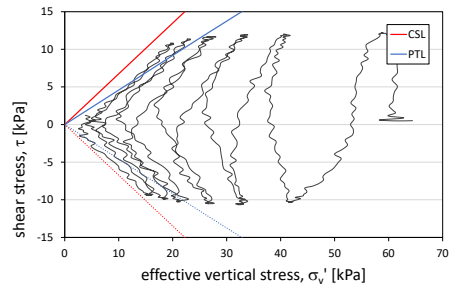
(a)



(b)



(c)



(d)

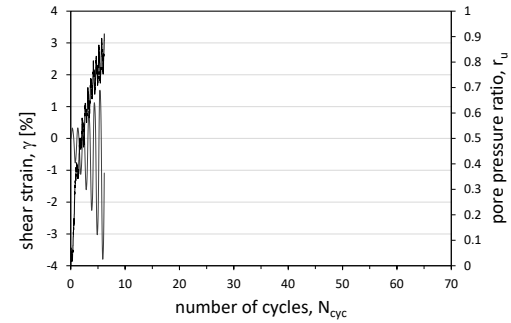
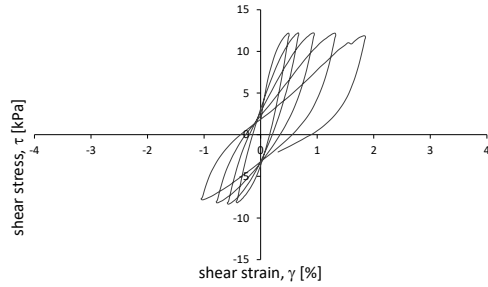
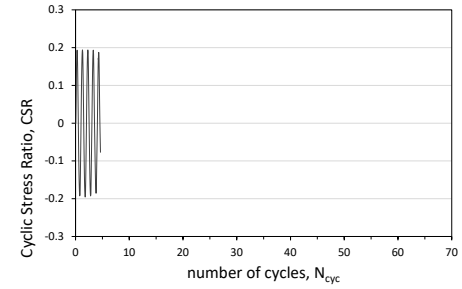


Figure 5-43: Results of cyclic simple shear test on SMpi (BH2-U.S.1) with CSR=0.18 in τ - γ (a), CSR- N_{cyc} (b), τ - σ'_v (c) and γ - r_u - N_{cyc} (d) planes.

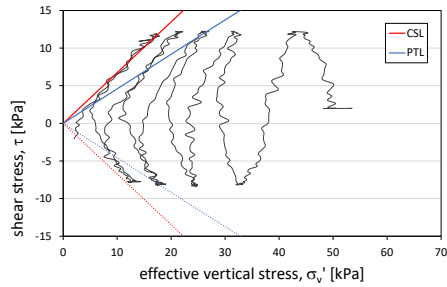
(a)



(b)



(c)



(d)

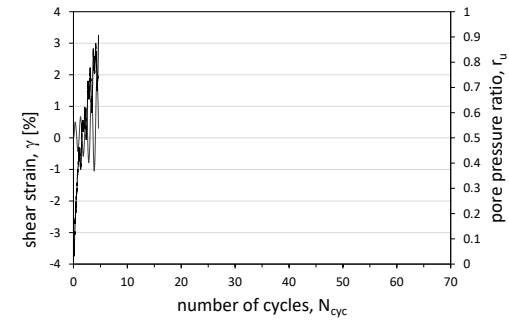
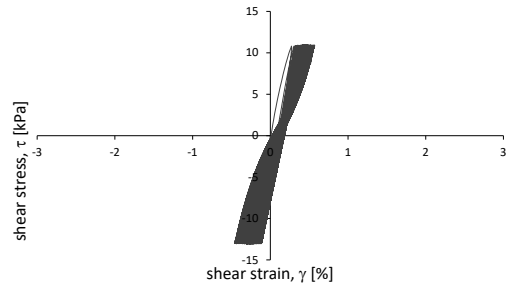
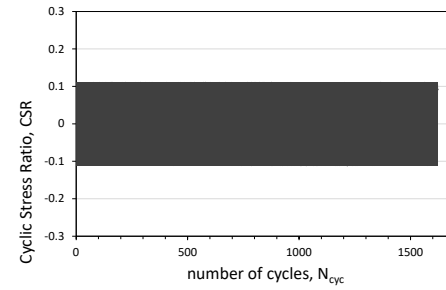


Figure 5-44: Results of cyclic simple shear test on SMpi (BH2-U.S.1) with CSR=0.19 in τ - γ (a), CSR- N_{cyc} (b), τ - σ'_v (c) and γ - r_u - N_{cyc} (d) planes.

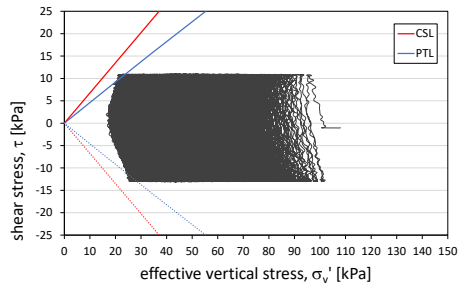
(a)



(b)



(c)



(d)

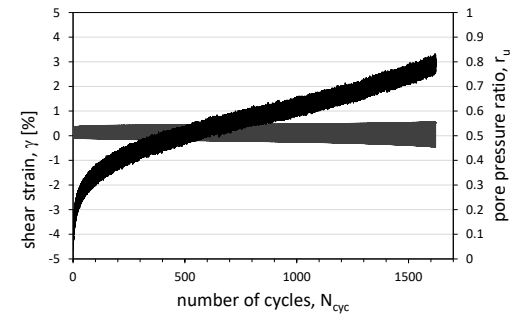
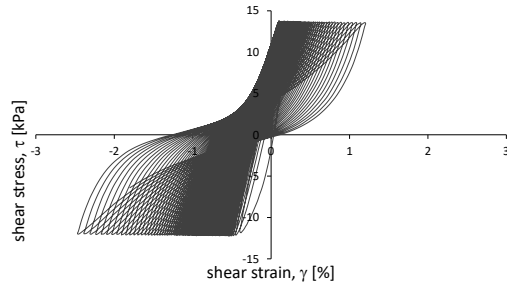
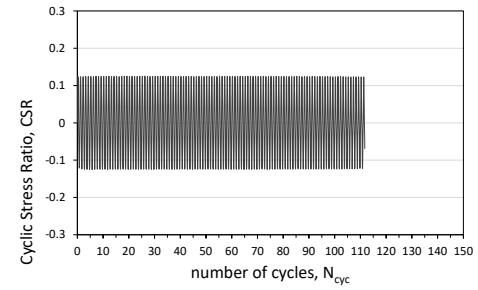


Figure 5-45: Results of cyclic simple shear test on SMca (BH2-U.S.3) with CSR=0.11 in τ - γ (a), CSR- N_{cyc} (b), τ - σ_v' (c) and γ - r_u - N_{cyc} (d) planes.

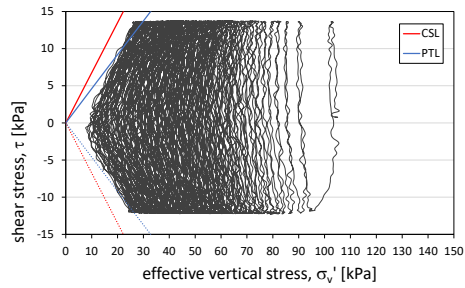
(a)



(b)



(c)



(d)

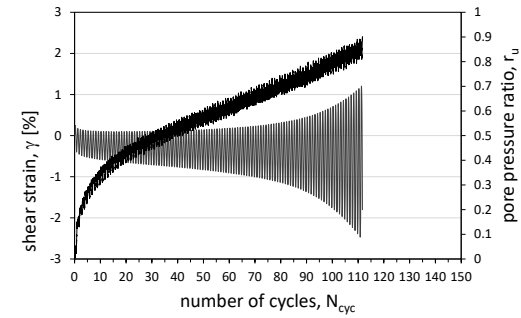
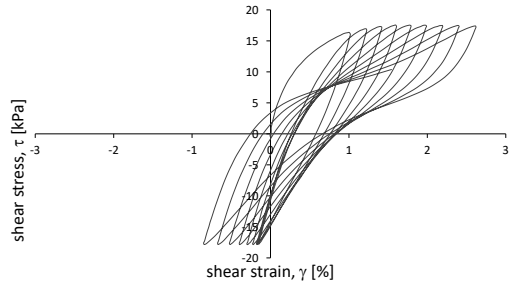
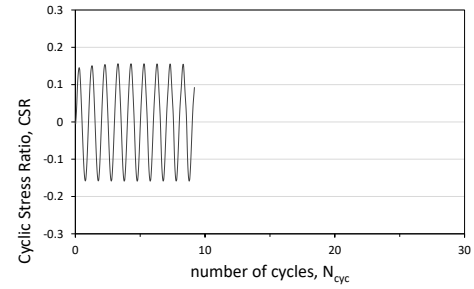


Figure 5-46: Results of cyclic simple shear test on SMca (BH2-U.S.3) with CSR=0.12 in τ - γ (a), CSR- N_{cyc} (b), τ - σ'_v (c) and γ - r_u - N_{cyc} (d) planes.

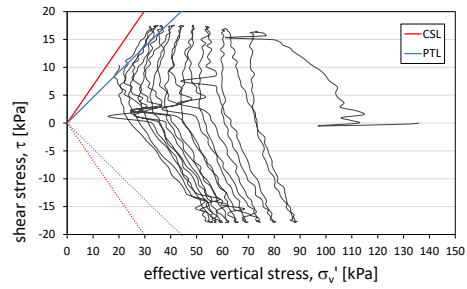
(a)



(b)



(c)



(d)

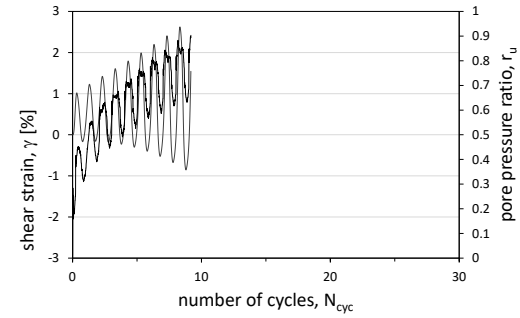
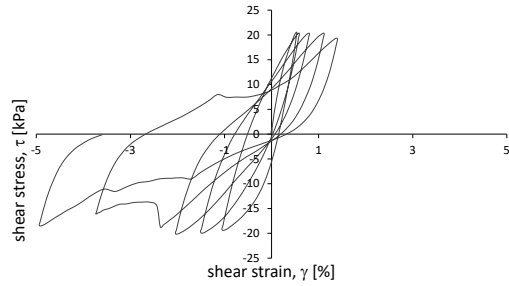
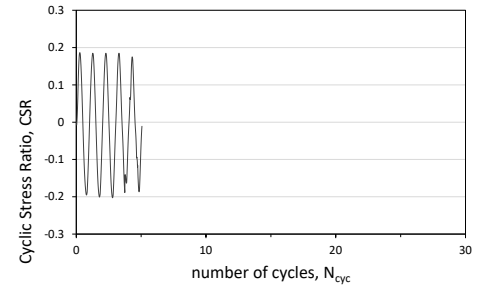


Figure 5-47: Results of cyclic simple shear test on SMca (BH2-U.S.3) with CSR=0.16 in τ - γ (a), CSR- N_{cyc} (b), τ - σ_v' (c) and γ - r_u - N_{cyc} (d) planes.

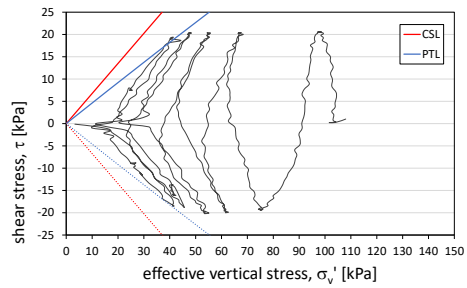
(a)



(b)



(c)



(d)

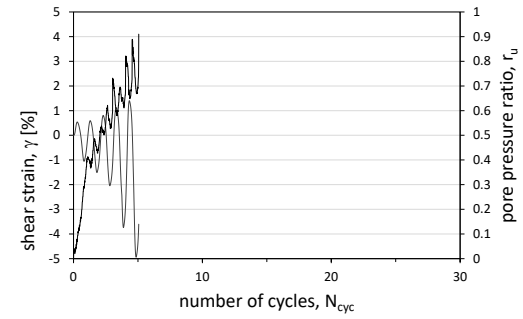


Figure 5-48: Results of cyclic simple shear test on SMca (BH2-U.S.3) with CSR=0.19 in τ - γ (a), CSR- N_{cyc} (b), τ - σ_v' (c) and γ - r_u - N_{cyc} (d) planes.

By applying different CSR values and evaluating the number of cycles to liquefaction, a series of points in the CRR- N_L plane can be defined. These points contribute to the definition of the cyclic resistance curve. Table 5-10 and Table 5-11 show a summary of the results of the tests carried out.

Table 5-10: Summary of CSS tests on sample BH2-U.S.1 (SMpi).

	e^*	σ'_v [kPa]	σ'_h [kPa]	k_0	N_L	CRR
CSS1	0.73	47.1	31.1	0.66	130	0.09
CSS2	0.61	50.6	20.7	0.41	63	0.11
CSS3	0.66	51.6	21.3	0.41	14	0.13
CSS4	0.63	52.7	23.5	0.45	33	0.13
CSS5	0.55	57.9	20.3	0.35	7	0.16
CSS6	0.47	64.4	27.2	0.42	6	0.18
CSS7	0.49	52.8	31.8	0.60	5	0.19

*at the end of consolidation phase

Table 5-11: Summary of CSS tests on sample BH2-U.S.3 (SMca).

	e^*	σ'_v [kPa]	σ'_h [kPa]	k_0	N_L	CRR
CSS1	0.82	108.0	32.8	0.30	1700	0.11
CSS2	0.96	104.0	35.6	0.34	112	0.12
CSS3	0.89	124.8	70.1	0.56	9	0.16
CSS4	0.83	108.0	49.8	0.46	5	0.19

*at the end of consolidation phase

The same results are reported in graphical form (Figure 5-49 and Figure 5-50).

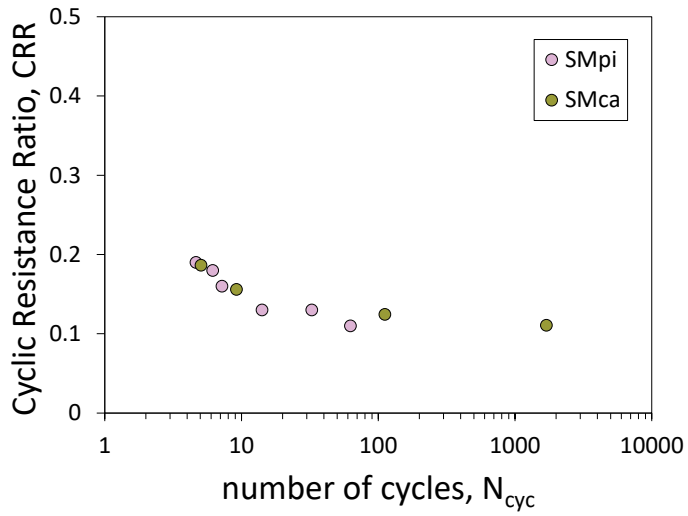


Figure 5-49: CSS test results in the plane N_{cyc} -CRR.

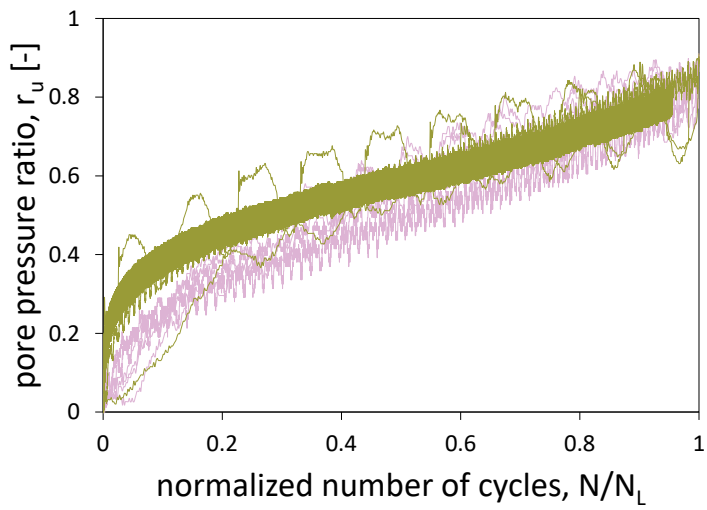


Figure 5-50: CSS test results in the plane N/N_L - r_u .

5.1.9 Cyclic torsional shear test

The lack of non-linearity curves associated with the SFCO formation in the laboratory investigation database collected for the Seismic Microzonation necessitated the execution of a cyclic torsional shear test on sample BH1-U.S.2. The test was conducted from a consolidation stress value of 180 kPa, a value consistent with the in-situ effective stress at the sample depth.

The measured trends of modulus of normalised stiffness and damping with strain are shown in Figure 5-51.

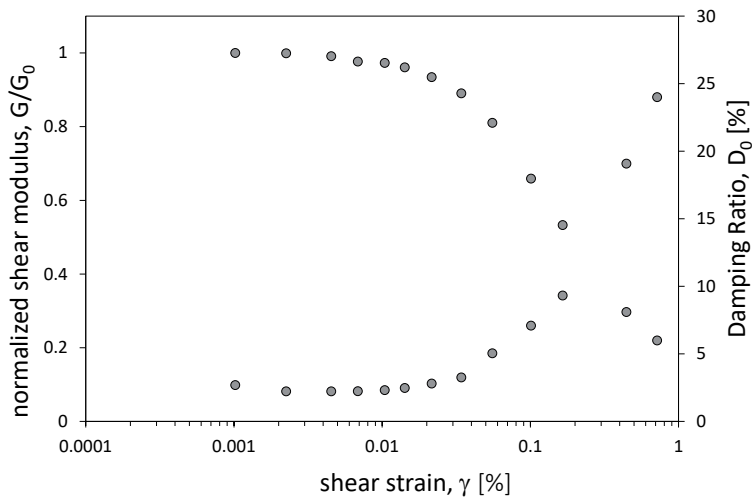


Figure 5-51: Variation of normalised stiffness and damping with shear strain for the formation indicated with SFCO.

5.2 Lacco Ameno study area

The study area is located in the 'Fango' area in the municipality of Lacco Ameno (Figure 5-52).

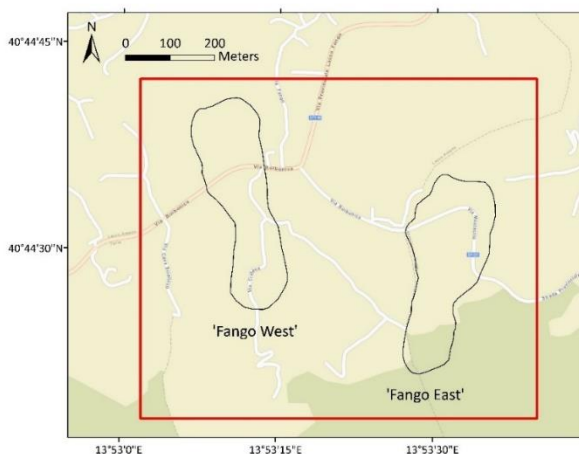


Figure 5-52: Study area for slope stability analysis. The two perimeters refer to 2 landslides mapped by the CARG project falling in the same area.

The area falls in the 2001, 2002 and 2003 MOPS. Uncamped areas have been classified as potentially unstable (SMIII studies).

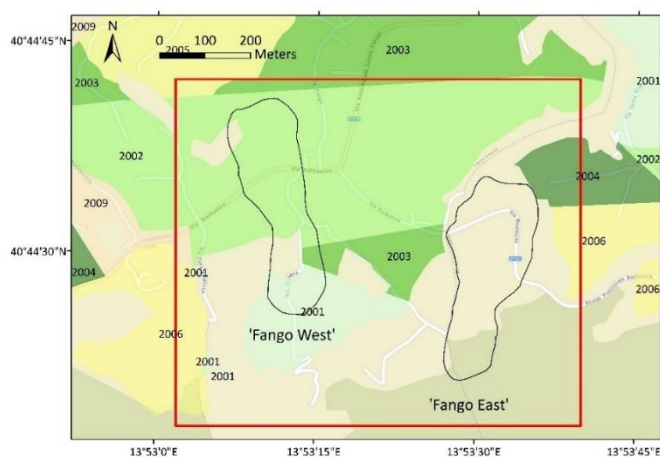


Figure 5-53: Homogeneous micro-zones in seismic perspective (MOPS) classification (MS studies) in 'Fango' study area.

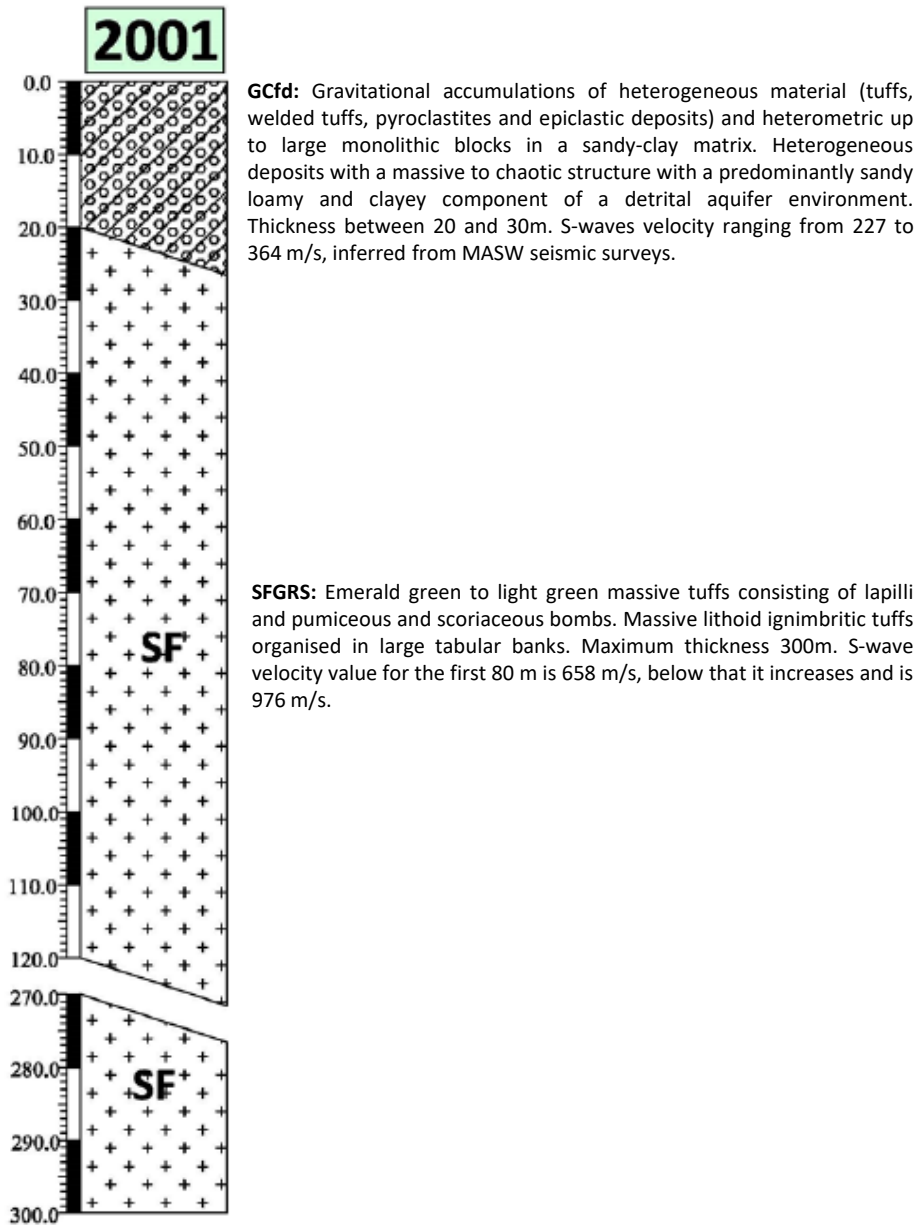
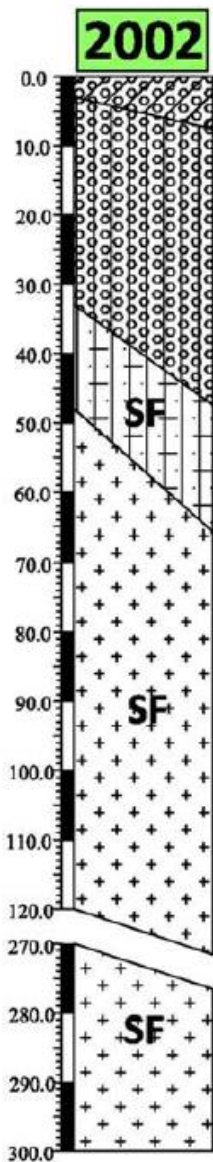


Figure 5-54: MOPS 2001: stratigraphic column with lithostratigraphic description.



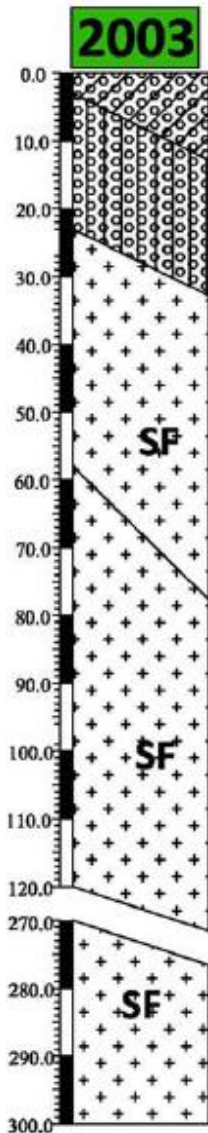
GCfd: Gravitational accumulations of heterogeneous material (tuffs, welded tuffs, pyroclastites and epiclastic deposits) and heterometric up to large monolithic blocks in a sandy-clay matrix. Heterogeneous deposits with a massive to chaotic structure with a predominantly sandy loamy and clayey component of a detrital aquifer environment. Thickness between 3 and 10 m. Median S-wave velocity, inferred from surface seismic surveys and the 'Fango' Array, of 297 m/s.

GMcd: Very coarse massive epiclastic deposits formed by mega blocks (>10m) and intensely fractured tuff blocks. These are debris avalanche deposits resulting from the gravitational collapse of the northern sector of the Mount Epomeo horst. Heterometric deposits varying in grain size from gravel to silt, containing large, fractured and altered granular tuffaceous blocks. Thickness between 30 and 45 m. Median S-wave velocity, inferred from the values of the surface seismic surveys and the 'Fango' Array, equal to 448 m/s.

SFCO: Weakly to medium lithified yellowish and greenish massive to weakly textured epiclastites composed of fine ash, lava lithics and tuffs in a fine clayey matrix varying in colour from greenish to yellow often containing plurimetrical olistolites. Variable thickness from 15 to 20 m. Median S-wave velocity, inferred from surface seismic surveys and the 'Fango' Array, of 667 m/s.

SFGRS: Emerald green to light green massive tuffs consisting of lapilli or pumiceous and scoriaceous bombs. Massive lithoid ignimbritic tuffs organised in large tabular banks. Maximum thickness 300 m. S-wave velocity, inferred from the 'Fango' Array, equal to 667 m/s for a thickness of 33 m and equal to 947 m/s for a further thickness of 150 m.

Figure 5-55: MOPS 2002: stratigraphic column with lithostratigraphic description.



GCfd: Gravitational accumulations of heterogeneous material (tuffs, welded tuffs, pyroclastites and epiclastic deposits) and heterometric up to large monolithic blocks in a sandy-clay matrix. Heterogeneous deposits with a massive to chaotic structure with a predominantly sandy loamy and clayey component of a detrital aquifer environment. Thickness between 3 and 18 m. Median S-wave velocity, inferred from surface seismic survey values, of 315 m/s.

GMcd: Very coarse massive epiclastic deposits formed by mega blocks (>10m) and intensely fractured tuff blocks. These are debris avalanche deposits resulting from the gravitational collapse of the northern sector of the Mount Epomeo horst. Heterometric deposits varying in grain size from gravel to silt, containing large, fractured and altered granular tuffaceous blocks. Maximum thickness 20 m. S-wave velocity, inferred from measurements taken on the island of Ischia in correspondence with this formation, of 450 m/s.

SFGRS: Weakly to moderately lithified yellowish and greenish massive to weakly structured epiclastites, often containing plurimetrical olistolites. Between 35 and 50 m thick. S-wave velocity, derived from measurements on the island of Ischia in correspondence with this formation, of 670 m/s.

SFGRS: Emerald green to light green massive tuffs consisting of lapilli or pumiceous and scoriaceous bombs. Massive lithoid ignimbric tuffs organised in large tabular banks. Maximum thickness 300 m. S-wave velocity, inferred from seismic Arrays carried out on the island of Ischia, equal to 970 m/s.

Figure 5-56: MOPS 2003: stratigraphic column with lithostratigraphic description.

In the same area, Synthetic Aperture Radar (SAR) data are available. They consist of European Remote Sensing (ERS), Environmental Satellite (ENVISAT) and COSMO-SkyMed (CSK) scenes acquired in descending and ascending mode allowing to cover a significant time span of analysis of about 25 years over the study area. ERS and ENVISAT data covers the time interval from June 1992 to December 2000 and from April 2003 to July 2010. COSMO-SkyMed (CSK) data covers the time interval from August 2017 to August 2019. What immediately stands out is the lack of points due to the lack of reflectors (being in an area with few houses and a lot of vegetation). In particular for ERS and ENVISAT data, the resolution is very low (see Figure 5-57 and Figure 5-58).

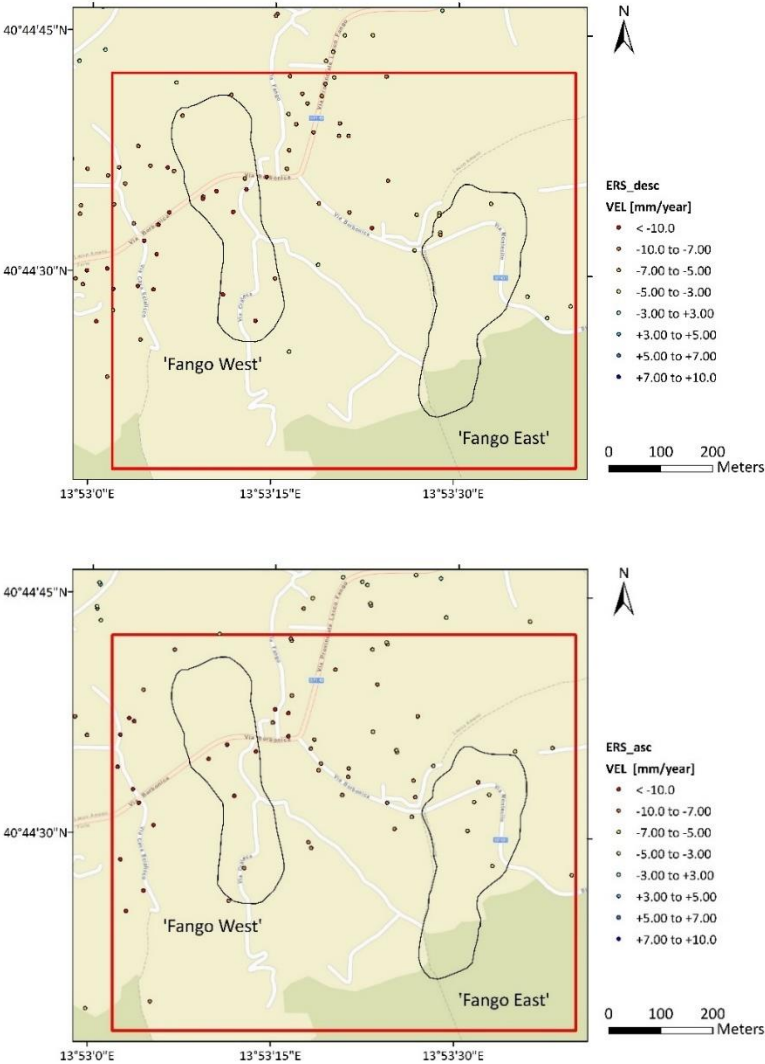


Figure 5-57: Velocity maps [mm/year] derived by processing of descending (above) and ascending (below) ERS (1992-2000) SAR data.

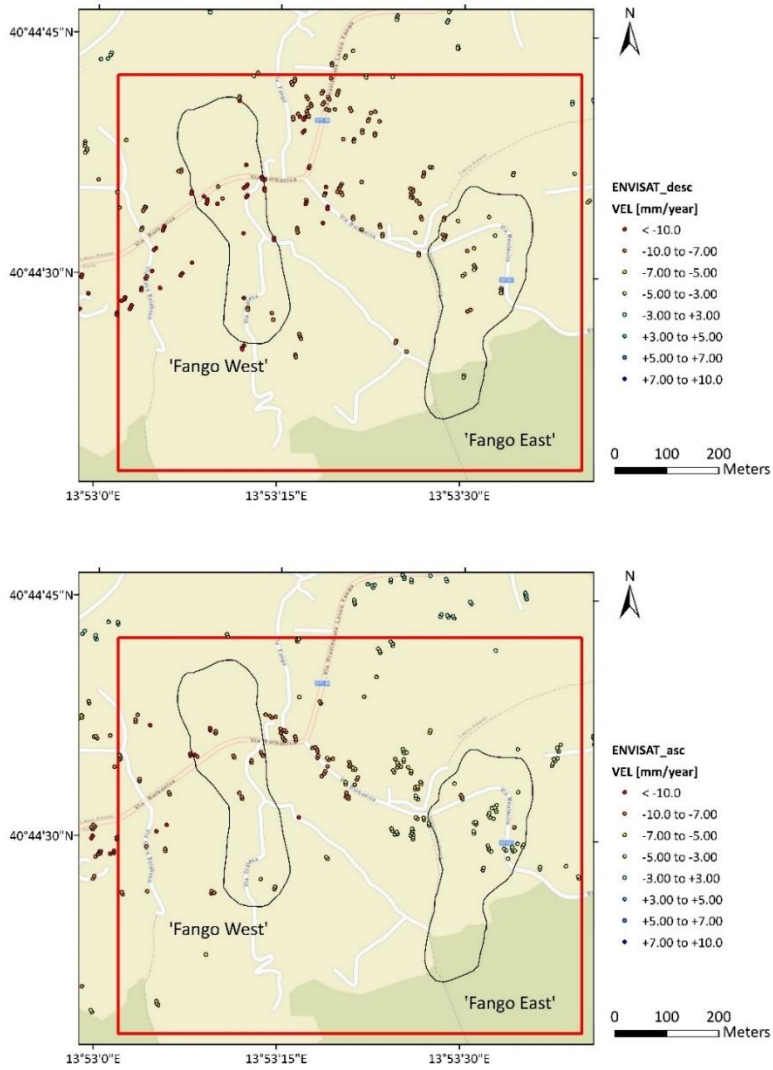


Figure 5-58: Velocity maps [mm/year] derived by processing of descending (above) and ascending (below) ENVISAT (2003-2010) SAR data.

More interesting data can be observed from the images taken by Cosmo-SkyMed in the aftermath of the earthquake in August 2017.

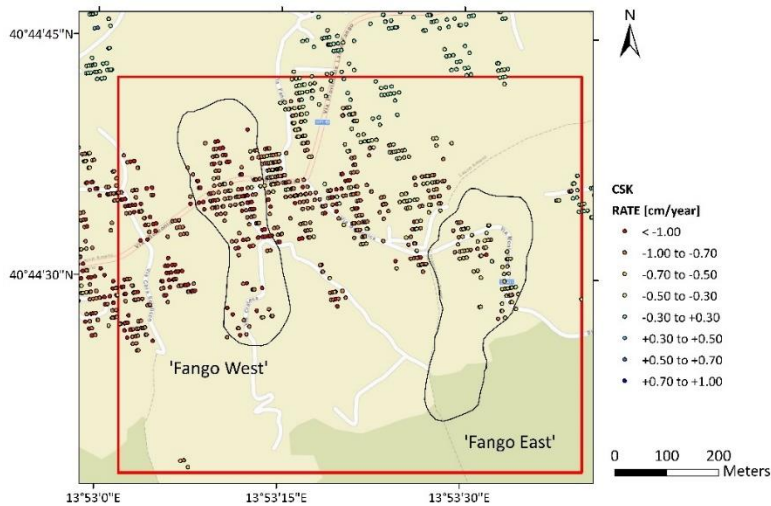


Figure 5-59: Velocity maps [cm/year] derived by processing of COSMO-SkyMed (2017-2019) SAR data.

To observe the damages caused by the earthquake of August 21, an interferometric pair must be chosen, i.e. two radar images acquired on the same orbit (one pre-event and one post-event) that can generate a good interferogram.

Figure 5-60 shows the obtained interferogram in terms of displacement before and after the 2017 earthquake event. The same figure shows the ground coseismic effects, among which fractures and small rock falls, that have been induced over an area of about 2.5 km² (Azzaro et al. 2017; EMERGEIO Working Group, Nappi et al. 2018).

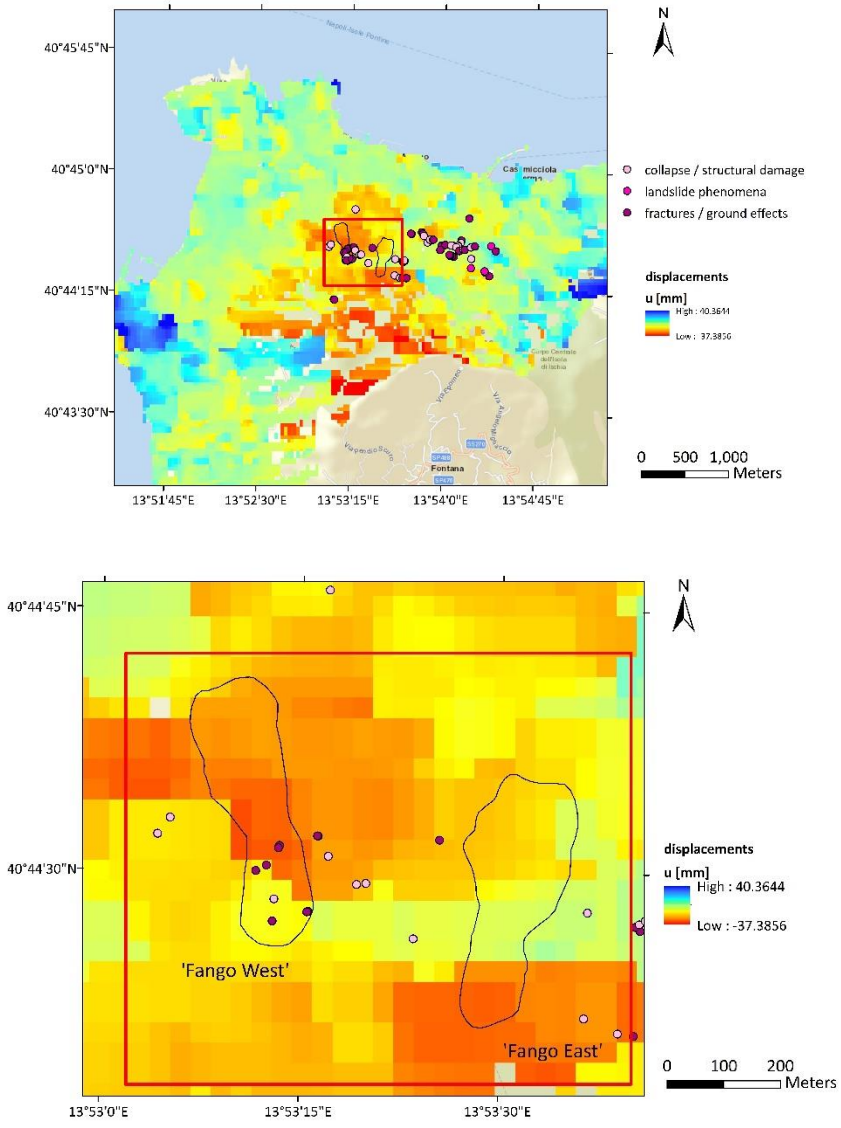


Figure 5-60: Interferogram in terms of displacement before and after the 2017 earthquake event. The same figure shows the ground coseismic effects (Azzaro et al. 2017; EMERGEO Working Group, Nappi et al. 2018).



Figure 5-61: Example of coseismic ruptures on Crateca road (from Nappi et al. 2017).

Both the satellite data and the distribution of the seismic effects suggested to further investigate the landslide which in this investigation was named as 'Fango West'.

5.2.1 Boreholes, SPT

Figure 5-62 shows the location of the boreholes carried out within the UniNA-MASLIDE project.

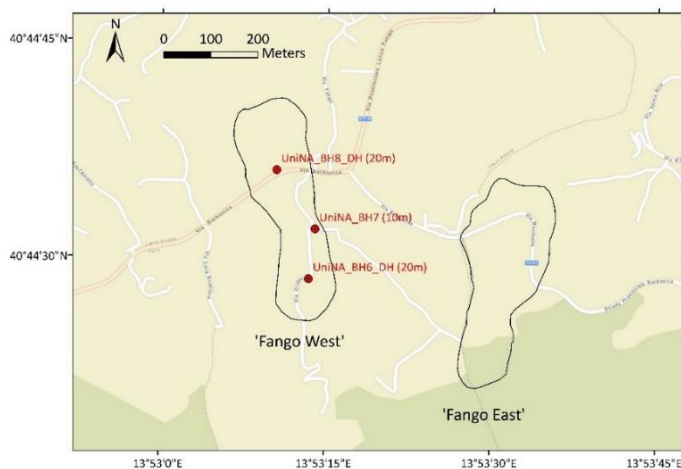


Figure 5-62: Boreholes location and depth reached in brackets UniNa (2022) for the characterisation of the landslide named 'Fango West'.

A summary of the investigations carried out is given below in both tabular (Table 5-12) and graphic form: the stratigraphic columns are described in terms of formations from both a geological (Figure 5-63) and geo-lithological (Figure 5-64) point of view (codes are from *Commissione Tecnica per la Microzonazione Sismica*, 2020).

Table 5-12: Overview of surveys carried out for the characterisation of the landslide 'Fango West'.

ID	depth from ground level	SPT	samples collected
UniNA_BH6_DH	20m	-	R.S.1 (11.10-11.30m) R.S.2 (13.50-13.75 m) U.S.1 (17.00-17.50 m) R.S.3 (20.10-20.30)
UniNA_BH7	10m	-	R.S.1 (5.00-5.30 m)
UniNA_BH8_DH	20m	SPT1 (16.00-16.10 m): R	U.S.1 (7.00-7.25 m) U.S.2 (7.30-7.45 m) U.S.3 (7.75-7.90 m) U.S.4 (10.40-10.55 m) U.S.5 (14.30-14.50 m) U.S.6 (15.10-15.50 m)

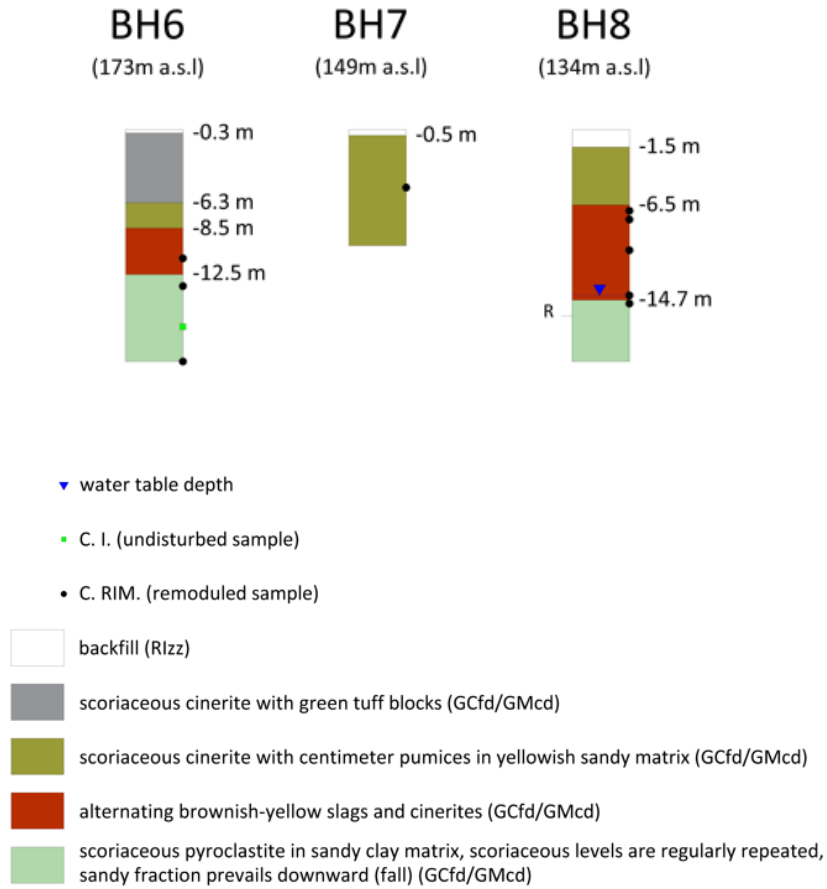


Figure 5-63: Stratigraphic columns with geological description.

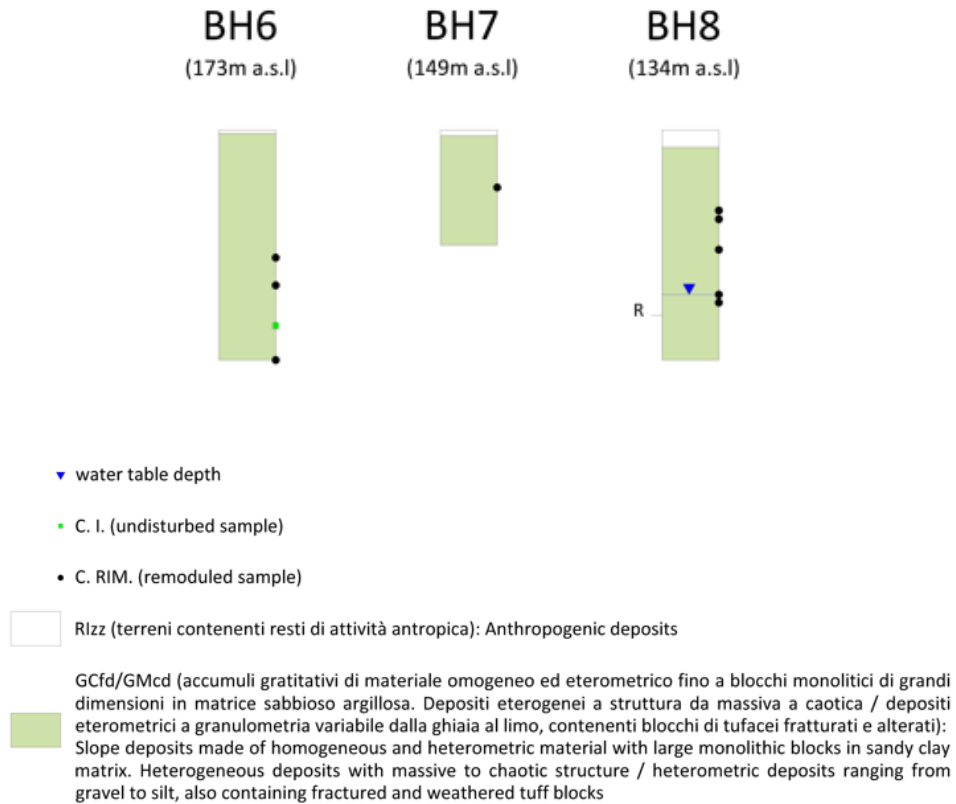


Figure 5-64: Stratigraphic columns with geo-lithological description (codes are from SM studies).

5.2.2 Down-hole tests

Boreholes BH6_DH and BH8_DH were equipped with PVC tubes and a zero-shrinkage mortar casting in the borehole-tubes cavity to perform down-hole tests necessary for the definition of the wave velocity profile up to a depth of 20 m. S-wave and P-wave velocity profiles for BH6 (Figure 5-65 and Figure 5-66) and BH8 (Figure 5-67 and Figure 5-68) are shown below.

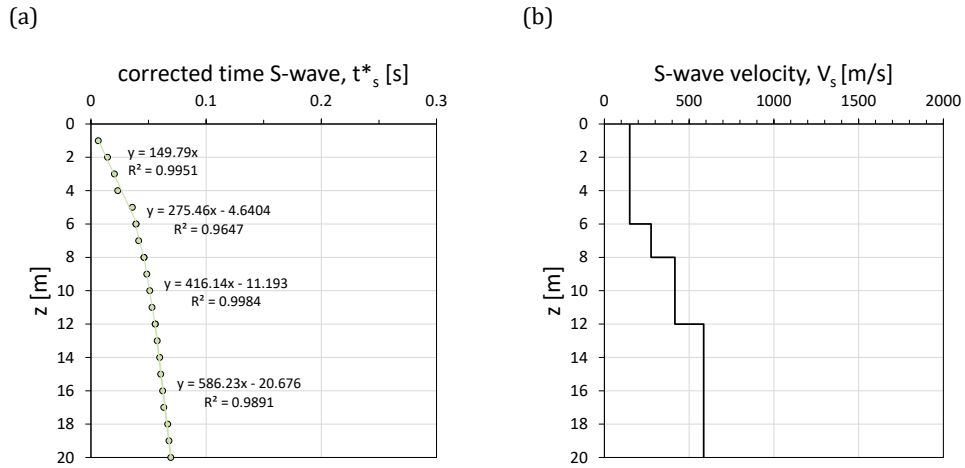


Figure 5-65: Dromochrone (a) and S-wave velocity profile (b) measured in BH6.

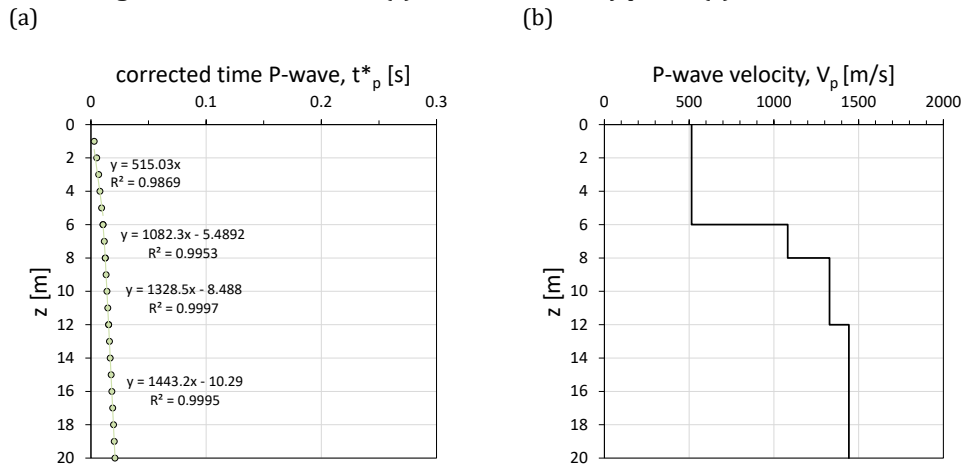
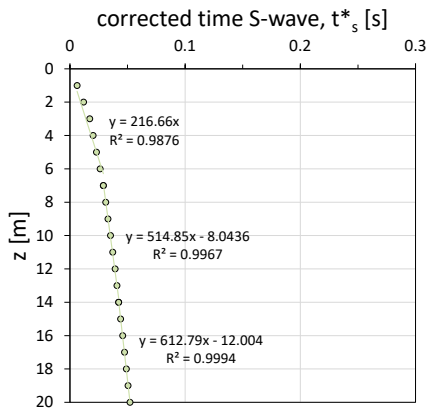


Figure 5-66: Dromochrone (a) and P-wave velocity profile (b) measured in BH6.

(a)



(b)

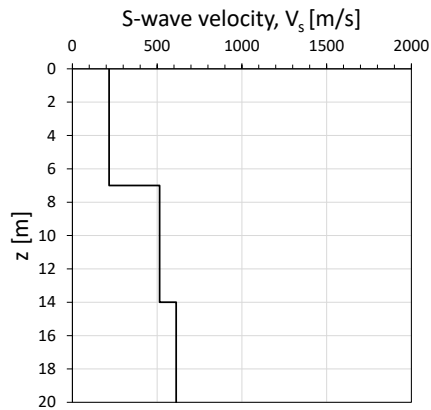
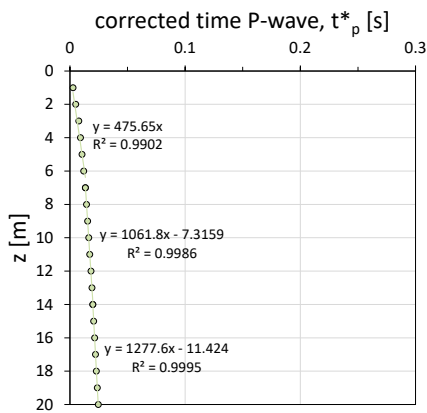


Figure 5-67: Dromochrone (a) and S-wave velocity profile (b) measured in BH8.

(a)



(b)

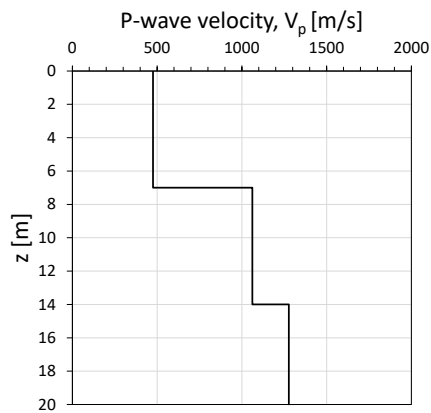


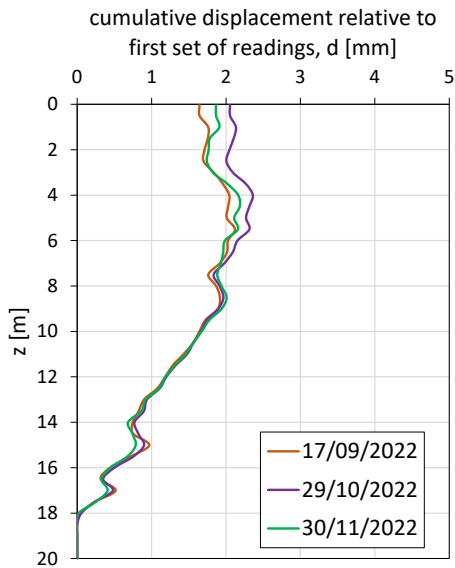
Figure 5-68: Dromochrone (a) and P-wave velocity profile (b) measured in BH8.

5.2.3 Inclinometric measurements

After the execution of the down-hole seismic surveys, BH6_DH and BH8_DH were conditioned along their entire length, with aluminium inclinometer tubes, external diameter ϕ 53 mm. Readings from mid-September to the end of November 2022 are

reported in Figure 5-69. The displacements observed are always less than 2-3mm with a maximum at the interface of the first two layers.

(a)



(b)

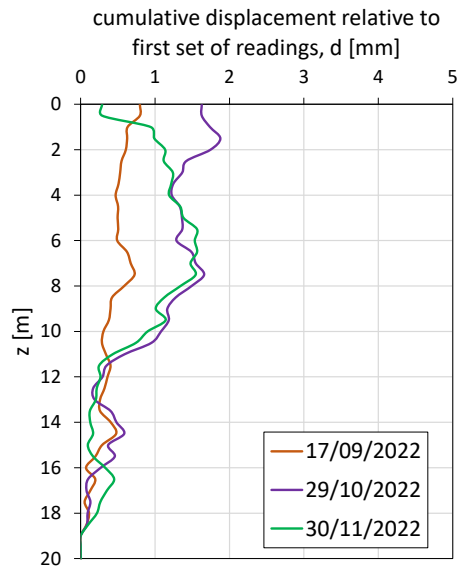


Figure 5-69: Incliner measurements taken at BH6 (a) and BH8 (b) from mid-September to the end of November 2022.

5.2.4 Electrical Resistivity Tomography

Results from Electrical Resistivity Tomography (ERT) are useful to identify general trends of the thicknesses and the main heterogeneities of the soils under examination. The location of the ERTs carried out in 'Fango' study area is shown in Figure 5-70.

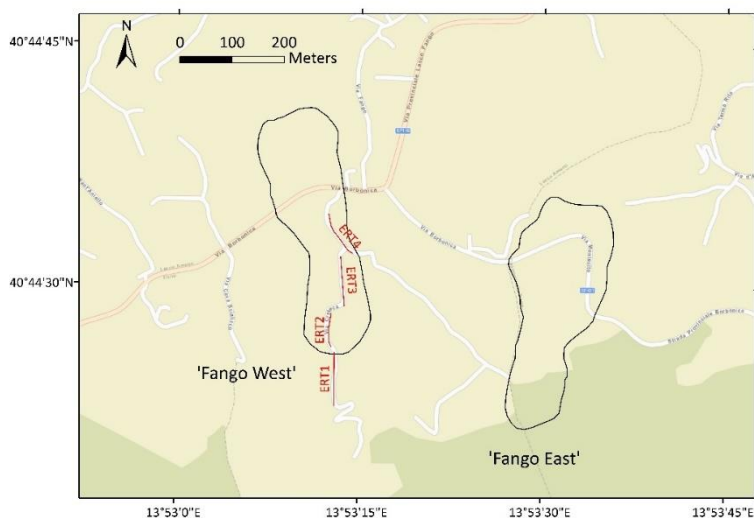


Figure 5-70: Location of ERT performed in 'Fango' area within the UniNA-MASLIDE project.

In order to provide more detailed subsurface resistivity models, it was decided to adopt both the Wenner-Schlumberger configuration (so as to be able to highlight any variations in resistivity horizontally and vertically) and the Dipole-Dipole configuration (thus obtaining a greater depth of investigation and greater horizontal resolution) for each individual standoff. The length of the spreads, for logistical issues, is limited. The ERT1 array of 93.00 m was carried out in the highest topographically investigated sector of Monte Epomeo, along the main road, with a distance between the electrodes of 3.00 m. Proceeding downstream, a second array ERT2 was located, with a total length of 46.50 m, and a distance between electrodes of 1.50 m. The most superficial deposits show resistivities correlated with the presence of reworked and backfilled materials. Proceeding downwards, there is a significant decrease in the measured resistivities, probably due to the granulometric assortment of the deposits

(presence of fine and medium fine ash), which have a good degree of humidity. In the resistivity sections in the Dipole-Dipole configuration, a gradual increase in resistivity values is observed from about 18-20m from the base (ERT1) and from about 5-6m (ERT2), which can be correlated with the presence of substrate consisting mainly of coarse-grained deposits (pumice, slag and tuffaceous deposits). The resistivity models for both configurations are reported in and Figure 5-71 and Figure 5-72.

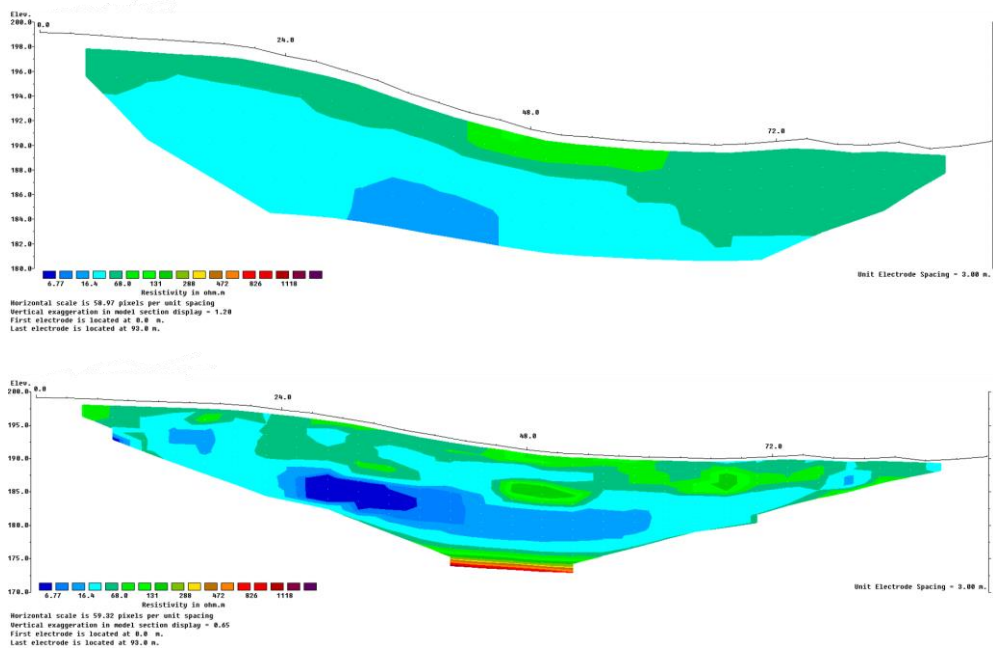


Figure 5-71: ERT1 results in both Wenner-Schlumberger (above) and Dipole-Dipole (below) configuration.

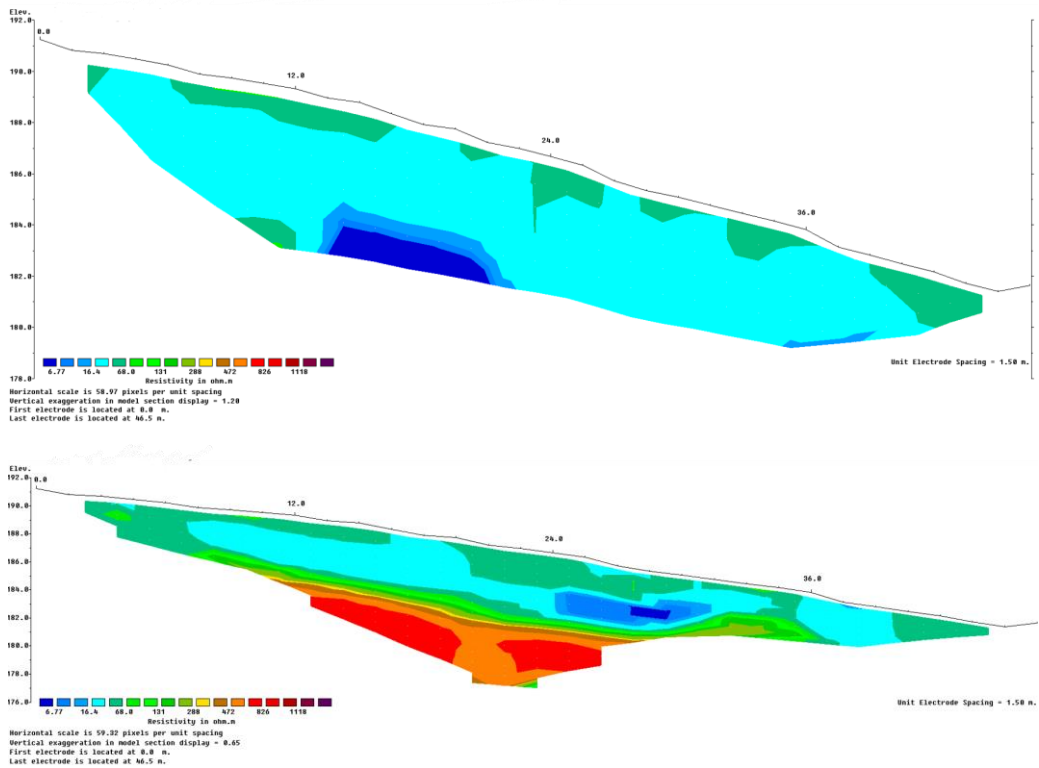


Figure 5-72: ERT2 results in both Wenner-Schlumberger (above) and Dipole-Dipole (below) configuration.

The 93.00 m ERT3 electrical tomography array was also carried out along the main road, between geognostic boreholes BH6 and BH7, with a distance between the electrodes of 3.00 m. Towards the valley, in the topographically lowest sector of the main road leading to Mt. Epomeo, a final electrical tomography spread of 93.00 m was carried out, called ERT4 in the vicinity of borehole S7, with a distance between electrodes of 3.00 m. Finally, in the Dipole-Dipole configuration, a gradual increase in the resistivity values is observed from approximately 15-17 m from the borehole (ERT3), to be correlated with the presence of substrate consisting mainly of coarse-grained deposits (pumice, slag and tuffaceous deposits). For ERT4, there are areas characterised by low resistivity values, to be correlated with the probable presence of

surface circulation waters. In both resistivity pseudo-sections, a net horizon is intercepted, characterised by an increase in resistivity values, at a depth varying from approximately 3 to 6 m from the ground surface, to be correlated with the presence of coarse-grained deposits. The resistivity models for both configurations are reported in Figure 5-73 and Figure 5-74.

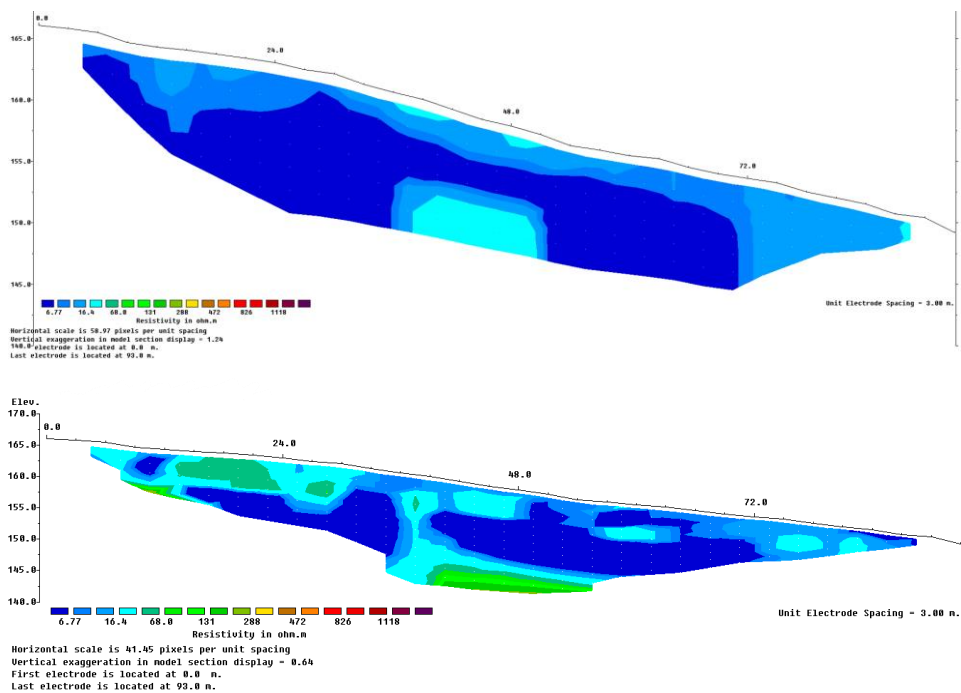


Figure 5-73: ERT3 results in both Wenner-Schlumberger (above) and Dipole-Dipole (below) configuration.

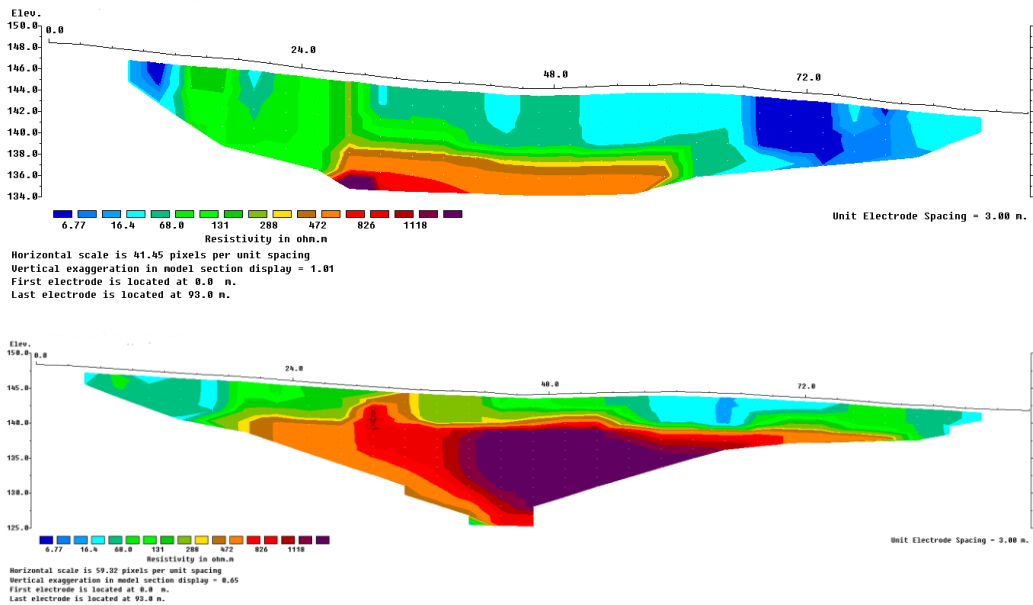


Figure 5-74: ERT4 results in both Wenner-Schlumberger (above) and Dipole-Dipole (below) configuration.

5.2.5 Microtremor Horizontal to Vertical Spectral Ratio analysis

15 ambient noise measurements, called A01-A15, were carried out in the same area (Figure 5-75).

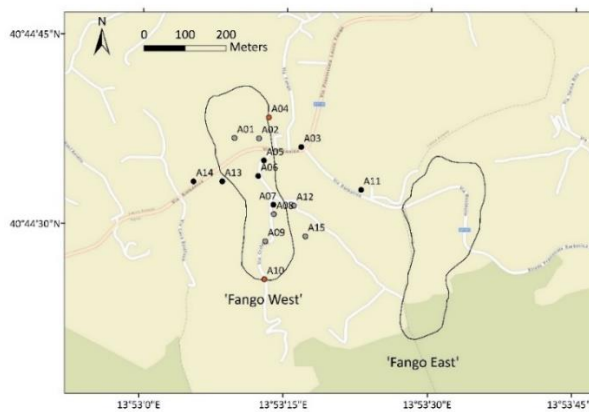


Figure 5-75: Location of HVSR performed within the UniNA-MASLIDE project.

As already mentioned at §5.1.4 the data processing was carried out using the Geopsy software as per the recommendations of the SESAME (Site Effects Assessment Using Ambient Excitations) consortium (Acerra et al. 2004).

In Figure 5-75 the measurement points are plotted with the same colours according to their similarities in terms of amplification functions and fundamental frequency.

As for the noise measurements made in Casamicciola Terme, they show a quite stable low frequency peak ($f_0 < 1$ Hz) in the investigated area despite the high variability in the shallow geological units. The observation of low-frequency peak has suggested the presence of a deep bedrock and a low impedance contrast (see §6). Details of the fundamental frequency values and H/V functions are shown in Figure 5-76.

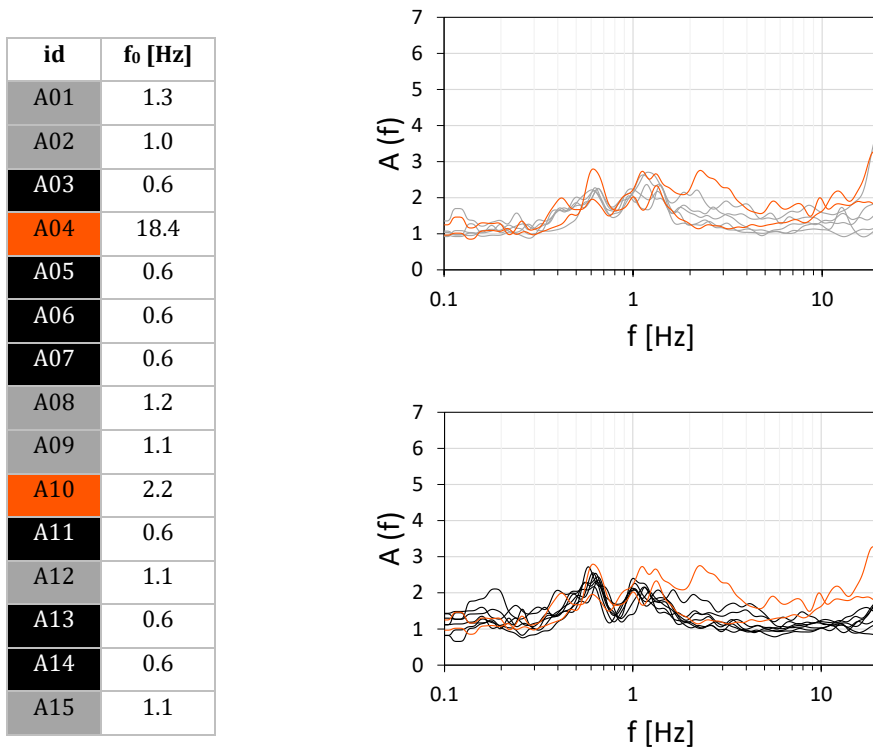


Figure 5-76: Fundamental frequencies and amplification functions separated by zone. The amplification function relevant to the sites A04 and A10 with higher fundamental frequency values are plotted in orange.

Details of each individual registration are given in the Appendix A.2.

5.2.6 Physical properties

Two grain-size distribution curves (Figure 5-77 and Table 5-13) were obtained from the remoduled samples R.S.1 and R.S.2 taken from borehole BH6. The main physical properties are shown in Table 5-14.

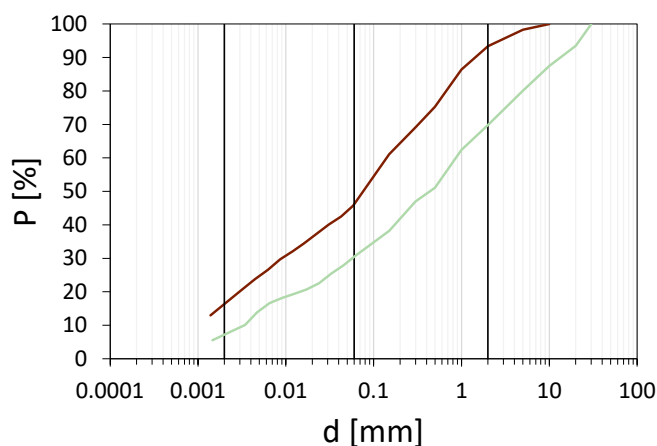


Figure 5-77: Grain-size distributions of the materials shown in Figure 5-63.

Table 5-13: Grain-size distributions values.

	sample	gravel	sand	silt	clay
	[-]	[%]	[%]	[%]	[%]
	BH6 - R.S.1 (11.10-11.30m)	7	47	30	16
	BH6 - R.S.2 (13.50-13.75m)	30	39	24	7

Table 5-14: Material properties.

	sample	G_s	d₅₀	UC	FC
	[-]	[g/cm ³]	[mm]	[-]	[%]
	BH6 - R.S.1 (11.10-11.30m)	2.5	0.086	146	49
	BH6 - R.S.2 (13.50-13.75m)	2.5	0.446	296	32

5.2.7 Direct shear tests

Three drained direct shear (DS) test was performed on the only undisturbed sample taken (BH6-U.S.1) to estimate drained strength parameters. The specimen was tested at natural water content up to the peak value, after which it was saturated until the residual strength value was reached. Figure 5-78 shows the results of these tests.

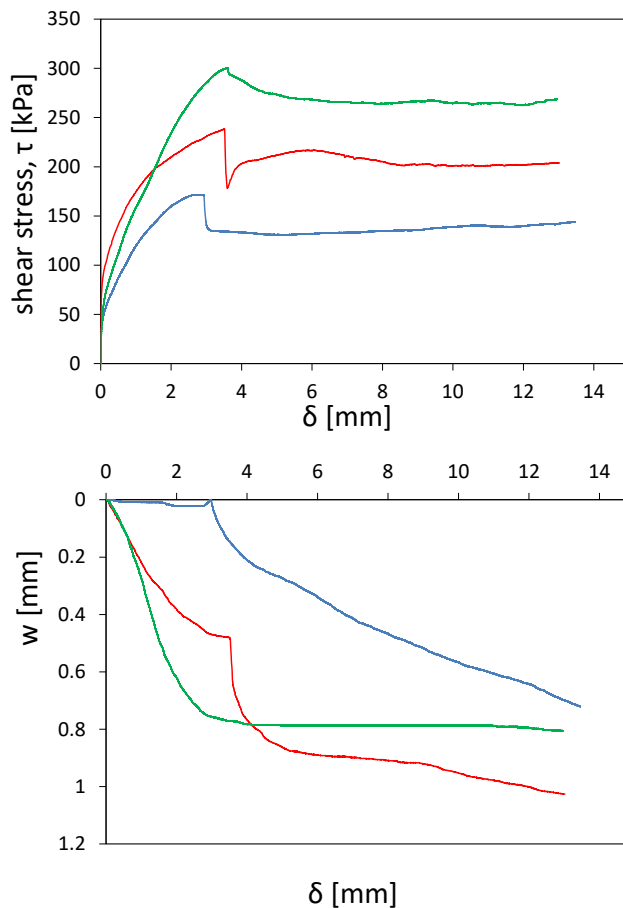


Figure 5-78: Results direct shear test of in plane τ - δ (above) and w - δ (below).

Figure 5-79 shows the envelope in the Mohr plane for peak (a) and residual values (b). The latter can be found in Table 5-15 and Table 5-16, respectively.

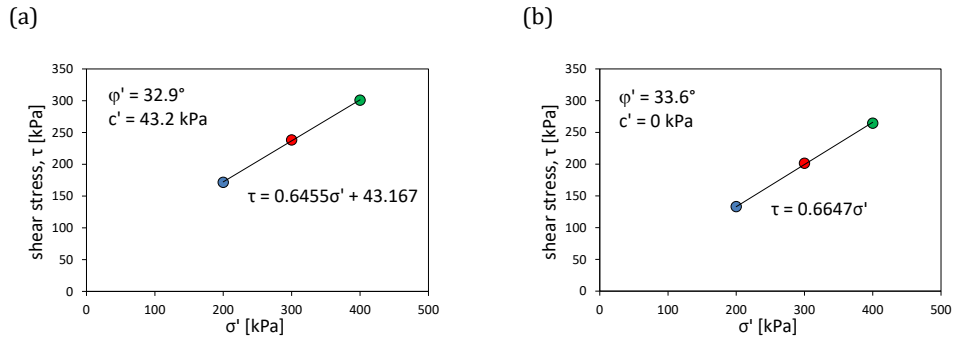


Figure 5-79: Results of the direct shear test: envelope of peak (a) and residual (b) values in the Mohr plane.

Table 5-15: Direct shear test results: peak values.

	σ' [kPa]	τ [kPa]	τ/σ'	ϕ'_{peak} [°]	ϕ'_{peak} [°]
■	200	171.6	0.86	40.6	32.9
■	300	238.2	0.79	38.5	
■	400	300.6	0.75	36.9	

Table 5-16: Direct shear test results: residual values.

	σ' [kPa]	τ [kPa]	τ/σ'	ϕ'_{res} [°]	ϕ'_{res} [°]
■	200	133.1	0.67	33.7	33.6
■	300	201.2	0.67	33.8	
■	400	264.4	0.66	33.5	

6. Geotechnical model

The geotechnical subsurface model can be defined according to the level of analysis. While screening criteria and simplified approaches require a limited number of data, advanced analyses may require the definition of a larger number of experimental data. The subsoil geotechnical model for the 2 verticals at Casamicciola Terme and for the selected slope at Lacco Ameno in the 'Fango' area have been firstly defined on the bases of the results of the site and laboratory tests, discussed in the previous chapter. In the following, all the necessary ingredients for both liquefaction susceptibility and slope instability analyses are explained in detail.

6.1 Casamicciola Terme test site

In order to perform one-dimensional site response analysis, it is necessary to define a shear wave velocity profile extending down to the bedrock, i.e. that corresponding to V_s greater than or equal to 800 m/s. The velocity profiles reported for BH1 (Figure 5-15) and BH2 (Figure 5-17) do not satisfy such conditions being the V_s less than 500m/s at a depth of 50 m. For this reason it was necessary to perform an inversion procedure of the ambient noise measurements adjacent to BH1 and BH2, C15 and C04 respectively (Figure 6-1). The inversions were performed with the aid of the *GEOPSY* software. This is a programme package designed within the framework of the European SESAME project for the analysis, interpretation and inversion of data mainly from environmental noise recordings for the dynamic characterisation of a site. The Geopsy.org project consists of a series of interrelated but independent programmes, or modules, of which the main ones are Geopsy (for interpreting experimental data) and Dinver (for inversions). Inversions are performed in the software according to an iterative process derived from Sambridge's algorithm (1999), implemented in C++ by Wathelet (2008): Neighbourhood algorithm, based on Monte Carlo method.

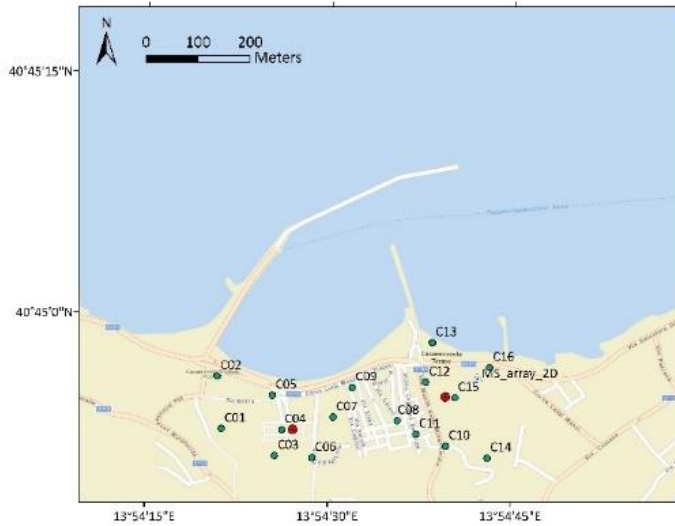


Figure 6-1: Location of environmental noise measurements adjacent to boreholes BH1 and BH2. The same figure also shows the location of a 2D array carried out during the SM studies.

The key point of inversion is to define the parameters by identifying the information already known about the ground structure and the information that needs to be extracted (see Figure 6-2).



Figure 6-2: Example of parameter input panel for inversion.

The software allows domains to be created for V_p , V_s , layer thicknesses h , density and Poisson's coefficient. In this case, the inversion procedure was constrained to downhole measurements in the two boreholes in the first 50 m (see Figure 6-3 and Figure 6-4).

Once the analysis is started, the programme shows the generated models and the state of iterations as well as the best-fits solutions obtained, i.e. those characterised by

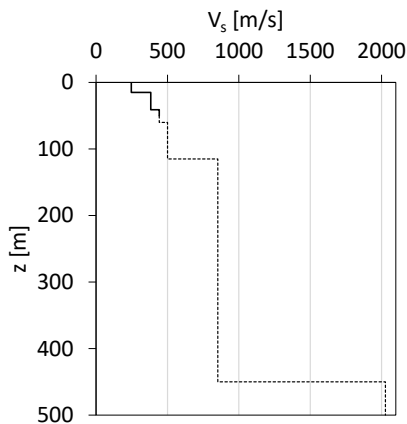
the minimum misfit. The latter, in the present case, are reported in Table 6-1 and Figure 6-3 (for BH1), Table 6-2 and Figure 6-4 (for BH2).

Table 6-1: Parameters of the best-fit model derived from the inversion of array data (C15) for BH1.

	H	γ	ρ	V_s	ν
	[m]	[kN/m ³]	[kg/m ³]	[m/s]	[-]
SM	5	19.51	2000	247	0.28
	5	19.51	2000	247	0.46
	5	17.81	1800	247	0.46
SFCO	26	20.33	2100	383	0.47
SFGRS	19	17.89	1800	442	0.45
	55	17.89	1800	500	0.25
	335	17.89	1800	853	0.25
	half-space	17.89	1800	2027	0.25

*boldface indicates directly measured quantities

(a)



(b)

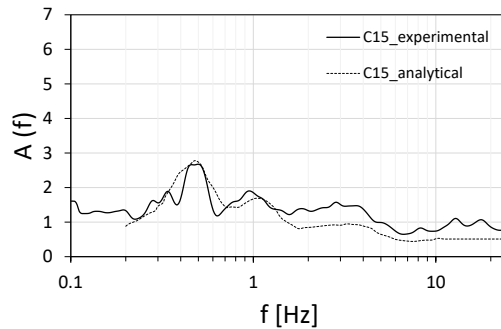


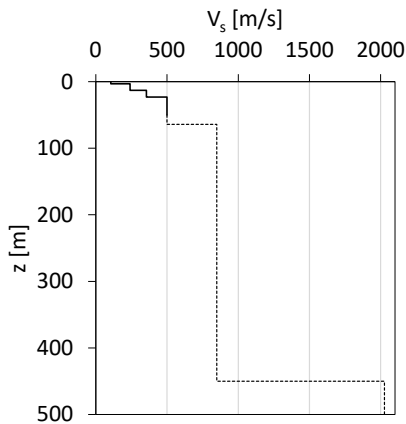
Figure 6-3: Best-fit model derived from inversion of array data (C15) for BH1: S-wave velocity profile (a) and comparison of experimental and analytical H/V ratio (b).

Table 6-2: Parameters of the best-fit model derived from the inversion of array data (C04) for BH2.

	H	γ	ρ	V_s	ν
	[m]	[kN/m ³]	[kg/m ³]	[m/s]	[-]
SM	3	19.51	2000	106	0.37
	3	19.51	2000	241	0.47
	7	17.81	1800	241	0.47
SFCO	10	20.33	2100	356	0.39
SFGRS	41	17.89	1800	500	0.42
	386	17.89	1800	853	0.25
	half-space	17.89	1800	2027	0.25

*boldface indicates directly measured quantities

(a)



(b)

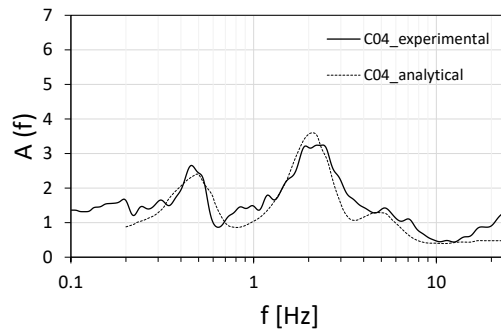


Figure 6-4: Best-fit model derived from inversion of array data (C04) for BH2: S-wave velocity profile (a) and comparison of experimental and analytical H/V ratio (b).

The difference between the two profiles reflects what has already been mentioned, i.e. the presence of two zones characterised by a different value of the fundamental frequency; in particular, a first peak is observed in both amplification functions (which depends on the deep impedance contrast at a depth of 450 m), while the second peak, which is missing in BH1 but present in BH2, is attributable to the shallower depth of

the bedrock. For each of the formations, it is necessary to assign a non-linearity curve. These describe the variation of normalised shear modulus G/G_0 and damping ratio D_0 with the deformation level. The geotechnical model does not consider the difference between the two formations SMpi and SMca, which will be directly referred to as SM from now on. The results of RCTS tests performed on the same material during the SM studies were used to characterize the non-linear behaviour of this formation. For the SFCO formation, the non-linearity curves were derived from the RCTS tests reported in §5.1.9. For the SFGRS formation, the results of tests on Neapolitan tuff were considered (Vinale et al. 1988). A summary is shown in Figure 6-5.

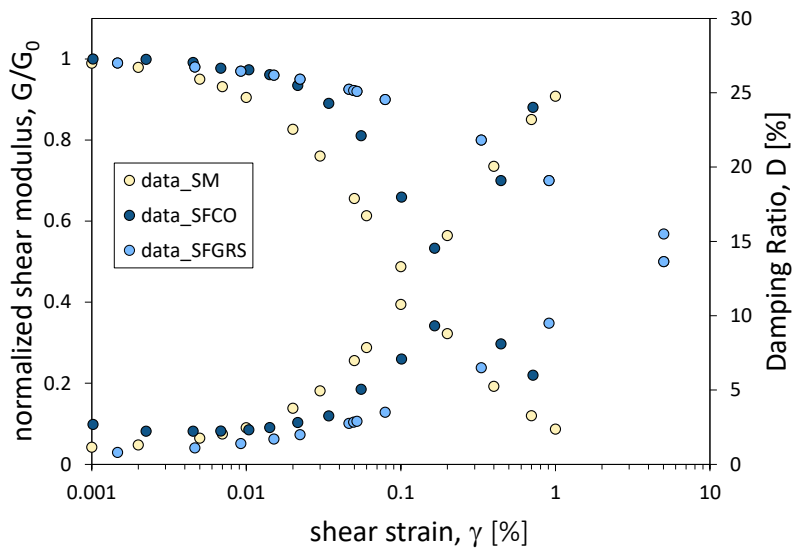


Figure 6-5: Experimental dependency of normalised shear modulus and damping ratio on shear strain for SM (from MS studies), SFCO (from this study) and SFGRS (Vinale et al. 1988).

In order to complete the geotechnical subsurface model, the definition of cyclic resistance curves (§5.1.9) is also required. They will be used to perform coupled analyses in effective stresses with the SCOSSA-PWP code (Tropeano et al. 2019). Details will be provided later.

6.2 Lacco Ameno test site

In the same way, in order to perform two-dimensional site response analysis, it is necessary to define a shear wave velocity profile extending down to the bedrock. The boreholes, limited to a depth of 20 m, again did not reach a S-wave velocity value of 800 m/s. For this reason, also in this case, it was necessary to carry out an inversion procedure of the ambient noise measurements (as already explained at §6.1) adjacent to BH6 and BH8, A09 and A01 respectively.

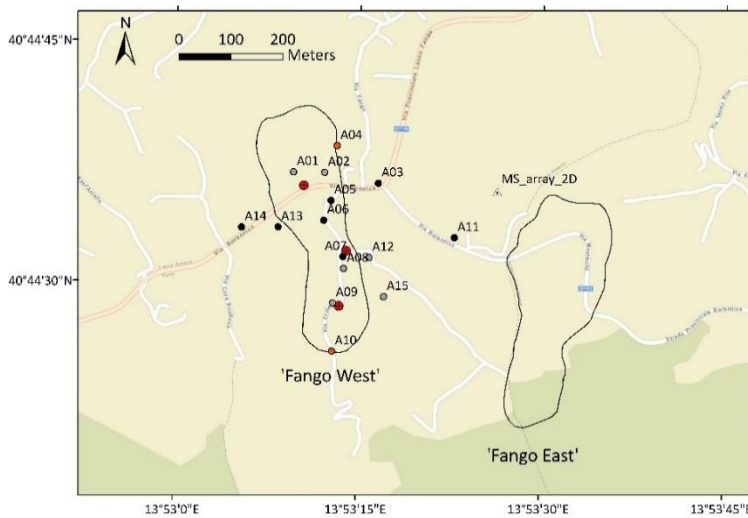


Figure 6-6: Location of environmental noise measurements adjacent to boreholes BH6 and BH8. The same figure also shows the location of a 2D array carried out during the Microzonation studies.

The inversion procedure was constrained to downhole measurements in the two boreholes in the first 20 m. For deeper layers, the constraint is given by a 2D array made in the same area (Figure 6-6) in MS studies. The results of the latter are shown in Figure 6-7 and Table 6-3.

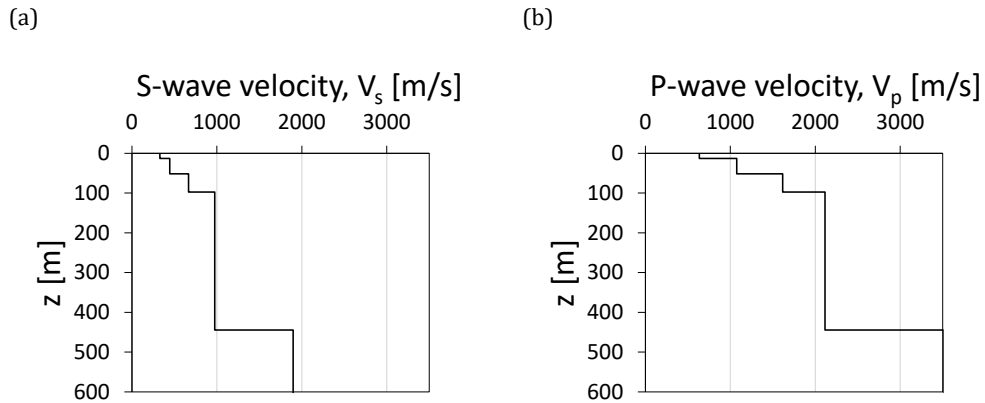


Figure 6-7: S-wave (a) and P-wave (b) velocity profile obtained from the 2D array made in the same study area in SM studies.

Table 6-3: Numerical values of the profiles in Figure 6-7.

H	V_p	V_s	α	ν
[m]	[m/s]	[m/s]	[-]	[-]
13	636	328	1.94	0.32
38.6	1075	446	2.41	0.40
46.1	1616	667	2.42	0.40
346.9	2115	974	2.17	0.37
-	3512	1897	1.85	0.29

The best-fit solution is also given, i.e. the ones characterised by the minimum misfit. The latter, in the present case, are reported in Table 6-4 and Figure 6-8 (for BH6), Table 6-5 and Figure 6-9 (for BH8).

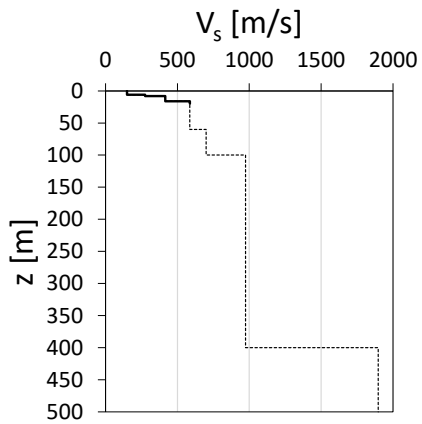
The inversion made for all environmental noise measurements, constrained by the MOPS (Figure 5-54, Figure 5-55 and Figure 5-56) and with a detailed geological study, allowed the lito-stratigraphic section shown in Figure 6-10. The same section, shown in the Figure 6-11, identifies the formations from a geo-lithological point of view.

Table 6-4: Parameters of the best-fit model derived from the inversion of array data (A09) for BH6.

H	γ	ρ	V_s	ν
[m]	[kN/m ³]	[kg/m ³]	[m/s]	[-]
6	15.10	1.5	150	0.45
2	15.10	1.5	275	0.47
8	15.10	1.5	416	0.45
44	20.33	1.5	586	0.40
40	17.89	1.8	700	0.40
300	17.89	1.8	974	0.37
half-space	17.89	1.8	1897	0.29

*boldface indicates directly measured quantities

(a)



(b)

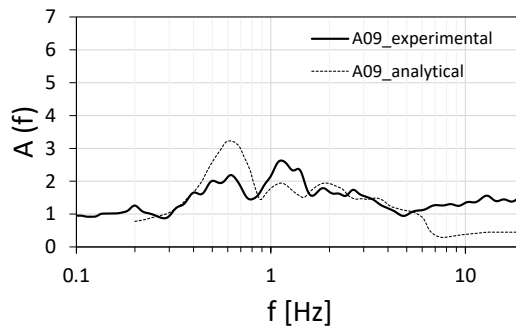


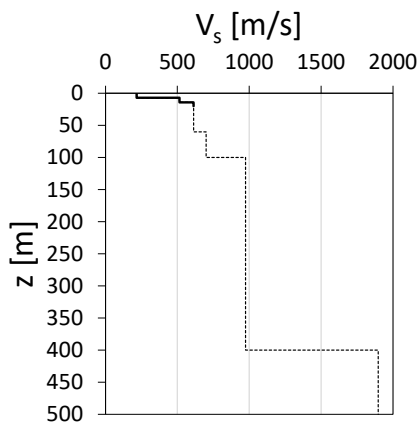
Figure 6-8: Best-fit model derived from inversion of array data (A09) for BH6: S-wave velocity profile (a) and comparison of experimental and analytical H/V ratio (b).

Table 6-5: Parameters of the best-fit model derived from the inversion of array data (A01) for BH8.

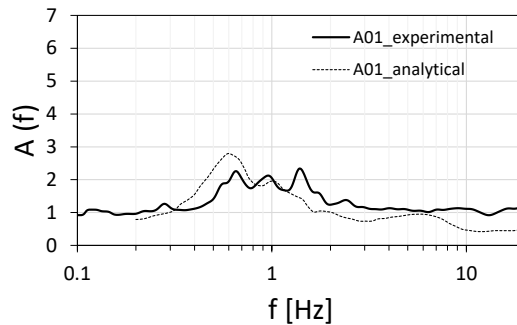
H	γ	ρ	V_s	ν
[m]	[kN/m ³]	[kg/m ³]	[m/s]	[-]
7	15.10	1.5	217	0.37
7	15.10	1.5	515	0.35
46	15.10	1.5	613	0.35
40	20.33	2.1	700	0.40
300	17.89	1.8	974	0.37
half-space	17.89	1.8	1897	0.29

*boldface indicates directly measured quantities

(a)



(b)

**Figure 6-9:** Best-fit model derived from inversion of array data (A01) for BH8: S-wave velocity profile (a) and comparison of experimental and analytical H/V ratio (b).

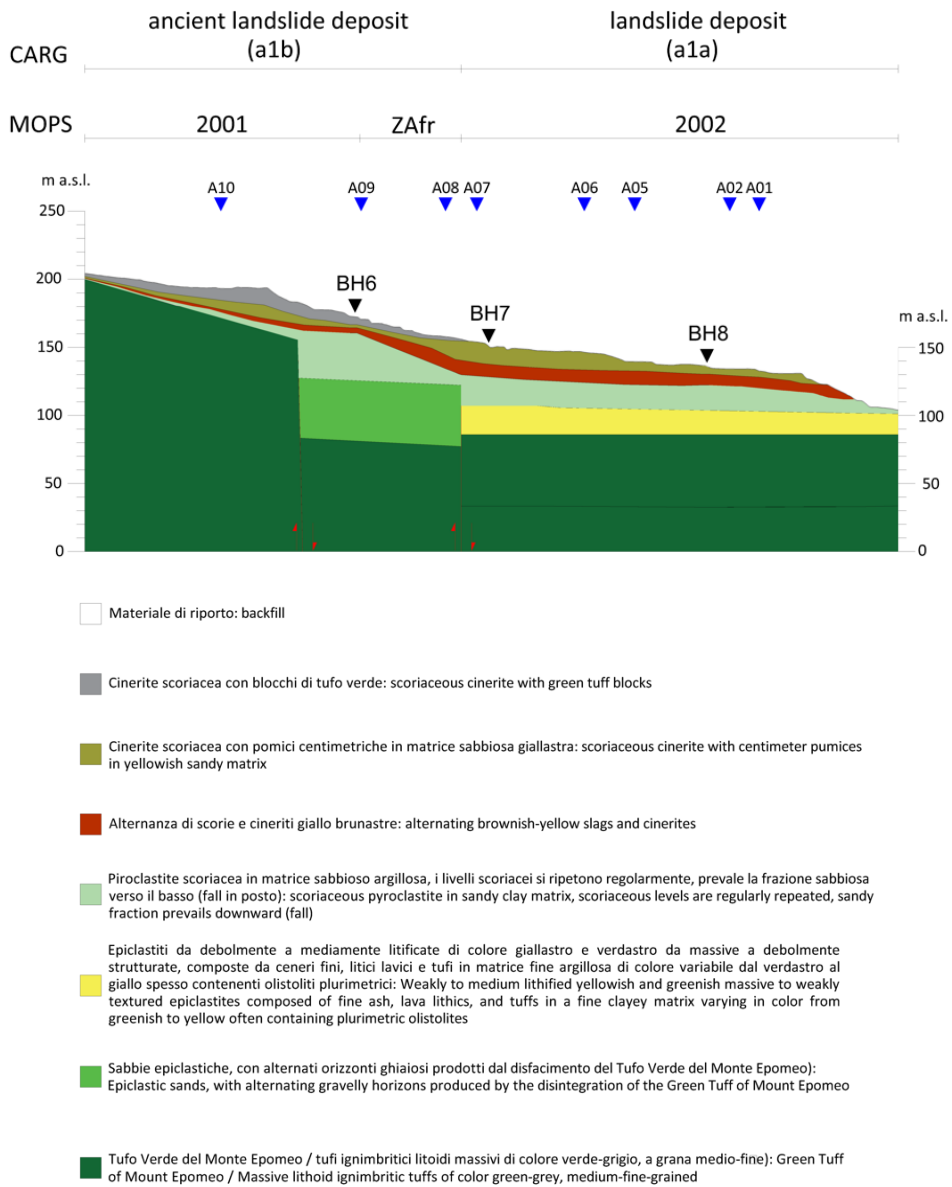


Figure 6-10: 2D litho-stratigraphic section assumed for slope stability analyses.

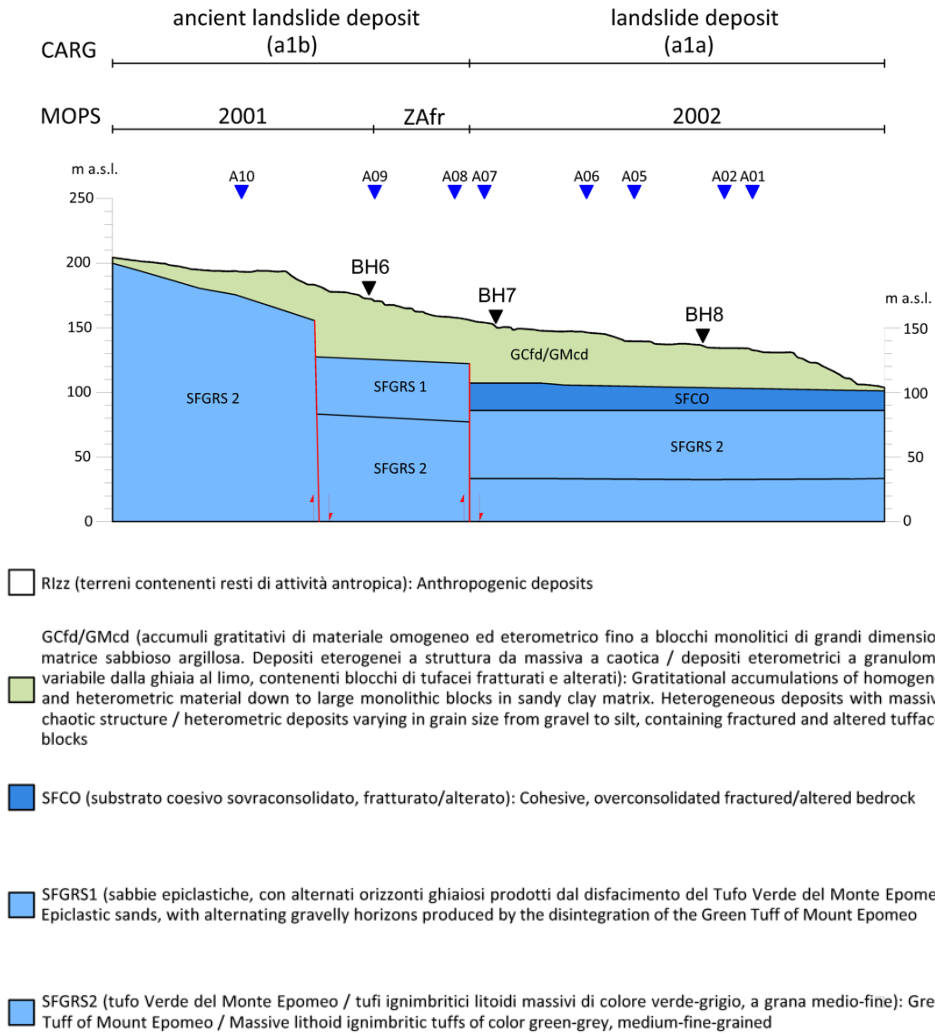


Figure 6-11: 2D geo-lithological section assumed for slope stability analyses (codes are from Commissione Tecnica per la Microzonazione Sismica).

Also in this case, it was necessary to assign non-linearity curves to the different soil layers. For the formation referred to as GC/GM the results of RCTS tests performed on the same material during the MS studies were used. For the SFCO formation, the non-linearity curves were derived from a test done ad hoc in this work and introduced

previously (§5.1.9). For the SFGRS formation, the results of tests on Neapolitan tuff were considered (Vinale et al. 1988).

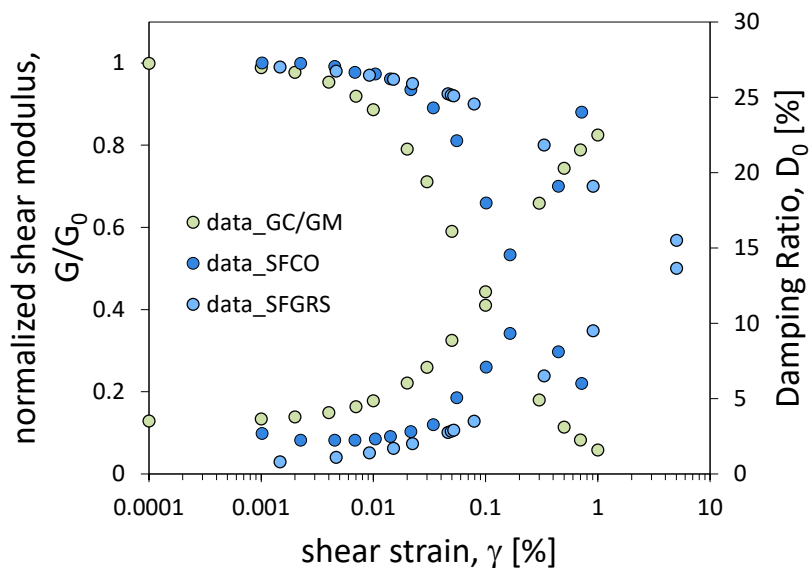


Figure 6-12: Experimental dependency of normalised shear modulus and damping ratio on shear strain for GC/GM (from MS studies), SFCO (from this study) and SFGRS (Vinale et al. 1988) .

To complete the model, strength parameters are required: for the indicated GC/CM soil layer, the friction angle and cohesion values were evaluated by ad hoc simple shear tests, already discussed in §5.2.7. For the formations known as SFCO and SFGRS, typical values reported in the literature for this soil formations were assumed. A summary is shown in Table 6-6.

Table 6-6: Strength parameters assigned to each formation identified in the Figure 6-11.

	γ [kN/m ³]	c' [kPa]	ϕ [°]
GC/GM	15.1	0	33.6
SFCO	20.3	25	33.0
SFGRS1	17.9	15	35.0
SFGRS2	17.9	15	35.0

7. Results

7.1 Seismic input

7.1.1 Synthetic parameters and shakemaps

For simplified liquefaction analyses, carried out in the coastal area of the municipality of Casamicciola Terme, it was adopted the customary approach, adopted by the national code (NTC 2018), based on the *Probabilistic Seismic Hazard Analysis* (PSHA): the value of reference of the peak ground acceleration, a_r , is given by the combination of the limit state (related to a probability of exceedance, P_R) and the return period, T_R .

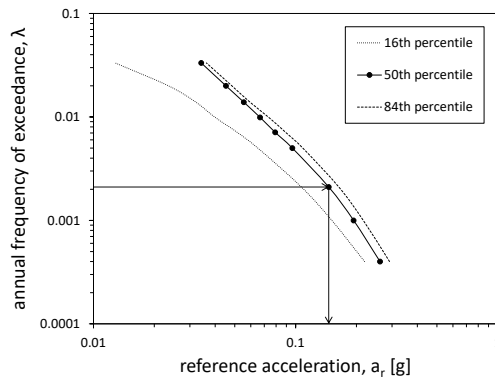


Figure 7-1: Hazard curves for 16th, 50th and 84th percentiles for Casamicciola Terme municipality.

The median hazard curve shown in Figure 7-1 provides the value $a_r=0.152g$, by assuming SLV ($P_R=10\%$) with return period, $T_R=475$ years. The corresponding de-aggregation histogram, reported in Figure 7-2, shows the distribution of the relative contribution to the *hazard curve* of the magnitude-epicentral distance bins.

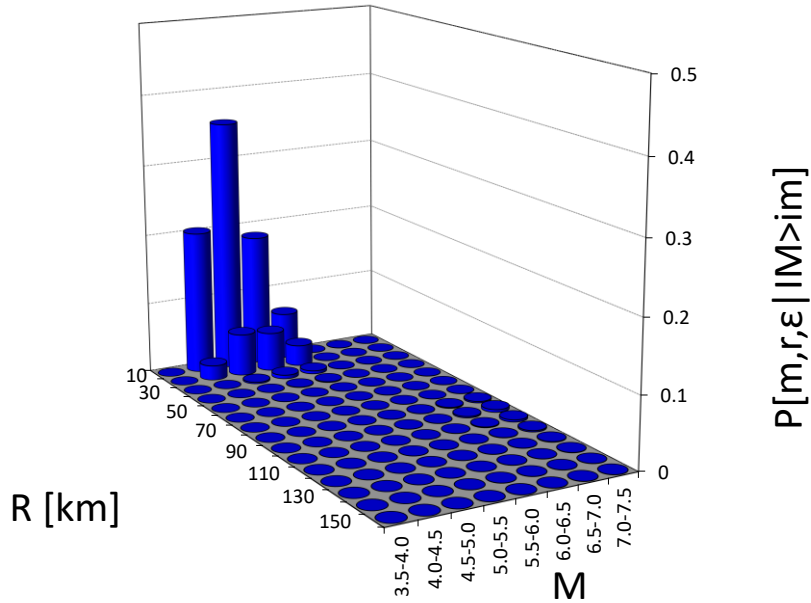


Figure 7-2: De-aggregation analysis for Casamicciola Terme site study.

Table 7-1: De-aggregation of reference acceleration in terms of M , R and ϵ (median values).

M	R	ϵ
4.91	7.58	0.699

The reference acceleration, a_r , has been modified to obtain the acceleration at surface, as:

$$a_s = S_S \cdot S_T \cdot a_r \quad \text{Eq. 7-1}$$

where S_S is the stratigraphic coefficient as a function of the reference acceleration, a_r , and the soil type classification (in this case C), while the topographic S_T coefficient is set equal to one.

Table 7-2: Peak surface acceleration used for liquefaction assessment with semi-empirical approaches.

a_r [g]	S_s	a_s [g]
0.152	1.492	0.227

The magnitude, reported in Table 7-1, is necessary for the quantification of the magnitude scaling factor MSF, already defined in §4.2.1.

On the other hand, for slope stability analyses on a territorial scale, the seismic action has been evaluated considering a *Deterministic Seismic Hazard Analysis* (DSHA), i.e. simulating the Maximum Historical Earthquake (MHE) that occurred in Casamicciola in 1883. To this end, an *ad hoc* Ground Motion Prediction Equation (GMPE) for volcanic areas (Lanzano et al. 2019) has been used to simulate the distribution of acceleration at bedrock (Figure 7-3a), by considering a point-source and isotropic attenuation model starting from the position of the epicenter and the magnitude of the event reported by the CPT15 catalogue (Rovida et al. 2022). As seen before, the reference acceleration, a_r , has been modified to obtain the acceleration at the surface, a_s (Figure 7-3a), according to Eq. 7-1.

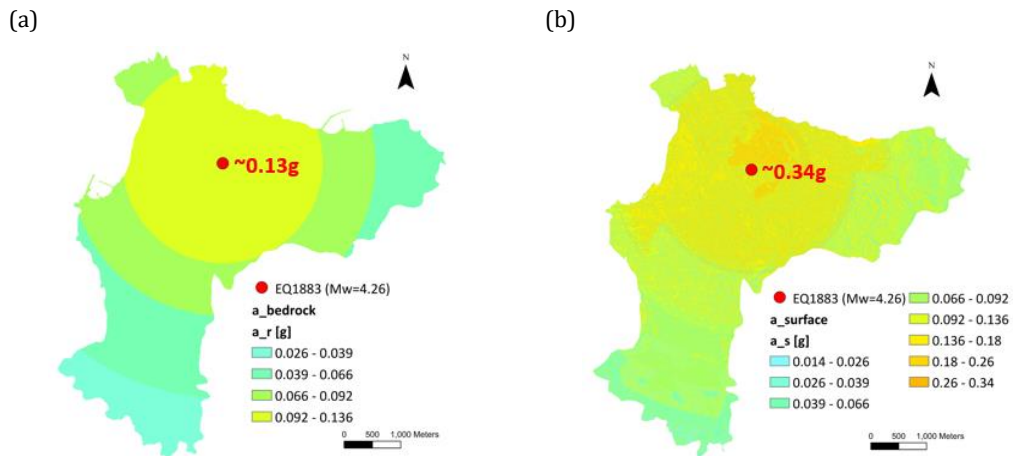


Figure 7-3: Maps of acceleration at bedrock (a) and surface (b).

In this case, the nonlinear stratigraphic amplification factor, S_s , was evaluated as variable between 1.3 and 1.9 with the relationships proposed by Tropeano et al. (2018) (see Eq. 4-19 and Table 4-2). It was assigned on the basis of the map in Figure 7-4a, obtained by integrating the Grade I Seismic Microzonation map of the area with the soil type classification map proposed by Forte et al. (2019) for the whole Italian territory.

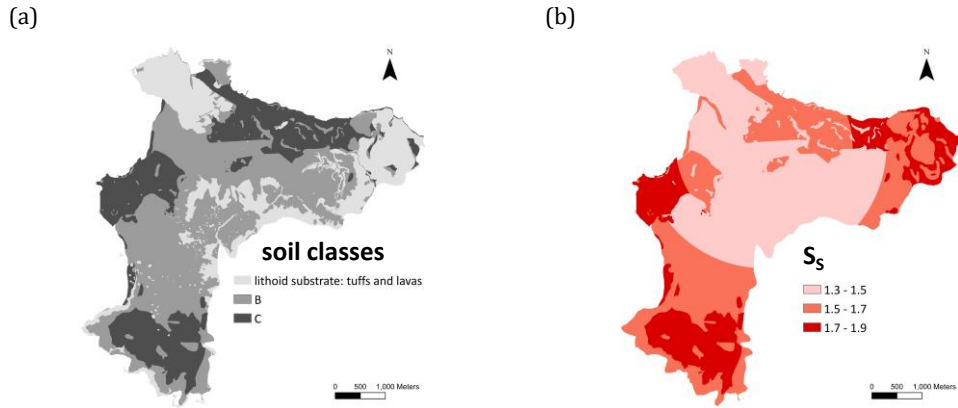


Figure 7-4: Soil type classification (a) and stratigraphic amplification factor (b) maps.

The topographic factor, S_T , was evaluated as variable between 0.5 and 1.4 from the slope curvature α' to take into account the amplification or attenuation of the seismic motion in case of convex or concave geometry (see Table 4-3).

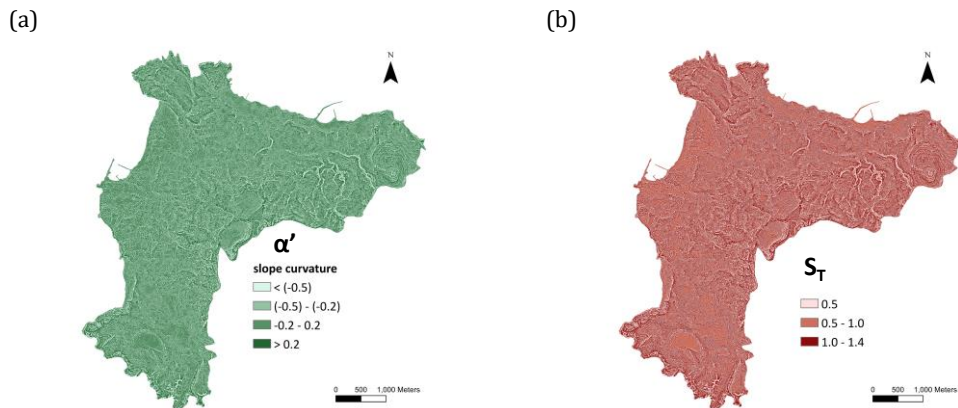


Figure 7-5: Slope curvature (a) and topographic factor (b) maps.

7.1.2 Code-compatible accelerograms

Regarding the selection of natural accelerograms, the approach used in SM studies was adopted. In these studies, recordings were selected through the software *In-Spector* (Acunzo et al. 2014). The set of seven accelerograms was selected to be, on average, code-compatible (according to specific tolerance criteria) over a period of interest (0.1s - 1.1s) with respect to the reference spectrum. The NTC 2018 defines a minimum tolerance of 10%, while it does not define a maximum tolerance, which has been set at 30%. The natural accelerograms were selected from those present in the Engineering Strong-Motion database (<https://esm.mi.ingv.it>, Luzi et al. 2016) and having well-defined characteristics in terms of:

- magnitude range and source-site distance;
- type of focal mechanism of the event;
- site soil class of the recording location.

With reference to the magnitude intervals selection criterion, the de-aggregation diagram (Figure 7-2) is a useful tool to check the contribution of the various seismogenic sources to the hazard. In the case of Ischia, less restrictive criteria for the choice of recordings were adopted about site soil class and focal mechanism of the source, to include recordings related to nearby events and characterised by hypocentral depths comparable to those of the sources present in the study area. The final record selection was carried out considering events with the following characteristics:

- site Classification: A, A* or Undefined (to include accelerometer records related to nearby events);
- minimum and maximum magnitude for record selection: 4 - 5.5;
- type of magnitude: M_w (moment magnitude) or M_l (local magnitude);
- minimum and maximum epicentral distance for record selection: 0-20 km;
- focal mechanism: normal fault, strike-slip fault and undefined fault.

Figure 7-6 reports the natural accelerogram time histories and their spectra compared with reference NTC 2018, 475 year spectrum.

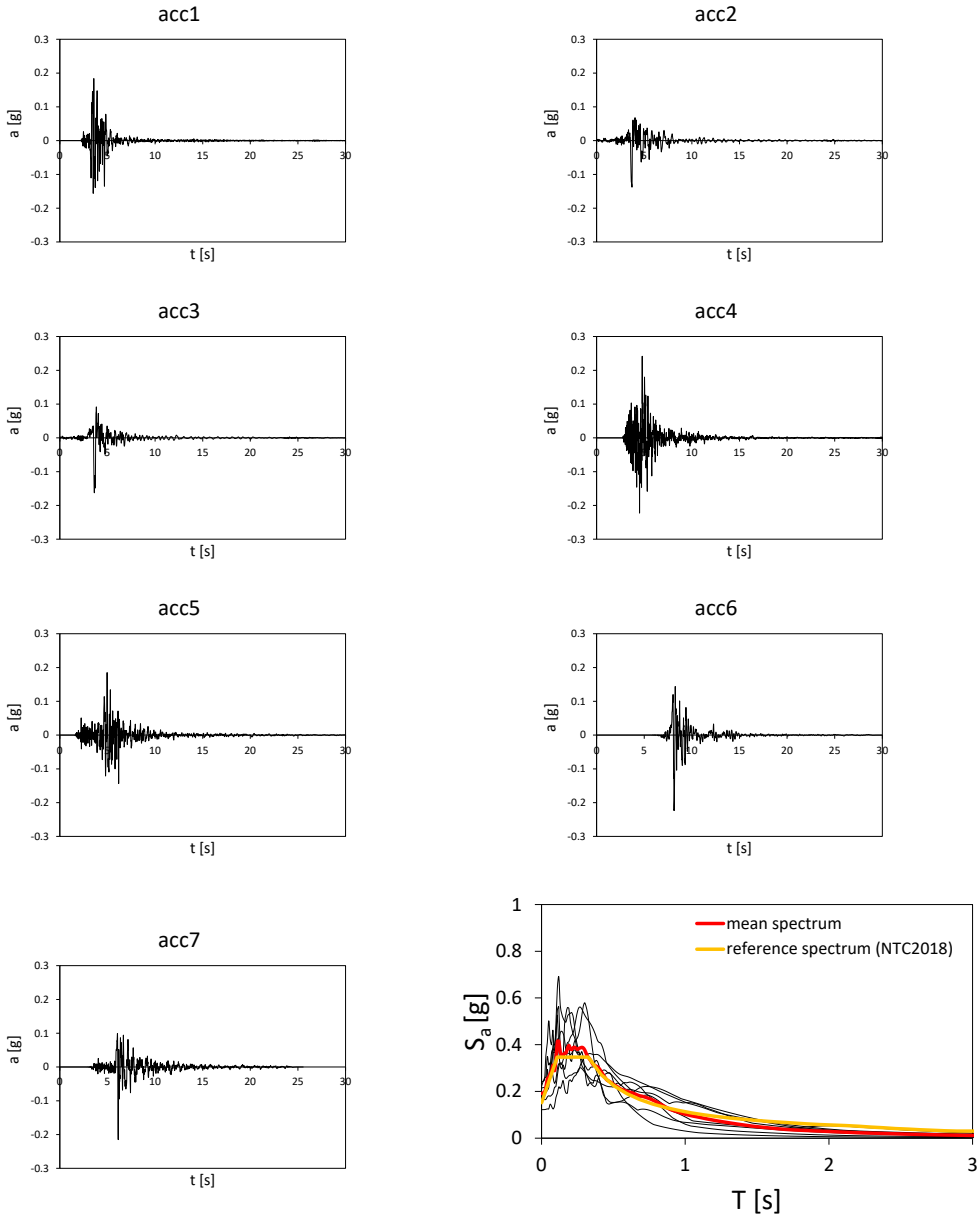


Figure 7-6: Natural accelerogram time histories and response spectra (in black), average spectrum (in red) and reference NTC 2018, 475 year spectrum (in orange).

7.1.3 Simulated accelerograms with EXSIM code

In this study, for simulating high-frequencies of the volcanic earthquakes on Ischia island, the stochastic finite-fault methodology with a dynamic corner frequency concept is used (§4.1.1.2).

One software with a good compromise between simplicity and reliability is *EXSIM* (Motazedian & Atkinson, 2005; Boore, 2009; Atkinson & Assatourians 2015). It is an open-source simulation algorithm, written in FORTRAN, that generates time series of ground motion for earthquakes. The starting point of any simulation is the definition of the fault geometry. Figure 7-7 shows the key parameters that define the orientation of the fault, the strike and dip angles.

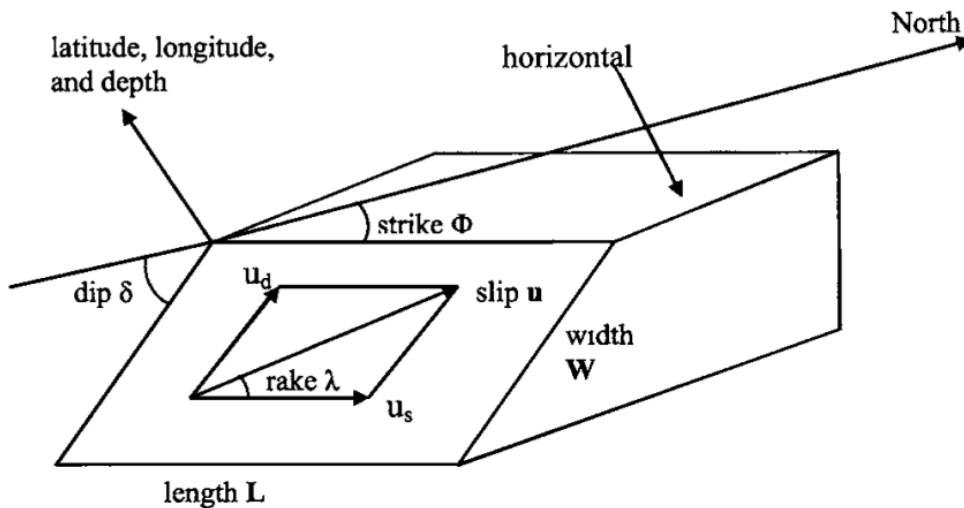


Figure 7-7: Definition sketch of fault plane dimension and geometry.

The strike angle is defined as the bearing of the fault trace (the surface projection of the upper edge of the fault) measured clockwise from North in degrees. The dip angle is defined as the angle that the inclined fault plane forms with a horizontal surface.

A parameter also important is the rake, that defines the relative sense of movement between the two sides of the fault and thus the type of mechanism (normal, reverse or strike-slip).

Regarding the 2017 Ischia earthquake, the source mechanism of the 2017 has been differently interpreted by various authors (De Novellis et al. 2018; Calderoni et al. 2019; Nazeri et al. 2021) (Figure 7-8).

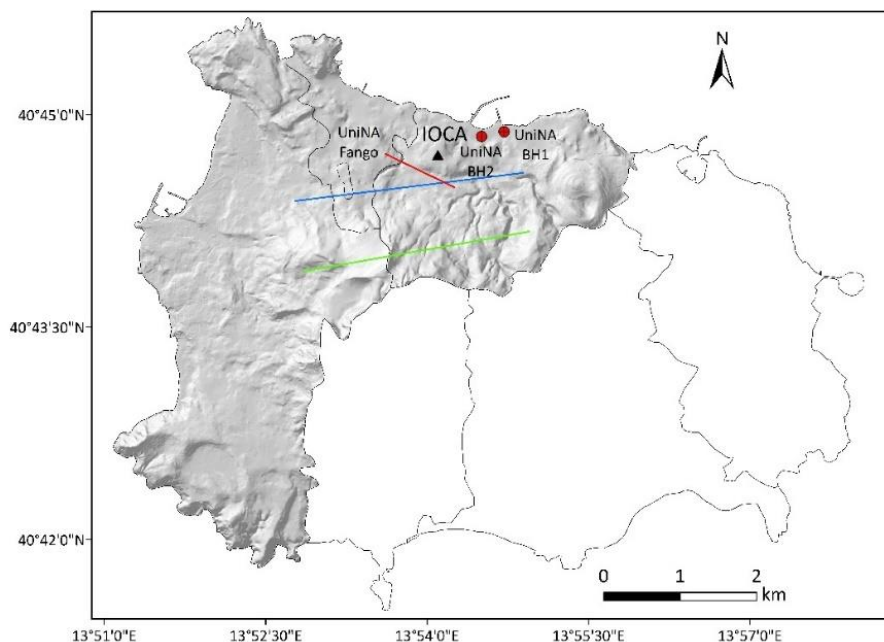


Figure 7-8: Source mechanisms proposed in the literature for the 2017 Ischia earthquake: in blue (De Novellis et al. 2018), in green (Calderoni et al. 2019) and in red (Nazeri et al. 2021). The black triangle indicates the location of the IOCA accelerometer station.

In order to investigate the source geometry and kinematics, De Novellis et al. (2018) exploited seismological, Global Positioning System, Sentinel-1 and COSMO-SkyMed differential interferometric synthetic aperture radar coseismic measurements. Their best-fit solution consists of an E-W striking, south dipping normal fault. Also Calderoni et al. (2019) analyzed seismic, Global Positioning System and interferometric synthetic aperture radar data. The modeled deformation field is consistent with a source model consisting of a WSW-ESE striking, north dipping normal fault. Nazeri et al. (2021) analysis showed that the rupture nucleated at about 600 m west of IOCA, along a 1 km, NW-SE striking fault (i.e., thrust with right-lateral component). Table 7-3 shows the main parameters of source models reported in Figure 7-8.

Table 7-3: Parameters for DN (De Novellis et al. 2018), C (Calderoni et al. 2019) and N (Nazeri et al. 2021) source models.

	DN	C	N
L [m]	3000	3000	1000
w [m]	1800	1458.1	800
strike [°]	83	260	115
dip [°]	67	50	55
rake [°]	-85	-102	145
fault type	N	N	R
M₀ [Nm]	1.8E+15	1.2E+15	2.5E+15
M_w	4.1	4.0	4.2
σ [bar]	1.57	1.60	33.16

M₀ is the seismic moment. The magnitude moment M_w can be assessed through Eq. 4-4. The static stress drop, σ, was assessed through the relationship of Madriaga (1977):

$$\sigma = \frac{8}{3\pi} \cdot \frac{M_0}{w^2 L} \quad \text{Eq. 7-2}$$

In all the EXSIM computations the S-wave velocity profile assumed by Nardone et al. (2020) for the shallower crust model of the Ischia island was considered. Table 7-4 shows the details of the model adopted to calculate the transfer function (Figure 7-9).

Table 7-4: Crustal S-wave velocity model.

Layer	Depth	Thickness	ρ	γ	V _s	D ₀
[-]	[m]	[m]	[kg/m ³]	[kN/m ³]	[m/s]	[%]
1	0	293	2200	21.57	1203	0.5
2	293	654	2400	23.53	1780	
half-space	947	-	2600	25.50	3098	
Mt. Epomeo Green Tuff Citara Tuff/Caldera sediment filing						
Trachytic lava with partial hydrothermal alteration, and old pyroclastic rock (older than 75 Kyr)						
Crystalline rocks/Laccolite						

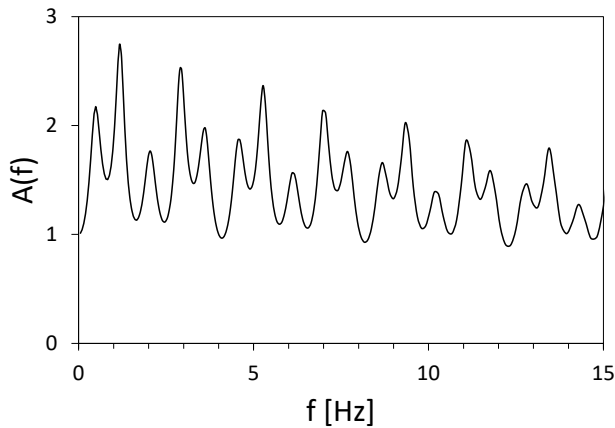


Figure 7-9: Crustal transfer function for EXSIM simulations.

A frequency-dependent anelastic attenuation model $Q(f) = 51f^{0.6}$ (Figure 7-10) was used. Given the relatively short source-to-site distances considered in this study, a $1/R$ geometrical spreading was considered (Figure 7-11). Also a path duration function was required to obtain the time history of ground motion simulations. The function used, proposed by Boore & Thompson (2014), is reported in Figure 7-12.

The fault planes were assumed to be rectangular and were subdivided into an appropriate number of sub-faults, which were modelled as point sources characterised by a ω^2 spectrum. The upper left corner of the fault was used as reference point.

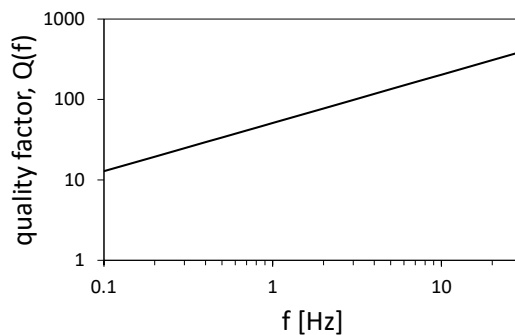


Figure 7-10: Frequency-dependent quality factor function for EXSIM simulations.

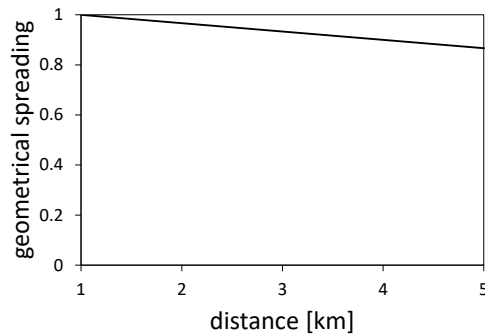


Figure 7-11: Geometrical spreading function for EXSIM simulations.

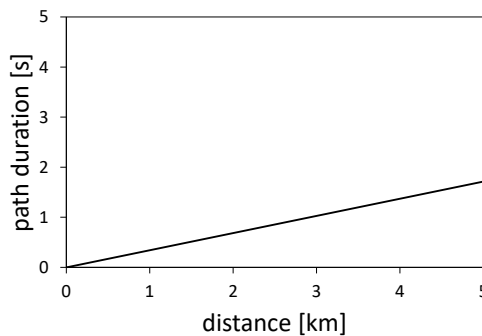
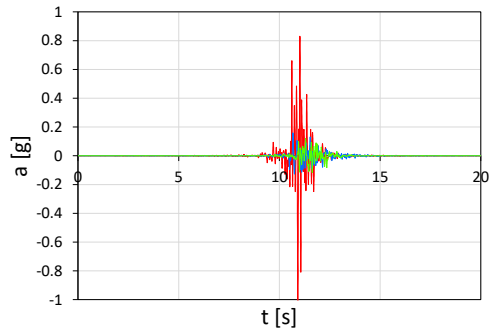


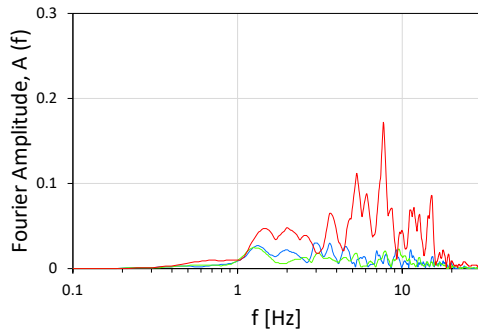
Figure 7-12: Path duration function for EXSIM simulations.

With reference to local effects, surface layers were not taken into account in the modeling in order to obtain the reference motion at the bedrock. Thus the simulated signals will then be used as input for ad hoc site response analyses with one- and two-dimensional software. Figure 7-13, Figure 7-14 and Figure 7-15 show the accelerograms simulated at the three test site Casamicciola BH1 and BH2, Fango west slope) considered in this study with respective response and Fourier spectra.

(a)



(b)



(c)

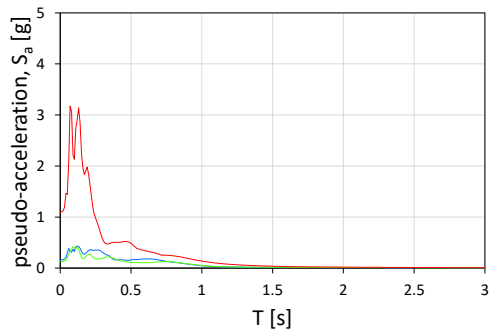
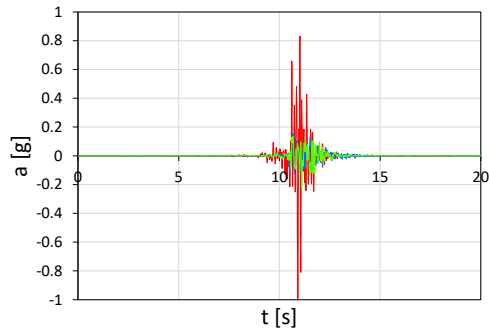
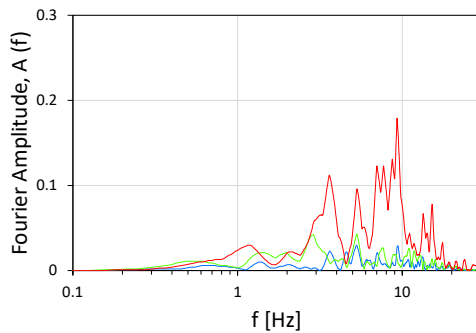


Figure 7-13: Simulated signals at UniNA_BH1 (a) and their Fourier Amplitude (b) and pseudo-acceleration response (c) spectra. The different colours indicate the different source models used: in blue (De Novellis et al. 2018), in green (Calderoni et al. 2019) and in red (Nazeri et al. 2021).

(a)



(b)



(c)

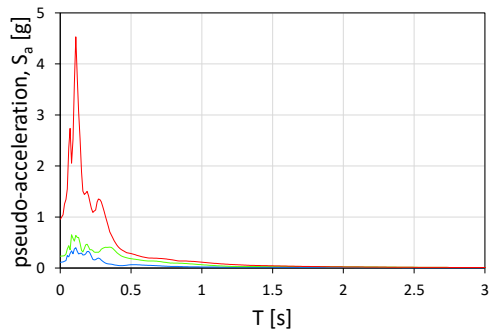
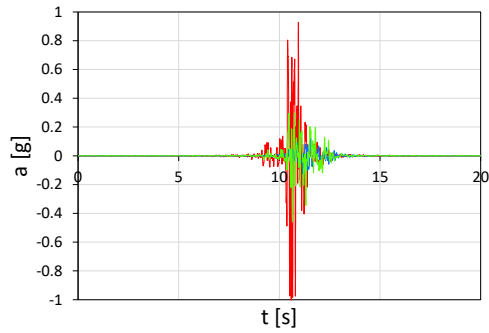
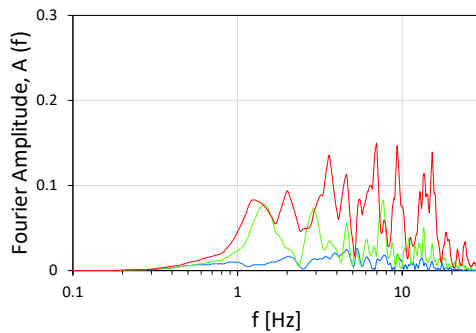


Figure 7-14: Simulated signals at UniNA_BH2 (a) and their Fourier Amplitude (b) and pseudo-acceleration response (c) spectra. The different colours indicate the different source models used: in blue (De Novellis et al. 2018), in green (Calderoni et al. 2019) and in red (Nazeri et al. 2021).

(a)



(b)



(c)

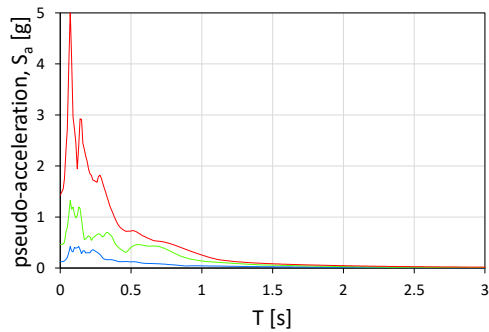


Figure 7-15: Simulated signals at UniNA_Fango (a) and their Fourier Amplitude (b) and pseudo-acceleration response (c) spectra. The different colours indicate the different source models used: in blue (De Novellis et al. 2018), in green (Calderoni et al. 2019) and in red (Nazeri et al. 2021).

Table 7-5, Table 7-6 and Table 7-7 provide a summary of the motion parameters of the accelerograms just shown.

Table 7-5: Synthetic motion parameters for UniNA_BH1 for the different source mechanisms.

source model	R _{JB}	PGA	PGV	PGD	AI	T _m	T _p	D ₅₋₉₅
	[km]	[g]	[cm/s]	[cm]	[m/s]	[s]	[s]	[s]
De Novellis et al. 2018	0.82	0.159	6.005	0.692	0.086	0.268	0.12	1.808
Calderoni et al. 2019	0.57	0.120	5.099	0.736	0.059	0.243	0.12	1.410
Nazeri et al. 2021	0.98	1.088	26.472	1.598	1.730	0.150	0.08	0.880

Table 7-6: Synthetic motion parameters for UniNA_BH2 for the different source mechanisms.

source model	R _{JB}	PGA	PGV	PGD	AI	T _m	T _p	D ₅₋₉₅
	[km]	[g]	[cm/s]	[cm]	[m/s]	[s]	[s]	[s]
De Novellis et al. 2018	0.79	0.112	4.305	0.442	0.057	0.168	0.10	1.940
Calderoni et al. 2019	0.55	0.233	7.582	1.508	0.133	0.236	0.08	1.374
Nazeri et al. 2021	0.76	0.956	25.765	2.013	2.159	0.143	0.12	0.664

Table 7-7: Synthetic motion parameters for UniNA_Fango for the different source mechanisms.

source model	R _{JB}	PGA	PGV	PGD	AI	T _m	T _p	D ₅₋₉₅
	[km]	[g]	[cm/s]	[cm]	[m/s]	[s]	[s]	[s]
De Novellis et al. 2018	0.39	0.123	4.635	0.721	0.063	0.222	0.10	0.100
Calderoni et al. 2019	0.24	0.460	14.197	2.002	0.522	0.263	0.14	0.140
Nazeri et al. 2021	0.31	1.426	42.046	3.582	3.312	0.170	0.08	0.818

It can be observed that different source mechanisms lead to different results. This is due to the different ways of inverting the only available data, which is the recording at the IOCA accelerometer station. Specifically, with regard to the simulations carried out for the Casamicciola Terme study area, the use of the De Novellis and Calderoni source models lead to *PGA* values that do not exceed 0.2g, with significant durations, D_{5-95} , of less than 2 seconds. On the other hand, Nazeri's source model provides *PGA* values of around 1g with durations of less than one second. In the same way, in the simulations performed in the 'Fango' study area, more conservative results are obtained using the model proposed by Nazeri. The differences can be explained both by the different source mechanisms and the fact that Nazeri et al. (2021) did refined modeling of high-frequency signals up to 3 Hz, while De Novellis and Calderoni modeling of this event mainly concerned a lower frequency band (0.1–2Hz). In any case, the dynamic analyses reported in the following have been carried out with all three models proposed in the literature in order to assess the influence of the uncertainties relevant to source mechanism and crustal propagation.

7.2 Liquefaction susceptibility assessment

7.2.1 Screening criteria

As already explained at §4.2.1, the national code (NTC 2018) provides criteria for the exclusion of liquefaction analyses, which are applied on a territorial scale in the study area. In particular, by cross-referencing the information from the geo-lithological map (Figure 7-16a) and the map representing the depths of the water table from ground level (Figure 7-16b) it was possible to perimeter potentially liquefiable areas, i.e. those characterised by surface covers of granular soils and water table depths less than 15m (Figure 7-17).

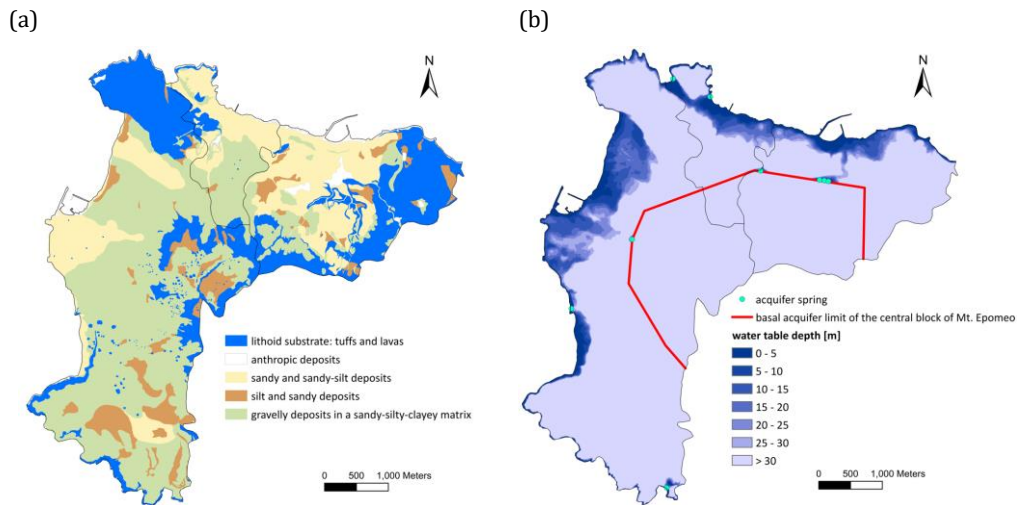


Figure 7-16: Geolithological map of the N-W sector of the island of Ischia (modified from Toscano et al. 2019) and (b) aquifer depth map (in m) of the same area (modified from Piscopo et al. 2019).

The susceptible areas correspond to the coastal areas of the three analysed municipalities (Figure 7-17).

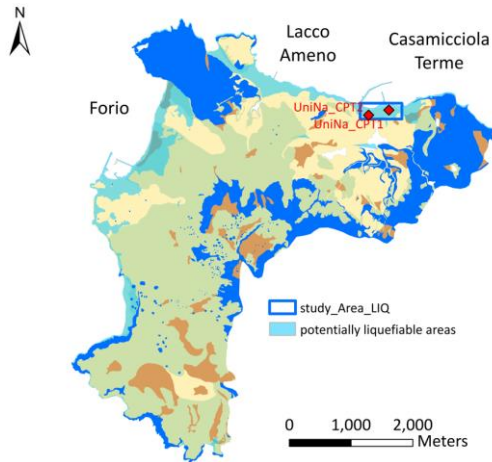


Figure 7-17: Screening criteria applied on a territorial scale: in light blue the potentially liquefiable areas. The same map shows the location of the CPT tests carried out within the UniNA-MASLIDE project.

Further confirmation of the liquefiability of these soils in the Casamicciola Terme coastal zone can be obtained from the CPT test results, shown in Figure 5-14: indeed from values of the normalised tip and sleeve friction resistances, it is possible to assess the 'Soil Behaviour Type Index' I_c according to Eq. 4-16. The results in graphical form are shown for CPT1 and CPT2 in Figure 7-18 and Figure 7-19, respectively.

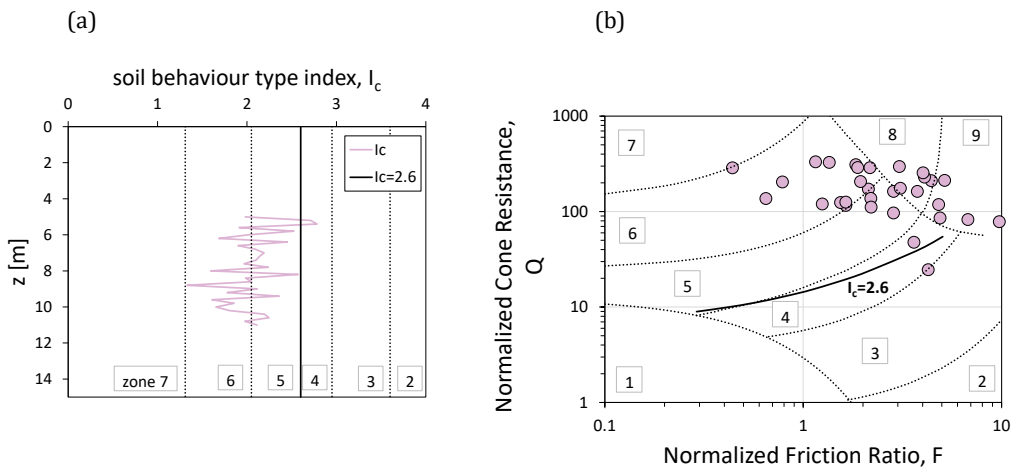


Figure 7-18: CPT1 results: 'Soil Behaviour Type Index' trend with depth (a) and Robertson's abacus (b).

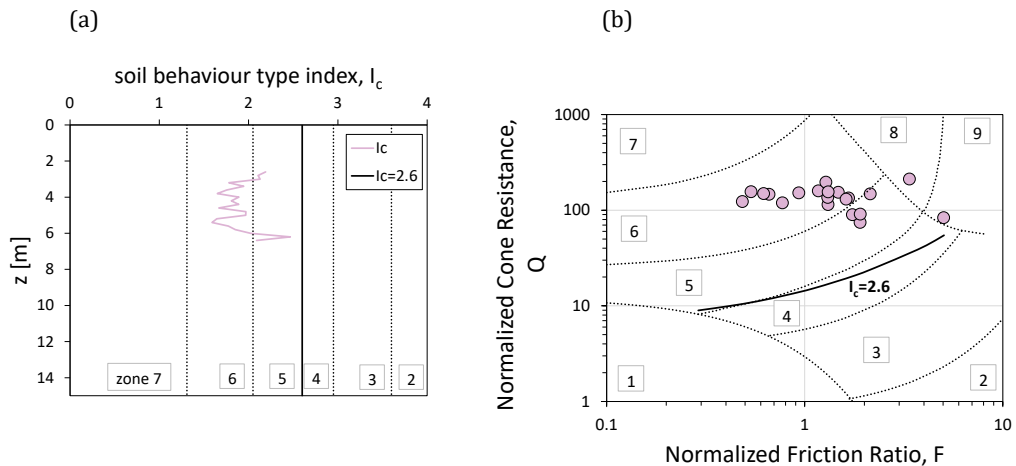


Figure 7-19: CPT2 results: ‘Soil Behaviour Type Index’ trend with depth (a) and Robertson’s abacus (b).

As already seen in Figure 5-29, the grain-size curves of the material, defined as SM_{pi} , fall within the ranges of potentially liquefiable soils proposed by the national code (NTC 2018).

The Robertson classification criterion shown in Figure 4-7 confirms what aforesaid, i.e. that the soil consists of sands (clean sand to silty sand) and sand mixtures (silty sand to sandy silt). The calculated index almost always has a value of less than 2.6 and therefore the involved soils are potentially liquefiable.

7.2.2 Semi-empirical methods

The liquefaction analyses according to the semi-empirical methods, already discussed at §4.2.1, are reported below. The analyses were carried out according to the procedure proposed by Boulanger & Idriss (2014) using the results of SPT tests performed in the BH1 and BH2 boreholes as well as the results of CPT tests adjacent to the same boreholes. The analyses from shear wave measurements according to the procedure proposed by Andrus & Stokoe (2000) are not reported because in all cases

the value of the normalised S-wave velocity, V_{S1} , is greater than the limit upper value, V_{Sc1} .

In these approaches, the analyses are conducted by comparing the capacity (CRR) versus demand (CSR). The former is assessed from the results of penetrometric tests while the latter is expressed as a function of the maximum shear stress at the depth at which the assessment is being performed. The latter was evaluated both from the maximum surface acceleration according to the national code (NTC 2018) approach and by performing seismic response analyses in total stresses considering as input motion both the code-compatible and simulated accelerograms reported in the previous section.

The results are shown in the following figures, where CSR as determined in accordance with the different methods, is plotted against the corrected and normalized parameters $(N_1)_{60cs}$ and q_{c1Ncs} . The limit curves of CRR are plotted on the same charts, in order to separate the data points relevant to liquefaction (above) and non-liquefaction conditions (below). The comparison between CSR and CRR is also reported in terms of z-depth profiles.

In BH1, it can be noticed that the assessment based both on $(N_1)_{60cs}$ and q_{c1Ncs} is almost always satisfied. On the other hand, in BH2, liquefaction occurs for the lowest value of $(N_1)_{60cs}$ and q_{c1Ncs} .

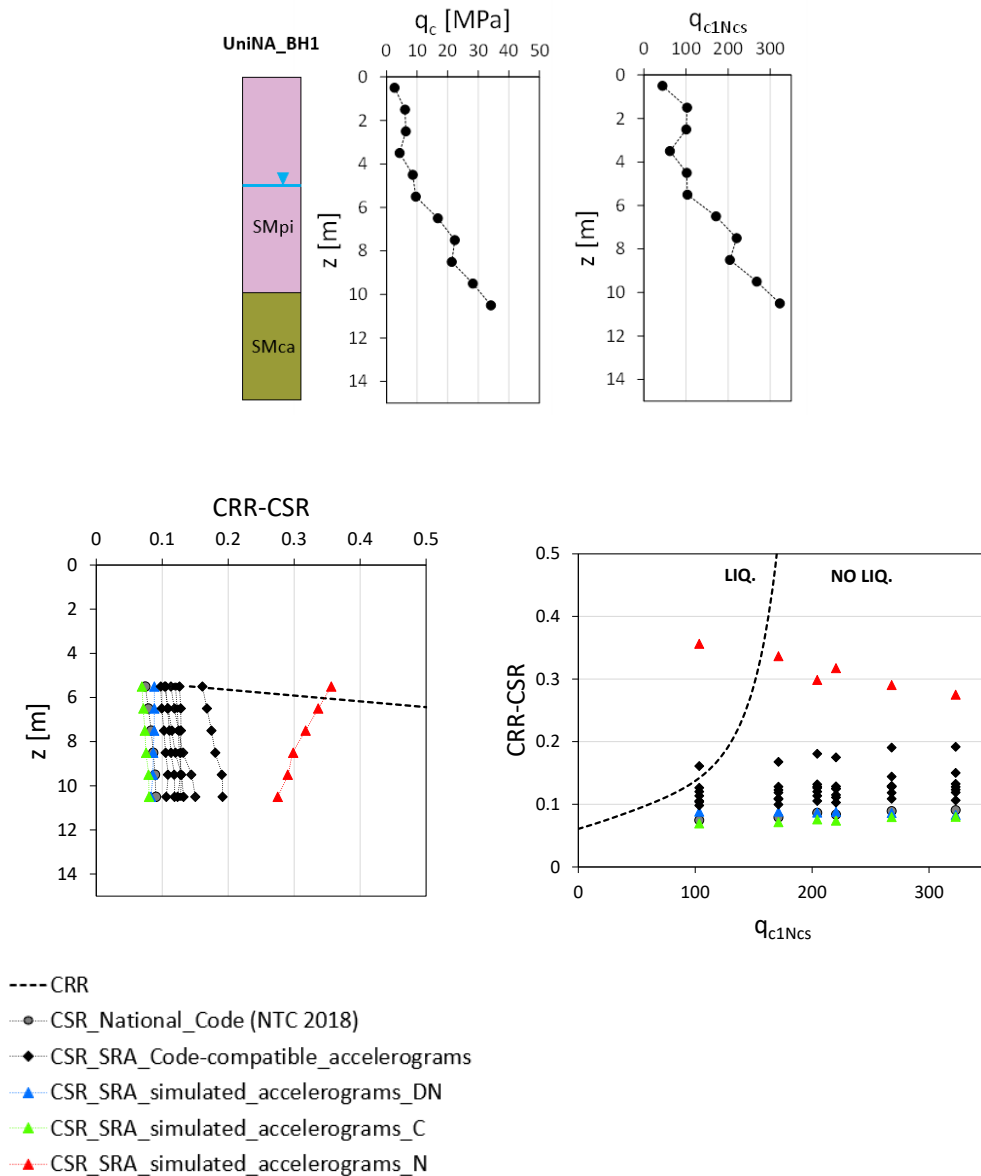


Figure 7-20: Simplified liquefaction analyses for borehole BH1 from CPT test results: tip resistance q_c and respective corrected and normalised value q_{c1Ncs} with depth (above) and comparison between CSR and CRR (bottom).

*in the case of non-plastic fine content, as in the present case, $q_{c1N} = q_{c1Ncs}$

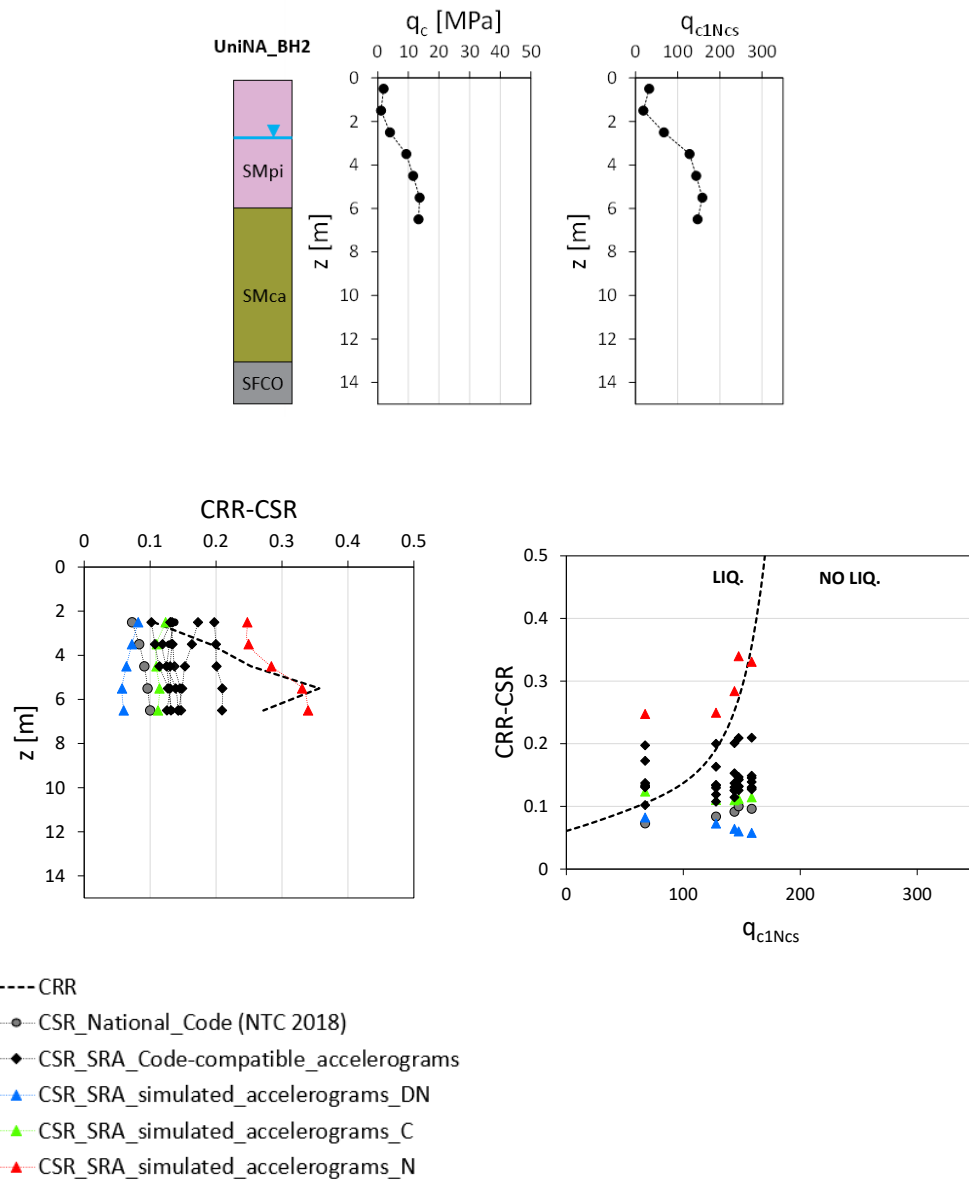


Figure 7-21: Simplified liquefaction analyses for borehole BH2 from CPT test results: tip resistance q_c and respective corrected and normalised value q_{c1Ncs} with depth (above) and comparison between CSR and CRR (bottom).

*in the case of non-plastic fine content, as in the present case, $q_{c1N} = q_{c1Ncs}$

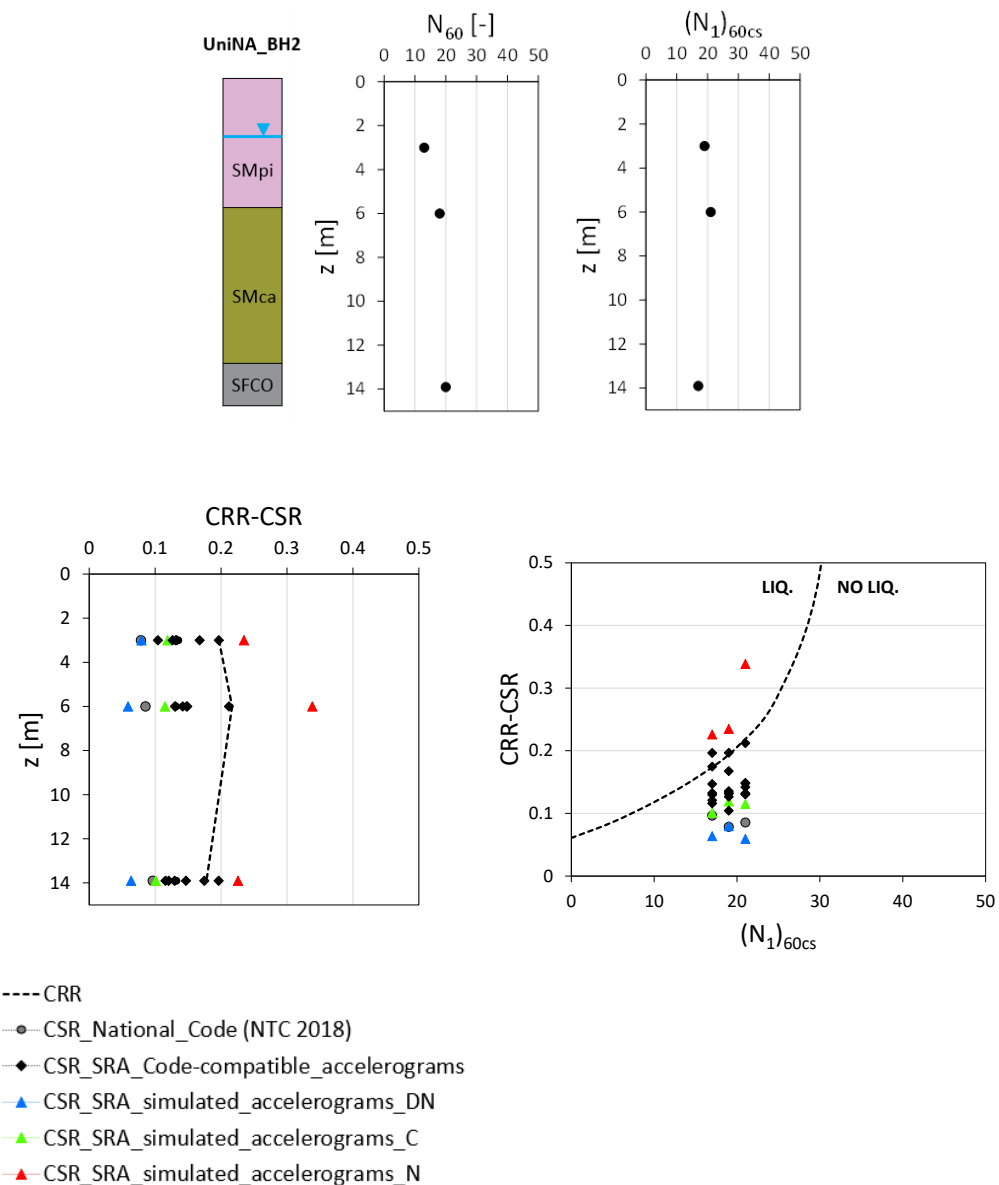


Figure 7-23: Simplified liquefaction analyses for borehole BH2 from SPT test results: blows count N_{60} and respective corrected and normalised value $(N_1)_{60cs}$ with depth (above) and comparison between CSR and CRR (below).

*in the case of non-plastic fine content, as in the present case, $(N_1)_{60}=(N_1)_{60cs}$

Once calculated the safety factor FS as the ratio between CRR and CSR, it is possible to evaluate the Liquefaction Potential Index, LPI (Iwasaki et al. 1978), according to Eq. 4-41. Liquefaction Severity Number, LSN (Tonkin & Taylor, 2013), was also evaluated according to Eq. 4-43. The post-liquefaction volumetric strain, ε_v in this simplified procedure, was evaluated using a relationship proposed by Zhang et al. (2002), through a relationship with the equivalent clean sand normalized CPT tip resistance for different factors of safety (see Figure 4-15). The values of both LPI and LSN as a function of reference acceleration (a_r), Arias intensity (AI) and significant duration (D_{5-95}) for BH1 (Figure 7-24) and BH2 (Figure 7-25) are reported below.

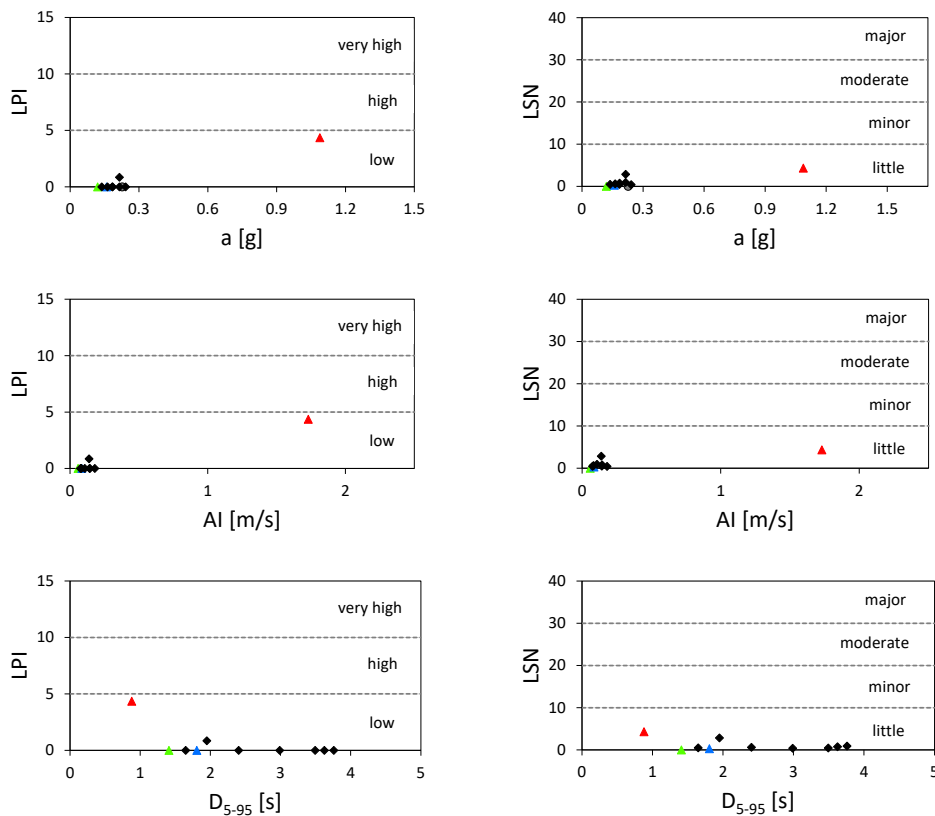


Figure 7-24: Results of simplified liquefaction analyses for borehole BH1: LPI (on the left) and LSN (on the right) as a function of synthetic input motion parameters. The different colours indicate the different source models used: in blue (De Novellis et al. 2018), in green (Calderoni et al. 2019) and in red (Nazeri et al. 2021). In black code-compatible accelerograms.

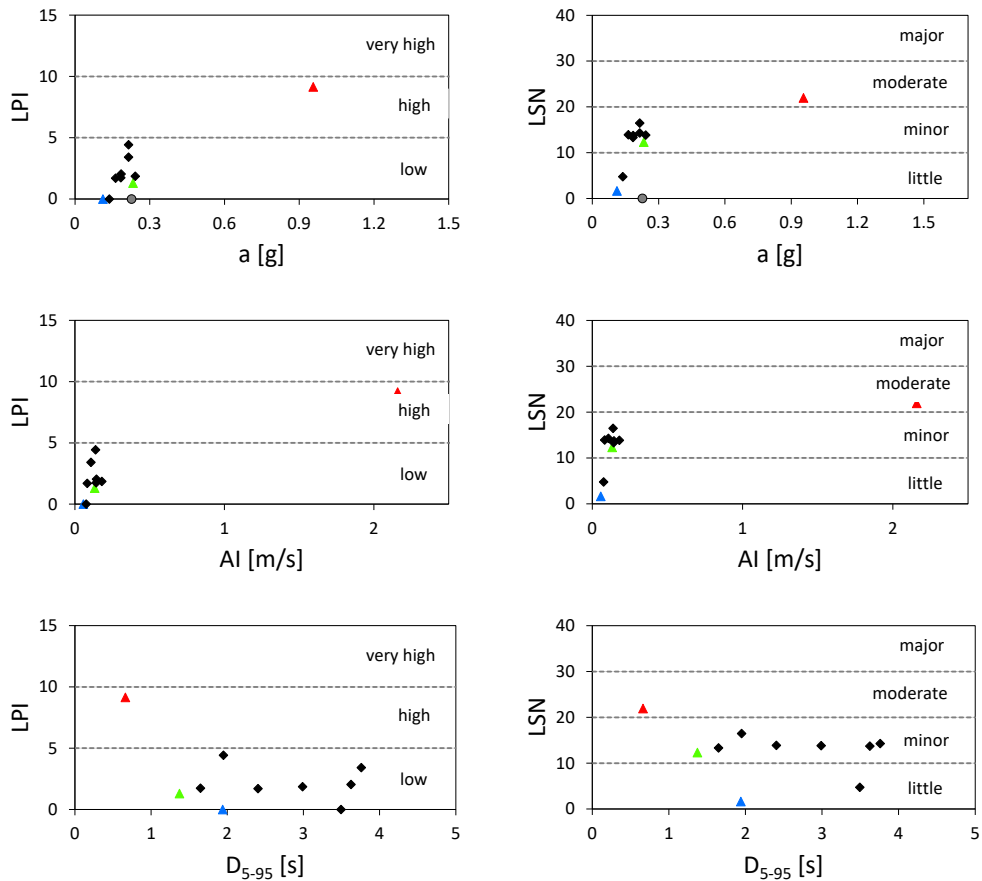


Figure 7-25: Results of simplified liquefaction analyses for borehole BH2: LPI (on the left) and LSN (on the right) as a function of synthetic input motion parameters. The different colours indicate the different source models used: in blue (De Novellis et al. 2018), in green (Calderoni et al. 2019) and in red (Nazeri et al. 2021). In black code-compatible accelerograms.

Following the classifications reported in Table 4-4 and Table 4-5, it is possible to make an evaluation of liquefaction-induced damage.

For BH1 the liquefaction risk is very low in any case. The same is also true for BH2 except in one case where high degree of risk is expected according to LPI and moderate damage according to LSN.

7.2.3 Simplified dynamic analyses

The results of the simplified dynamic analysis, obtained using an equivalent linear approach with the STRATA code (Kottke & Rathje, 2023), were used again to assess liquefaction potential by comparing CSR, as obtained from the accelerogram propagated at the depths of interest ($z=7.5\text{m}$ and $z=12.5\text{m}$ for BH1, $z=4.5\text{m}$ and $z=9.5\text{m}$ for BH2), with the cyclic resistance ratio, CRR, as inferred from the cyclic resistance curve measured by laboratory tests (§5.1.8). Since the maximum resistance of soil was experimentally obtained by applying regular stress histories, in order to compare CSR with CRR it was necessary to convert the irregular earthquake load into an equivalent cyclic stress history with an amplitude $\tau_{eq}=0.65\tau_{max}$. Such a conversion was done by means of relationships provided by literature that correlate the number of equivalent cycles, N_{eq} , to synthetic parameters representing the earthquake records. The correlation used is that proposed by Biondi et al. (2012), reported in Eq. 7-3:

$$\ln N_{eq} = \alpha + \beta \cdot \ln a_{max} + \gamma \cdot \ln AI + \delta \cdot \ln \nu_0 + \varepsilon \cdot \ln D_{5-95} \quad \text{Eq. 7-3}$$

where:

- a_{max} is the maximum acceleration;
- AI is Arias intensity;
- D_{5-95} is the significant duration evaluated in the range $5\% < AI < 95\%$;
- ν_0 is the frequency of zero crossings.

All the above parameters must be meant as referred to the signals propagated at the depths of $z=7.5\text{m}$ and $z=12.5\text{m}$ for BH1, $z=4.5\text{m}$ and $z=9.5\text{m}$ for BH2.

Biondi et al. 2012 proposed four different models (2V - 3V1 - 3V2 - 4V) according to the number of parameters considered in the correlations; the relevant coefficients are listed in Table 7-8. In this case, the 3-variable model 3V1 was used.

The equivalent cyclic stress ratios, from site response analyses, are reported in Figure 7-26 against the equivalent number, N_{eq} , evaluated for each earthquake by means of the previous correlations. The same charts, for comparison, show the liquefaction curve obtained by interpolating with the model suggested by Chiaradonna

et al. (2018) the laboratory data points representing the attainment of liquefaction in terms of the stress-based criterion ($r_u=0.9$).

Table 7-8: Coefficients for N_{eq} correlation (Biondi et al. 2012).

model	parameters	α	β	γ	δ	ϵ
2V	a_{max} - AI	-0.095	-1.760	0.839	-	-
3V1	a_{max} - AI - D_{5-95}	0.440	-2.148	0.995	-	-0.393
3V2	a_{max} - AI - v_0	-2.255	-2.212	1.114	0.868	-
4V	a_{max} - AI - v_0 - D_{5-95}	-1.814	-2.426	1.194	0.829	-0.241

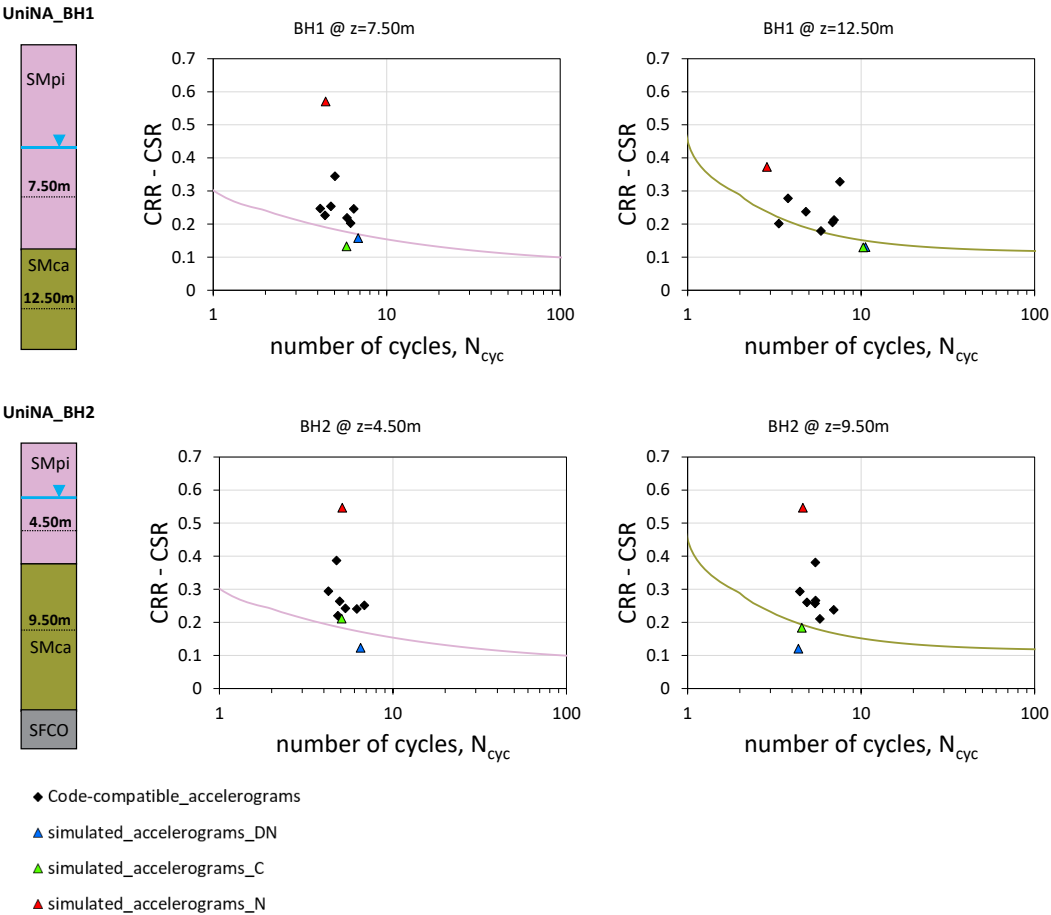


Figure 7-26: Results of the assessment based on the comparison with cyclic resistance curve for BH1 (above) and BH2 (below). DN, C, and N refer respectively to the De Novellis et al. (2018), Calderoni et al. (2019) and Nazeri et al. (2021) source models.

Liquefaction conditions should correspond to the data points lying above the cyclic resistance curve; as shown in Figure 7-26, almost all of the CSR- N_{eq} combination computed for code-compatible accelerograms provide values above the maximum resistance expressed by the cyclic curve. As far as simulated accelerograms are concerned, the analysis is always satisfied unless the one simulated with the model of Nazeri et al. (2021).

7.2.4 Advanced dynamic analyses with SCOSSA-PWP code

One-dimensional seismic response analyses in effective stress in both verticals BH1 and BH2 were carried out with the SCOSSA-PWP code (Tropeano et al. 2019). This latter is a computer code for one-dimensional seismic response analysis that models the soil profile as a system of consistent lumped masses connected by viscous dampers and springs. The non-linearity curves assigned to the different materials are shown in Figure 6-5. From the experimental data, it is possible to define the non-linear hysteretic response of the soil layers using the modified MKZ (Matasovic & Vucetic, 1995) along with extended Masing rules (Phillips & Hashash, 2009). The backbone curve for a monotonic loading path is given by:

$$F_{bb} = \frac{\delta_G G_0 \gamma}{1 + \beta \left(\frac{\gamma}{\gamma_r} \frac{\delta_G}{\delta_\tau} \right)^{s'}} \quad \text{Eq. 7-4}$$

where γ is the shear strain level, G_0 is the initial shear modulus, γ_r is the reference shear strain, β and s' are dimensionless factors and δ_τ and δ_G are degradation index functions. The modulus degradation index function, δ_G , is defined as:

$$\delta_G = \sqrt{1 - r_u} \quad \text{Eq. 7-5}$$

while the corresponding stress degradation index function, δ_τ , is given by:

$$\delta_\tau = 1 - r_u^\mu \quad \text{Eq. 7-6}$$

where μ is an exponential constant that expresses the sensitivity of the backbone curve to pore water pressure changes.

For expressing the stress-strain relationship in unloading-reloading conditions the formulation of Phillips & Hashash (2009) has been generalised by Moreno-Torres (2010) to introduce the degradation indexes:

$$F_{ur}(\gamma) = F^*(\gamma_m) \left[\frac{G_0 \delta_G (\gamma - \gamma_c)}{1 + \beta \left(\frac{\delta_G}{\delta_\tau} \right)^{s'} \left(\frac{\gamma - \gamma_c}{2\gamma_r} \right)^{s'}} - \frac{G_0 \delta_G (\gamma - \gamma_c)}{1 + \beta \left(\frac{\delta_G}{\delta_\tau} \right)^{s'} \left(\frac{\gamma_m}{\gamma_r} \right)^{s'}} \right] + \frac{G_0 \delta_G (\gamma - \gamma_c)}{1 + \beta \left(\frac{\delta_G}{\delta_\tau} \right)^{s'} \left(\frac{\gamma_m}{\gamma_r} \right)^{s'}} + \tau_c \quad \text{Eq. 7-7}$$

where γ_c and τ_c are the reversal shear strain and shear stress, respectively, γ_m is the maximum shear strain attained during the time history, and $F^*(\gamma_m)$ is a damping reduction factor, defined as follows:

$$F^*(\gamma_m) = \frac{D_{\text{exp}}(\gamma)}{D_{\text{Mas}}(\gamma)} = p_1 - p_2 \left[1 - \frac{G(\gamma_m)}{G_0} \right]^{p_3} \quad \text{Eq. 7-8}$$

where p_1 , p_2 and p_3 are non-dimensional parameters obtained from the best-fit of the ratio between the strain-dependent hysteretic damping measured in laboratory tests D_{exp} , and that calculated using the conventional Masing rules, D_{Mas} ; $G(\gamma_m)$ is the secant modulus corresponding to the maximum shear strain γ_m .

Table 7-9 shows the parameters obtained through non-linear multi-regression of the experimental data points. The corresponding curves are shown in Figure 7-27.

Table 7-9: MKZ and Phillips & Hashash (2009) model parameters.

	MKZ			P&H (2009)			
	γ_r [%]	β	s'	D_0	p_1	p_2	p_3
SM	0.09538	1.00204	0.99971	1.0	0.67965	0.16092	2.66804
SFCO	0.20410	1.02416	1.10392	2.2	0.69942	0.08717	0.12563
SFGRS	5.02419	1.02792	0.53522	0.5	2.13443	2.82522	3.08364

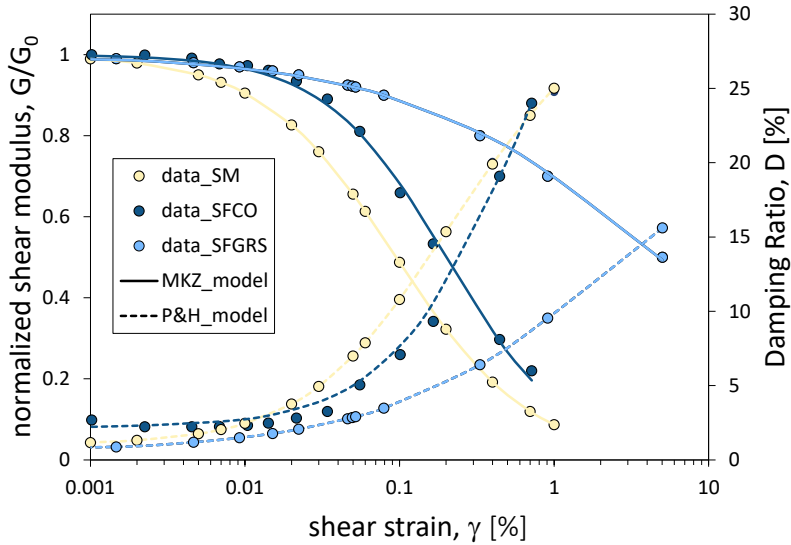


Figure 7-27: Non-linearity curves of SM (light yellow), SFCO (dark blue) and SFGRS (light blue).

The pore pressure build-up is computed with the simplified model (PWP) by adopting a damage parameter, κ , which permits avoiding the use of empirical criteria to convert the irregular shear loading into an equivalent number of cycles (Chiaradonna et al. 2018). The model is based on simple relationships and allows a calibration of the parameters based on the results of cyclic laboratory tests. From these latter, the number of cycles at liquefaction, N_L , is related to the cyclic resistance ratio, CRR, as follows:

$$\frac{(CRR - CSR_t)}{(CSR_r - CSR_t)} = \left(\frac{N_r}{N_L} \right)^\alpha \quad \text{Eq. 7-9}$$

where (N_r, CSR_r) is a reference point, CSR_t is the asymptotic value of CRR as the number of cycles tends to infinity and α is the slope of the regression line obtained from reporting the experimental data on a log-log scale. The parameters CSR_t and α are used to compute the damage parameter, κ , for any loading pattern (see Chiaradonna et al. (2018) and Tropeano et al. (2019) for details).

The pore pressure model is defined by a relationship between the normalized number of cycles, N/N_L , and the pore pressure ratio, r_u , through the following function:

$$r_u = a \left(\frac{N}{N_L} \right)^b + c \left(\frac{N}{N_L} \right)^d \quad \text{Eq. 7-10}$$

where a , b and d are curve-fitting parameters. c depends on a according to the relationship:

$$c = r_{u,\max} - a \quad \text{Eq. 7-11}$$

Figure 7-28 and Figure 7-29 show the experimental results of CSS tests (see Figure 5-49 and Figure 5-50) interpreted with the model discussed here. The model parameters are shown in Table 7-10 and Table 7-11, respectively.

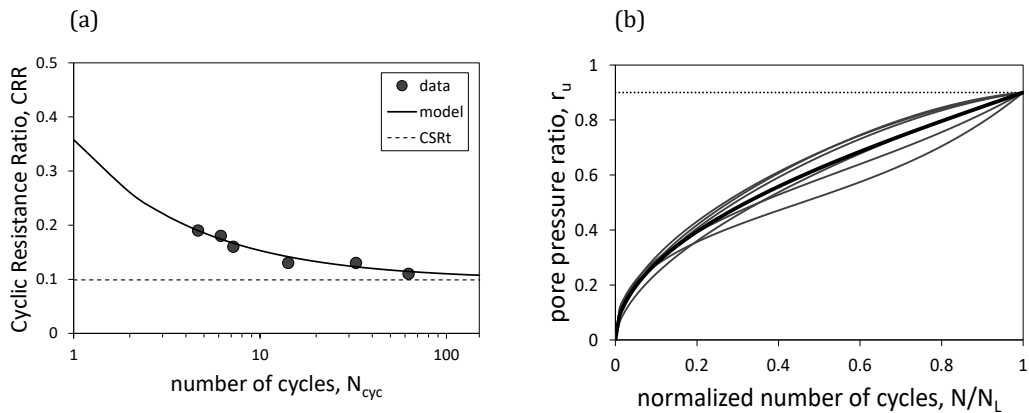


Figure 7-28: Experimental and modelled liquefaction strength of BH2-U.S.1 expressed as cyclic stress ratio vs number of cycles (a) and excess pore pressure ratio relationship (b).

Table 7-10: BH2-U.S.1: Parameters of pore water pressure (PWP) model.

CSR _t	α	CSR _r	N _r	a	b	c	d
0.10	1.47	0.14	15	0.882	0.500	0.018	4

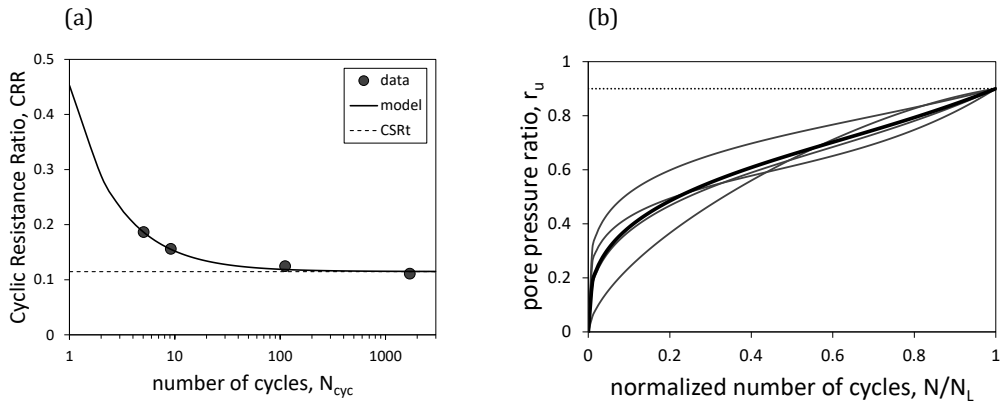


Figure 7-29: Experimental and modelled liquefaction strength of BH2-U.S.3 expressed as cyclic stress ratio vs number of cycles (a) and excess pore pressure ratio relationship (b).

Table 7-11: BH2-U.S.3: Parameters of pore water pressure (PWP) model.

CSR_t	α	CSR_r	N_r	a	b	c	d
0.11	1.04	0.14	15	0.815	0.323	0.085	4

Figure 7-30 shows a summary of the geotechnical model for BH1 and BH2 with all the necessary input data to perform seismic response analyses in effective stresses with SCOSSA-PWP.

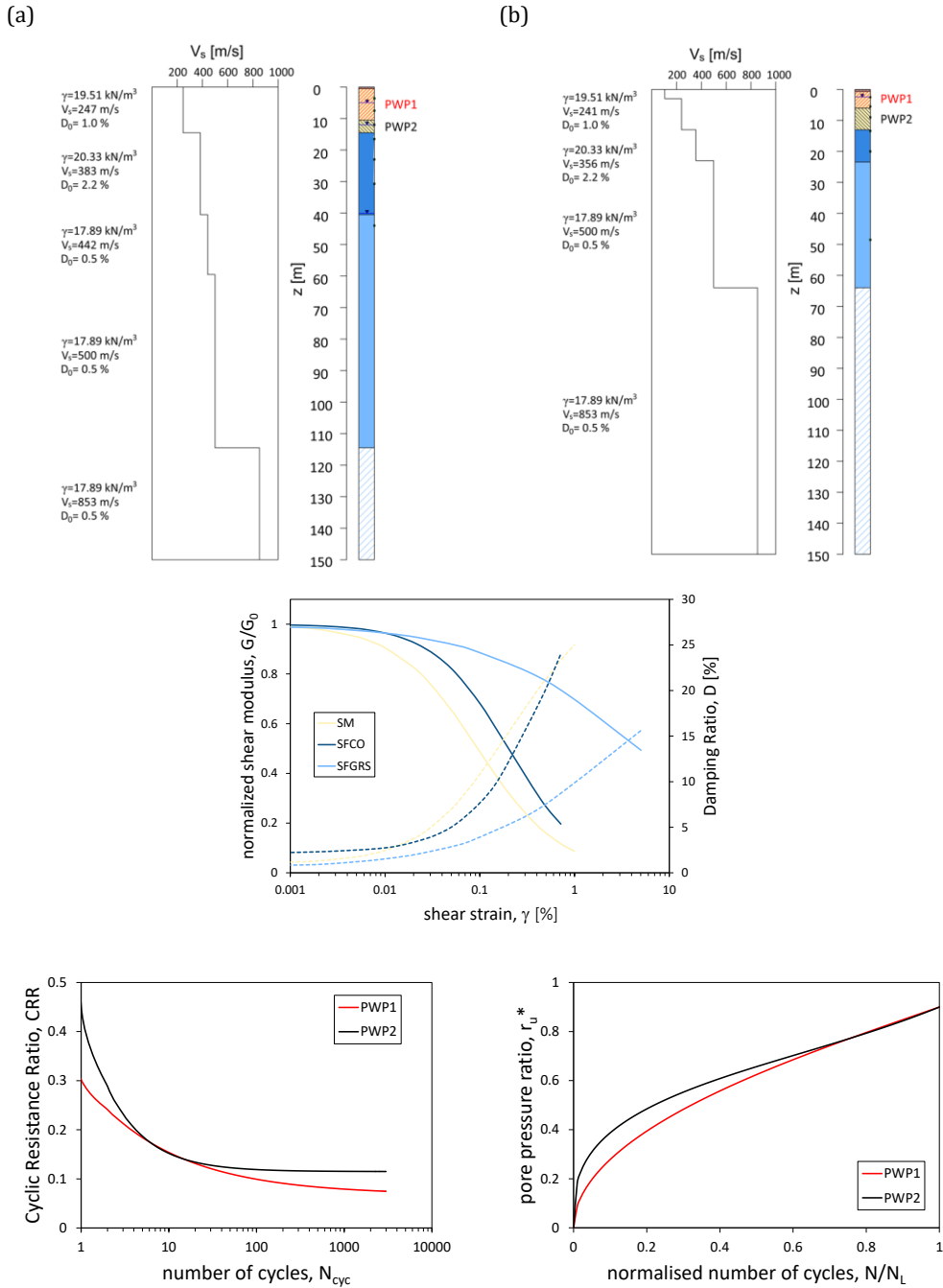


Figure 7-30: Geotechnical model for BH1 (a) and BH2 (b).

The analyses were carried out for the two verticals under examination (BH1 and BH2) by considering as input both the seven code-compatible accelerograms and the simulated ones, discussed in §7.1. In addition, analyses were carried out in both undrained and drained conditions. For the latter, hydraulic conductivity k and oedometric modulus E_{oed} values have been added to the conventional input parameters. It is worth remembering that the code assumes a dissipation of pore pressures through Terzagli's one-dimensional consolidation theory, see Tropeano et al. 2019 for details. Table 7-12 and Table 7-13 report the input parameters for the analyses for boreholes BH1 and BH2, respectively.

Table 7-12: Input parameters for dynamic analyses with SCOSSA-PWP for borehole BH1.

	H	γ	V_s	D_0	k	E_{oed}
	[m]	[kN/m ³]	[m/s]	[%]	[m/s]	[kPa]
SM1	10	19.51	247	1.0	3.2E-06	7169
SM2	5	17.81	247	1.0	1.5E-05	11627
SFCO	26	20.33	383	2.2	1.1E-10	7500
SFGRS1	19	17.89	442	0.5	8.0E-06	15000
SFGRS2	55	17.89	500	0.5	8.0E-06	15000
SFGRS3	335	17.89	853	0.5	8.0E-06	15000
half-space	-	17.89	2027	0.5	-	-

*boldface indicates directly measured quantities

Table 7-13: Input parameters for dynamic analyses with SCOSSA-PWP for borehole BH2.

	H	γ	V_s	D_0	k	E_{oed}
	[m]	[kN/m ³]	[m/s]	[%]	[m/s]	[kPa]
SM1	3	15.16	106	1.0	3.2E-06	4690
SM1	3	19.51	241	1.0	3.2E-06	6063
SM2	7	17.81	241	1.0	1.5E-05	8692
SFCO	10	20.33	356	2.2	1.1E-10	7500
SFGRS1	41	17.89	500	0.5	8.0E-06	15000
SFGRS2	386	17.89	853	0.5	8.0E-06	15000
half-space	-	17.89	2027	0.5	-	-

*boldface indicates directly measured quantities

The results of the undrained and drained analyses are plotted in terms of vertical profiles of maximum acceleration, maximum shear stress and r_u . The maximum

acceleration profiles show the highest value is reached in all the cases between 10 and 15 m. Furthermore, the profiles of the peak value of r_u show that the excess pore pressure accumulation reaches the conventional limit value of 0.9 in the same depth range.

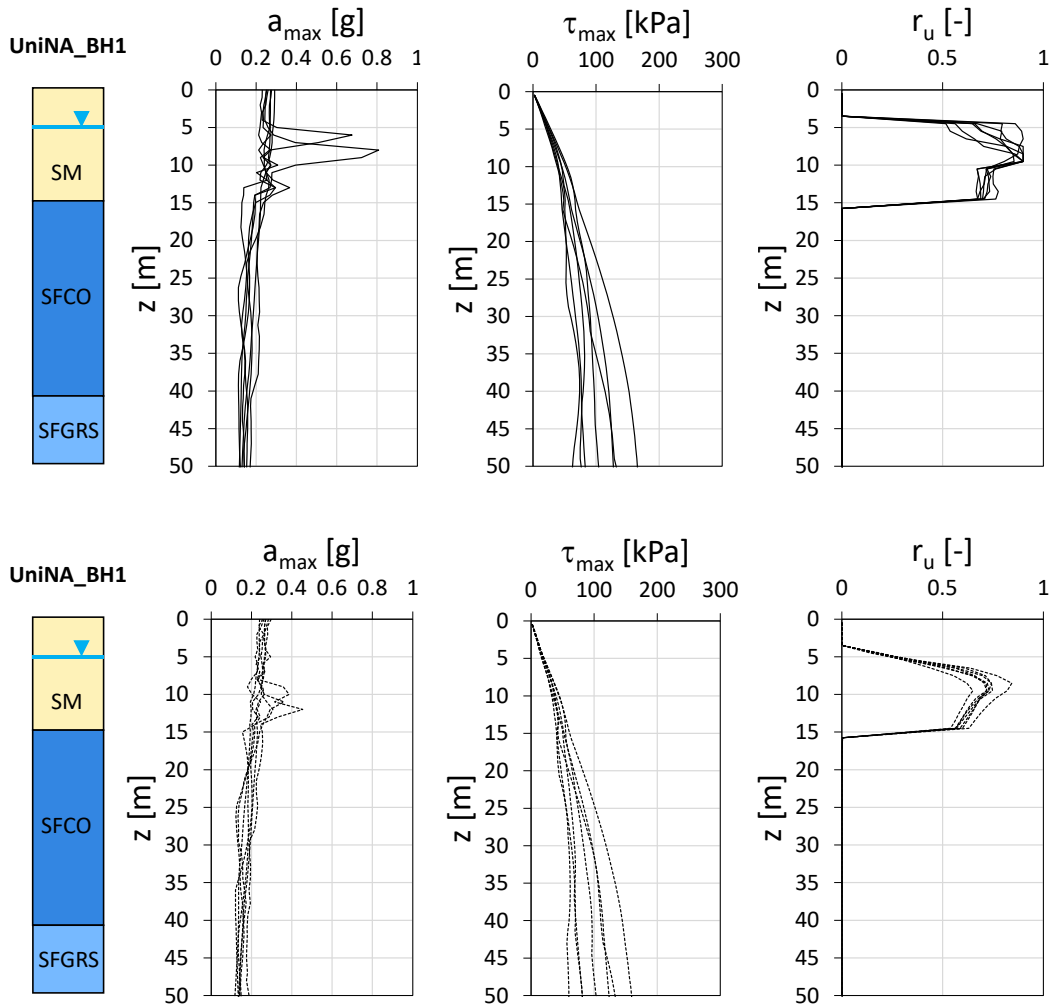


Figure 7-31: Seismic response analyses in effective stresses with the SCOSSA-PWP code for borehole BH1 using code-compatible accelerograms: profiles of a_{\max} , τ_{\max} and r_u with depth in undrained (above) and drained (bottom) conditions.

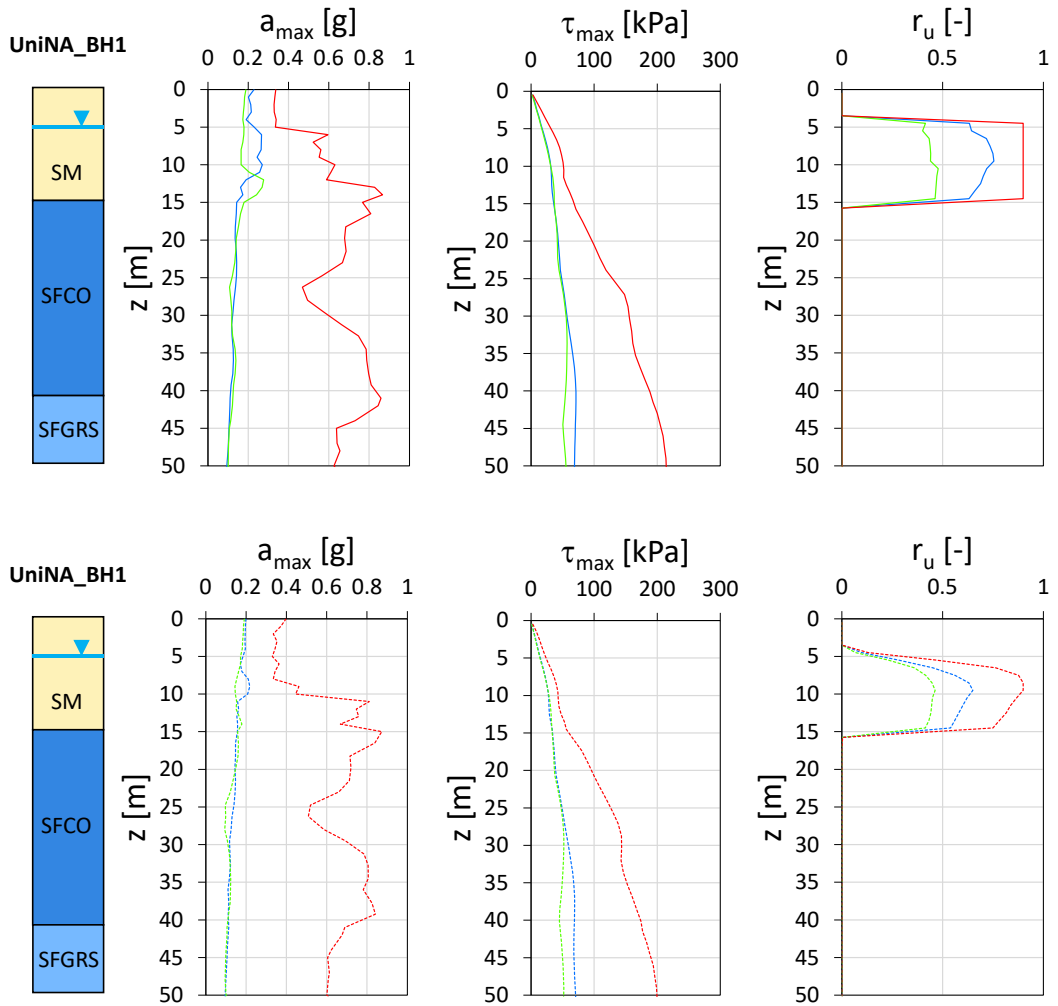


Figure 7-32: Seismic response analyses in effective stresses with the SCOSSA-PWP code for borehole BH1 using simulated accelerograms (blue, green and red are respectively associated with the De Novellis, Calderoni and Nazeri source models): profiles of a_{\max} , τ_{\max} and r_u with depth in undrained (above) and drained (bottom) conditions.

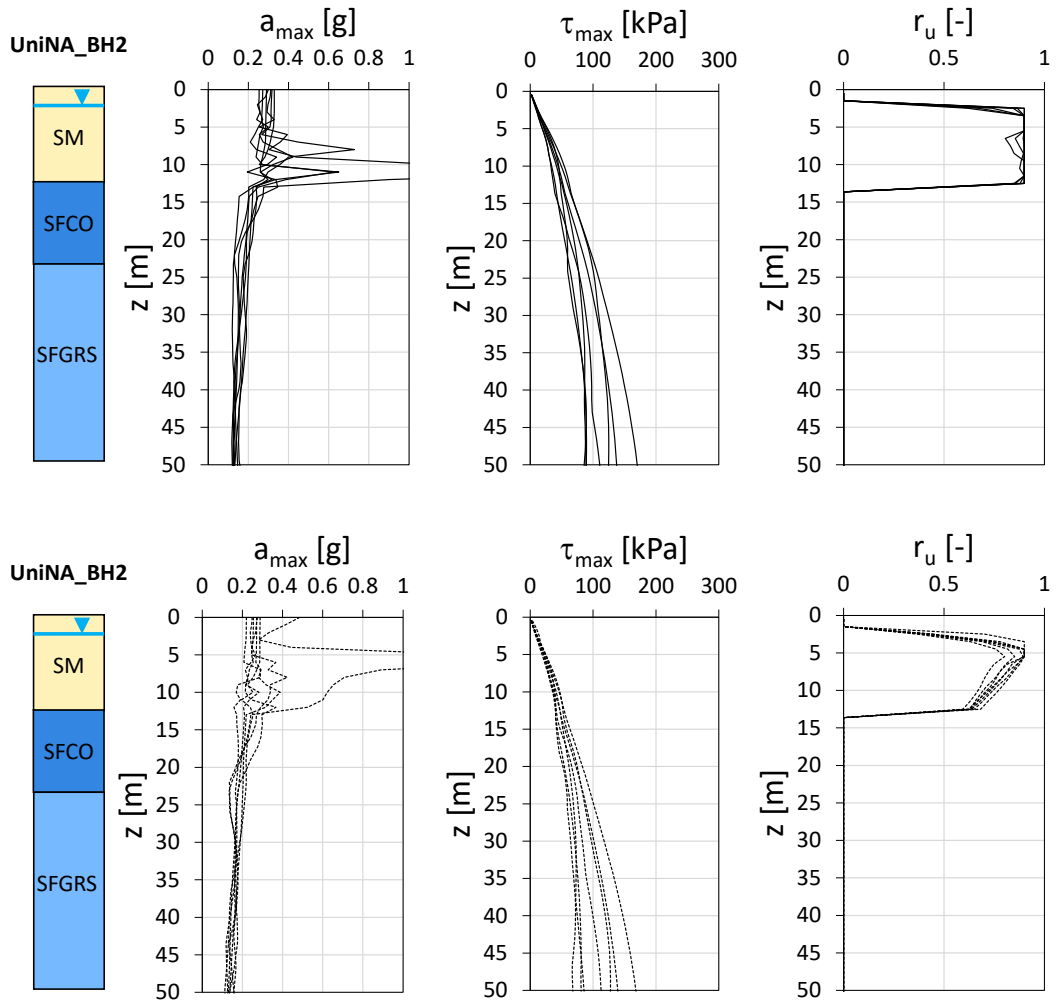


Figure 7-33: Seismic response analyses in effective stresses with the SCOSSA-PWP code for borehole BH2 using code-compatible accelerograms: profiles of a_{\max} , τ_{\max} and r_u with depth in undrained (above) and drained (bottom) conditions.

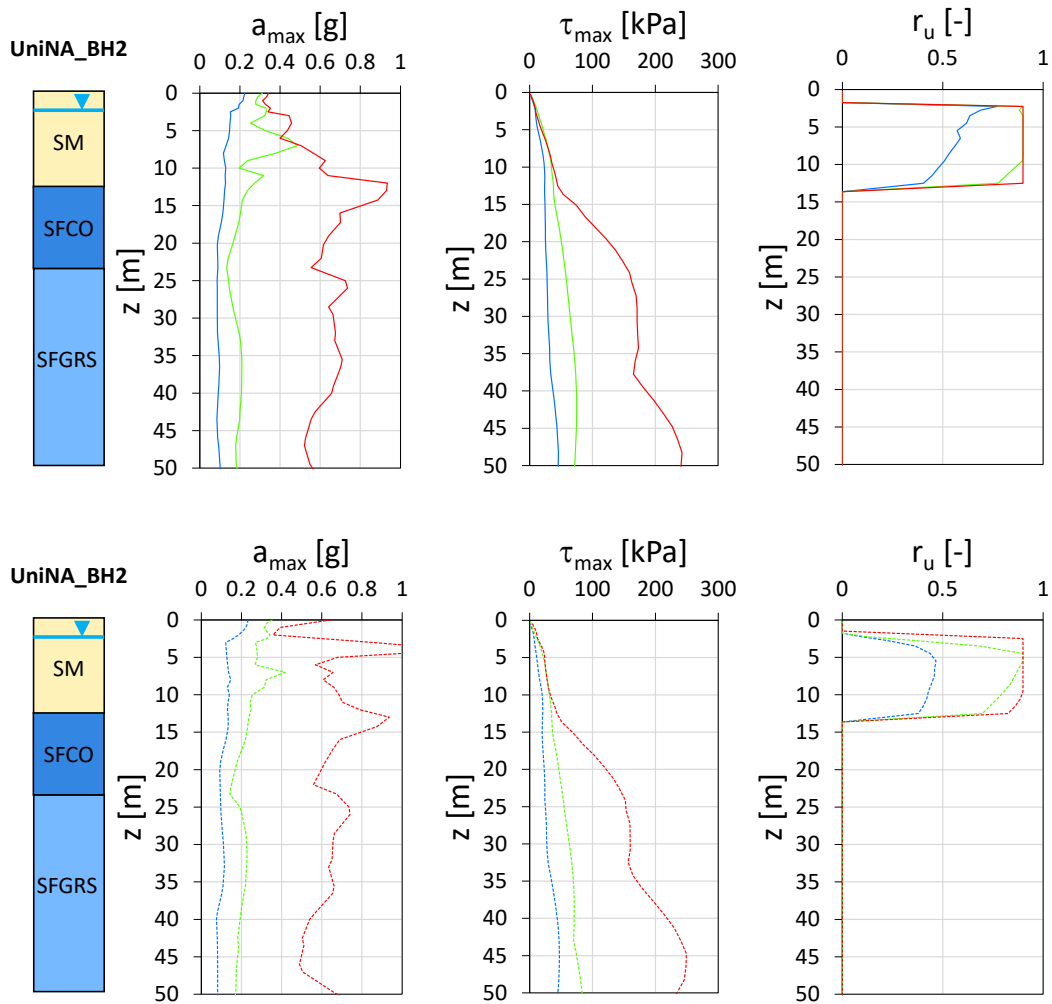


Figure 7-34: Seismic response analyses in effective stresses with the SCOSSA-PWP code for borehole BH1 using simulated accelerograms (blue, green and red are respectively associated with the De Novellis, Calderoni and Nazeri source models): profiles of a_{\max} , τ_{\max} and r_u with depth in undrained (above) and drained (bottom) conditions.

The results of the coupled analyses in terms of excess pore water pressure ratio (r_u) allow a straightforward evaluation ε_v from the oedometric compression curve (Figure 4-16), and thus a more rigorous assessment of the Liquefaction Severity Number, LSN (Tonkin & Taylor, 2013). From r_u values it is also possible to assess the 'Induced

Damage Parameter' (Chiaradonna et al. 2020), related to the free-field post-seismic volumetric consolidation settlement, according to Eq. 4-45.

The values of both LSN and I_{AM} as a function of reference acceleration (a_r), Arias intensity (AI) and significant duration (D_{5-95}) for BH1 (Figure 7-35) and BH2 (Figure 7-36) are reported below.

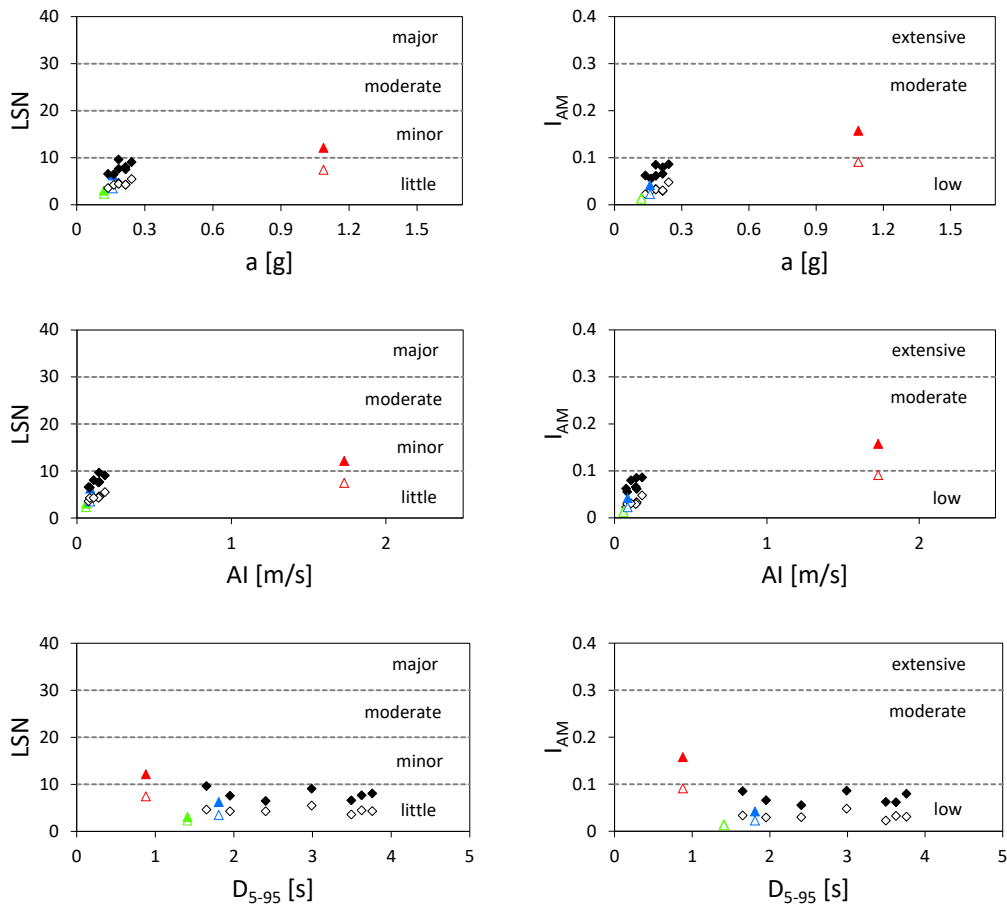


Figure 7-35: Results of advanced liquefaction analyses for borehole BH1: LSN (on the left) and I_{AM} (on the right) as a function of synthetic input motion parameters. The symbols full and empty refer to undrained and drained analyses respectively. The different colours indicate the different source models used: in blue (De Novellis et al. 2018), in green (Calderoni et al. 2019) and in red (Nazeri et al. 2021). In black code-compatible accelerograms.

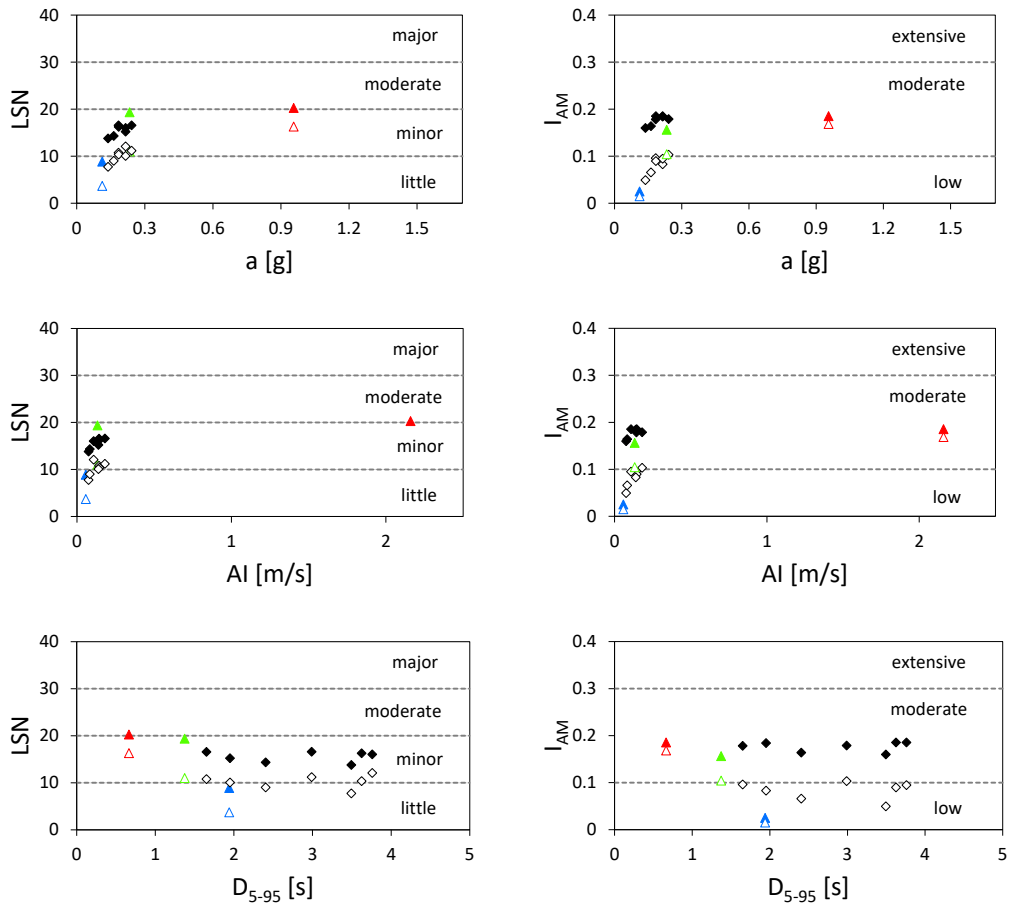


Figure 7-36: Results of advanced liquefaction analyses for borehole BH2: LSN (on the left) and I_{AM} (on the right) as a function of synthetic input motion parameters. The symbols full and empty refer to undrained and drained analyses respectively. The different colours indicate the different source models used: in blue (De Novellis et al. 2018), in green (Calderoni et al. 2019) and in red (Nazeri et al. 2021). In black code-compatible accelerograms.

Following the classifications reported in Table 4-4 and Table 4-6, it is possible to make an evaluation liquefaction-induced damage.

Although the results of advanced analyses show more severe results, the LSN and I_{AM} values lead to a classification of damage between low and moderate.

7.3 Slope stability assessment

7.3.1 Seismic performance at territorial scale

At a territorial scale, Level II methods proposed for seismic slope stability assessment can be implemented by combining seismological, topographic, geological and geotechnical data through *GIS* (Geographical Information System). The different approaches usually define the seismic hazard by synthetic ground motion parameters, refer to the infinite slope model for the stability analysis and adopt empirical relationships to predict earthquake-induced displacements. An outline of the procedure adopted in this study, already introduced in §4.2.2, is shown in Figure 7-37 and Figure 7-38. It followed the Newmark (1965) approach, which is particularly suitable for modeling category II instability mechanisms (slumps and slides), because the unstable soil volume is considered as a rigid-plastic block that experiences no internal deformation until the onset of the sliding. The triggering occurs when the acceleration overpasses the ‘critical acceleration’ threshold, a_c , which can be calculated by combining Eq. 4-46 and Eq. 4-47.

In this study, the slope angle and curvature were calculated from a Digital Terrain Model (DTM), with square cells 5×5 m wide. The physical and mechanical parameters were attributed to the lithological complexes, identified in Figure 7-16a, from the synthesis of a dataset (Table 7-14) derived from the collection of 24 laboratory tests (20 direct shear and 4 triaxial tests) available from 12 previous borehole investigations collected in the area (see Figure 5-1 and Figure 5-2).

Unit weight volume (γ), effective cohesion (c') and friction angle (φ') were statistically processed: the resulting maps are shown in Figure 7-40. The depth of sliding surface (D) was defined by assuming an average thickness of 3 m: this depth refer to the shallow layers already involved by the earthquake-induced landslides in the past.

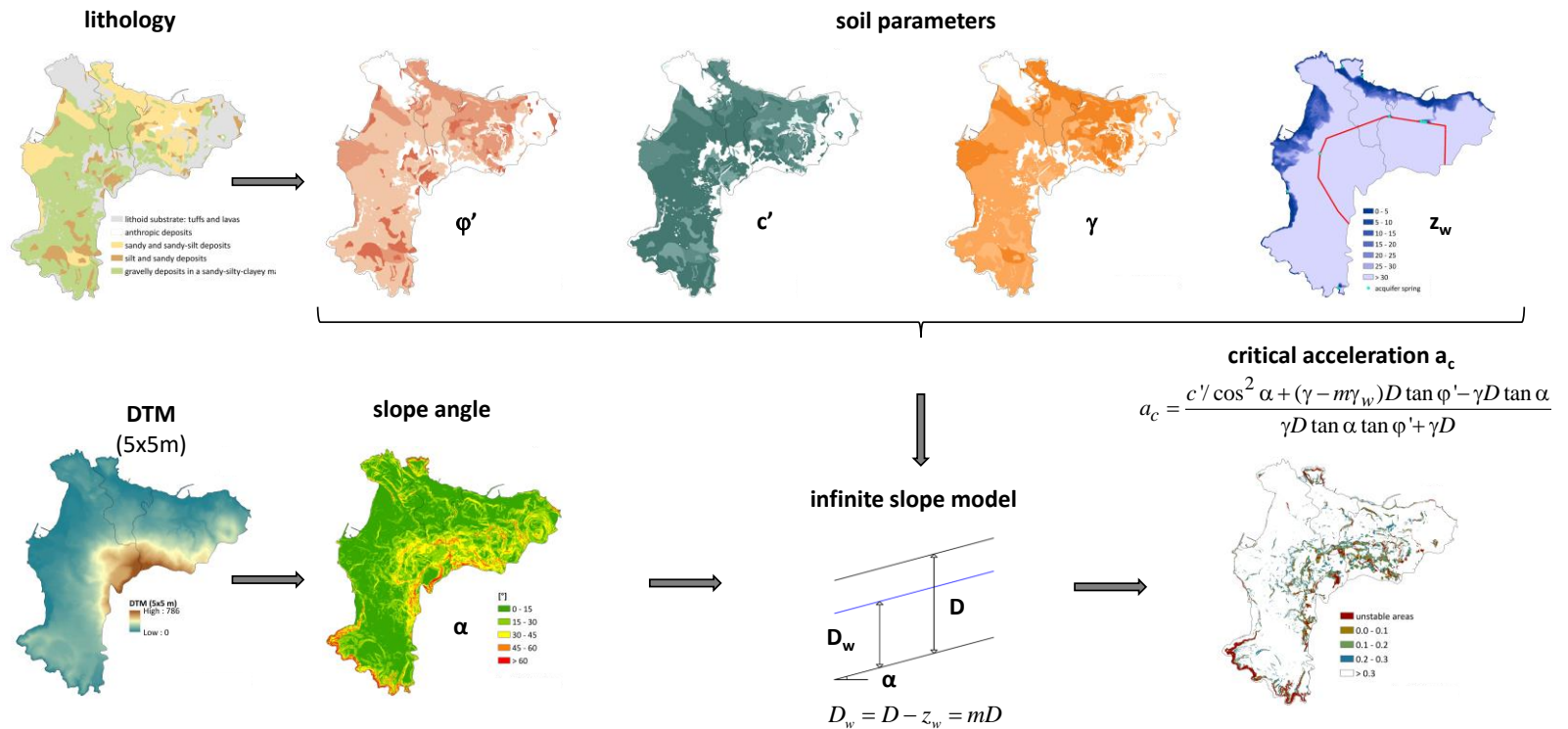


Figure 7-37: Flowchart of the procedure followed at territorial scale showing the relevant maps (1).

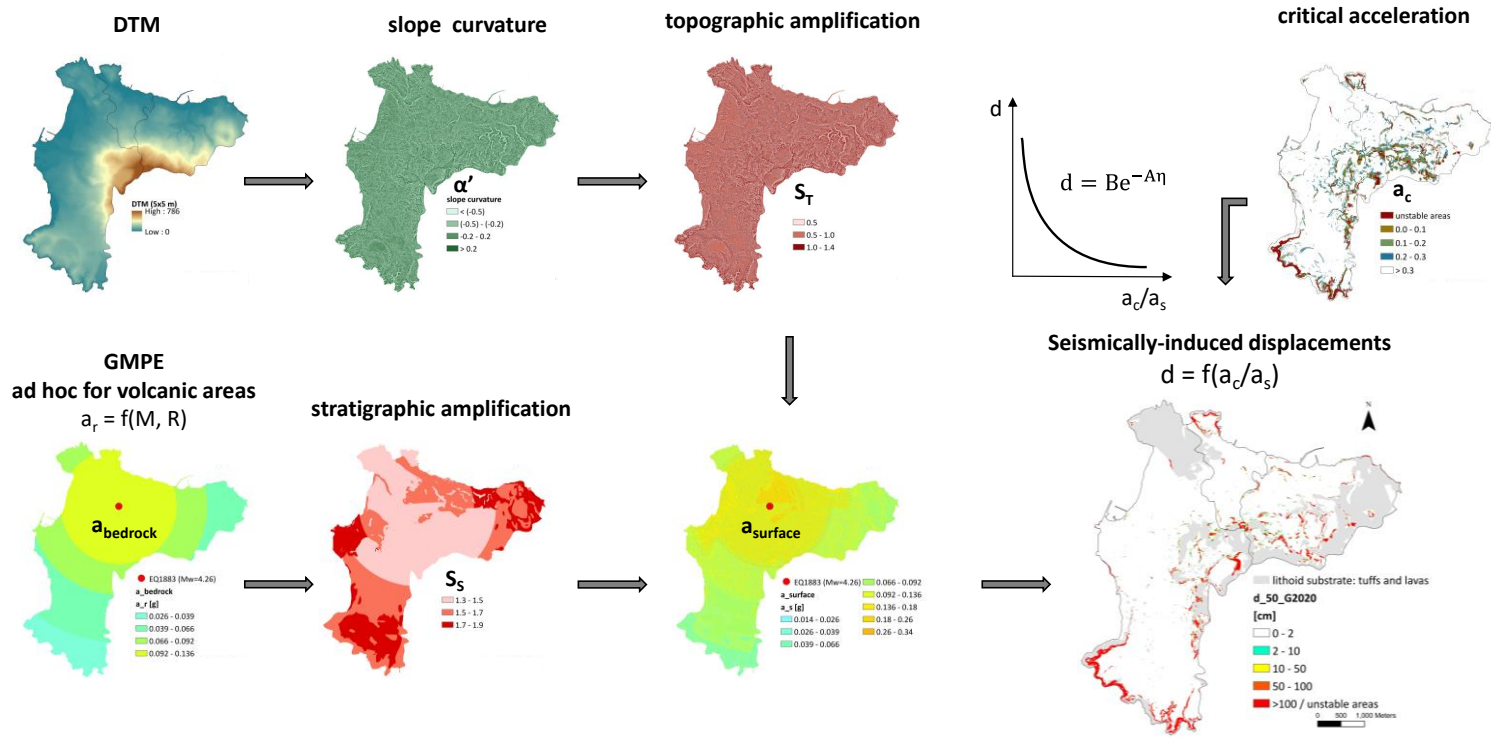
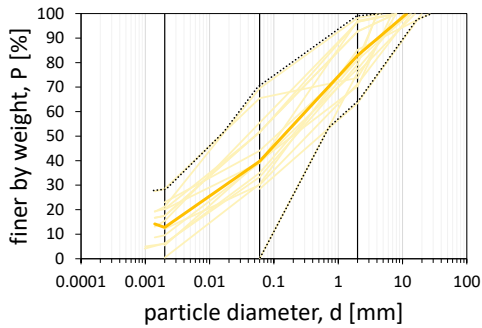


Figure 7-38: Flowchart of the procedure followed at territorial scale showing the relevant maps (2).

Table 7-14: Unit weight and strength parameters.

X	\bar{X}	s_x	CoV [%]	p^{16}	p^{50}	p^{84}	X=sample \bar{X} =sample mean s_x =standard deviation CoV=coefficient of variation p^{16} =16 th percentile p^{50} =50 th percentile p^{84} =84 th percentile	
γ	15.7	2.3	0.1	13.1	16.0	17.6		
c'	13.2	16.0	1.2	0.0	8.4	19.9		
φ'	32.3	5.3	0.2	27.7	31.3	35.6		
γ	14.9	7.7	0.5	14.4	15.1	15.3		
c'	10.3	12.5	1.2	0.0	7.2	19.3		
φ'	32.4	4.4	0.1	29.1	31.6	37.5		
γ	15.0	no data available						
c'	10.0							
φ'	30.0							
γ	14.0	no data available						
c'	0.0							
φ'	25.0							

(a)



(b)

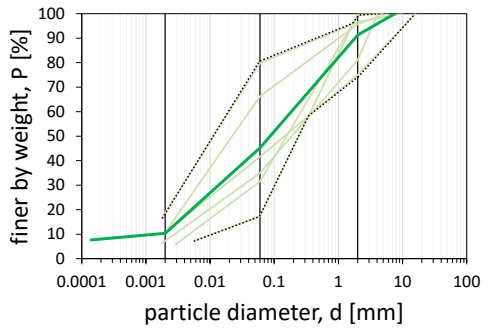


Figure 7-39: Grain-size distribution of the soil formations shown in the Table 7-14. The thicker line type refers to the average curve.

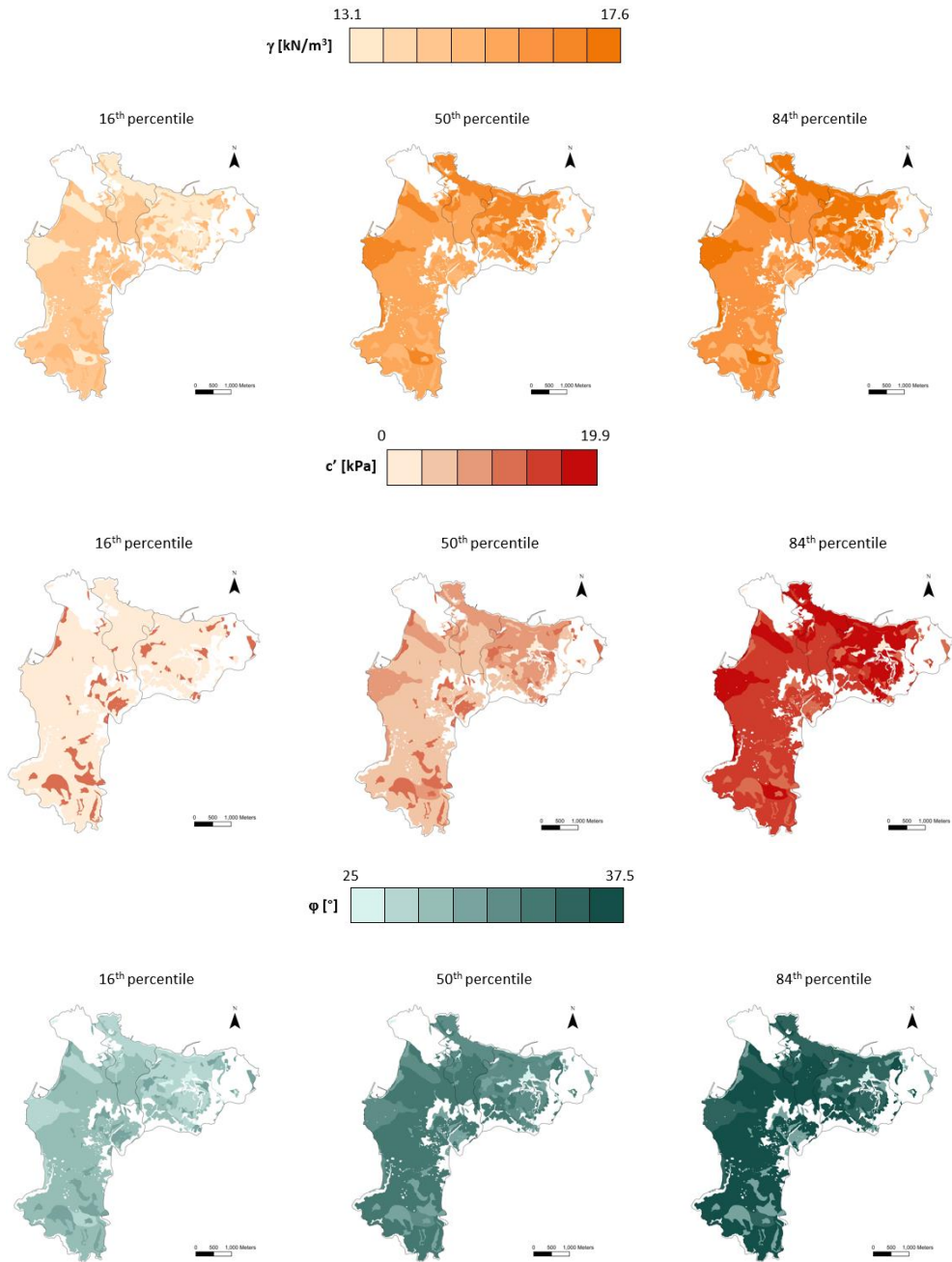


Figure 7-40: Unit weight and strength parameters maps for different percentile values.

By following the procedure shown in the Figure 7-37, it was possible to obtain susceptibility maps in terms of critical acceleration, i.e. the value above which the slope starts to move. Three different maps of critical acceleration have been obtained considering the statistical variability of the physical and mechanical properties synthesised in Table 7-14.

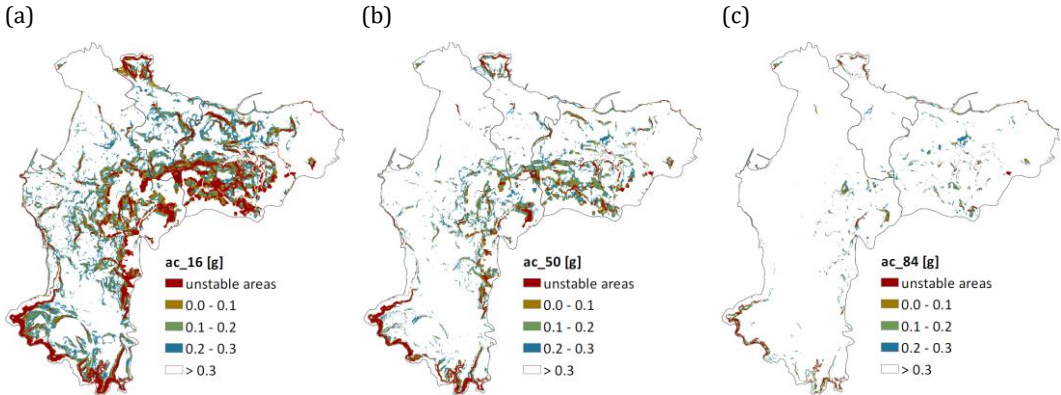


Figure 7-41: Maps of critical acceleration for 16th (a), 50th (b) and 84th (c) percentile.

By combining the critical acceleration map (Figure 7-41) with the ground motion distributions (Figure 7-3), the permanent displacements could be calculated with the semi-empirical relationship proposed by Gaudio et al. (2020):

$$d = B \cdot e^{-A \frac{a_c}{a_s}} \tag{Eq. 7-12}$$

where A and B are coefficients depending on the soil classes (Figure 7-4a) and on the range of values of the acceleration expected at surface (Figure 7-3b).

The main results of the proposed methodology are presented in the maps of Figure 7-42 in terms of spatially distributed displacements. Such displacements are classified according to five different classes, from very low (white zones) to unstable areas (red zones) corresponding to as many susceptibility classes. When considering the outcomes associated to the 16th percentile input parameters (Figure 7-42a), about 10% of the total area is characterised by earthquake-induced displacements greater than 1 m. Less conservative results are obtained considering the 50th or 84th percentile

(Figure 7-42b and Figure 7-42c), for which the unstable areas drop to the less than 4% and 1%, respectively. Therefore, the amount of territory potentially unstable in seismic conditions appears less extended than that mapped in the official landslide inventories (see Figure 2-10).

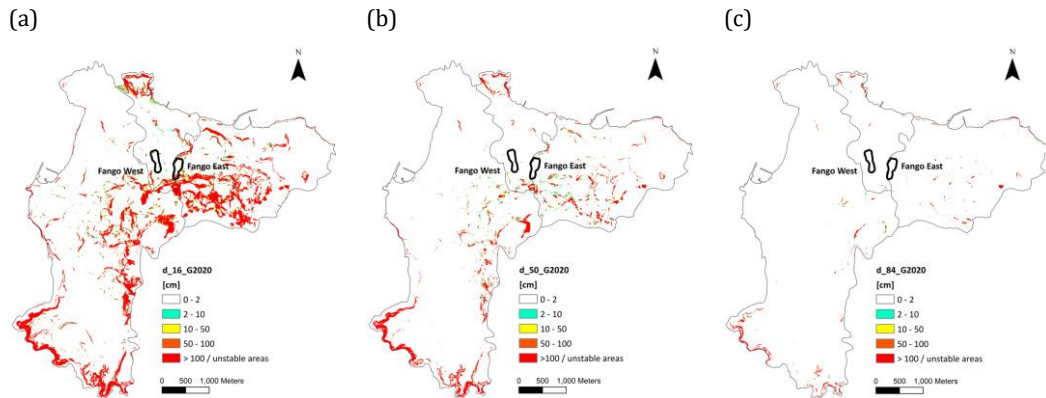


Figure 7-42: Maps of earthquake-induced displacements for 16th (a), 50th (b) and 84th (c) percentile. The same maps show the landslides within the study area.

These maps can be useful to manage the emergency after a strong-motion event and planning a priority scale of interventions to mitigate the instability risk individuating the potentially unstable areas. Leaving aside the unstable areas located south of the municipality of Forio consisting of coastal cliffs overlooking the sea, the areas where attention needs to be focused are located between the municipalities of Casamicciola and Lacco Ameno, along the slopes of Mt. Epomeo (Gargiulo et al. 2022).

The same maps show the perimeters of the landslides in the study area: as can be seen from this simplified approach, the displacements are almost negligible. These results will have to be confirmed by advanced analyses.

7.3.2 Advanced dynamic analyses with FLAC code

The numerical modeling of the studied landslide was carried out with FLAC (*Fast Lagrangian Analysis of Continua*, Itasca 2019). The materials are represented by elements, or zones, which form a grid that can be modified depending on the particular geometry of the problem. Each zone behaves according to a selected stress-strain relationship (constitutive model) provided by the user. If the material yields and the analysis is set for large strain calculations, the grid deforms consequently and moves with the material that is represented.

The accuracy of a numerical model strongly depends on the mesh size and on the choice of boundary conditions. In general, the criteria to be taken into account when building a numerical model are:

- Accuracy of the seismic wave transmission

Kuhlemeyer & Lysmer (1973) suggest that the accuracy of wave transmission in a numerical model depends on the frequency content and material properties. In particular, the maximum zone size should be less than 10 times the wavelength corresponding to the maximum frequency:

$$l_{\max} < \frac{\lambda}{10} \quad \text{Eq. 7-13}$$

Eq. 7-13 can be also written as:

$$l_{\max} < \frac{V_s}{10f_{\max}} \quad \text{Eq. 7-14}$$

where V_s is the shear wave velocity and f_{\max} the maximum frequency that needs to be transmitted in the model. The f_{\max} depends on the acceleration time series and can be found with a Fourier analysis.

- Boundary conditions

One of the main aspects of numerical models is the choice of boundary conditions and their distance from the center. Seed et al. (1975) proposed that the extension of the boundaries should be around half the width of the section length in order to ensure

wave absorption. However, beyond a certain distance, the motion should be representative of free-field conditions; in dynamic problems, this is not always modeled. In FLAC, this is accomplished by enforcing the free-field boundary condition on the sides with a 1D column that simulates the extended medium (free-field boundary). At the base of the model, the elastic half-space usually represents adequately the condition that the medium extends indefinitely. This is modelled with viscous dashpots (quiet boundary in FLAC) as described by Lysmer & Kuhlemeyer (1969). Figure 7-43 shows the section and a scheme of the boundary conditions and the mesh used in the numerical models of the case study. As reported by the FLAC manual, when the quiet boundary is used, a shear stress time history is applied at the base of the model.

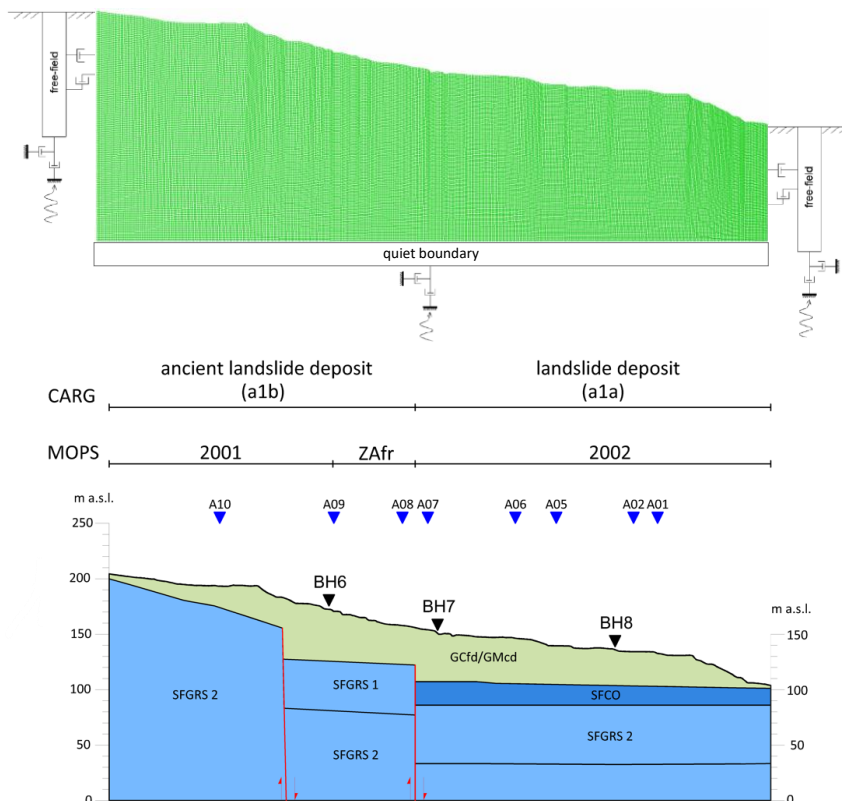


Figure 7-43: Section (above) and FLAC dynamic scheme for the boundary conditions and numerical mesh (below).

For each of the formations, it was necessary to define the physical-mechanical parameters (Table 7-15) for slope stability analyses and displacement calculations.

Table 7-15: Physical-mechanical parameters of the model for each formation identified in Figure 6-11.

	γ [kN/m ³]	c' [kPa]	ϕ [°]	V_s [m/s]	G [Pa]	K [Pa]
GC/GM	15.1	0	33.6	300	1.39E+08	6.47E+08
SFCO	20.3	25	33.0	700	1.02E+09	4.74E+09
SFGRS1	17.9	15	35.0	700	8.94E+08	4.17E+09
SFGRS2	17.9	15	35.0	974	1.73E+09	8.08E+09

In addition, it was necessary to account for nonlinear and dissipative dynamic behaviour of materials. This requires the definition of the nonlinear decay of stiffness and increase of hysteretic damping with shear strain amplitude. In this work, the hysteretic damping formulation (Itasca, 2019) has been used for the Mohr-Coulomb-type materials. It is a degradation relationship accounting for the variation of secant shear modulus, M_s , with cyclic strain amplitude, γ (Eq. 7-15).

$$M_s(\gamma) = \frac{\bar{\tau}}{\gamma} \quad \text{Eq. 7-15}$$

where:

$$\bar{\tau} = \frac{\tau}{G_0} \quad \text{Eq. 7-16}$$

Thus, if the relationship $M_s(\gamma)$ is known, the normalized tangent modulus, M_t , can be evaluated as follows:

$$M_t = \frac{d\bar{\tau}}{d\gamma} = M_s(\gamma) + \gamma \frac{dM_s(\gamma)}{d\gamma} \quad \text{Eq. 7-17}$$

The incremental shear modulus used in the simulation instead of G_0 will be given by $G_0 M_t$, where M_t is evaluated for each time increment. This reduction in the shear modulus brings about the nonlinear behaviour of the material, and therefore energy dissipation.

It is important to notice from Eq. 7-17, that $M_s(\gamma)$ must be a continuous function and that experimental data points must be fitted to it. FLAC provides some functions to match a given degradation relationship. In this case, a 4-parameters sigmoid curve (Eq. 7-18) was chosen to fit the experimental and empirical data.

$$M_s = y_0 + \frac{a}{1 + \exp\left(-\frac{L - x_0}{b}\right)} \quad \text{Eq. 7-18}$$

where a , b , x_0 , y_0 are matching parameters and $L = \log_{10}(\gamma)$.

The non-linearity curves assigned to the different materials are shown in Figure 6-12. Figure 7-44 shows the curves describing the non-linear behaviour of materials. The parameters of the Sig4 function are shown in Table 7-16.

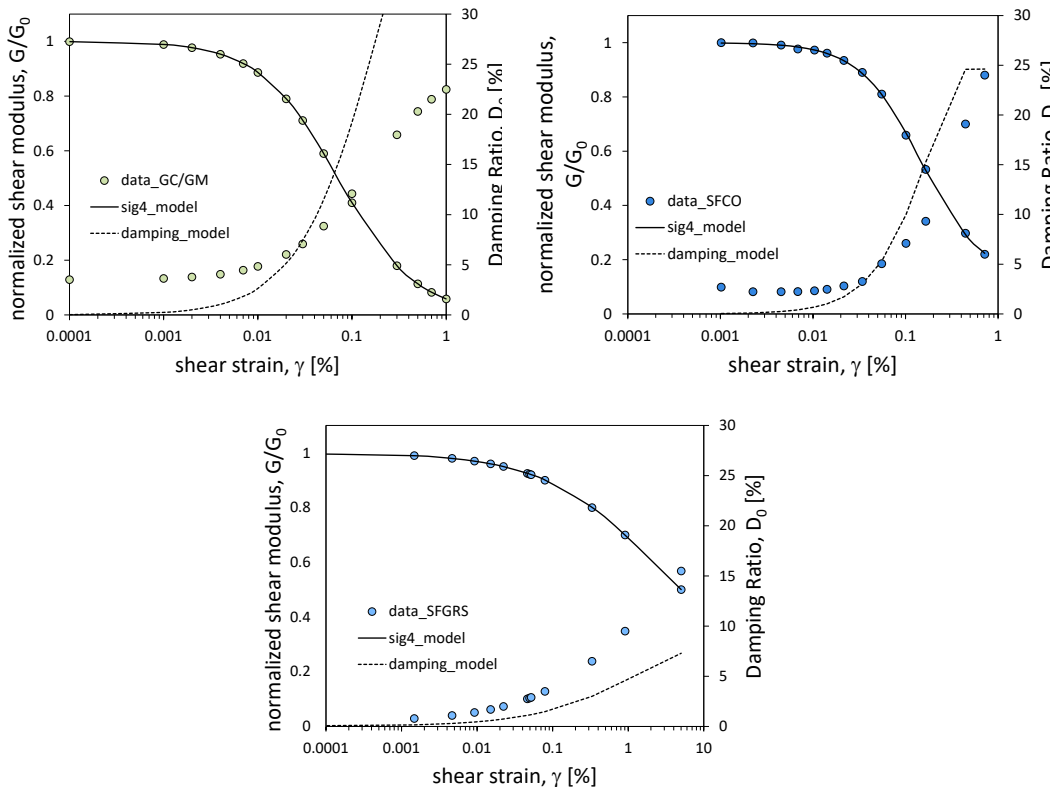


Figure 7-44: Comparison between the experimental and analytical non-linearity curves of the formations identified in Figure 6-11.

Table 7-16: Parameters of the sigmoid function for each formation.

	a	b	x₀	y₀
GC/GM	1.00000	-0.41361	-1.15036	0.00000
SFCO	0.87591	-0.33403	-0.83125	0.12409
SFGRS1/SFGRS2	0.80199	-0.73337	0.33203	0.19801

The numerical results obtained for the ‘Fango West’ landslide, using the Mohr-Coulomb model, are shown below. Instead of showing results for all ground motions reported in §7.1, in this sub-section only selected results in terms of deformation patterns and displacement fields are shown. These selected results refer to the three simulated accelerograms for which differences are visible. The results for the accelerogram 5 are given as an example since for all other code-compatible accelerograms, no or little between-model differences were observed.

Figure 7-45, Figure 7-46 and Figure 7-47 show the maximum shear strain increment and the horizontal displacements, respectively, for simulated and acc5 code-compatible accelerograms. The shear strain increment, *ssi*, is defined as follows:

$$ssi = \frac{1}{2} \sqrt{(\varepsilon_{xx} - \varepsilon_{yy})^2 + 4\varepsilon_{xy}^2} \quad \text{Eq. 7-19}$$

In Eq. 7-19 ε_{xx} , ε_{yy} , and ε_{xy} represent the horizontal, vertical, and shear strain component of the strain tensor.

These inputs produced limited *ssi* values and displacements. In any case, they show similar *ssi* and displacement values and spatial distributions. The greatest displacements occur in the highest part of the landslide with values up to 20 cm in the worst case.

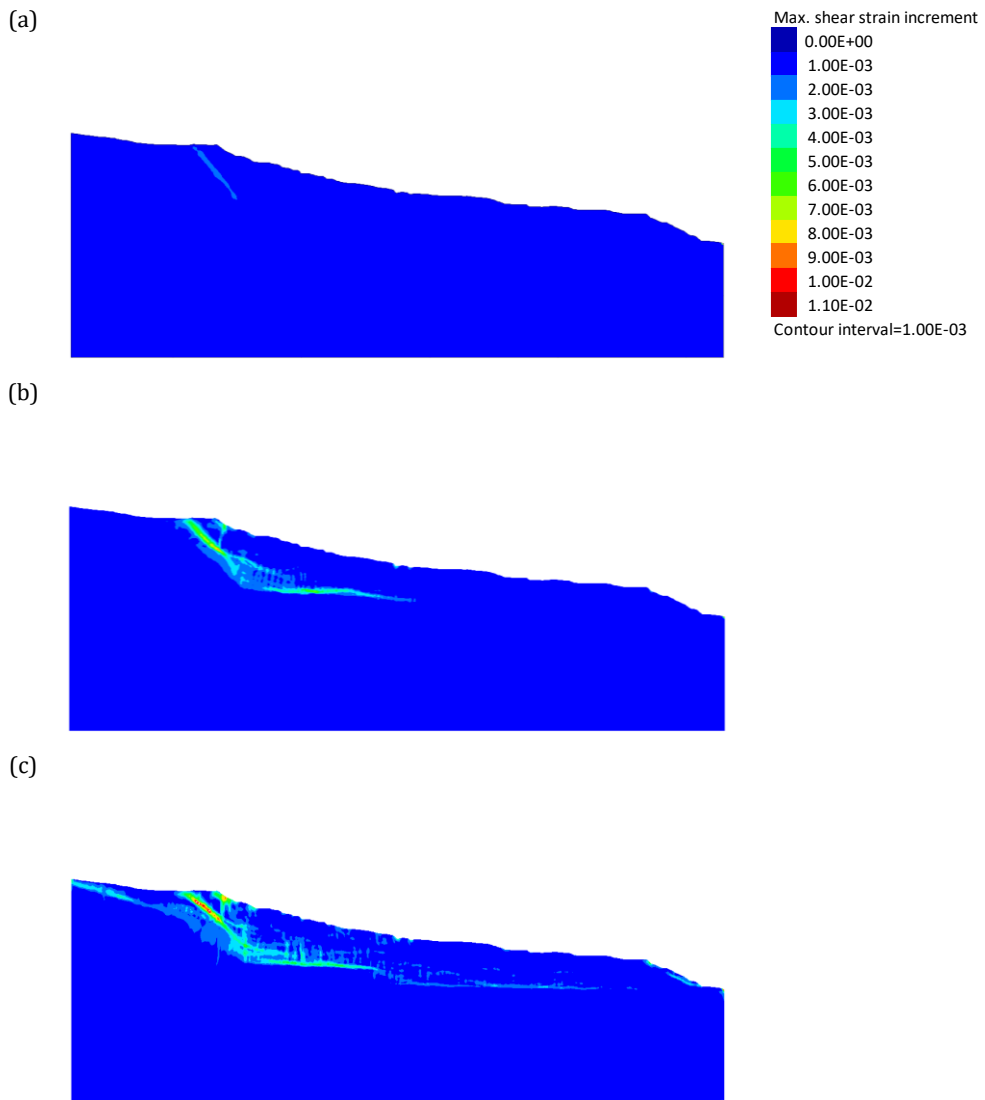


Figure 7-45: Results of advanced dynamic analysis with FLAC using as input the signals simulated with the source model of De Novellis (a), Calderoni (b) and Nazeri (c): contours of the maximum shear strain increment.

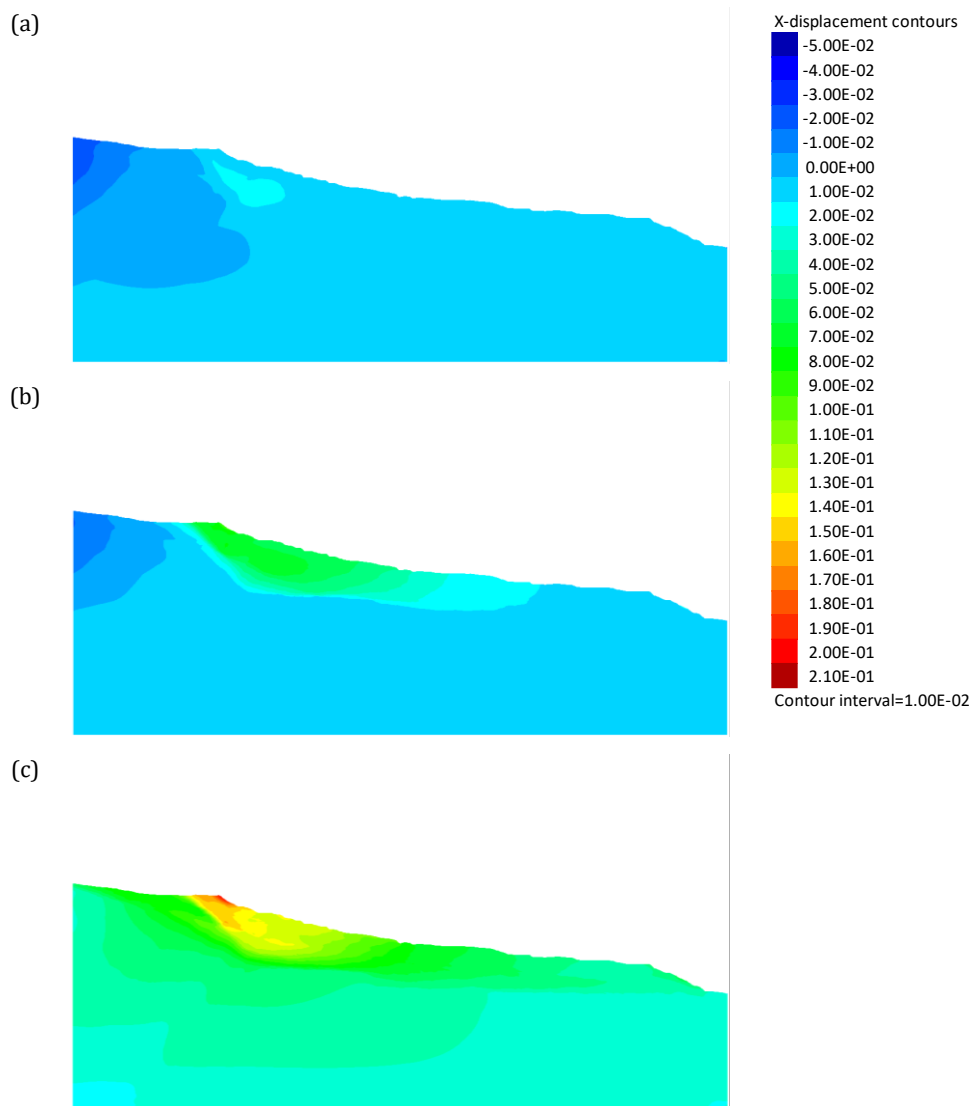


Figure 7-46: Results of advanced dynamic analysis with FLAC using as input the signals simulated with the source model of De Novellis (a), Calderoni (b) and Nazeri (c): contours of the horizontal displacements.

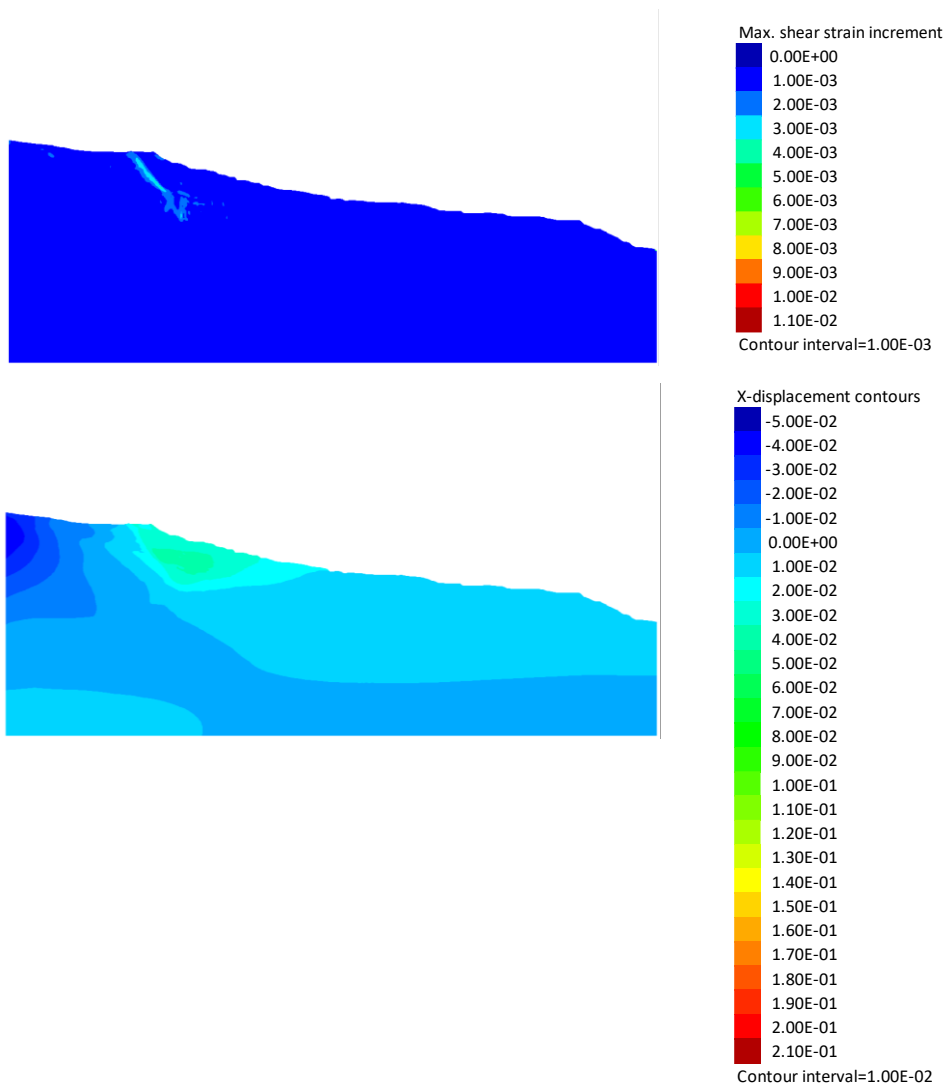


Figure 7-47: Results of advanced dynamic analysis with FLAC using as input the acc5 code-compatible accelerogram: maximum shear strain increment (above) and horizontal displacements (below) contours.

8. Conclusions

On 21 August 2017, at 20.57, a $M_w=3.91$ earthquake was felt in Ischia and the Phlegraean area of the municipality of Naples. After this event, Seismic Microzonation (SM) studies were carried out for the municipalities of Casamicciola Terme, Lacco Ameno, and Forio. They were limited to the evaluation of the transient effects of seismic motion, being the main objective for the planning and management of reconstruction process. These studies left out the evaluation of the seismic induced instability conditions of the subsoil of these three municipalities with respect to landslides and liquefaction. Nevertheless, these aspects cannot be overlooked for a sustainable land use planning of the territory, for the following reasons:

- about 48% of the area of the three municipalities, mainly along the North-West slopes of the Epomeo mountain, is classified as unstable from official national landslide archives and maps (IFFI and PAI);
- a significant part of the sandy coastline deposits of the three municipalities was classified as ‘attention zone’ for liquefaction potential by the SM studies (Toscano et al. 2019);
- fast earthflows following extreme meteoric events occurred in 2009 (Santo et al. 2012) and, very recently, in 2022, testify the significant susceptibility to instability phenomena of the shallow soil covers characterizing the above mentioned slopes, especially in the Casamicciola municipality;
- there are clear and well-documented evidences in the literature (Guadagno & Mele, 1995; Del Prete & Mele, 2006) and in national databases (CEDIT, Martino et al. 2021) of significant ground failures induced by historical earthquakes with relatively low magnitude in the territory of Lacco Ameno and Forio municipalities.

Hence, the aim of this research activity, endorsed by the Committee for the emergency management after the 2017 Ischia earthquake and self-financed by the

University of Napoli Federico II, was the study of earthquake-induced instabilities through a multi-level approach in the NW sector of the Ischia island.

For both instability mechanisms, a four-levels approach was followed. The main outcomes (or limitations) of the study will be described hereafter, following the ideal sequence described in Table 4-1, i.e.: i) definition of the seismic action, ii) subsoil characterization, iii) results of the analyses.

Reference input motion

A primary importance was given to the definition of reference input motion in terms of synthetic ground motion parameters (for Level I and Level II simplified analyses addressed to produce maps at territorial scales) and time histories of acceleration for Level III and IV dynamic analyses at the representative test sites selected. As a matter of fact, in addition to the code-compatible natural accelerograms already used for the SM studies, several synthetic accelerograms were simulated with the EXSIM code by assuming three different source models proposed by various authors for the 2017 event.

Subsoil characterization

An essential part of this work was devoted to the collection and organization of pre-existing information and new investigations carried out in the framework of the UniNA-MASLIDE project.

The starting point was the geo-lithological map and the definition of the MOPS developed in the microzonation studies, which respectively allowed to classify the field and laboratory investigations on the basis of the dominant nature of soil covers and defining the recurrent stratigraphic sequences.

The existing database of field and laboratory tests adopted for SM studies on site amplification was quantitatively and qualitatively enough populated and rather uniformly distributed on the territory of the three municipalities.

However, the field investigation dataset mainly consisted of surface and borehole geophysical tests (namely, 4 ERT, 212 HVSR, 34 MASW, 4 passive arrays, 20 Down-Hole tests) while a low amount of vertical profiles of penetration tests was available in the same areas, highlighting the deficiency of field strength data. Moreover, piezometric measurements were very poor and not recorded for enough continuous seasonal periods.

As a consequence, in the MASLIDE project additional environmental noise measurements and Electrical Resistivity Tomographies were executed throughout the test areas selected for slope instability and liquefaction analyses. Direct site investigations consisted of couples of boreholes drilled down to 20m and 50m, respectively, with the aim of identifying the depths of a likely sliding surface and/or of the seismic bedrock. Down-hole tests were executed in both cases, as well as SPT and CPT tests for the liquefaction test sites only. The comparison of borehole layerings with ERT contour plots, as well as the integration of the S- and P- wave velocity profiles resulting from DH tests with the fundamental frequencies resulting from environmental noise measurements were of crucial importance for the site characterization, permitting to reconstruct the stratigraphic setting and to extend the geotechnical model down to the seismic bedrock.

The existing laboratory dataset consisted of 24 grain size distributions, 24 measurements of physical properties at the natural state and 20 torsional shear tests (all of which executed for the SM studies). Static shear strength tests were indeed very few, consisting of 20 direct shear and 4 triaxial tests. It was rather surprising that, whatever the geo-lithological classification of the formation from which the samples were taken, the average grain size distribution, as well as the mean values of the unit weight and of the strength parameters, were poorly variable. Needless to say, no cyclic strength tests were available among the existing laboratory data.

Hence, for investigating on liquefaction susceptibility of the coastal shallow sandy deposits at Casamicciola, the laboratory testing program developed in this study included the execution of a monotonic and a series of cyclic simple shear tests in

undrained conditions. These latter led to an accurate definition of the cyclic resistance curves for 2 undisturbed samples of sands and silty sands retrieved at depths down to 15 m. On the same samples, the physical properties, the one-dimensional loading-unloading compressibility and the hydraulic conductivity were measured, in order to calibrate the constitutive model required for dynamic effective stress analyses. Only for one sample it was possible to measure significant values of the Atterberg limits (required for the assessment of liquefaction potential through empirical charts), being these volcanic materials mainly characterised by the presence of non-plastic ash fine content.

On the other hand, for slope stability assessment, the laboratory tests were much less numerous, consisting of the evaluation of the physical properties and of direct shear tests for the characterization of peak and residual strength.

Multi-level stability analyses

A 4-level approach was applied for both phenomena.

At territorial scale, a Level I screening criterion was adopted to map potentially liquefiable areas, by cross-referencing the information from the geo-lithological map and the mean seasonal groundwater depth desumed from the literature: as expected, the zones deserving further in-depth analyses correspond to the coastal sandy deposits of the three municipalities. In particular, the area chosen for higher level liquefaction analyses in the municipality of Casamicciola Terme falls within the 'attention area' identified by the SM studies.

The results of the dynamic and static penetrometric tests as well as Down-Hole tests were used for a critical assessment of chart-based Level II empirical methods. The CSR was evaluated from the maximum surface acceleration according to the national code (NTC 2018) approach, i.e. by multiplying the reference rock outcrop acceleration by a stratigraphic amplification factor. As an intermediate Level between II and III, the

chart-based methods were also used by assuming CSR as resulting from equivalent linear seismic response analyses in total stresses, considering both the code-compatible and simulated accelerograms as reference input motions. The resistance was not corrected to account for the presence of the fine content because, as already mentioned, the silty fraction consists of non-plastic volcanic ash. Finally, following a truly Level III approach, the cyclic stress ratio obtained from simplified dynamic analyses was compared to the cyclic resistance curves measured in the laboratory by assuming an equivalent number of cycles resulting from the application of empirical correlations with synthetic ground motion parameters.

The results obtained along the two verticals BH1 and BH2 are in substantial agreement: the safety factor is lower than unity only at the shallower depths at BH2, due to the shallower water table. However, the evaluation of both LPI (Iwasaki et al. 1978) and LSN (Tonkin & Taylor, 2013) indices lead to state that the damage potentially induced by liquefaction is expected to be low to moderate.

At Level IV, one-dimensional seismic response analyses in effective stress were carried out along verticals BH1 and BH2 with the SCOSSA-PWP code (Tropeano et al. 2019). The results of the undrained and drained analyses were reported in terms of vertical profiles of maximum acceleration, maximum shear stress and excess pore pressure ratio, r_u . The distributions of the maximum acceleration profiles show that the highest values of excess pore pressure ratio are reached in all cases between 10 and 15 m. Furthermore, the profiles of the peak value of r_u show that the excess pore pressure accumulation reaches the conventional liquefaction threshold of 0.9 in the same range of depths. From r_u profiles, both LSN (Tonkin & Taylor, 2013) and I_{AM} (Chiaradonna et al. 2020) indices were evaluated, showing that the results of advanced analyses are in agreement with previous levels: again, the LSN and I_{AM} values lead to a classification of damage between low and moderate.

It is possible to conclude that most of the analyses carried out show a liquefaction-induced damage in free-field conditions between low and moderate, with settlements

at ground level not exceeding 10 cm, the severity of which should be assessed according to the type of above ground structure.

A Level I mapping for slope stability appeared as meaningless, being the upper bound magnitude-distance curve relevant to Category II (sliding) mechanisms characterized by a magnitude threshold of 4.5, i.e. higher than the maximum potential value predictable for the seismic source, whatever its definition.

The slope stability analysis at Level II territorial scale was carried out by applying a displacement-based approach, using predictive equations calibrated through an extensive use of Newmark-type methods with reference to the Italian seismic database (Gaudio et al. 2020). The seismic action was defined using a Deterministic Seismic Hazard Analysis (DSHA), i.e. by simulating historical earthquake in terms of source location and magnitude, and implementing ground motion prediction equations specifically defined for volcanic areas (Lanzano et al. 2019). The physical and mechanical parameters of the model were statistically processed.

The results were presented through different maps, obtained by statistically varying the model parameters, individuating the areas potentially unstable in terms of earthquake-induced slope displacements. These maps can be useful to manage the emergency after a strong-motion event and planning a priority scale of interventions to mitigate the instability risk individuating the potentially unstable areas. Leaving aside the unstable areas located south of the municipality of Forio, consisting of coastal cliffs overlooking the sea, the areas where attention needs to be focused are located between the municipalities of Casamicciola and Lacco Ameno, along the slopes of Mt. Epomeo.

Level III analyses (simplified dynamic) were carried out on the slope test site at Fango hamlet. The calculated displacements are equal to zero. In fact, from the application of Newmark's method, the critical acceleration is never exceeded: this is mainly attributable to the limited slopes of the landslide under investigation.

In the end Level IV (advanced dynamic) analyses were carried out on the same slope. The results confirm what predicted by large-scale approaches, with displacements as high as 20 cm in the worst case.

9. References

Acerra C., Aguacil G., Anastasiadis A., Atakan K., et al. (2004). *Guidelines for the implementation of the H/V spectral ratio technique on ambient vibrations measurements, processing and interpretation.*

Acunzo G., Pagliaroli A., Scasserra G. (2014). *In-Spector: un software di supporto alla selezione di accelerogrammi naturali spettrocompatibili per analisi geotecniche e strutturali.* 33° Convegno Nazionale GNGTS, Bologna 25-27 Novembre 2014, volume 2, 107-114, ISBN: 978-88-940442-2-5.

AGI (2005). *Aspetti geotecnici della progettazione in zona sismica. Linee Guida.* Patron Editore, Bologna, 402 pp.

Aki K. (1967). *Scaling law of seismic spectrum.* Journal of Geophysical Research, 72(4), 1217–1231.

Alessio G., Esposito E., Ferranti L., Mastrolorenzo G., Porfido S. (1996). *Correlazione tra sismicità ed elementi strutturali nell'isola d'Ischia.* II Quaternario 9, 303–308.

Andrus R.D. & Stokoe K.H. (2000). *Liquefaction resistance of soils from shear-wave velocity.* Journal of Geotechnical and Geoenvironmental Engineering. ASCE, 126 (11), 1015-1025.

Assatourians K. & Atkinson G. (2012). *EXSIM12: A Stochastic Finite-Fault Computer Program in FORTRAN.* <http://www.seismotoolbox.ca> (last accessed November 2014).

Atkinson G. & Assatourians K. (2014). *Implementation and Validation of EXSIM (A Stochastic Finite-Fault Ground-Motion Simulation Algorithm) on the SCEC Broadband Platform.* Seismological Research Letters. 86. 48-60. 10.1785/0220140097.

Ausilio E., Costanzo A., Silvestri F., Tropeano G. (2008). *Prediction of seismic slope displacements by dynamic stick-slip analyses*. Seismic Engineering International Conference (MERCEA'08), Reggio Calabria and Messina, Italy. 1, 475-484.

Azzaro R., Del Mese S., Graziani L., Maramai A., Martini G., Paolini S., Screpanti A., Verrubbi V., Arcoraci L., Tertulliani A. (2017). *QUEST- Rilievo macrosismico per il terremoto dell'isola di Ischia del 21 agosto 2017. Rapporto finale*. Rapporto interno, DOI 10.5281/zenodo.886047.

Baratta M. (1901). *I terremoti d'Italia. Saggio di storia, geografia e bibliografia sismica italiana*. (ristampa anastatica, Sala Bolognese 1979). Torino 1901.

Biondi G., Cascone E., Rampello S. (2011). *Valutazione del comportamento dei pendii in condizioni sismiche*. Rivista Italiana di Geotecnica, 45 (1), 11-34.

Biondi G., Cascone E., Di Filippo G. (2012). *Affidabilità di alcune correlazioni empiriche per la stima del numero di cicli di carico equivalente*. Rivista Italiana di Geotecnica, 46 (2), 11-41.

Boore D.M. (1983). *Stochastic simulation of high-frequency ground motions based on seismological models of the radiated spectra*. Bulletin of the Seismological Society of America 73 (6A): 1865–1894. doi: <https://doi.org/10.1785/BSSA07306A1865>

Boore D.M. (2003). *Simulation of ground motion using the stochastic method*. Pure and Applied Geophysics, 160, 635–675.

Boore D.M. (2009). *Comparing stochastic point-source and finite-source ground-motion simulations: SMSIM and EXSIM*. Bulletin of The Seismological Society of America. 99. 10.1785/0120090056.

Boore D.M. & Thompson E. (2014). *Path Durations for Use in the Stochastic-Method Simulation of Ground Motions*. Bulletin of the Seismological Society of America. 104. 10.1785/0120140058.

Boulanger R.W. & Idriss, I.M. (2007). *Evaluation of Cyclic Softening in Silts and Clays*. Journal of Geotechnical and Geoenvironmental Engineering - J GEOTECH GEOENVIRON ENG. 133. 10.1061/(ASCE)1090-0241(2007)133:6(641).

Boulanger R.W. & Idriss I.M. (2014). *CPT and SPT liquefaction triggering procedures*. Report No UCD/GCM-14/01, University of California at Davis, California, USA.

Brune J. (1970). *Tectonic stress and the spectra of seismic shear waves from earthquakes*. J. Geophys. Res. 75, 4997–5009.

Brune J. (1971). *Correction to J. Brune (1970)*. J. Geophys. Res. 76, 5002.

Caccavale M., Matano F., Sacchi M. (2017). *An integrated approach to earthquake-induced landslide hazard zoning based on probabilistic seismic scenario for Phlegrean Islands (Ischia, Procida and Vivara), Italy*. Geomorphology, 295:235-259. doi:10.1016/j.geomorph.2017.07.010

Calderoni G., Di Giovambattista R., Pezzo G., Albano M., Atzori S., Tolomei C., Guido V. (2019). *Seismic and Geodetic Evidences of a Hydrothermal Source in the M_d 4.0, 2017, Ischia Earthquake (Italy)*. Journal of Geophysical Research: Solid Earth. 124. 10.1029/2018JB016431.

Carlino S., Cubellis E., Luongo G., Obrizzo F. (2006). *On the mechanics of caldera resurgence of Ischia Island (southern Italy)*. In C. Troise, G. De Natale, & C. R. J. Kilburn (Eds.), Mechanisms of activity and unrest at large calderas: Geol. Soc. London Sp. Publ (Vol. 269, pp. 181–193). London: The Geological Society.

Carlino S., Cubellis E., Iannuzzi R., Luongo G. (2010). *A conceptual model of geological risk in the Ischia Island (Italy): highlights on volcanic history, seismicity and flooding*.

Cassignol C. & Gillot P.Y. (1982). *Range and effectiveness of unspiked potassium-argon dating: experimental ground work and applications*. Numerical Dating in Stratigraphy, 159-179.

Castro G. (1975). *Liquefaction and cyclic mobility of sands*. J Geotech Eng Div 101(GT6): 552-569.

Celico P., Stanzione D., Esposito L., Formica F., Piscopo V., Rosa B. (1999). *La complessità idrogeologica di un'area vulcanica attiva: l'Isola di Ischia (Napoli-Campania)*. Boll. Soc. Geol. It. 118. 485-504.

Chiaradonna A., Tropeano G., d'Onofrio A., Silvestri F. (2018). *Development of a simplified model for pore water pressure build-up induced by cyclic loading*. Bulletin of Earthquake Engineering, 16(9):3627–3652. <https://doi.org/10.1007/s10518-018-0354-4>

Chiaradonna A., Lirer S., Flora A. (2020). *A liquefaction potential integral index based on pore pressure build-up*. Engineering Geology, 272, 105620.

Cubellis, E. (1985). *Il terremoto di Casamicciola del 28 luglio 1883: analisi degli effetti, modellizzazione della sorgente ed implicazioni sulla dinamica in atto*. Boll. Soc. Nat. Napoli, 94, 157-186.

Cubellis E. & Luongo G. (1998) - *Il terremoto del 28 luglio 1883. Danni, vittime ed effetti al suolo*. In: Luongo G. (ed.) *Il terremoto del 28 luglio 1883 a Casamicciola nell'isola d'Ischia*, Presidenza del Consiglio dei Ministri, Dipartimento per i Servizi Tecnici Nazionali, Servizio Sismico Nazionale.

Cubellis E., Luongo G., Marturano A. (2007). *Seismic hazard assessment at Mt. Vesuvius: Maximum expected magnitude*. Journal of Volcanology and Geothermal Research. 162. 139–148. 10.1016/j.jvolgeores.2007.03.003.

De Novellis V., Carlino S., Tramelli A., Pepe, S. et al. (2018). *The 21 August 2017 Ischia (Italy) Earthquake Source Model Inferred From Seismological, GPS, and DInSAR Measurements*. Geophysical Research Letters. 10.1002/2017GL076336.

De Rossi M.S. (1884). *Raccolta di fatti, relazioni, bibliografie sul terremoto di Casamicciola del 28 Luglio 1883 con brevi osservazioni*. *Bullettino del Vulcanismo Italiano*, 11:65-131.

de Vita S., Sansivero F., Orsi G., Marotta E. (2006). *Cyclical slope instability and volcanism related to volcano-tectonism in resurgent calderas: the Ischia island (Italy) case study*. *Engineering Geology* 86.2-3 (2006): 148-165.

Del Prete S. & Mele R. (2006). *The contribution of historical and archival research in the assessment of landslide susceptibility of Ischia island - in italian*. *Rendiconti della Società Geologica Italiana*. 2. pp. 29-47.

Evangelista L. & Santucci de Magistris F. (2011). *Upgrading the simplified assessment of the liquefaction susceptibility for the city of Naples, Italy*. Proc of the V International Conference on Earthquake Geotechnical Engineering, Santiago, 10–13 January 2011, Paper n. 8.10.

Forte (2014). *Integrated approach to the analysis of earthquake-triggered landslides and their impact on road infrastructures*. Ph.D. thesis, University of Naples Federico II.

Forte G., Fabbrocino S., Fabbrocino G., Lanzano G., Santucci de Magistris F., Silvestri F. (2017). *A geolithological approach to seismic site classification: an application to the Molise Region (Italy)*. *Bulletin of Earthquake Engineering*, 15(1):175-198, doi:10.1007/s10518-016-9960-1.

Forte G., Chioccarelli E., Falco M., Cito P., Santo A., Iervolino I. (2019). *Seismic soil classification of Italy based on surface geology and shear-wave velocity measurements*. *Soil Dynamics and Earthquake Engineering*. 122. 79-93. 10.1016/j.soildyn.2019.04.002.

Galli P. (2000). *New empirical relationships between magnitude and distance for liquefaction*. *Tectonophysics*, 324, 169-187.

Gargiulo F., Forte G., d'Onofrio A., Santo A., Silvestri F. (2022). *Seismic Performance of Slopes at Territorial Scale: The Case of Ischia Island*. In: Wang L., Zhang J.M., Wang R. (eds) Proceedings of the 4th International Conference on Performance Based Design in Earthquake Geotechnical Engineering (Beijing 2022). PBD-IV 2022. Geotechnical, Geological and Earthquake Engineering, vol 52. Springer, Cham. https://doi.org/10.1007/978-3-031-11898-2_113

Gaudio D., Rauseo R., Masini L., Rampello S. (2020). *Semi-empirical relationships to assess the seismic performance of slopes from an updated version of the Italian seismic database*. Bulletin of Earthquake Engineering. 10.1007/s10518-020-00937-6.

Golesorkhi R. (1989). *Factors influencing the computational determination of earthquake-induced shear stresses in sandy soils*. Ph.D. thesis, University of California, Berkeley, 395 pp. 1989.

Guadagno F. & Mele R. (1995). *La fragile isola d'Ischia*. Geologia Applicata e Idrogeologia. 30. 177-187.

Hanks T.C. & Kanamori H. (1979). *A Moment Magnitude Scale*. Journal of Geophysical Research, 84, 2348-2350. <http://dx.doi.org/10.1029/JB084iB05p02348>.

Harder L.F. & Boulanger R.W. (1997). *Application of K_σ and K_α Correction Factors*. Proc., NCEER Workshop on Evaluation of Liquefaction Resistance of Soils, State Univ. of New York at Buffalo, 195-218.

HAZUS (2003). *Earthquake Loss Estimation Methodology: Technical and User's Manuals*. Washington D.C. Federal Emergency Management Agency – FEMA.

Idriss I.M. (1999). *An Update to the Seed-Idriss Simplified Procedure for Evaluating Liquefaction Potential*. Proceedings of TRB Workshop on New Approaches to Liquefaction, Federal Highway Administration, Washington DC, 10 January 1999.

Idriss I.M. & Boulanger R.W. (2008). *Soil liquefaction during earthquakes*. Monograph MNO-12, Earthquake Engineering Research Institute, Oakland, CA, 261 pp.

Iervolino I. & Giorgio M. (2018). *È possibile evitare il superamento delle azioni di progetto nell'area epicentrale di terremoti forti? Is it possible to avoid exceedance of design spectra in the epicentral area of strong earthquakes?* Progettazione Sismica. 8. 10.7414/PS.8.3.25-32.

Iervolino I., Galasso C., Cosenza E. (2009). *REXEL: computer aided record selection for code-based seismic structural analysis*. Bulletin of Earthquake Engineering, 8, 339-362.

Ishihara K. (1985). *Stability of natural deposits during earthquakes*. In: Proceedings of the 11th International Conference on Soil Mechanics and Foundation Engineering. San Francisco, CA, USA, 1, 321-376.

ISSMGE (1999). *Manual for Zonation on Seismic Geotechnical Hazards (revised version)*. Technical Committee for Earthquake Geotechnical Engineering, TC4, International Society for Soil Mechanics and Geotechnical Engineering. The Japanese Geotechnical Society, Tokyo.

ITASCA (2019). *FLAC, Fast Lagrangian Analysis of Continua, User's Guide, Version 8.1*. Itasca Consulting Group, Inc., Minneapolis, MN.

Iwasaki T., Tatsuoka F., Tokida K., Yasuda S. (1978). *A practical method for assessing soil liquefaction potential based on case studies at various sites in Japan*. Proceedings 2nd International Conference on Microzonation National Science Foundation, Washington, DC.

Johnston-Lavis H. J. (1885). *Monograph of the earthquakes of Ischia*.

Kanamori H. & Anderson D. (1975). *Theoretical Basis of Some Empirical Relations in Seismology*. Bulletin of the Seismological Society of America. 65. 1073-1095.

Keefer D.K. (1984). *Landslides caused by earthquakes*. Geological Society of America Bulletin, 95, 406-421.

Kottke A. & Rathje E. (2023). *Technical Manual for Strata*.

Kramer S.L. (1996). *Geotechnical Earthquake Engineering*. Prentice-Hall Inc, Upper Saddle River, NJ.

Kuhlemeyer R.L. & Lysmer. J. (1973). *Finite Element Method Accuracy for Wave Propagation Problems*. Journal of the Soil Dynamics Division, 99, 421-427.

Kuribayashi E. & Tatsuoka F. (1975). *Brief Review of Soil Liquefaction during Earthquakes in Japan*. Soils and Foundations, Japanese Geotechnical Society, 15(4): 81-92.

Lanzano G. & Luzi L. (2019). *A ground motion model for volcanic areas in Italy*. Bulletin of Earthquake Engineering. 10.1007/s10518-019-00735-9.

Lanzo G. & Silvestri F. (1999). *Risposta sismica locale: teoria ed esperienze*. Hevelius Edizioni, Benevento.

Licata V., d'Onofrio A., Silvestri F. (2018). *Microstructural factors affecting the static and the cyclic resistance of a pyroclastic silty sand*. Géotechnique, 68(5):434-441. doi:10.1680/jgeot.16.P.319.

Luongo G., Cubellis E., Obrizzo F. (1987). *Ischia - Storia di un Isola Vulcanica*.

Luongo G., Carlino S., Cubellis E., Delizia I., Iannuzzi R., Obrizzo F. (2006). *Il terremoto di Casamicciola del 1883: una ricostruzione mancata*. Alfa Tipografia, Napoli, 64 pp.

Luzi L., Puglia R., Russo E., ORFEUS, W.5. (2016). *Engineering strong motion database, version 1.0*. Istituto Nazionale di Geofisica e Vulcanologia, Observatories & Research Facilities for European Seismology.

Lysmer J. & Kuhlemeyer R.L. (1969). *Finite Dynamic Model for Infinite Media*. Journal of Engineering Mechanics Division, 95, 859-878.

Madiai C. (2009). *Correlazioni tra parametri del moto sismico e spostamenti attesi del blocco di Newmark*. Rivista Italiana di Geotecnica.

Mancini M., Caciolli M. C., Gaudiosi I., Alleanza G.A., Cavuoto G., Coltella M., Cosentino G., Di Fiore V., d'Onofrio A., Gargiulo F., Milana G., Pietrosante A., Pompa P.P., Silvestri F., Vassallo M. (2021). *Seismic microzonation in a complex volcano-tectonic setting: the case of northern and western Ischia Island (southern Italy)*. Italian Journal of Geosciences. 140. 1-26. 10.3301/IJG.2021.10.

Martino S., Prestininzi A., Romeo R.W. (2021). *Italian Catalogue of Earthquake-Induced Ground Failures (CEDIT)*.

Matasovic N. & Vucetic M. (1995). *Generalized Cyclic Degradation-Pore Pressure Generation Model for Clays*. Journal of Geotechnical Engineering, 121 (1): 33–42.

Mele L. (2020). *Experimental and theoretical investigation on cyclic liquefaction mechanisms and on the effects of some mitigation measures*. Ph.D. thesis, University of Naples Federico II.

Meletti C. & Valensise G. (2004). *Zonazione sismogenetica ZS9 – App.2 al Rapporto Conclusivo*.

Mercalli G. (1884). *I terremoti e le eruzioni dell'Isola d'Ischia*. La Rassegna Nazionale, 17, 40-52.

Molin P., Acocella V., Funicello R. (2003). *Structural, seismic and hydrothermal features at the border of an active intermittent resurgent block: Ischia Island (Italy)*. J Volcanol Geotherm Res 121:65–81. doi: 10.1016/S0377-0273(02)00412-2.

Motazedian D. & Atkinson G.M. (2005). *Stochastic finite-fault modeling based on a dynamic corner frequency*. Bull Seism Soc Am 95:995–1010.

Nappi R., Alessio G., Gaudiosi G., Nave R., Marotta E., Siniscalchi V., Civico R., Pizzimenti L., Peluso R., Belviso P., Porfido S. (2018). *The 21 August 2017 M_d 4.0 Casamicciola Earthquake: First Evidence of Coseismic Normal Surface Faulting at the Ischia Volcanic Island*. Seismological Research Letters. 89. 1323–1334. 10.1785/0220180063.

Nappi R., Porfido S., Paganini E., Vezzoli L., Ferrario M. F., Gaudiosi G., Alessio G., Michetti A. (2021). *The 2017, $M_D=4.0$, Casamicciola Earthquake: ESI-07 Scale Evaluation and Implications for the Source Model*. Geosciences. 11. 44. 10.3390/geosciences11020044.

Nardone L., Manzo R., Galluzzo D., Pilz M., Carannante S., Di Maio R., Orazi M. (2020). *Shear wave velocity and attenuation structure of Ischia island using broad band seismic noise records*. J. of Volcanology and Geothermal Research. 401.106970. 10.1016/j.jvolgeores.2020.106970.

Nazeri S., Zollo A., Adinolfi G., Amoroso O., Picozzi M. (2021). *The 2017, M_w 3.9, Ischia Earthquake (Southern Italy): Source mechanism from the modelling of seismic, geodetic, and geological data and relation to the volcano resurgence mechanism*. 10.1002/essoar.10504375.1.

Newmark N.M. (1965). *Effects of earthquakes on dams and embankments*. The V Rankine Lecture of the British Geotechnical Society, Géotechnique, 15(2):139-160.

Nocentini M., Tofani V., Gigli G., Fidolini F., Casagli N. (2015). *Modeling debris flows in volcanic terrains for hazard mapping: the case study of Ischia Island (Italy)*. Landslides 2015(12):831–846 doi:10.1007/s10346-014-0524-7.

NTC (2018). *D.M. 17/01/2018. Aggiornamento delle Norme Tecniche per le Costruzioni*. Gazzetta Ufficiale, n.42 del 20/02/2018 – supplemento ordinario n.8.

Palmieri L. & Oglialoro A. (1884). *Sul terremoto dell'isola d'Ischia della sera del 28 luglio 1883*. In Atti della Reale Accademia delle Scienze Fisiche e Matematiche di Napoli, s.II, vol.1, Napoli.

Phillips C. & Hashash Y. (2009). *Damping formulation for nonlinear 1D site response analyses*. Soil Dynamics and Earthquake Engineering. 29. 1143-1158. 10.1016/j.soildyn.2009.01.004.

Piscopo V., Lotti F., Formica F., Lana L., Pianese L. (2019). *Groundwater flow in the Ischia volcanic island (Italy) and its implications for thermal water abstraction*. Hydrogeology Journal. 28. 1-23. 10.1007/s10040-019-02070-4.

Rampello S., Callisto L., Fagnoli P. (2006). *Valutazione del coefficiente sismico equivalente*. Rapporto del Task 6.3 'Stabilità dei pendii', Consorzio ReLUIS.

Rapolla A., Paoletti V., Secomandi M. (2010). *Seismically-induced landslide susceptibility evaluation: Application of a new procedure to the island of Ischia, Campania Region, Southern Italy*. Engineering Geology. 114:10-25. doi:10.1016/j.enggeo.2010.03.006.

Robertson P.K. & Wride C.E. (1998). *Evaluating cyclic liquefaction potential using the Cone Penetration Test*. Canadian Geotechnical Journal, 35 (3):442-459.

Robertson P.K. (1990). *Soil classification using the cone penetration test*. Canadian Geotechnical Journal - CAN GEOTECH J. 27. 151-158. 10.1139/t90-014.

Robertson. P.K. (2016). *Cone Penetration Test (CPT)-based soil behavior type (SBT) classification system – an update*. Canadian Geotechnical Journal, 53 (12).

Rovida A., Locati M., Camassi R., Lolli B., Gasperini P., Antonucci A. (2022). *Italian Parametric Earthquake Catalogue (CPTI15), version 4.0*. Istituto Nazionale di Geofisica e Vulcanologia (INGV). <https://doi.org/10.13127/CPTI/CPTI15.4>

Sambridge M. (1999). *Geophysical inversion with a neighbourhood algorithm—I. Searching a parameter space*. Geophysical Journal International. Volume 138, Issue 2, Pages 479–494. <https://doi.org/10.1046/j.1365-246X.1999.00876.x>

Sanchez-Sesma F.J. (1990). *Elementary solutions for response of a wedge-shaped medium to incident SH and SV waves*. Bulletin of Seismological Society of America 80: 737–742.

Santo A., Di Crescenzo G., Del Prete S., Di Iorio L. (2012). *The Ischia island flash flood of November 2009 (Italy): phenomenon analysis and flood hazard*. J. Phys. Chem. Earth, doi:10.1016/j.pce.2011.12.004.

Sbrana A. & Toccaceli R.M. (2011). *Isola di Ischia. Foglio 464, Carta Geologica della Regione Campania, scala 1:10.000. Note Illustrative*. Regione Campania, Assessorato difesa del Suolo, pp. 216.

Seed H., Idriss I., Makdisi F., Banerjee N. (1975). *Representation of irregular stress-time histories by equivalent stress series in liquefaction analyses*.

Silvestri F. & d’Onofrio A. (2014). *Risposta sismica e stabilità dei centri abitati e infrastrutture*. Relazione generale I Sessione “Analisi e gestione del rischio sismico”. Atti del XXV Convegno Nazionale AGI: La Geotecnica nella difesa del territorio e delle infrastrutture dalle calamità naturali.

Silvestri F. & Santucci de Magistris F. (2015). *Liquefazione dei terreni e instabilità dei pendii in condizioni sismiche*. In “Gestione e mitigazione dei rischi naturali”, Doppiovoce di P. Trautteur, Napoli.

Silvestri F., Aiello V., Barile A., Costanzo A., Puglia R., Pescatore T.S., Lo Russo E., Pinto F., Tornesello D. (2006). *Analisi e zonazione della stabilità dei pendii in condizioni sismiche: applicazioni di metodi tradizionali ed avanzati ad un'area di studio*. Questioni di Ingegneria Geotecnica – Scritti in onore di Arturo Pellegrino, 2, 617-660. Hevelius, Benevento.

Silvestri F., Forte G., Calvello M. (2016). *Multi-level approach for zonation of seismic slope stability: Experiences and perspectives in Italy*. Panel report. 12th International Symposium on Landslides, Napoli (Italy), 12-19 June 2016 ‘Landslides and Engineered Slopes. Experience, Theory and Practice’ (Eds: Picarelli L., Scavia C., Aversa S., Cascini L.), 1:101-118.

Simonelli A.L. & Fortunato E. (1996). *Effects of earth slope characteristics on displacement based seismic design*. Proc. XI World Conference on Earthquake Engineering, Acapulco. Pergamon, Oxford.

Tonkin & Taylor (2013). *Canterbury Earthquakes 2010 and 2011, Land reports as at 29 February 2012*. 108 pp. Earthquake Commission.

Torgoev A., Havenith H.B., Lamair L. (2013). *Improvement of seismic landslide susceptibility assessment through consideration of geological and topographic amplification factors*. JAG 2013, 17-18/09 Grenoble, France.

Toscano A., Cuccurullo F., D'Anna A. (2019). *Microzonazione sismica di III livello del Comune di Casamicciola Terme. Relazione Illustrativa*. Piano degli studi di microzonazione sismica di III livello dei Comuni di Casamicciola, Lacco Ameno e Forio, ai sensi del D.L. 28 settembre, 109 art. 18, comma 1. <http://www.commissarioricostruzioneischia.it/Esiti-Microzonazione.html>.

Tropeano G., Gazzaneo D., Ausilio E., Silvestri F. (2012). *Parametri di intensità sismica per la stima degli spostamenti permanenti di pendii omogenei*. IARG 2012, Padova.

Tropeano G., Chiaradonna A., d'Onofrio A., Silvestri F. (2015). *An innovative computer code for 1D seismic response analysis including shear strength of soils*. Géotechnique. 66. 1-11. 10.1680/jgeot.SIP.15.P.017.

Tropeano G., Silvestri F., Ausilio E. (2017). *An uncoupled procedure for performance assessment of slopes in seismic conditions*. Bulletin of Earthquake Engineering, 15(9):3611-3637, doi:10.1007/s10518-017-0113-y.

Tropeano G., Ausilio E., Silvestri F. (2017). *Evaluation of seismic demand for earthquake-triggered landslides*. IARG 2017, Matera.

Tropeano G., Soccodato F., Silvestri F. (2018). *Re-evaluation of code-specified stratigraphic amplification factors based on Italian experimental records and numerical seismic response analyses*. Soil Dynamics and Earthquake Engineering. 10.1016/j.soildyn.2017.12.030.

Tropeano G., Chiaradonna A., d'Onofrio A., Silvestri F. (2019). *A numerical model for non-linear coupled analysis on seismic response of liquefiable soils*. Computers and Geotechnics, 105: 211-227. <https://doi.org/10.1016/j.compgeo.2018.09.008>

Varnes D.J. (1978). *Slope movement, types and processes*. In: Landslides, Analysis and Control, Schuster R.L. and Krizek R.J. (Eds.). National Academy of Science, Report 176, Washington DC, 11-35.

Vezzoli L. (1988). *Island of Ischia*. Quaderni de La Ricerca Scientifica 114 (10). CNR, Roma, pp 1–134.

Wathelet M. (2008). *An improved neighborhood algorithm: parameter conditions and dynamic scaling*. Geophysical Research Letters, 35(9).

Youd T. & Perkins D. (1978). *Mapping Liquefaction-Induced Ground Failure Potential*. ASCE J Geotech Eng Div. 104. 433-446. 10.1061/AJGEB6.0000612.

Zhang G., Robertson P., Brachman, R. (2002). *Estimating liquefaction-induced ground settlements from CPT for level ground*. Canadian Geotechnical Journal. 39. 1168-1180. 10.1139/t02-047.

Appendix A.1

The following figures report the individual H/V recordings shown in Figure 5-24 and Figure 5-26 in terms of both amplification function and azimuth.

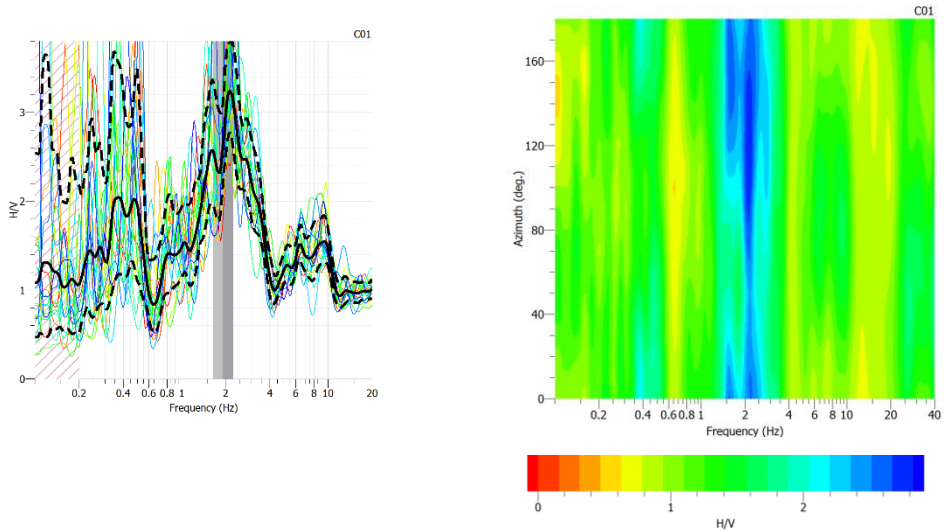


Figure A.1-1: C01 HVSR curve (left) and azimuth graph (right).

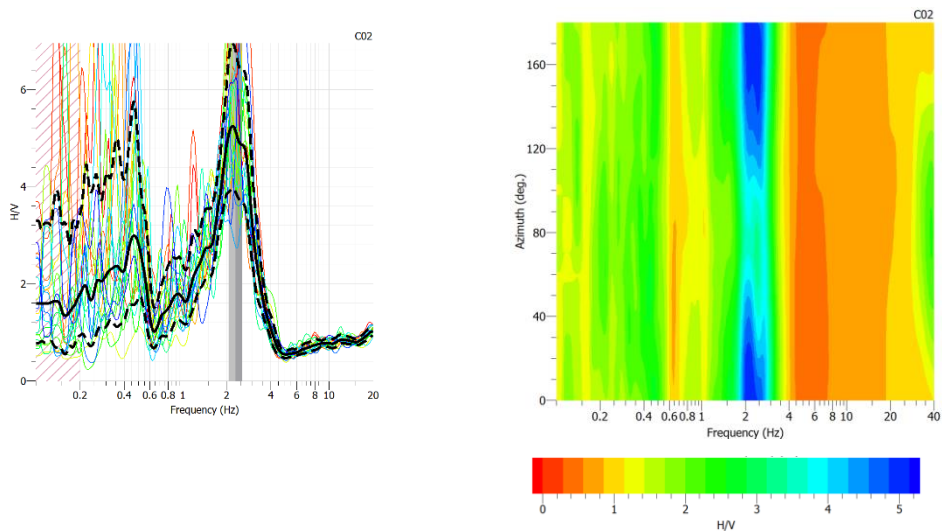


Figure A.1-2: C02 HVSR curve (left) and azimuth graph (right).

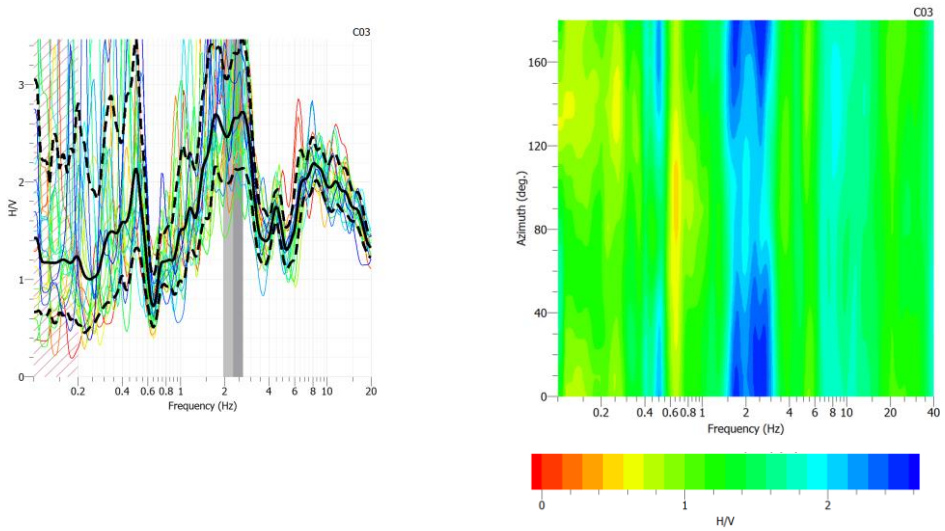


Figure A.1-3: C03 HVSR curve (left) and azimuth graph (right).

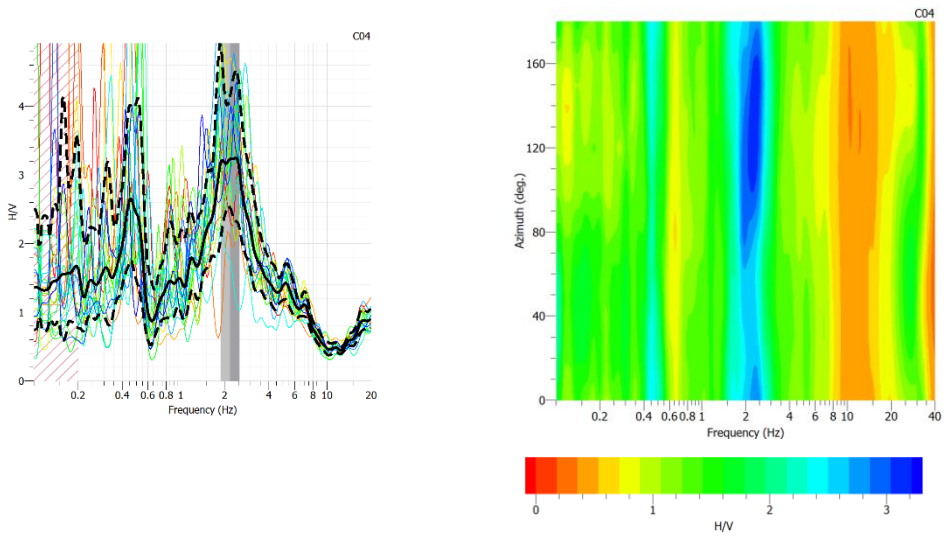


Figure A.1-4: C04 HVSR curve (left) and azimuth graph (right).

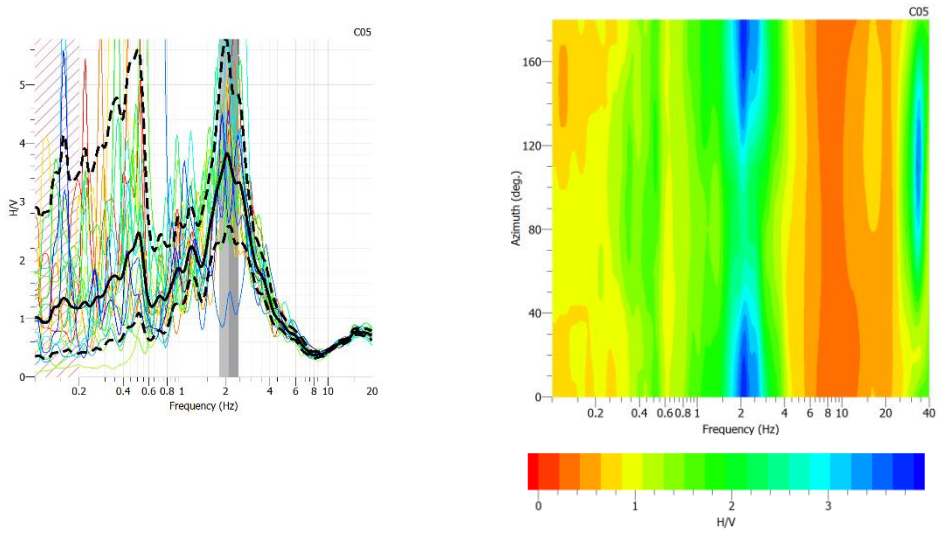


Figure A.1-5: C05 HVSR curve (left) and azimuth graph (right).

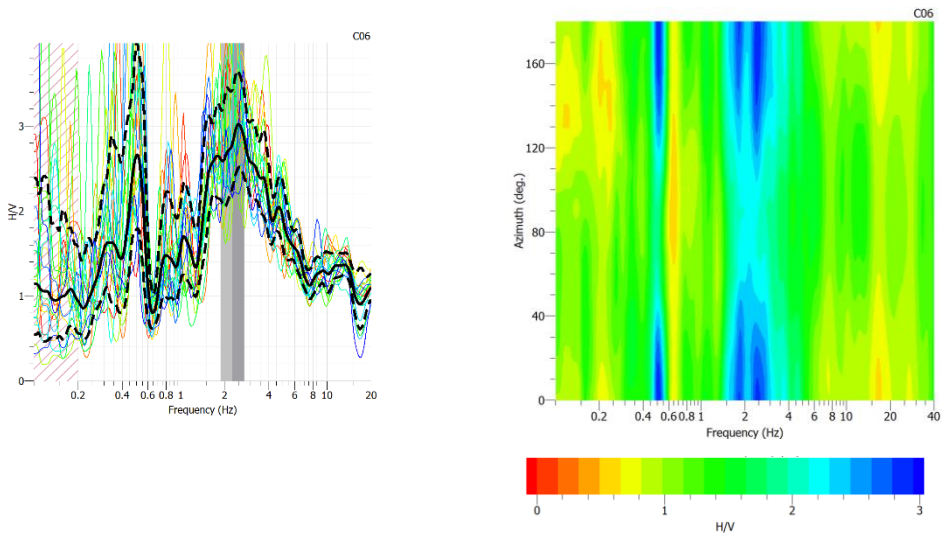


Figure A.1-6: C06 HVSR curve (left) and azimuth graph (right).

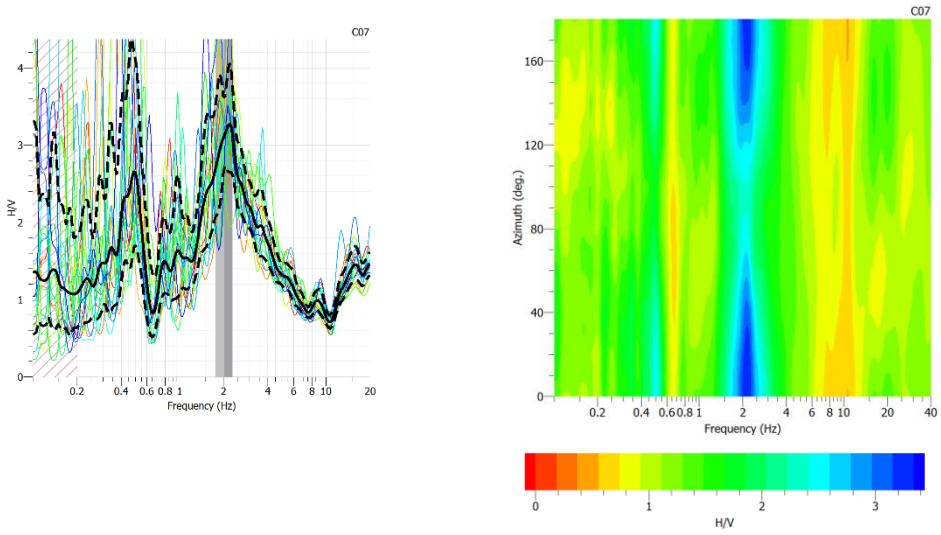


Figure A.1-7: C07 HVSR curve (left) and azimuth graph (right).

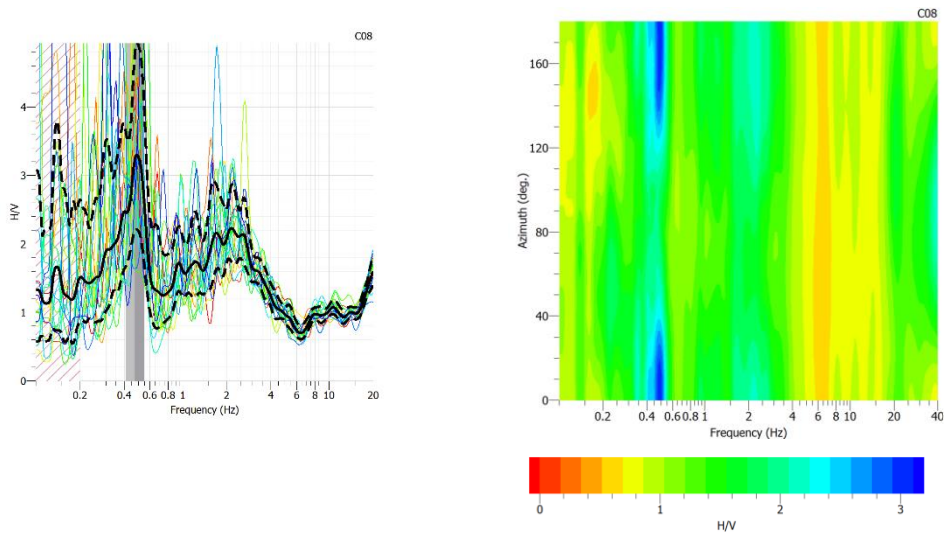


Figure A.1-8: C08 HVSR curve (left) and azimuth graph (right).

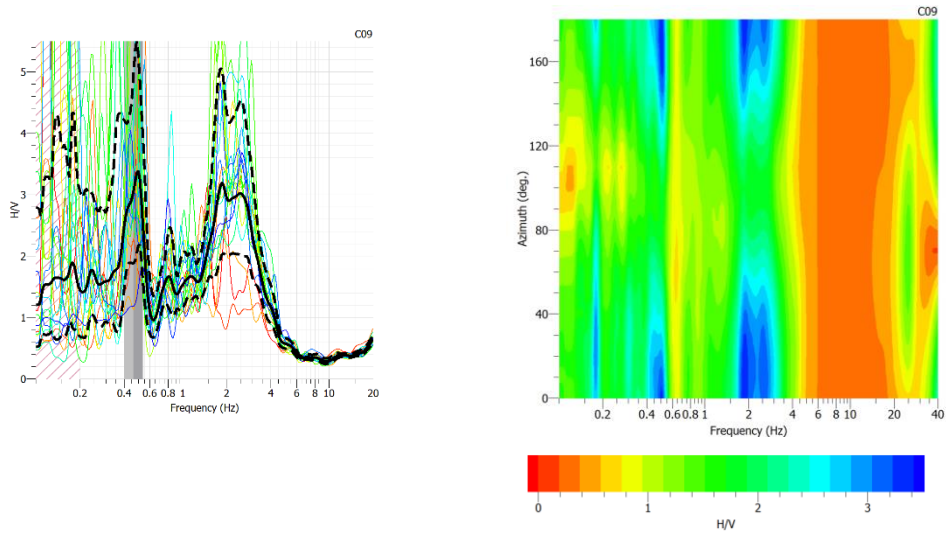


Figure A.1-9: C09 HVSR curve (left) and azimuth graph (right).

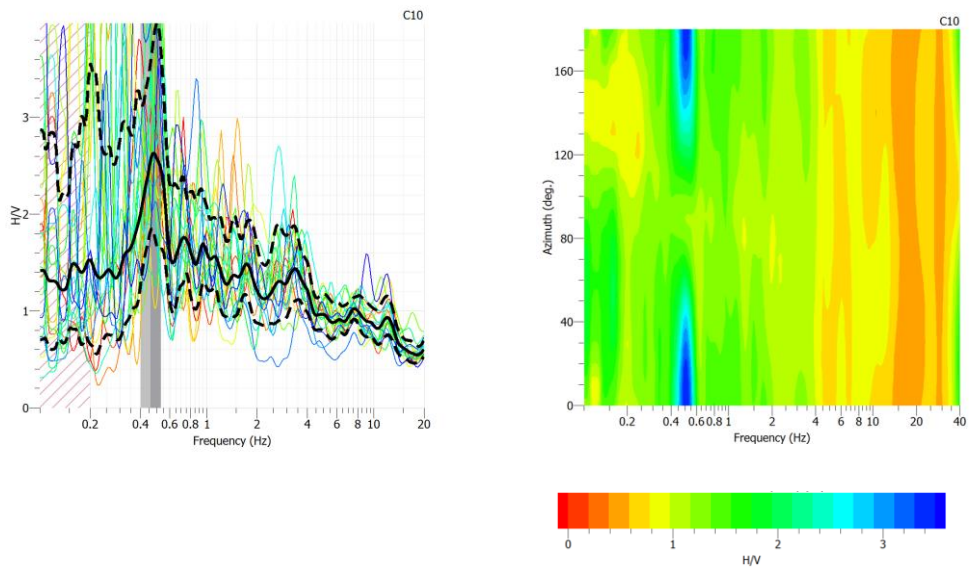


Figure A.1-10: C10 HVSR curve (left) and azimuth graph (right).

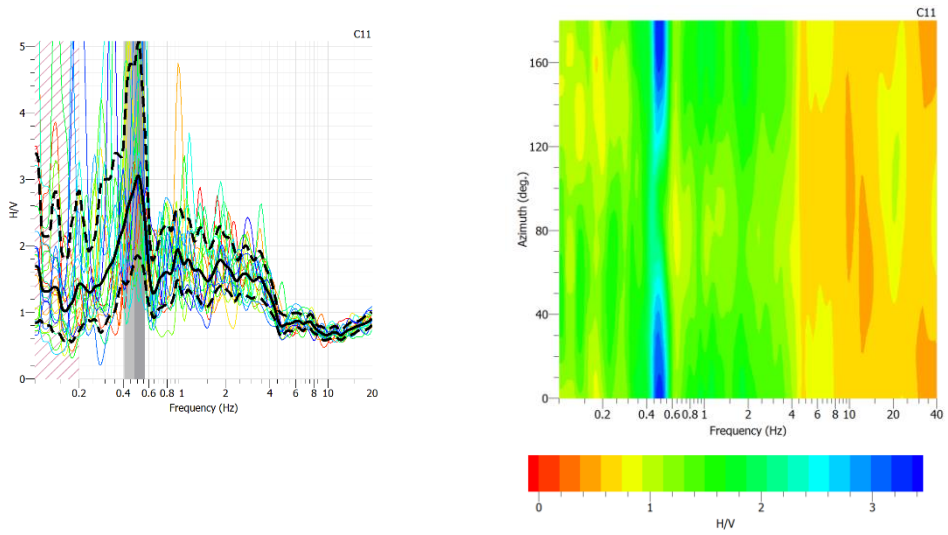


Figure A.1-11: C11 HVSR curve (left) and azimuth graph (right).

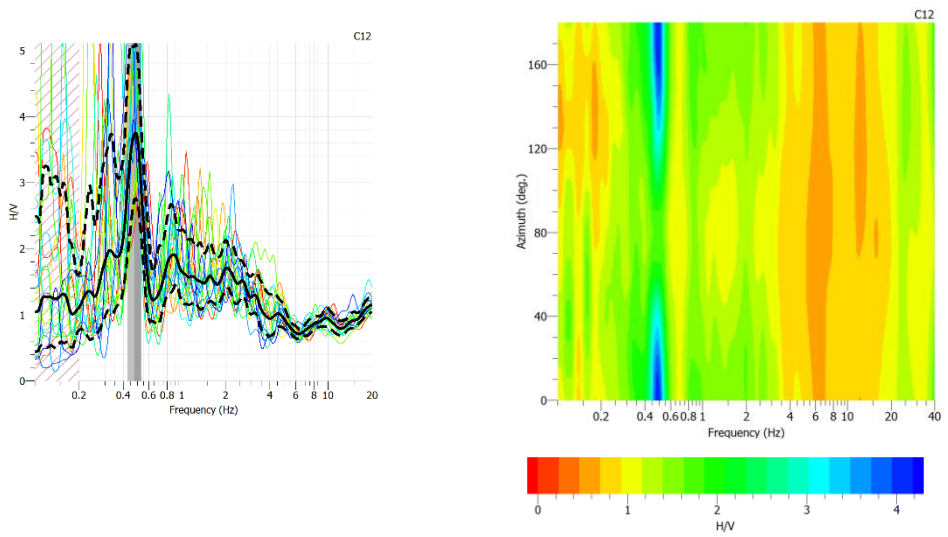


Figure A.1-12: C12 HVSR curve (left) and azimuth graph (right).

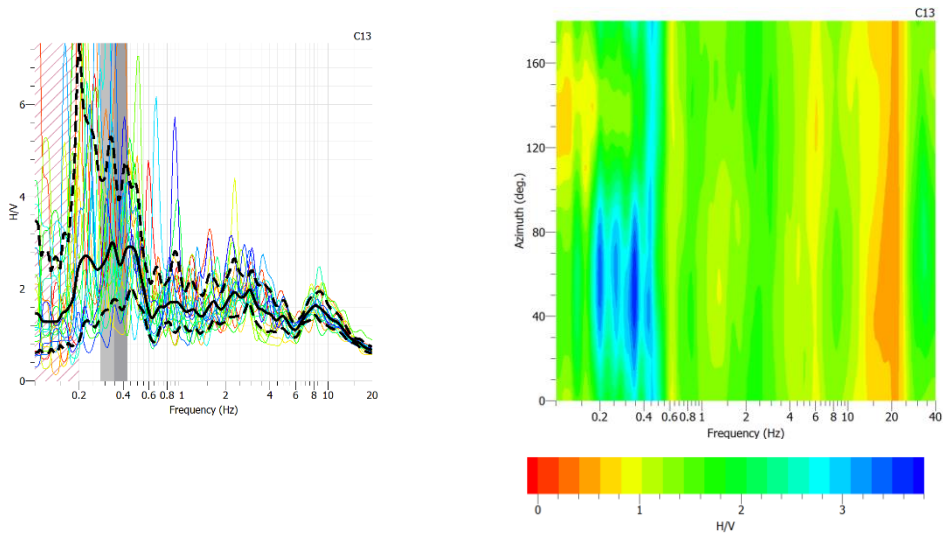


Figure A.1-13: C13 HVSR curve (left) and azimuth graph (right).

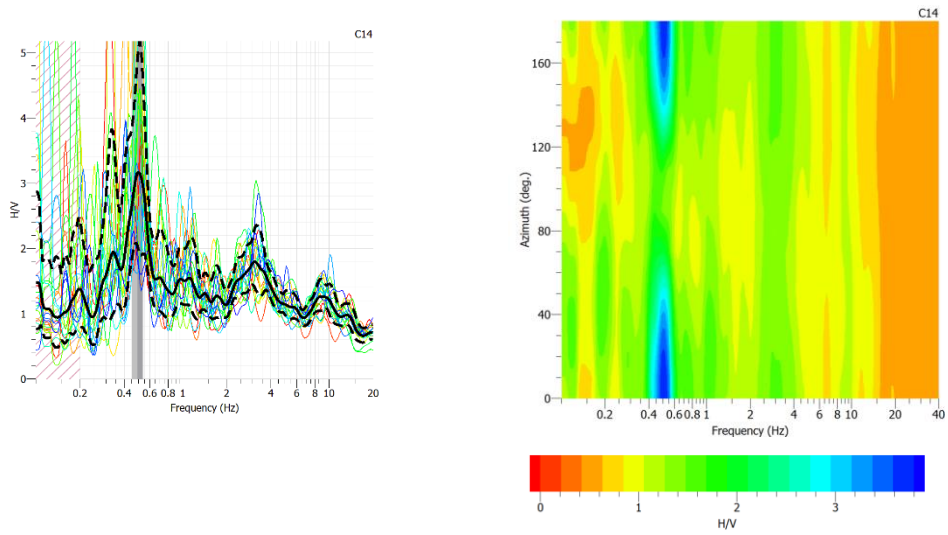


Figure A.1-14: C14 HVSR curve (left) and azimuth graph (right).

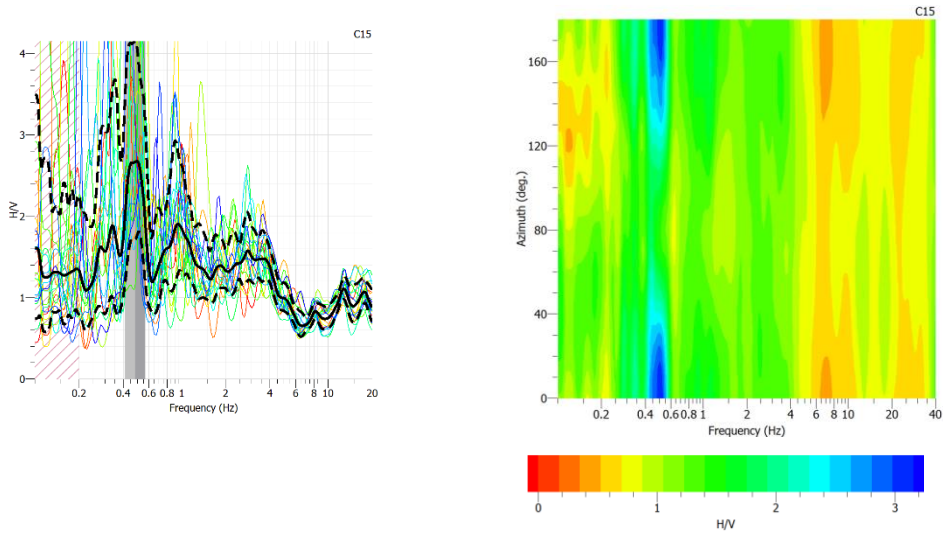


Figure A.1-15: C15 HVSR curve (left) and azimuth graph (right).

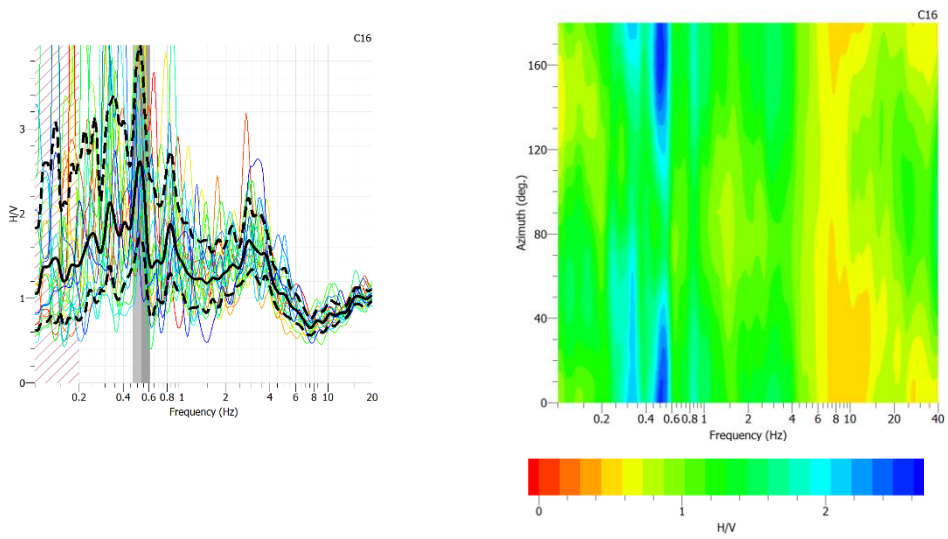


Figure A.1-16: C16 HVSR curve (left) and azimuth graph (right).

Appendix A.2

The following figures report the individual H/V recordings shown in Figure 5-75 in terms of both amplification function and azimuth.

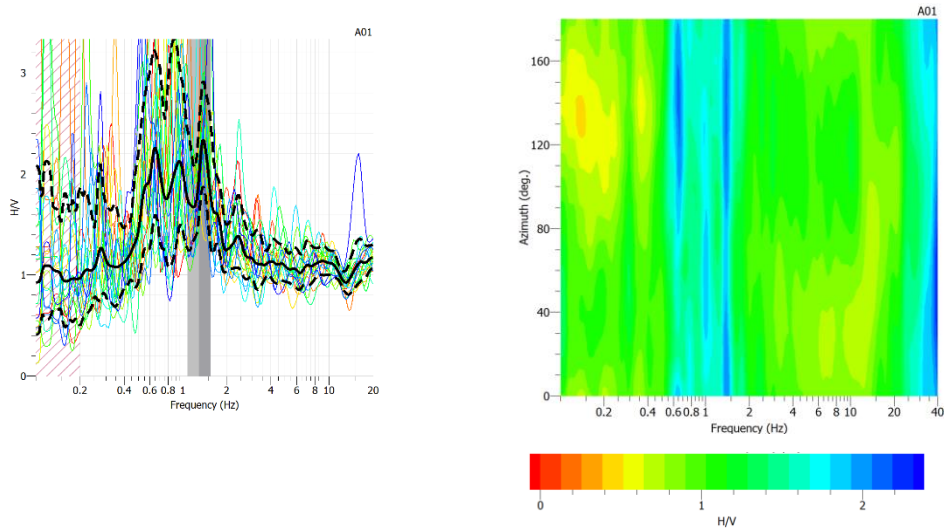


Figure A.2-1: A01 H/VSR curve (left) and azimuth graph (right).

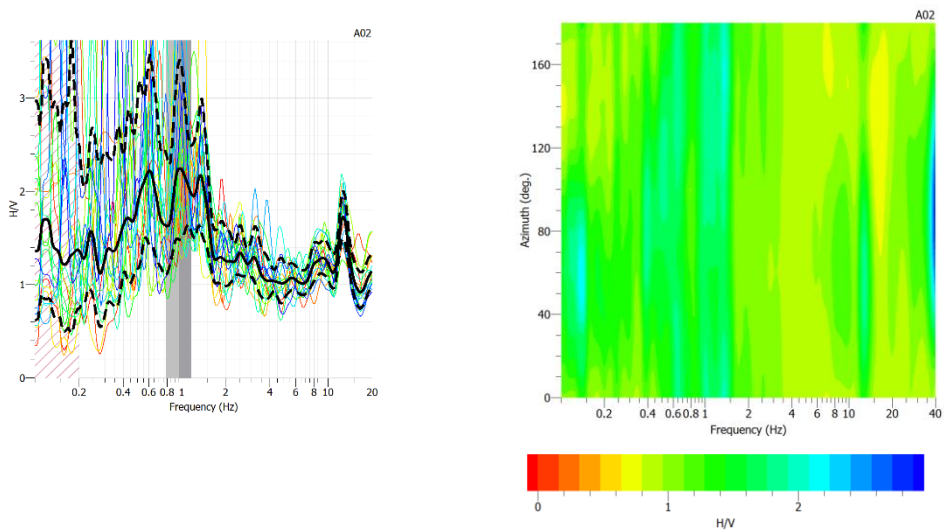


Figure A.2-2: A02 H/VSR curve (left) and azimuth graph (right).

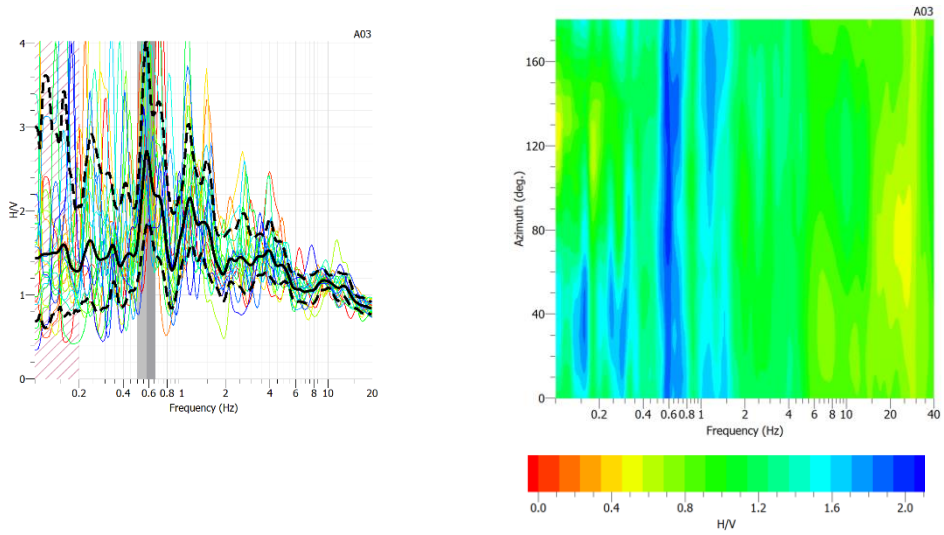


Figure A.2-3: A03 HVSR curve (left) and azimuth graph (right).

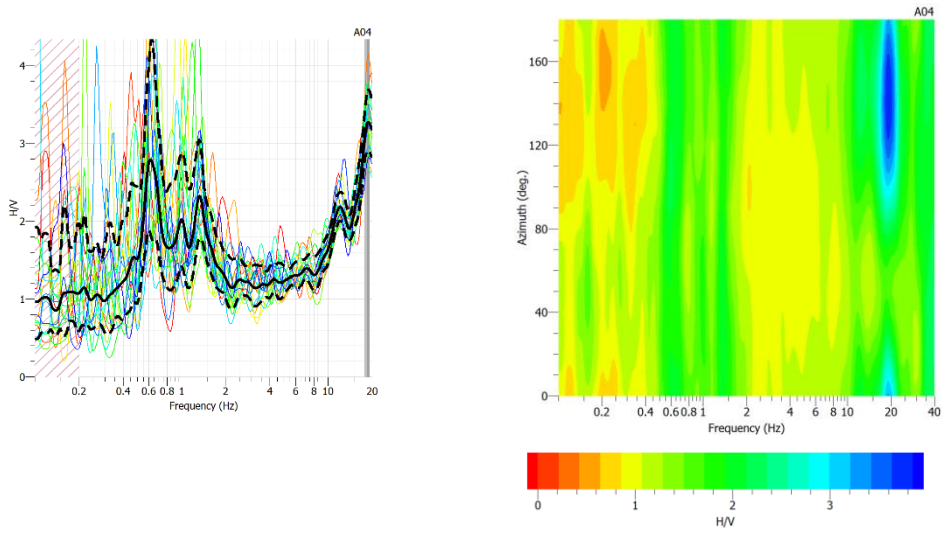


Figure A.2-4: A04 HVSR curve (left) and azimuth graph (right).

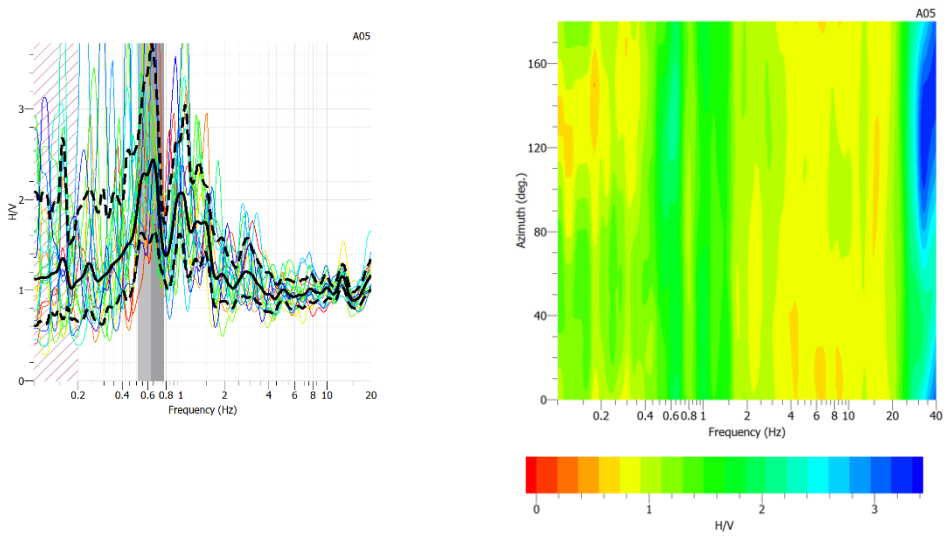


Figure A.2-5: A05 HVSR curve (left) and azimuth graph (right).

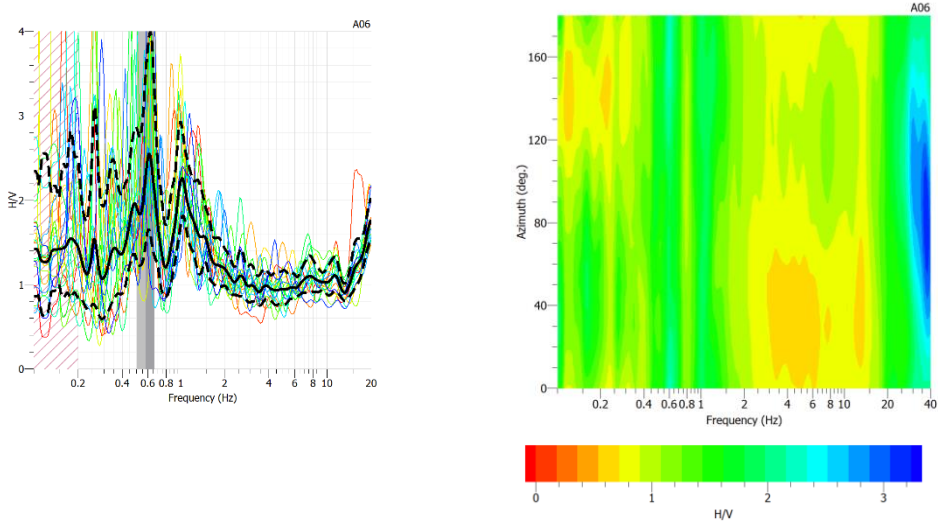


Figure A.2-6: A06 HVSR curve (left) and azimuth graph (right).

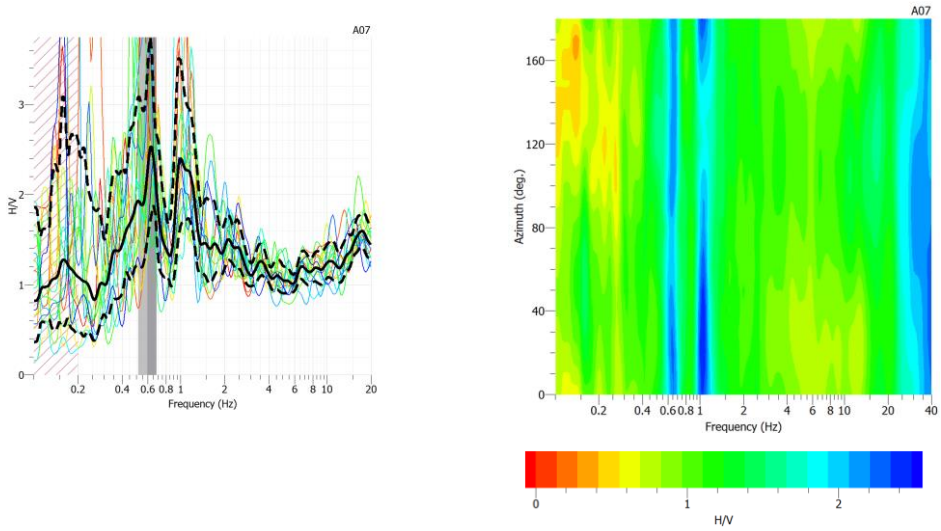


Figure A.2-7: A07 HVSR curve (left) and azimuth graph (right).

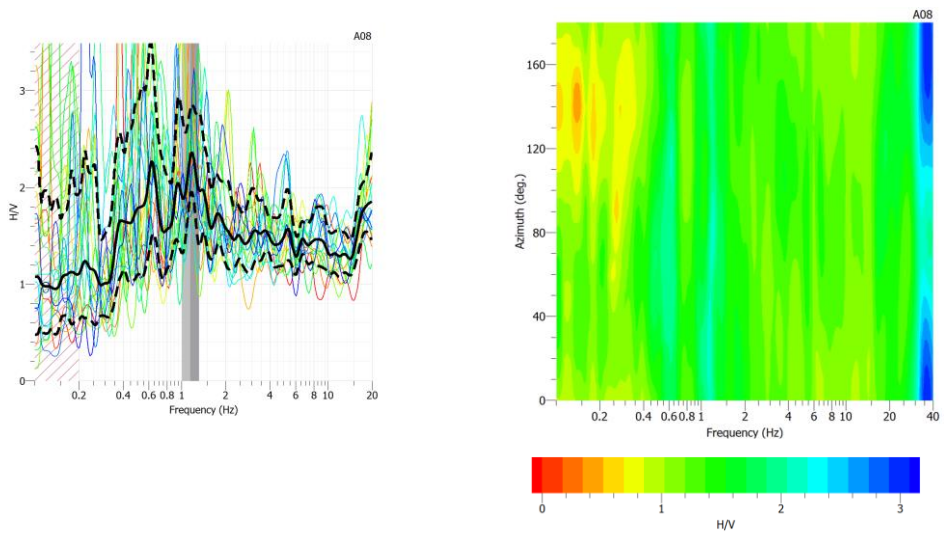


Figure A.2-8: A08 HVSR curve (left) and azimuth graph (right).

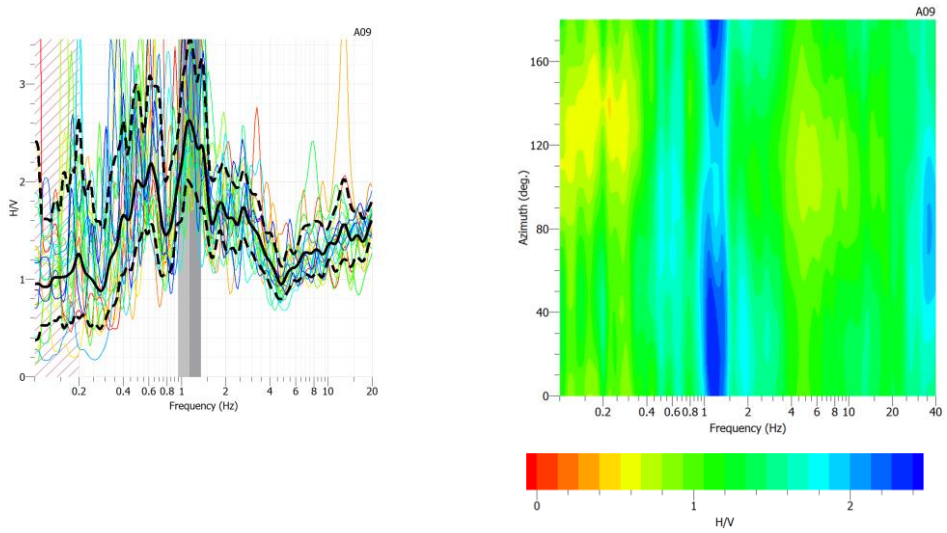


Figure A.2-9: A09 HVSR curve (left) and azimuth graph (right).

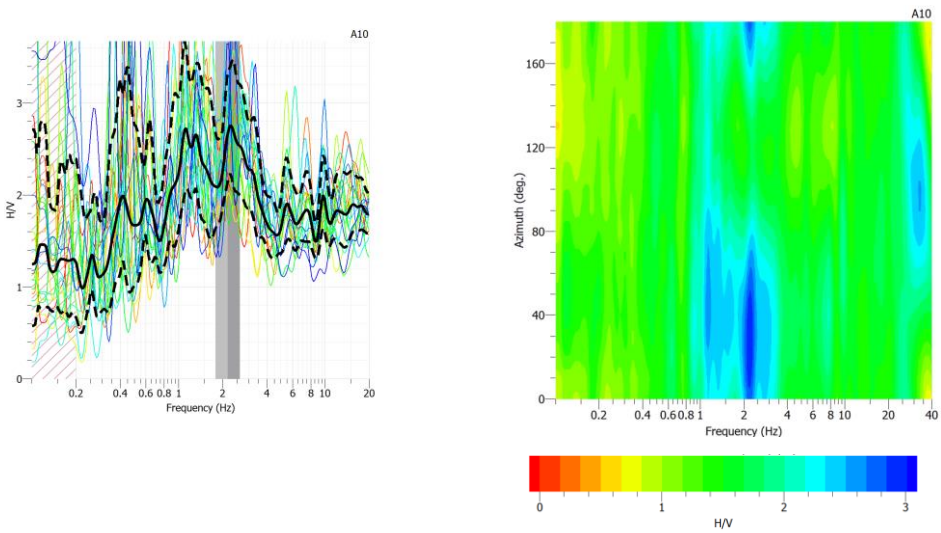


Figure A.2-10: A10 HVSR curve (left) and azimuth graph (right).

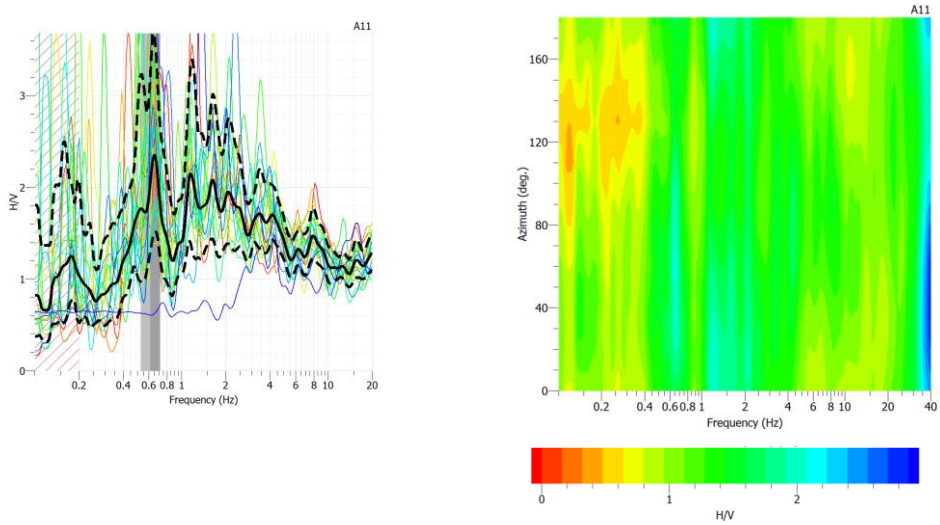


Figure A.2-11: A11 HVSR curve (left) and azimuth graph (right).

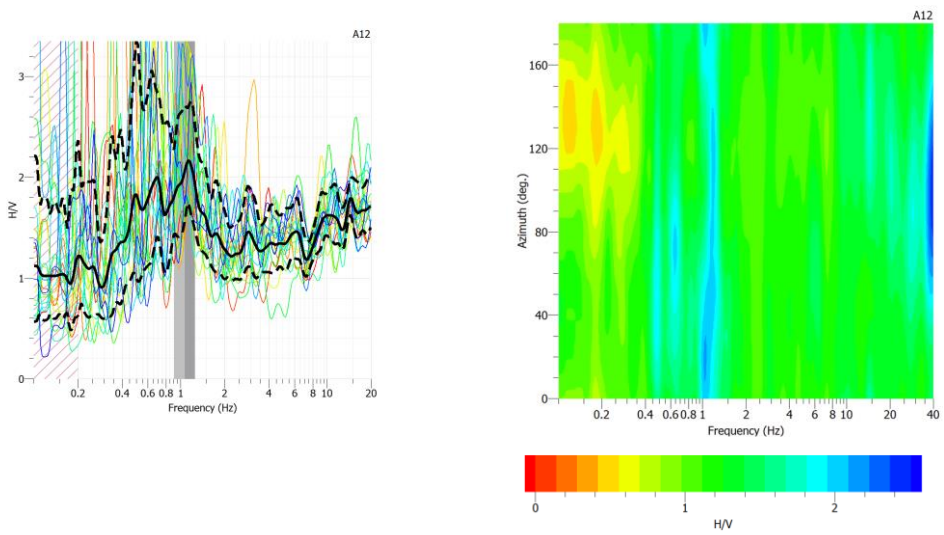


Figure A.2-12: A12 HVSR curve (left) and azimuth graph (right).

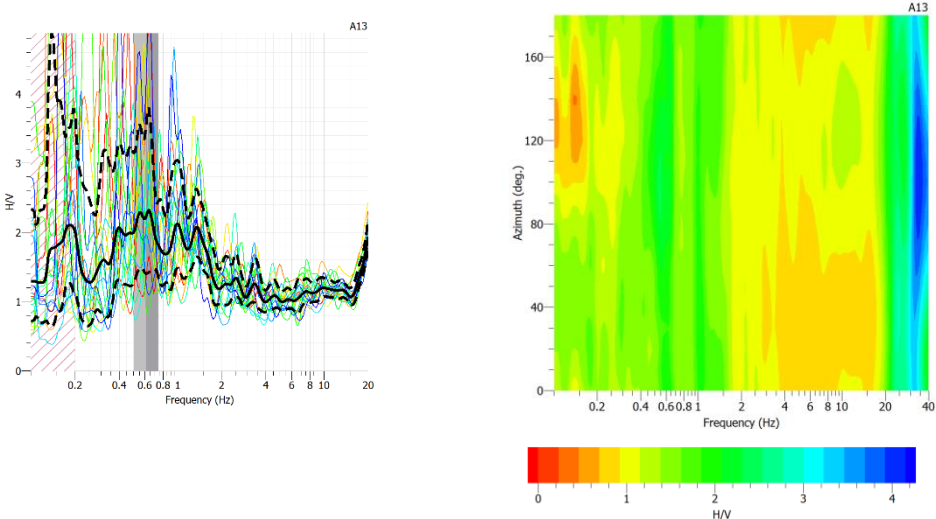


Figure A.2-13: A13 HVSR curve (left) and azimuth graph (right).

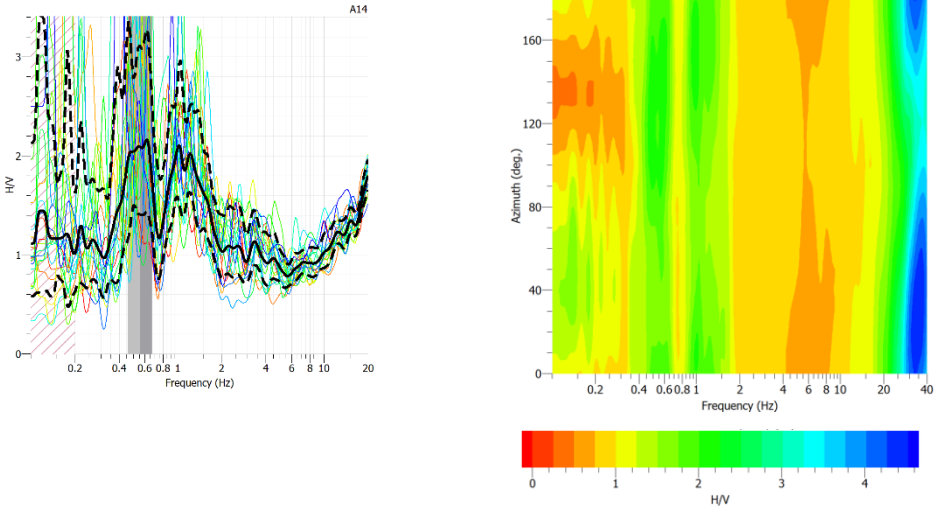


Figure A.2-14: A14 HVSR curve (left) and azimuth graph (right).

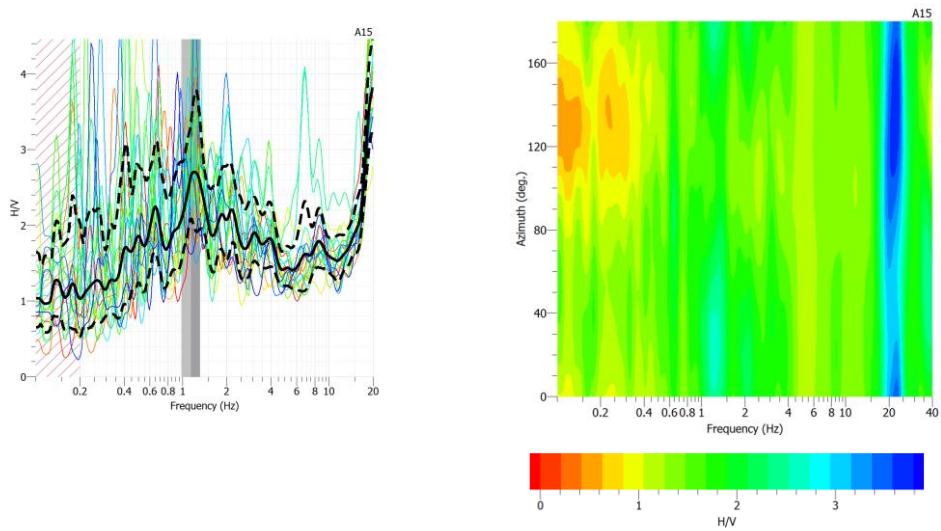


Figure A.2-15: A15 HVSR curve (left) and azimuth graph (right).